BNL 52321
UC-413
(Nuclear Physics –
DOE/OSTI-4500—R75)

PROCEEDINGS OF THE SYMPOSIUM ON RHIC DETECTOR R&D

October 10 - 11, 1991

Edited by
Y. Makdisi and A.J. Stevens

BROOKHAVEN NATIONAL LABORATORY
ASSOCIATED UNIVERSITIES, INC.
UPTON, NEW YORK 11973
UNDER CONTRACT NO. DE-AC02-76CH00016
UNITED STATES DEPARTMENT OF ENERGY

Printed in the United States of America
Available from
National Technical Information Service
U.S. Department of Commerce
5285 Port Royal Road
Springfield, VA 22161

NTIS price codes:
Printed Copy: A12; Microfiche Copy: A01

Preface

Detector R&D for the Relativistic Heavy Ion Collider has been underway for nearly three years now, a period in which the ideas for experiments at RHIC have moved from workshop sketches to fairly complete conceptual designs for large detectors. Accordingly, the R&D program is becoming less of a generic exploration of detector technologies for RHIC, and more of a focussed effort to optimize the design and implementation of specific detector types. At this juncture it seemed appropriate that the interested community take an opportunity to assess what has been learned from the program so far, and what directions are being taken in the next phase.

That was the spirit in which this Symposium was organized. The meeting provided an opportunity for public presentation of the progress and status of on-going R&D projects which are being carried out as part of the RHIC detector program, as well as other work which is relevant to the development of RHIC detectors. These proceedings include written reports of nearly all of these presentations.

Since its inception the aim of the R&D program has been to develop the detector technologies needed for experiments in the RHIC environment, and to ensure that the techniques and resources for implementing these technologies are well established within the RHIC user community. In determining the central priorities for this R&D, and evaluating individual proposals, Brookhaven Laboratory has been guided by a Detector Advisory Committee which, since its creation in 1988, has been chaired by Lee Schroeder, of Lawrence Berkeley Laboratory. Members who have served on this committee during its three-year lifetime are: Peter Braun-Munzinger of SUNY-Stony Brook, M. Breidenbach, SLAC, Howard Gordon, BNL, Hans Gutbrod, CERN/GSI, Robert Klanner, DESY, Andrew Lankford, UC-Irvine, Stan Majewski, CEBAF, and Bernhard Mecking of CEBAF.

Among the highest priorities for the R&D agenda has been the development of monolithic readout electronics to help meet the challenge posed by the high particle multiplicities in RHIC collisions, calling for detector systems with upwards of 10^5 readout channels. A number of groups have begun the work of developing compact, low-power, low-cost circuits using VLSI techniques to make it possible to amplify, store, and ultimately digitize data directly on the detector in high-density packages with very low cost per channel. In this volume are reports of work now being carried out in centers of activity that have been established at LBL, MIT, Oak Ridge and Brookhaven.

Also reported here are the development and evaluation of a number of detector technologies that are now being incorporated into designs for RHIC experiments, for which the R&D program has provided an early start. These include particle identification utilizing fine-grain time-of-flight arrays and new methods for reading out ring imaging Cerenkov and transition radiation detectors, the development of silicon detectors for tracking and multiplicity measurement near the vertex, high resolution electromagnetic calorimetry, and the refinement of real-time and off-line methods for information flow and trigger processing to cope with the high volume of data represented by each event at RHIC. In addition, a large collaboration has carried out an extensive series of measurements in particle beams at Brookhaven's AGS to optimize the design of hadron filters for muon identification at RHIC.

In the fiscal years 1989-91 a total of about 3.5 million dollars of RHIC R&D funds have gone into these efforts. In nearly every case, these funds have been supplemented by support from the institutions at which the work was being carried out. Also, a program of generic detector R&D for nuclear physics, established by the Department of Energy's Division of Nuclear Physics, has supported several projects related to the needs of RHIC experiments.

The symposium also provided a forum for presentation of detector R&D requests for fiscal year 1992. The Detector Advisory Committee met for a day following the symposium to discuss its recommendations. On the basis of the Committee's recommendations, initial allocations of R&D funds are being made to support the efforts of the STAR and PHENIX collaborations as they proceed toward final designs for the first two large detectors for RHIC.

This was the final meeting of the Detector Advisory Committee. From here on the R&D effort will focus primarily on specific projects in response to the R&D plans developed by the two large detector collaborations and the "small" RHIC experiments for which proposals are now beginning to appear. In bringing the program to this point, the Committee's work has been a big factor in defining the scope of the first research at RHIC.

Thomas W. Ludlam
January, 1992

Editors Note

The articles in these Proceedings represent an enormous diversity of topics ranging from design and development of specialized integrated circuitry to test beam measurements to novel algorithms for track finding. Rather than attempting to divide these topics into broad categories, with inevitably overlapping boundaries, the articles appear herein in the order that the oral presentations were made in the Symposium, whose agenda is reproduced on page xii. The presentations marked by an asterisk in the agenda do not have written contributions in these Proceedings.

We wish to thank the participants and contributors to these Proceedings for a successful Symposium. Special thanks are extended to Bonnie Sherwood for her tireless organizational support prior to, during, and following the Symposium. The assistance of the BNL Photography and Graphics Arts Division in preparing these Proceedings for publication is also gratefully acknowledged. All photographs were taken by Roger Stoutenburgh.

Yousef Makdisi and Alan J. Stevens

Brookhaven National Laboratory

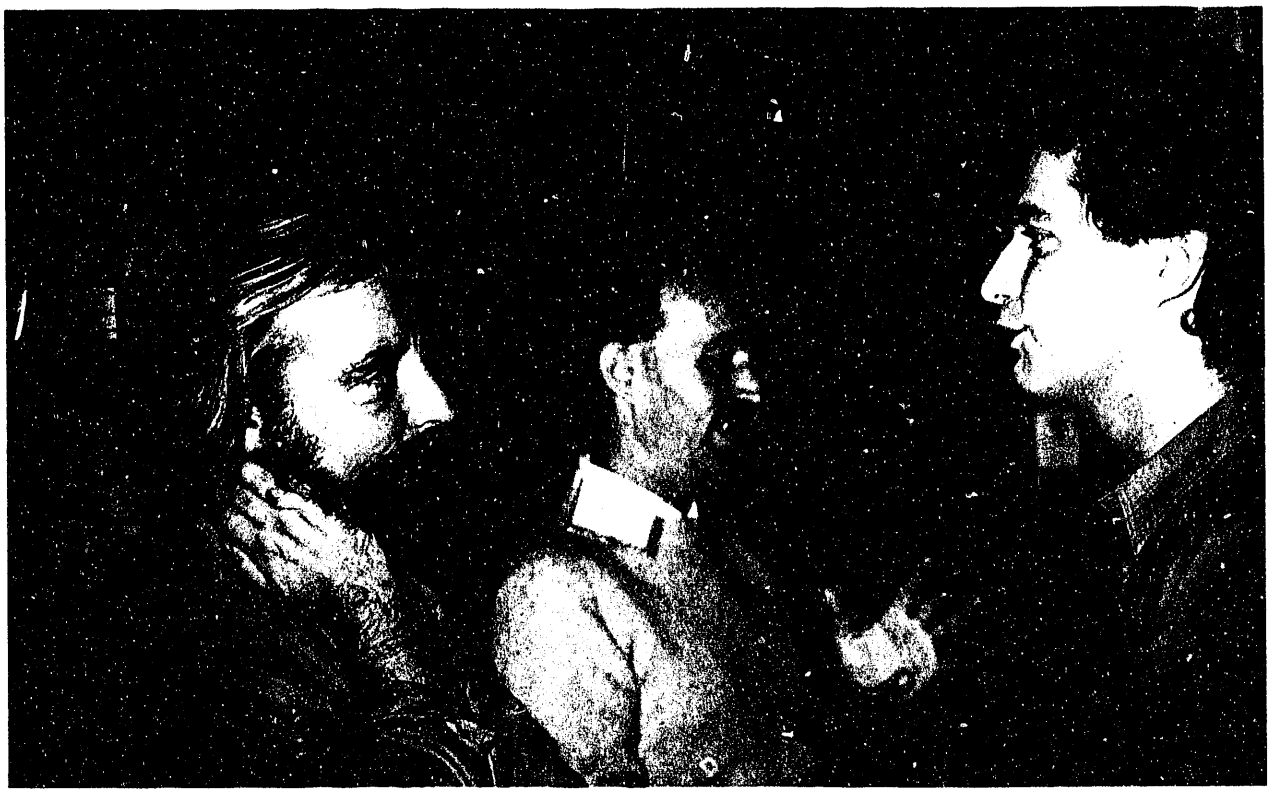

TABLE OF CONTENTS

Contributions

LIST OF PARTICIPANTS
Symposium on Detector R&D for RHIC
October 10-12, 1991

N.N. Ajitanand, SUNY-Stony Brook
Yasuyuki Akiba, BNL, Univ. of Tokyo
Peter Beery, Univ. of Calif.-Riverside
Rene Bellwied, Wayne State Univ.
Peter Bond, BNL
P. Braun-Munzinger, SUNY-Stony Brook
Chuck Britton, ORNL
Wit Busza, MIT
C.-S. Chan, BNL, CCNY
Ziping Chen, BNL
S.U. Chung, BNL
Wilfred E. Cleland, Univ. of Pittsburgh
Thomas M. Cormier, Wayne State Univ.
James B. Costales, LLNL
Efstratios Efstathiadis, BNL, CCNY
Asher Etkin, BNL
Joachim Fischer, BNL
Ken Foley, BNL
Anthony D. Frawley, Florida St. Univ.
Sean Gavin, BNL
David Goodwin, DOE-BAO
Howard Gordon, BNL
Wlodek Guryn, BNL
Hans Gutbrod, CERN, GSI
Miklos Gyulassy, LBL
Robert Hackenburg, BNL
Jerry R. Hall, Univ. of New Mexico
Clive Halliwell, Univ. of Ill.-Chicago
H. Hamagaki, Inst. for Nucl. Study, Japan
Joseph Harder, BNL
John Harris, LBL
Thomas K. Hemmick, SUNY-Stony Brook
David Hendrie, DOE
John C. Hill, Iowa State Univ.
S. Kahana, BNL
Morton Kaplan, Carnegie Mellon Univ.
Walter Kehoe, MIT
V. Paul Kenney, Univ. of Notre Dame
Paul N. Kirk, Louisiana State Univ.
Robert Klanner, DESY
T. Konstantinidis, MIT
Dennis Kovar, DOE
Martin Kramer, BNL, CCNY
H.W. Kraner, BNL
A. Lankford, Univ. of Calif.-Irvine
Micheal J. LeVine, BNL
William A. Love, BNL
Thomas W. Ludlam, BNL
Stan Majewski, CEBAF
Yousef I. Makdisi, BNL
T. Mark, McGill University, Canada
Sean McCorkle, BNL
Albert McGilvra, Michigan State Univ.
Y. Miake, Univ. of Tsukuba, Japan
Alice C. Mignerey, Univ. of Maryland
Jeffrey Mitchell, Yale
Bruce Moskowitz, BNL
Michael J. Murtagh, BNL
Shoji Nagamiya, Columbia Univ.
Nand Narain, DOE-BAO
Charles J. Naudet, LBL
Tapan Nayak, Nevis Lab., Columbia
Felix Obenshain, ORNL
Edward O'Brien, BNL
Paul O'Connor, BNL
Grazyna Odyniec, LBL
Satoshi Ozaki, BNL
Leo Paffrath, BNL
Gus Petitt, Georgia State Univ.
Franz Plasil, ORNL
Edward Platner, BNL
V.A. Polychronakos, BNL
Claude A. Pruneau, McGill Univ., Canada
Veljko Radeka, BNL
Seymour Rankowitz, BNL
Pavel Rehak, BNL
Louis Remsberg, BNL
Hans Georg Ritter, LBL

Dieter Roehrich, BNL
Mark J. Rhoades-Brown, BNL
Mark Sakitt, BNL
T.C. Sangster, LLNL
Alfred C. Saulys, BNL
Rolf P. Scharenberg, Purdue Univ.
Lee S. Schroeder, LBL
Jing Y. Shea, Univ. of Maryland
Graham C. Smith, BNL
Walter E. Sondheim, LANL
Johanna Stachel, SUNY-Stony Brook
Stephen Steadman, MIT
Eric G. Stern, Univ. of Pittsburgh
Alan Stevens, BNL
Frank W. Stubblefield, BNL
John P. Sullivan, LANL
E. Marcia Takagui, Univ. of Pittsburgh
Helio Takai, BNL
Michael Tannenbaum, BNL
Thomas Throwe, BNL
Fleming Videbaek, BNL
Andrew M. VanderMolen, Michigan State
Bernard Wadsworth, MIT
Jack Walton, LBL
Laurie Waters, LANL
Robert C. Welsh, Johns Hopkins Univ.
Sebastian N. White, BNL
Hans J. Willutzki, BNL
Alan Wintenberg, ORNL
Craig Woody, BNL
Nu Xu, SUNY-Stony Brook
Minghan Ye, BNL
James Yeck, DOE-BAO
Aki Yokosawa, ANL
Bert Yost, LeCroy Corp.
Glenn R. Young, ORNL
Bo Yu, BNL
John E. Yurkon, Michigan State Univ.
Kaihui Zhao, BNL
Y. Zhu, BNL, CCNY

Symposium on RHIC Detector R&D
October 10-11, 1991
Brookhaven Physics Department Auditorium

Agenda

Thursday, October 10

8:30 - 9:00	**REGISTRATION**	
9:00	Welcome; RHIC Project Status; * Symposium Overview *	S. Ozaki T. Ludlam
	SESSION 1 (V. Radeka, Chairman)	
9:45	IC Development for RHIC	B. Wadsworth, MIT
10:15	Monolithic Circuit Development for RHIC at ORNL	C. Britton, ORNL
10:45	**BREAK**	
11:00	Highly Integrated Electronics for a TPC Detector	H. Ritter, LBL
11:30	Monolithic Readout Development at BNL	P. O'Connor, BNL
12:00	Use of Logic Simulation Tools in Trigger Development	Eric Stern, U-Pitt.
12:30 - 2:00	**LUNCH**	
	SESSION 2 (W. Cleland, Chairman)	
2:00	Neural Network Computing Techniques for Tracking	M. Gyulassy, LBL
2:30	The Development of Silicon Multiplicity Detectors	C. Pruneau, McGill
3:00	Silicon Drift Development*	P. Rehak, BNL
3:30	**BREAK**	
	SESSION 3 (T. Hemmick, Chairman)	
3:50	Silicon Microstrip Vertex Detector	J. Sullivan, LANL
4:10	Silicon Vertex Tracker (SVT) for STAR	G. Odyniec, LBL
4:30	A Muon Filter at RHIC: Test Beam and Monte Carlo Results	G. Young, ORNL; L. Waters, LANL
5:30	End	
6:30	**Dinner, Berkner Hall**	
8:00	**Concert, Berkner Hall**	

Symposium on RHIC Detector R&D
October 10-11, 1991
Brookhaven Physics Department Auditorium

Agenda (cont'd.)

Friday, October 11

	SESSION 4 (S. Steadman, Chairman)	
9:00	Highly Segmented, High Resolution Time-of-Flight	T. Nayak, Columbia
9:30	Time-of-Flight with Silicon Avalanche Diodes	R. Scharenberg, Purdue
9:50	TPC Development for RHIC	E. Platner, BNL
10:20	Crystal Development for EM Calorimetry at RHIC	C. Woody, BNL
10:50	**BREAK**	
	SESSION 5 (H. Hamagaki, Chairman)	
11:15	Development of a TRD/Tracker	E. O'Brien, BNL
11:45	Liquid Argon Calorimeter Studies for RHIC *	D. Rahm, BNL
12:15 - 1:30	**LUNCH**	
1:30 - 5:30	**PRESENTATION OF NEW R&D PROPOSALS**	
1:30	J. Harris, LBL	STAR Collaboration
3:00	B. Wadsworth, MIT	RHIC Detector Electronics
3:20	**BREAK**	
3:35	S. Aronson, BNL	RE-2 Collaboration
4:30	F. Videbaek, BNL	RHIC Detector with Photomultiplier Readout
4:50	A. Frawley, Fla. St.	Prototype Straw Tube Detector
5:10	F. Firk, Yale	New Inorganic Scintillators
5:30	End of Symposium	

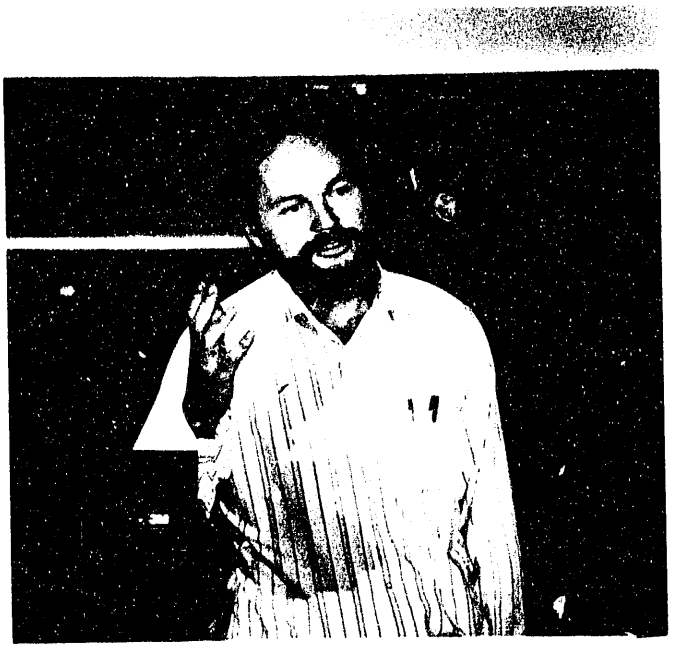

DEVELOPMENT OF ANALOG MEMORIES FOR RHIC DETECTOR FRONT-END ELECTRONIC SYSTEMS

PROGRAM SUMMARY INCLUDING IMPORTANT GOALS, CURRENT STATUS AND FUTURE PLANS

Submitted by Anastasios Konstantinidis,
Stephen Steadman and Bernard Wadsworth

Laboratory for Nuclear Science

Massachusetts Institute of Technology

9 September 1991

INTRODUCTION

Already under construction, the Superconducting Super Collider (SSC) and the Relativistic Heavy Ion Collider (RHIC) will become operational in the latter part of this decade. These collider accelerators for the next generation of high-energy and nuclear physics experiments demand detectors with very fast, highly integrated front-end electronic systems which have high channel density, low power dissipation, high reliability and an affordable cost.

While the detector electronics front-end systems for SSC and RHIC will be configured with the same design goals in mind, these goals will be achieved using different trade-offs in each case because of the marked difference in the respective machine operating parameters. For comparison, the beam crossing interval at SSC is 16nsec and the expected event rate is 100Mevents/sec; whereas, at RHIC, the corresponding numbers are 110nsec and 2k to 1Mevents/sec (Au-Au to p-p collisions). These significantly lower rates in RHIC should allow the use of more mature, less expensive technologies in front-end systems which will have lower power dissipation, higher reliability, and lower cost than their counterparts at the SSC.

We are initially concentrating on developing the switched-capacitor analog memory as the generic mechanism for storing detector signals pending generation of suitable triggers. Again, because of the more relaxed timing constraints in RHIC, the architecture of these memories should be simpler compared to corresponding devices at SSC; and it should be possible to use a technology such as a 2micron complementary metal-oxide-semiconductor (CMOS) process. Such processes are available readily and, especially for prototyping purposes, at very low cost.

So that we can eventually test these memories in a realistic setting -- in an actual detector system, we have begun to acquire some experience this year in the construction and testing of a small straw-tube array.

GOALS

Our development work is aimed at providing analog memories specifically tailored for calorimetry and particle identification applications at RHIC. We are concentrating our effort in two areas:

. Microarchitecture -- here we are experimenting at the circuit level with different configurations of the switched capacitor array. We expect to achieve at least a 13-bit dynamic range which represents the state-of-the-art as reported in the literature [1],[2]; and we hope to further improve on this. For example, if we improve the dynamic range by another factor of 4, we would be close to the 15-bit dynamic range considered desirable for calorimetry[3]. If such were the case, we could avoid the traditional dual-range solution and reduce the electronics up front by almost a factor of two. We expect to reduce the systematic sample-to-sample gain and offset variations so that the calibration load is reduced for the more demanding calorimetry applications and perhaps even eliminated for applications like pad chambers and scintillation counters. In this development, we shall be taking full advantage of RHIC's 110ns beam crossing interval in making the tradeoff between speed and accuracy.

. Macroarchitecture -- in this area, we are configuring analog memory architectures specifically for the physics and particular detector needs at RHIC. We are attempting to develop the optimal arrangement of first- and second-level memories, zero-suppression logic, multiplexing, and analog-digital conversion for these applications.

CURRENT STATUS

Personnel:

In FY91, we have had approximately 1.6 person-year equivalents(pye) assigned to this development project:

. A full-time design engineer (Konstantinidis, 1.0pye) has been working on the design of prototype chips and passing them through the silicon foundry. He also manages the workstation systems (see below); he is responsible for hardware/software maintenance, the installation of new releases of the tools, and for maintaining all the necessary documentation.

. Wadsworth (0.15pye) has been providing project direction and designing a test fixture for high performance analog memories.

. A technician (Ross, 0.2pye) is working on the layouts of multi-layer printed circuit boards required for the test fixture.

. MIT UROP* students (McNabb, Chen -- 0.3pye total) have been working on simulations of switched-capacitor circuits, on the development of special drivers required for the test fixture, and on commissioning our Tektronix LV511 integrated circuit tester, the major component of our analog memory test fixture.

. Steadman has been providing physics input for our work: he and Wadsworth have had ongoing discussions concerning the requirements for the front-end systems for MARS during the process of preparing two submissions of a Letter of Intent for that detector. In May 1991, Steadman and Wadsworth attended a 2-day conference, 'Electronics for Future Colliders', sponsored by LeCroy Corp.

Workstations and CAD tools:

This year, we upgraded our workstation facilities with the addition of a DECstation 3100 system which includes a 19-inch color monitor, 24MB memory, and 330MB internal and 1GB external hard disks. The design engineer has used this workstation almost exclusively, and the students have been using our VAX-station II/GPX system for their simulation work.

We continue to use the public domain tool-suite -- Magic, Spice, CAzM,etc. -- distributed and supported by the Massachusetts Microelectronics Center (M2C). We also have PSpice running on a 386/25MHz PC-AT compatible, and PSpice v5.0 running on the LNS central VAX computer facility.

Design and simulation:

. Spice vs CAzM: One of our first priorities was to establish confidence in an analog circuit simulator. We essentially had two options: Spice originating from UC/Berkeley, and CAzM from MCNC, Research Triangle Park, NC. Because of its superior performance in simulating a switched-capacitor test circuit, we selected CAzM. It simulates a given circuit faster than Spice, and, more importantly for our work, it treats charge more carefully. Consequently, , we use CAzM for our studies of charge injection and distribution in switched-capacitor circuits; and, for more general circuits, we also use PSpice.

---

* UROP -- Undergraduate Research Opportunities Program.

. Layout extraction: For the first half of FY91, we were somewhat hampered by the lack of a suitable layout extractor. This is the software tool which takes the geometrical data of an IC layout in combination with the parameters of the process used to fabricate the IC, and from these two derives the corresponding set of circuit elements. This set of circuit elements is then used as input to CAzM or Spice. Clearly, the results of an IC simulation are highly dependent on the performance of not only the simulator itself, but also the layout extractor.

It seems the double-poly process feature for creation of the high quality, floating capacitors needed in a switched-capacitor analog memory was sufficiently new that, at least in the public domain, no layout extractor was available to handle this feature. Fortunately, our collaborators (Alley et al.) at ORNL had anticipated this problem and had a version of an extractor available for us to beta-site test in March '91. Their software not only handles the double-poly feature in a layout, but it also does a much more satisfactory extraction of the parasitic resistive and capacitive components associated with the wiring between elements of the chip.

We have spent considerable effort this year in simulating the behavior of various switched-capacitor cell configurations. We have examined the injected charge in both grounded-capacitor and grounded-switch circuits as a function of input signal level and as a function of the relative timing of the cell switch gate drives; we have studied the effect of the various parasitic capacitances associated with the memory buses.

. New Circuit Configuration: Building on our simulation studies, we have developed a new circuit configuration which compensates for the effect of the analog bus parasitic capacitance; we call it 'the bus compensation scheme'. Briefly, the performance of a switched-capacitor analog memory which uses voltage-write/voltage-read is, in principle, independent of the cell-to-cell variation in the cell capacitance. In practice, this independence is lost because of the presence of parasitic capacitance on the bus.[4] The circuit we have developed reduces the effect of the bus parasitic capacitance by at least a factor of 10. We have used the grounded-capacitor cell configuration since it fits more naturally into this scheme; the only cell-to-cell gain variation remaining will be that due to the charge injected from the cell switch gate drives; we expect this contribution to cause a variation of about 1 part in 4,000.

. Readout Buffer: A key component of an analog memory is the readout buffer which drives the cell signal offchip. Initially, we underestimated the difficulty in obtaining a suitable buffer; we felt we could readily adapt an existing design for our needs. Such was not the case; and, having examined four different circuits up to that point, we discussed this problem with our Oak Ridge collaborators in a meeting at MIT in June. They subsequently sent us layouts of three different amplifiers they had designed, fabricated and tested; we selected the one ('AMP9B') which appeared to best suit our purposes, and we have incorporated this into our new chip design.

. Full-scale memory chip: Acting on RHIC management's encouragement to direct our work to a specific detector, we have configured a memory chip specifically for the MARS detector. The generic flavor of our work has been retained by incorporating the 'bus compensation scheme' to test the effectiveness of this approach in a working chip; but in most other respects the memory architecture has been determined by the needs of the MARS detector.

The memory is an 8-channel x 32-cell array which has multiplexed write and read cycles. The memory is generally in the write state, recording a sample for each beam crossing. For a beam crossing interval (BXI) of 110nsec, the overall delay provided by the pipeline is about 3.5usec. Keeping in mind that the accelerator engineers might increase the machine's luminosity by filling every second (rather than every third) bucket, we have based all our simulations and design on a BXI of 75nsec. In this case, the pipeline represents a delay of 2.4usec which is still adequate time, we feel, to

generate a first-level trigger in MARS. The trigger supplies a 5-bit beam crossing tag to the memory which then switches from the write state to the read state and selects the tagged cell for readout. The approach to be adopted in the MARS detector is to provide a minimum bias trigger and read all the level 1 data out to mass storage; this allows one to make more comprehensive cuts on the data off-line at a later stage. Consequently, the memory output is multiplexed to an ADC (which serves 16 channels), and the digitized data are loaded into a FIFO for transmission off the detector to the data acquisition system. [5, 6]

Again, trying to retain some of the generic flavor of our R&D, we have conceived an architecture for the front-end system such that the beam crossing tag supplied by the trigger logic serves as a cell capacitor tag -- to allow later calibration of the data on a cell-by-cell basis if required. We plan to submit this design to MOSIS for fabrication in the 16OCT91 run; we expect to receive the chips back late December.

Our submission of this design has been delayed somewhat by a revision in our thinking concerning the operating parameters for the processes we have been using. In April 1991, we became aware of a rumor that, after several months of operation, Buttler et al.[1] had observed a degradation in the performance of the analog pipelines they had developed for the Zeus calorimeter; it was said that this degradation was due to 'hot electron effects' in the region of the drains of the field effect transistors. This rumor prompted us to enquire about the process we had been using through MOSIS.

Having signed an agreement with Orbit Semiconductor, Inc.(the foundry in Sunnyvale, CA, which has been fabricating our MOSIS chips), we sought advice from the Orbit process engineer regarding safe operating conditions for their 2micron CMOS process. We had initially been told that we could safely use this process with Vdd = +5V and Vss = -5V, and we had been basing all our simulation and design work on those operating voltages. For a chip operating with 10V between the rails, the Orbit engineer recommended using a minimum gate length of 3microns (in place of the 2micron figure achievable in this process) to avoid 'short channel punchthrough'. Concerning hot electron effects, he noted that the onset of impact ionization in a 2-micron N-channel device occurs at about 7V. Impact ionization can cause charge to be injected into the gate oxide, and this in time can lead to a degradation of the device's mutual conductance and a shift in its threshold voltage. The phenomenon can also cause charge to be injected into the substrate, and this in turn can lead to parasitic bipolar action. The voltage at which the onset of this effect occurs can be raised by using what is known as a 'lightly doped drain' (LDD) -- an enhancement to the standard process which grades the field in the transistor's drain region. Such a technique reduces impact ionization effects but raises the device's ON-resistance (counter-productive for switch applications) and also the drain-source voltage at which saturation commences (counter-productive for amplifier applications). Since we are not able to consider the LDD approach -- our design tools cannot presently accommodate it; the non-standard process is more expensive; and, as we indicate, it has side effects which are at odds with other important design goals, we decided to adopt what we hope is a conservative approach: we have modified our design to use the 3micron minimum gate length, and have reduced the rail-to-rail voltage to 8V. But, clearly, we need to understand this situation somewhat better if we are to design reliable chips.

Modifying our designs -- including the standard cells we had used for our digital logic in the control section of the memory -- and redoing the simulations caused a delay of several weeks in this part of our program. But the experience is indicative of the learning process we must go through to have a proper grasp of the capabilities of this custom integrated circuit technology.

IC Fabrication:

. MOSIS: Our silicon foundry work this past year has been done almost exclusively through MOSIS using Orbit Semiconductor's 2micron CMOS processes. We have made five runs using the Tiny Chip (2.22mmx2.25mm) approach; and, as mentioned earlier, we plan one more run, closing 16 October 1991 -- a fullscale memory using the MOSIS 'small chip', which has a payload size of 4.6mmx 6.8mm and is supplied in a 40-pin DIP package.

The first two runs-- one implemented using an N-well process the other using a P-well process -- contained test structures (instances of minimum size FETs, diffusion resistances, different types of capacitors, etc). Our motivation for these first runs was two-fold:

- to gain experience in interfacing with MOSIS and in using the protocols necessary for transferring our design files from MIT to MOSIS;
- to characterize these processes and compare our results with the corresponding data supplied by MOSIS. Also, given the 510$ cost of a Tiny Chip run, we felt as beginners we could afford to make a couple of mistakes.

In the three subsequent runs, we fabricated prototype 3-channelx8-cell memories using the grounded-capacitor and grounded-switch cell configurations. The gates of the cell switches were brought directly to the chip pins to allow us to study the effect of variations in the relative timing between the gate drives to the n-FET and p-FET transistors in each cell switch.

. Massachusetts Microelectronics Center: We have access to M2C's 2micron CMOS, N-well, single poly, double metal process suitable for digital logic. The chip size is 4.6mm x 4.6mm, and the standard package is a 40-pin DIP. In runs this year, their average turnaround time has been impressive at 2 to 3 weeks. The Center is attempting to add a second poly layer to their existing process to make one that is more suitable for analog work. At their suggestion and at no cost to us, we ran three chips through the foundry to give them the opportunity to try the modifications to their process. This work is still in progress.

. Orbit Semiconductor, Inc.: In May 1991, we signed a Foresight Customer Agreement with Orbit Semiconductor, Inc., Sunnyvale, CA. This gives us direct access to the foundry processes which, up to this time, we have been accessing through MOSIS. Foresight runs have a faster turnaround (~5wks) than runs through MOSIS (~8wks), but they are more expensive for the 2-micron processes we are considering. For example:

	MOSIS			Orbit Semiconductor		
	Die size mm mm	#chips	Run cost	Die size mm mm	# chips	Run cost
'Tiny'	2.54x2.67	4	510$	2.4 x 2.4	12	1,500$
'Small'	4.83x7.11	12	2,540$	4.8 x 4.8	12	6,000$

Our primary motivation for signing the agreement at this stage has been to gain access to the process engineers at Orbit Semiconductor: in educating ourselves in this technology, we consider it important to be able to discuss some of the non-proprietary details of the process with the experts. In fact, as we mentioned earlier, this has already been a decisive factor in our work.

In spite of the increased cost, we fully intend to make use of this direct access to the Orbit processes at a later stage in our program when our chip designs are more complex and especially when we are preparing to make pre-production prototypes. It will be worth the additional money involved to be able to discuss the details of these chips first-hand with the Orbit process engineers: to be as confident as we can be about the successful outcome of these runs and the subsequent production runs.

Testing:

. Prototype chip testing: Early in the year, we received chips back from the foundry and set about testing them. We found the process parameters we were able to measure with our equipment to be in quite good agreement (generally within 5%) with those published by MOSIS. However, we found that this testing required a significant fraction of the total effort we could bring to bear on this project. At that time, we had a total of 20 chips in hand; and had we continued on that course, we would have accomplished little else than testing these initial prototypes. We therefore decided to abandon this testing (at some risk to our future results) in favor of making progress in our design and simulation work, and in the design of a test fixture for high performance analog memories. Nonetheless, this experience confirmed for us the amount of effort involved in proper testing which is an important component of any development program. At the outset of this R&D effort, we had anticipated the need for a test engineer who could work fulltime on designing test fixtures, including the necessary software, and do the testing once our program advanced to the stage of producing chips. We have now arrived at that stage and we need to get a test engineer on board so that the program can advance in a more conservative and timely fashion -- design, simulate, fabricate, test.

. Probe station: Part of the testing involves the capability of probing bare chips. In the early part of the program, such probing is required to access internal chip signals to compare practical results with those obtained earlier through simulation. It is necessary to have a high degree of confidence in the layout extractor and simulator if one wishes to effectively explore different circuit options without having to fabricate each one. In the later stages of our program, at the pre-production prototype level and beyond, we expect the probe station to play the essential role of probing chips at the wafer level.

We have made a thorough survey of probe stations from 7 vendors and we are in the process of requesting bids on a manual station. We expect this station to be delivered about the end of November.

. Test fixture for high performance analog memories: We have designed enhancements to our Tektronix LV511 integrated circuit tester which will enable us to test our analog memories at the 13- to 14-bit level. These enhancements include level shifters which take the +0.5V to +5.5V swing produced by the LV511 pin drivers and convert it to the +4V to -4V swing required by the analog memory's control inputs; and commercial, high performance sample-and-holds and analog-digital converters capable of digitizing both the memory's input signal and its output to 16 bits. We expect to have the fixture constructed (and tested!) by the time the memory chip is received from the foundry in late December.

. Prototype straw-tube array: In order to eventually test the developed electronics with an actual detector system, the group has begun to acquire experience with the construction and testing of a straw tube array. Together with undergraduates and an entering graduate student, and with the help of the Boston University group, a single tube (4mm dia.by 25cms long and filled with a gas mixture of 50% argon- 50% ethane) was constructed and tested with a 106Ru beta source. A 16-tube array has also been constructed and will be undergoing tests shortly. Plastic scintillator paddles are used to trigger on electrons emitted from the source, and time spectra are collected using a CAMAC TDC. This effort has been led by S.Steadman and G.Stephans.

When the prototype 8-channel memory chip is ready for more advanced testing, the 16-channel straw tube array will be available for use in a test-bed, initially with beta sources and later in beam.

PLANS FOR FY'92

During the first quarter of FY92, we expect to complete construction of the high performance test fixture, to debug the fixture and to characterize its performance as a measurement system. This work should be completed by the time the first fullscale memory chip is received from the foundry in late December. By the latter part of January 1992, we expect to have an initial characterization of the memory chip.

As noted earlier we are proposing to hire a test engineer; it is likely that we could get someone onboard by February 1992. This engineer's first responsibilities would include working with the analog memory test fixture and designing enhancements which will allow us to automatically test multichannel memories: the initial version of the tester requires manual intervention to switch the measuring ADC's between channels. These enhancements will include the addition of a suitable signal source to provide realistic cell-by-cell signal levels; an input multiplexer to direct this signal to specific channels of the memory; and multiplexers to connect the input and output ADCs to a specific channel of the memory -- all under the control of the test fixture's online computer. We hope to get these upgrades of the tester incorporated in the system by late August 1992.

The test engineer will also be responsible for testing using the probe station and the addition of suitable circuitry to allow us to examine the internal signals of the analog memory under dynamic conditions. This work is important in verifying, with a high confidence level, the performance of the layout extractor and analog circuit simulators we are using.

We cannot overstate the importance of developing a strong testing capability: both to allow prototyping in the early stages to proceed in a timely fashion, and later, to deal effectively with the large numbers of chips involved in the pre-production prototype and production stages of the project. We see this test engineer's responsibilities expanding in FY93 to include the design, fabrication, and use of test fixtures for more complex hybrid and board-level assemblies which incorporate our front-end chips.

On the design side, we plan to design a chip which has appropriate control logic to allow on-chip zero-suppression and an output multiplexer to allow connection to a single ADC which serves say, 8 to 16 memory channels. This chip will benefit from insights and knowledge gained from tests on our first memory chip. The work would proceed, with appropriate prototyping and testing using TinyChips, through the first half of 1992; and it would culminate in the design and layout of a fullscale memory chip which would be released to the foundry in September 1992. The chip will be supplied in a 64-pin DIP package.

In conjunction with this design work, we need to gain expertise in the use of our digital logic simulators, including GenRad's System HILO, so that we can quickly and more conveniently check the performance of digital systems.

ACKNOWLEDGEMENTS

This work is supported by the US Department of Energy through RHIC Detector R&D funds. We would like to thank the personnel at the Massachusetts Microelectronics Center for their continued support of the CAD tools; and we would also like to thank the Dean of Science at MIT for incremental funding in support of this project.

REFERENCES

1. Design and Performance of a 10MHz CMOS Analog Pipeline, W.Buttler et al., DESY 88-092, 1988.

2. A 4096 Cell Switched Capacitor Analog Waveform Storage Integrated Circuit, S.A.Kleinfelder, Trans.Nucl.Sci., Vol 37, No 3, 1230-1236, June 1990.

3. Summary of the Working Group on Readout Electronics, W.E.Cleland et al., Proceedings of the Third Workshop on Experiments and Detectors for a Relativistic Heavy Ion Collider [RHIC], July 1988, edited by B.Shivakumar and P.Vincent. BNL Document No.52185.

4. Technology-independent Design Considerations for Switched-Capacitor Analog Memories, B.F.Wadsworth, Laboratory for Nuclear Science Technical Report, 26 June 1989.

5. SCAM.1 -- A Functional Description, A.Konstantinidis and B.Wadsworth, LNS Electronics Facility Technical Note 91-7, 15 July 1991.

6. Readout Rates For The MARS Detector, B.F.Wadsworth, LNS Electronics Facility Technical Note 91-8, 21 August 1991.

MONOLITHIC CIRCUIT DEVELOPMENT FOR RHIC AT OAK RIDGE NATIONAL LABORATORY

G. T. Alley, C. L. Britton, Jr., E. J. Kennedy, D. F. Newport, A. L. Wintenberg
Instrumentation and Controls Division
and
G. R. Young
Physics Division
Oak Ridge National Laboratory, Oak Ridge, TN 37831-6006

ABSTRACT

The work performed for RHIC at Oak Ridge National Laboratory during FY '91 is presented in this paper. The work includes preamplifier, analog memory, and analog-digital converter development for Dimuon Pad Readout, and evaluation and development of preamplifier-shapers for silicon strip readout. The approaches for implementation are considered as well as measured data for the various circuits that have been developed.

INTRODUCTION

During FY '90 and FY '91, the Instrumentation and Controls and Physics Divisions of the Oak Ridge National Laboratory (ORNL) developed prototype electronics for the Dimuon Pad Readout experiment. The electronics were generic enough in function, however, to be useful for other applications within the RHIC detector environment.

The proposed pad readout chip architecture for RHIC experiments shown in Fig. 1 includes preamplifiers, analog memory, A/D converter circuitry, and appropriate tagging and crossing-select circuitry. Two approaches were considered for implementation: a consolidated readout with the preamp through the ADC on one chip, and a distributed readout where memory through the ADC was separate from the preamp chip. A consolidated solution was considered advantageous because there were few off-chip analog signals and the system cost might be reduced, but possibly it was not the best partitioning of technologies with respect to speed and noise, because the preamplifier could be implemented in bipolar with lower noise and higher speed.

This paper will highlight the five basic areas covered by the work at ORNL; preamplifiers, analog memory, analog/digital conversion, consolidated readout test chip and silicon strip electronics.

PREAMPLIFIERS - CONSOLIDATED READOUT

Two topologies of preamplifier and one topology of preamplifier-shaper were developed for consolidated pad readout interface. These were all fabricated in 2 μ CMOS and were designed to interface to pad capacitances in the range of 10-50 pF and exhibit a risetime adequate to process pad signals similar to Albrecht[1], et al. The schematic of the final topology chosen for the first consolidated test chip is shown in Fig. 2. The measurements for the preamplifier are given in Table I. The noise was measured with a 50 ns peaking time shaping amplifier. A picture of the outputs for detector capacitances of 0, 10, 26, and 53 pF is shown in Fig. 3. This circuit was

Research sponsored by the U. S. Department of Energy. The Oak Ridge National Laboratory is managed by Martin Marietta Energy Systems, Inc. for the U. S. Department of Energy under Contract No. DE- AC05-84OR21400

fabricated in 2 μ N-well CMOS with four circuits per chip to facilitate corner mounting on four adjacent pads.

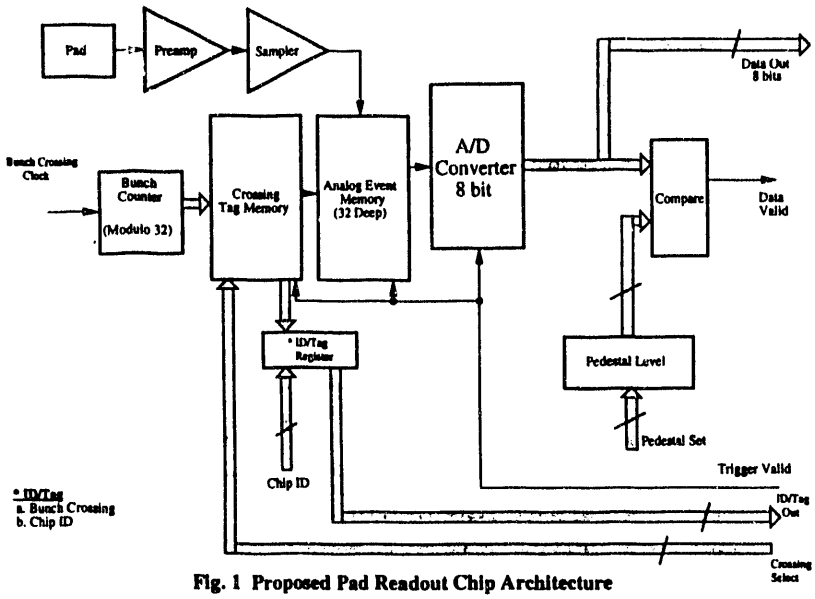

Fig. 1 Proposed Pad Readout Chip Architecture

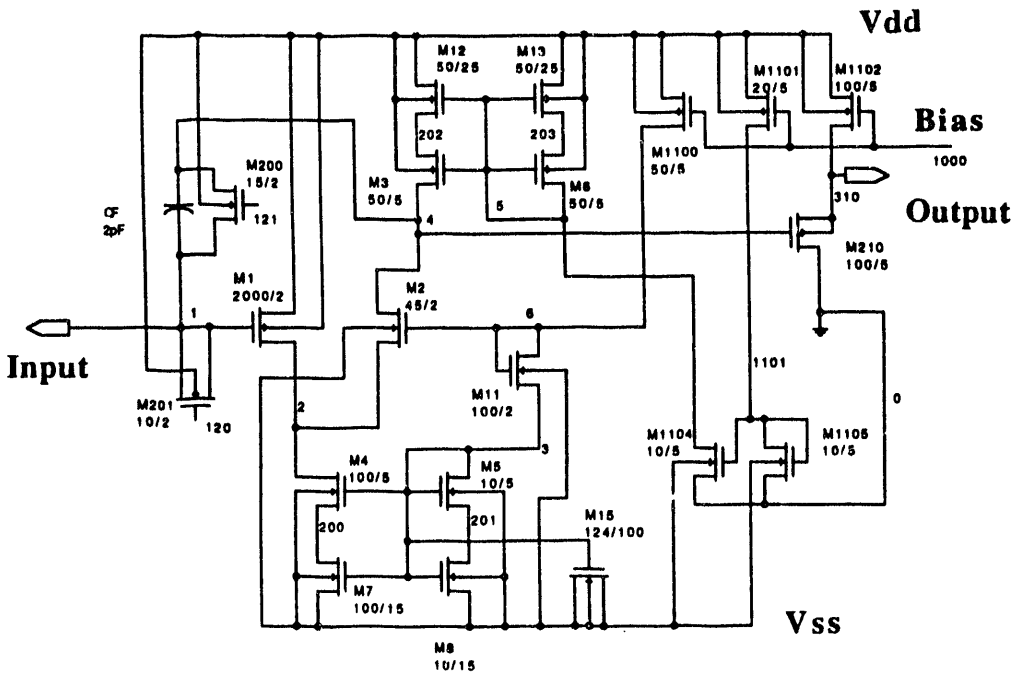

Fig. 2. CMOS preamplifier schematic.

TABLE I. CMOS N-well preamplifier measurements
Power dissipation = 5 mW / channel

Detector Capacitance	Noise	Risetime
10 pF	1600 e	22 ns
26 pF	3000 e	28 ns
53 pF	5200 e	38 ns

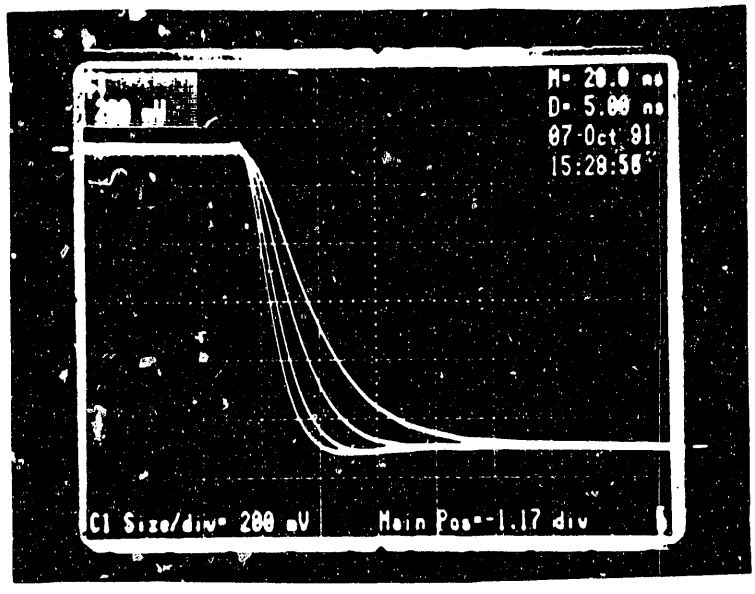

Fig. 3. Photograph of outputs for detector capacitances of 0, 10, 26, and 53 pF.

PREAMPLIFIER - DISTRIBUTED READOUT

A full custom bipolar preamplifier was designed at ORNL and fabricated through Harris Semiconductor in their VHF complementary bipolar process. This circuit, like the CMOS preamplifier, was also fabricated with four circuits to a chip. The VHF process was chosen because of its availability and radiation hardness. A paper outlining the details of this preamplifier was recently presented[2] so that measurements will not be presented here. The circuit topology is presented in Fig. 4 and the chip layout is presented in Fig. 5.

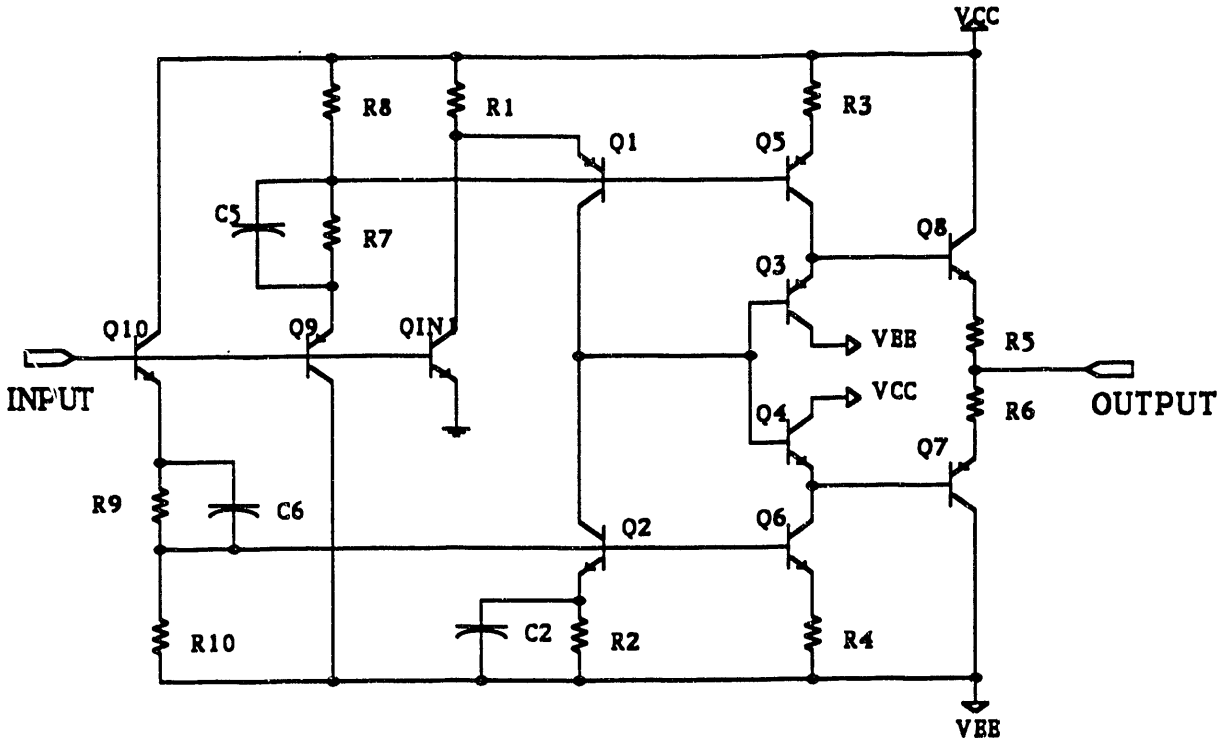

Fig. 4. Bipolar preamplifier schematic.

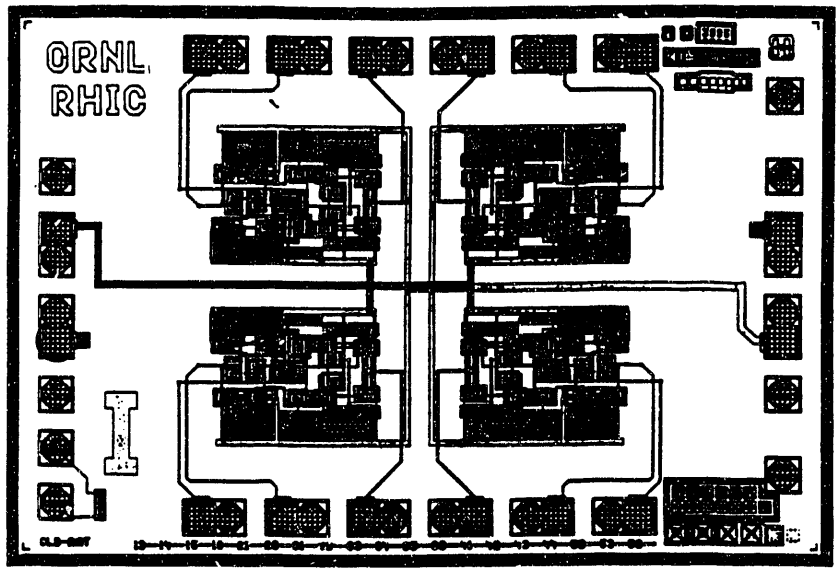

Fig. 5. Bipolar preamplifier layout.

ANALOG MEMORY

An analog memory is being developed as part of the pad readout electronics. The specifications for this memory were determined after careful consideration of the requirements of the pad readout system. One requirement is that the chip should be able to continue taking data while processing data requested by a first level trigger. Thus the analog memory must be capable of simultaneous reading and writing. Another consideration is the required time for first level trigger formation. Typical times are 200-500 ns in fixed target experiments. It is useful to have more time in RHIC experiments to allow for more detailed conditions on global variables such as multiplicity or transverse energy. These may require a few microseconds but probably less than 3 μs. Thus a memory that is 32 cells deep, which corresponds to 7.16 μs for day-one RHIC operation, or 3.58 μs if the RHIC bunch spacing is halved to 112 ns by doubling the number of bunches to 114, meets this requirement. The decision then remains whether to design the data acquisition system to convert all information to digital form after this first delay or to install a second level of analog delay which allows for the formation time of the second level trigger. In either case, another decision remains as to whether and where to 'freeze' the loading of the pipeline with new events when ADC and TDC conversions must be made. A simple design such as that shown in Fig. 1 for the pad readout could be used for the case where rates into single detector elements are low and the experiment's 'valid' trigger rate is of the order of only a few dozen per second. In that case the use of an ADC with a fast conversion time (<10 μs, as described below) would result in negligible deadtime.

Since the average rate for a given pad is expected to be very low, a charge sensitive preamp with continuous reset can be used along with a double correlated sampler. As indicated in Fig. 6, the double correlated sampler samples the baseline, samples the signal and subtracts the baseline from the signal. Sampling is achieved by storing the preamplifier output voltage on two capacitors, and subtraction is achieved by reversing one capacitor before discharging both with an integrator. Timing requires a 4 phase clock operating at twice the beam crossing frequency. Since the correlated sampler shown in Fig. 6 requires two beam crossings before it is reset, two identical sets of sampling capacitors and switches are used in an interleaved fashion so the correlator can provide an output at each beam crossing. Tests demonstrated that the double correlated sampler (v.1) was capable of operation at a 100 ns beam crossing rate, but with insufficient accuracy. Improvements and alternate designs are under consideration.

Several different analog memory configurations were considered[3]. The voltage-write, charge-read configuration shown in Fig. 7 was chosen for several reasons. The gain (output voltage/input voltage) depends only upon the ratio of CF to CN (the cell capacitance) and does not depend upon the (stray) capacitance of either bus. The gain relation does mean that the cell-to-cell gain variation can be no better than the matching of the capacitors, but only 7-8 bits of resolution are required for this application and the double-poly capacitors typically can be matched to near 10 bits. The grounded capacitor arrangement allows simultaneous read-write operation with only two switches per cell, and this in turn allows the use of a small geometry switch to achieve a short charging time constant. Another advantage of the voltage-write, charge-read configuration is that no bus reset switches are needed. The write bus is driven by a low impedance voltage source (correlated sampler), and the read bus is reset by the action of resetting the readout integrator.

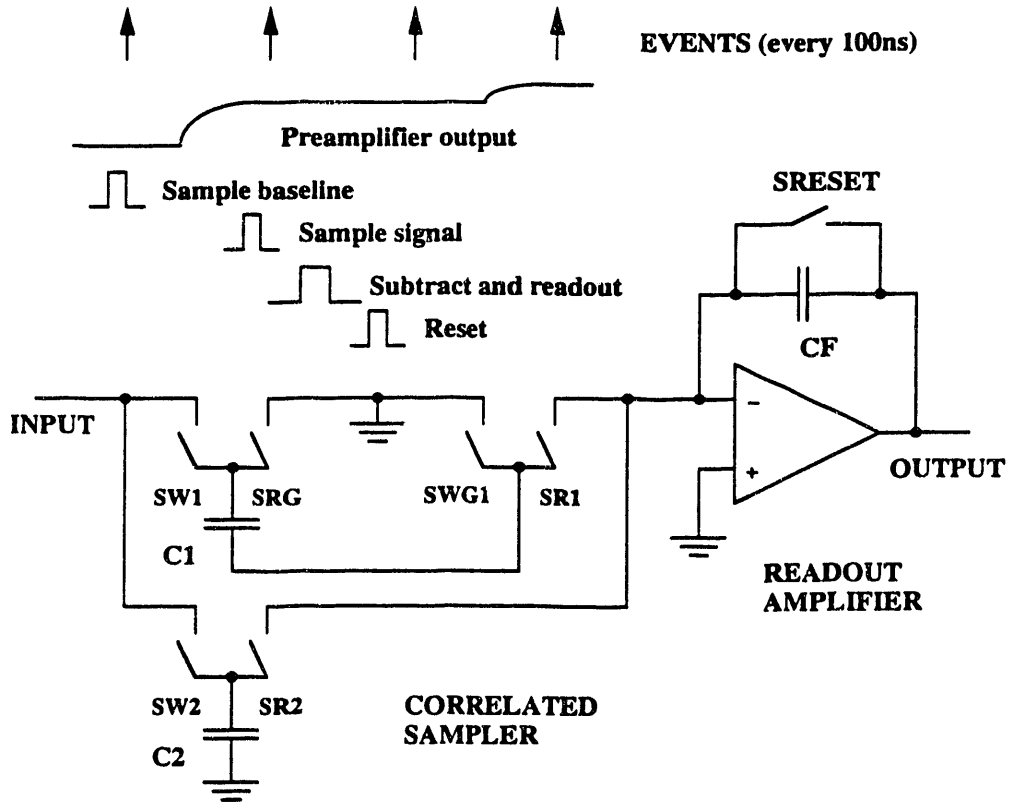

Fig. 6. Double correlated sampler block diagram.

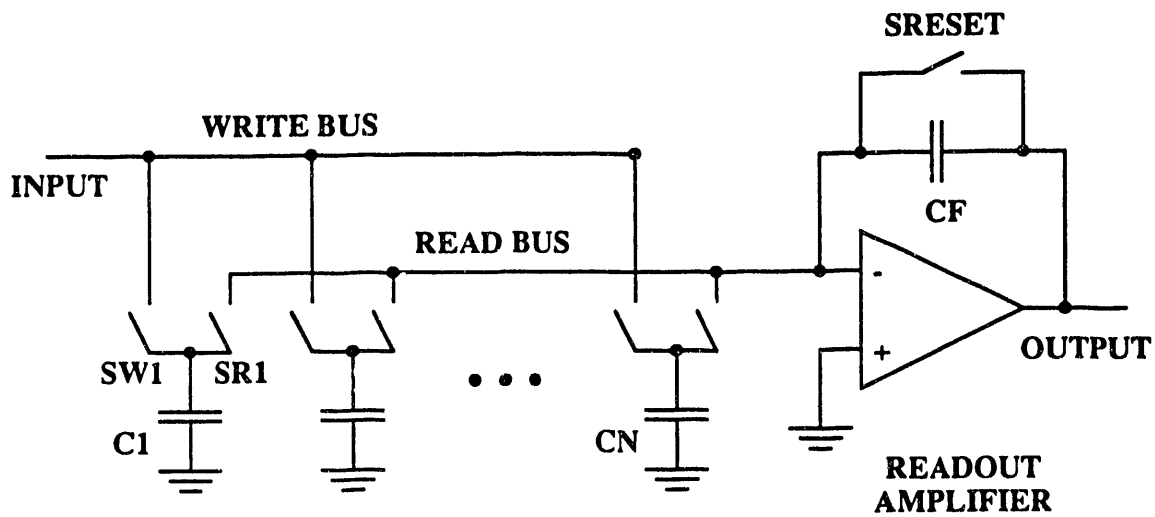

Fig. 7. Analog memory array switch level schematic.

Several versions of the analog memory have been fabricated using a 2μ p-well double poly CMOS process. The first chip has a double correlated sampler (version 1) and a 16 cell analog memory. The chip is structured as shown in Fig. 8. The analog memory array is capable of simultaneous read and write, and all cells are randomly accessible through the read and write address decoding logic. This allows operation as a pipeline by sequentially addressing cells, or the memory may be tested one cell at a time. This version of the analog memory was first tested for functionality, and then more detailed tests were conducted with the memory operating at a 10 MHz writing rate. 300 ns was allowed to readout a cell. The maximum cell-to-cell gain variation was found to be less than 0.3% (Fig. 9), and the average pedestal was 19 mV with an rms variation of 1.8 mV (Fig. 10). The analog memory linearity was good with a typical cell exhibiting less than ±0.15 % deviation from a best fit line over an input range of -3 V to +3 V (Fig. 11). The gain variations and nonlinearity are sufficiently small that the memory can operate with better than 8 bits of accuracy.

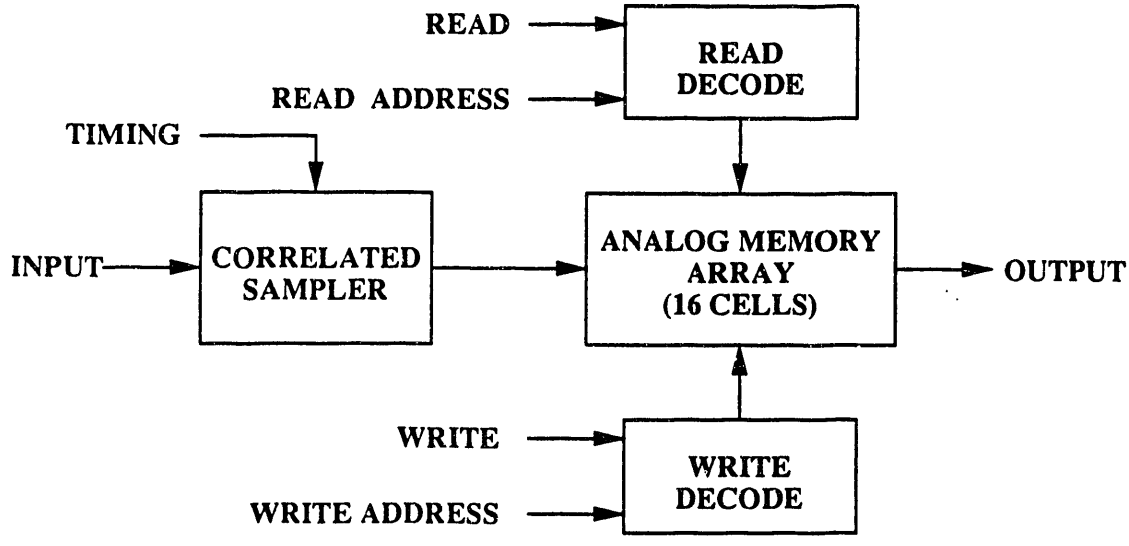

Fig. 8. Analog memory chip 1 block diagram.

Two additional analog memory chips have been or are currently in fabrication. Chip 2 has 4 parallel 16 cell pipelines and integral timing generators for controlling the double correlated sampler and writing sequentially to all 4 pipelines. The timing generator is shared by all pipelines. Individual memory cells are constructed so as to be arrayable in both directions. This allows deeper pipelines to easily be constructed and for pipelines to be addressed in parallel. Chip 3 has 2 complete channels with each channel comprising a 16 cell pipeline and another version (v. 2) of the double correlated sampler.

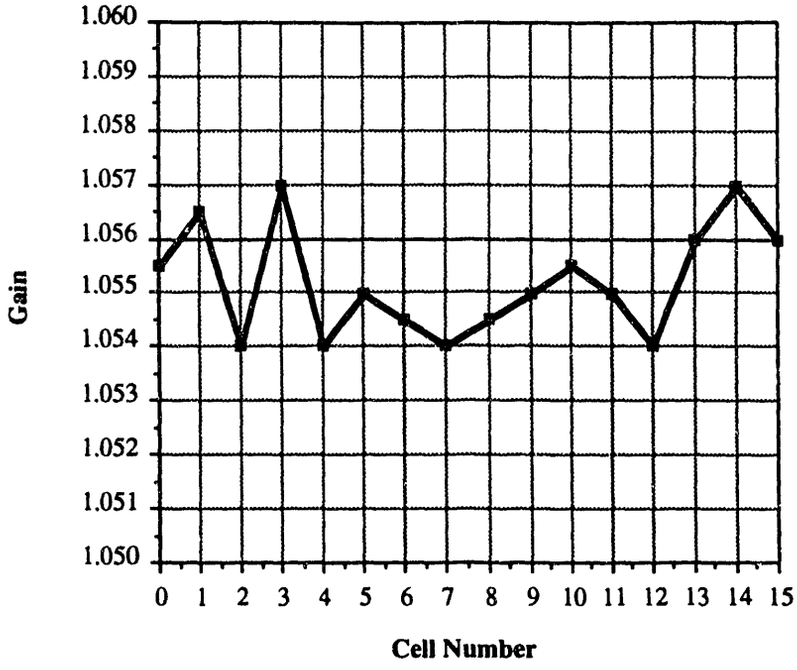

Fig. 9. Analog memory chip 1 gain variations.

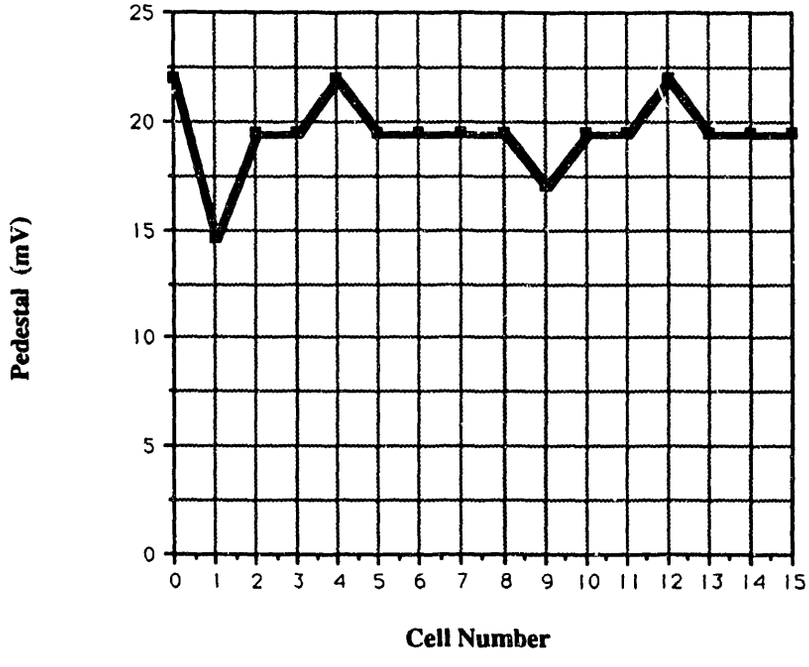

Fig. 10. Analog memory chip 1 pedestal voltages.

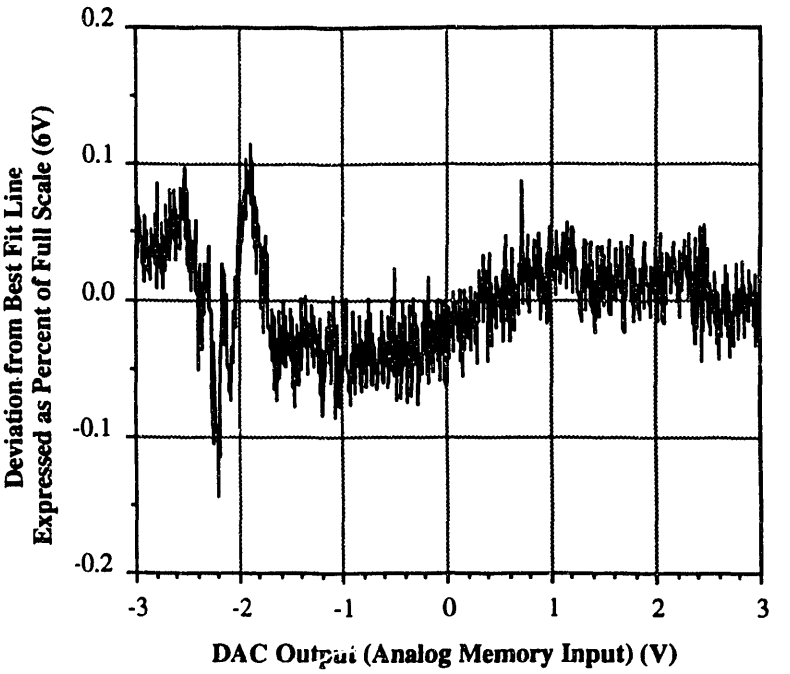

Fig. 11. Analog memory chip 1 integral linearity.

ANALOG/DIGITAL CONVERSION

A prototype 8 bit successive approximation analog/digital converter was designed and fabricated. The successive approximation approach was chosen because of the need to have an 8-10 bit converter that would finish conversion in less than 10 μs and utilize the available 112 ns beam clock. The design is of a topology similar to one published previously[4] that allows 10 bit monotonicity with only 6 bit capacitor matching. The present circuitry has the 4 bit resistor string, the 4 bit capacitor array, the successive approximation register, and the necessary conversion control logic. Future development will include a reference and 2-phase clock.

The measured differential nonlinearity was <1/2 LSB at 10 bits for a 7 μs conversion time and <1/2 LSB at 9 bits for 5 μs conversion time. The power dissipation was measured to be approximately 5.6 mW at 7.9 kHz conversion rate. A histogram of the counts per channel vs. channel number for a ramp input is shown in Fig. 12.

CONSOLIDATED READOUT TEST CHIP

A large chip (4.6 mm by 6.8 mm) was designed to provide an initial test of the consolidated readout system. This chip includes four v.4 preamplifiers, four v.1 double correlated samplers, four 32 cell analog memory arrays, a four-to-one analog multiplexer and one 8-bit successive approximation ADC (v.2) and on-chip timing generation for the samplers and analog memory. This chip has been fabricated but not tested. It is expected that this chip will answer some questions about crosstalk in a multichannel chip having both analog and digital circuitry.

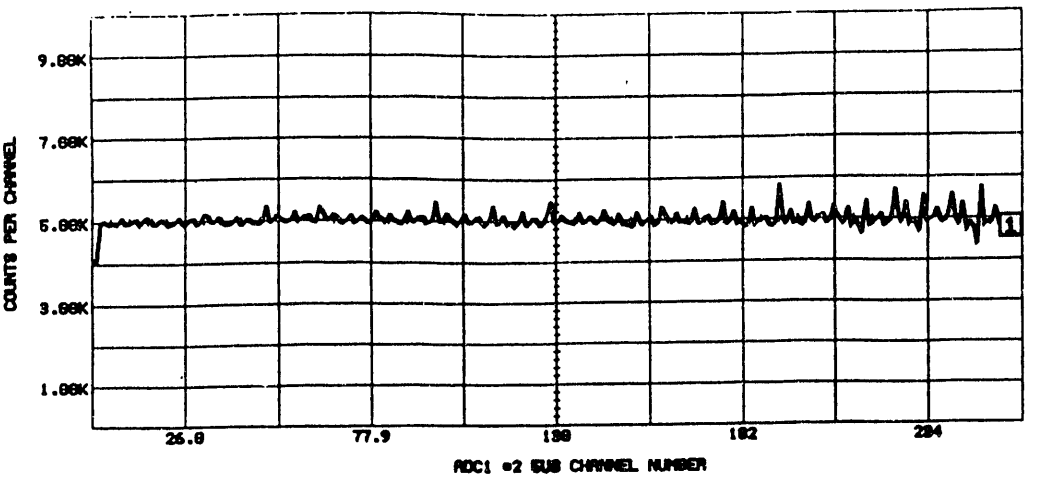

Fig. 12. Counts per channel vs. channel number.

SILICON STRIP ELECTRONICS - BVX PREAMPLIFIER-SHAPER

The BVX preamplifier-shaper was developed by ORNL with FNAL funding for the proposed BCD experiment. The features of the BVX preamplifier-shaper are the time-invariant feedback, a pitch of 85 μ, a peaking time of nominal value 200 ns, a nonlinear feedback resistor around the input stage to enable some detector leakage compensation, and a power dissipation of 1.2 mW per channel. The preamplifier-shaper was fabricated in an 8 channel per chip format in 2 μ P-well CMOS. The chips are presently being used in strip tests by RHIC experimenters at LANL.

SILICON STRIP ELECTRONICS - Hewlett Packard and AT&T processes

Development of fast peaking time (~ 20 ns) and low power dissipation preamplifier-shapers for silicon detectors has been underway for use in both RHIC and the SSC. Preamplifier-shapers with a 50 μ pitch have been designed and are presently in fabrication in a Hewlett Packard high frequency bipolar process with first silicon expected in March, 1992. A design in AT&T CBICU bipolar process will be submitted for fabrication in early 1992. These will be reported at a later date.

CONCLUSIONS

Several monolithic circuits have been developed for the Dimuon experiment at RHIC. Among these are preamplifiers, analog memory units, an ADC, and silicon strip preamplifiers. The blocks developed are generic enough to be useful not only in the proposed experiment, but in the new experiment as well.

REFERENCES

1. R. Albrecht et al., NIM A276, 131-9 (1989).

2. C. L. Britton, Jr., E. J. Kennedy, R. A. Todd, A. L. Wintenberg, and G. R. Young, " A Four-Channel Bipolar Preamplifier for RHIC Dimuon Pad Readout", Presented at the 1991 Nuclear Science Symposium, Nov. 1991.

3. A. Konstantinidas and B. Wadsworth, "Design Considerations for Switched-Capacitor Analog Memories," Conference Proceedings of the 1991 IEEE Nuclear Science Symposium, Nov. 1991.

4. Bahram Fotouhi and David A. Hodges, "High-Resolution A/D Conversion in MOS/LSI", IEEE Jour. Solid State Circuits, Vol. SC-14, No. 6, Dec. 1979, pp. 920-926.

HIGHLY INTEGRATED ELECTRONICS FOR THE STAR TPC

A.A. Arthur, F. Bieser, W. Hearn, S. Kleinfelder, T. Merrick
J. Millaud, T. Noggle, G. Rai, H.G. Ritter, H. Wieman
Lawrence Berkeley Laboratory,
Berkeley, CA 94720

ABSTRACT

The concept for the STAR TPC front-end electronics is presented and the progress toward the development of a fully integrated solution is described.

1. Introduction

It is the goal of the R+D program to develop the complete electronics chain for the STAR central TPC detector at RHIC. It is obvious that solutions chosen e.g. for ALEPH are not adequate for the 150000 channels that need to be instrumented for read-out. It will be necessary to perform all the signal processing, digitization and multiplexing directly on the detector in order to reduce per channel cost and the amount of cabling necessary to read out the information. We follow the approach chosen by the EOS TPC project [1], where the readout electronics on the detector consists of an integrated preamplifier, a hybrid shaping amplifier, an integrated switched capacitor array [2,3] and a highly multiplexed ADC. The STAR electronics will be further integrated so that approximately 16 channels of the preamplifier, the shaper, the analog store and the ADC will be contained in two integrated circuits located directly on the pad plane.

2. Preamplifier and Shaping Amplifier

The main emphasis of the R+D program for integrated TPC electronics has been in the development of an integrated shaping amplifier with time constants that are reproducible within a few percents. This is a complicated task since discrete component circuit techniques are not directly applicable to IC design. It is difficult to achieve the precision and consistency for the resistors and capacitors needed for uniformity of the time constants in all channels. We have decided to solve the problem with a simple approach: in parallel to the main capacitors we will use auxiliary capacitors that are switchable with a fuse for the final product and with digital registers during the development and test phase. This allows adjustment of individual time constants and to compensate for variations in the process parameters. Figure 1 schematically shows this principle.

The shaping amplifier will be combined with the integrated low noise preamplifier (4 channels per IC) developed for the EOS TPC [1]. The noise contribution of each channel measured after a shaping amplifier with a peaking time of 200ns is 550 electrons equivalent rms with an input capacitance of 8pf. The chip is equipped with a built in channel by channel switchable pulser system for both calibration and diagnostics. This feature will be included in the fully integrated RHIC system.

Work on the shaping amplifier has progressed in stages. We started with a digitally trimmed integrator chip and than proceeded to a integrator-differentiator. At this stage the amplifier was combined with the existing EOS preamplifier and now we are designing the digitally trimmed multipole shaping amplifier. All IC's are done in CMOS using the 2U 2-metal 2-poly process requiring no external devices.

The matching of peaking times between shaper channels was tested extensively. From several Quad Shaper IC's it was verified that the variation in time constants between the different channel on the same chip was sufficiently small to allow for all channels to be tuned simultaneously. Thus variations between wafers and process variations may be compensated for by setting a three-bit digital code on each chip and blowing metal fuses on the chip during testing.

For the implementation of the shaping amplifiers a high speed operational amplifier has been developed that performs well, is highly stable and easy to compensate. It is capable of closed loop bandwidth of over 25 MHz at a gain of up to 30, and it will be useful in future applications. It is a single stage design with open loop gain of about 70 db.

Figure 2 shows the schematics for a complete simple shaping amplifier. The time constants formed by the 5000 ohm resistors and 9 pf capacitors are trimmed by small switched capacitors. The first stage is an integrator and the second stage a differentiator. Two fast operational amplifiers are used.

A new multipole shaping amplifier is currently being built. The principles of this design are similar to the shaper described here except that it provides complex poles and has improved shaping characteristics.

3. Analog Memory and ADC

The second chip of the chain will contain a switched capacitor array and the ADC.

The SCA (Switched Capacitor Array) is designed to operate as an inexpensive, dense, low power, and high dynamic range analog memory, replacing CCD's and FADC/memory devices in large data acquisition systems. The main features and performance parameters of the latest 512 cell per channel SCA I.C. include:

1.2 Micron double metal, double polysilicon CMOS process.
16 Channels per chip, 512 cells per channel.
Die size 6.8 x 4.6 mm.
Serial cell addressing, multiplexed and buffered analog output.
Storage cell capacitance = 1 pF.
Input capacitance = 15 pF.
Average readout rate of 1 MHz.
<10 mW power consumption per channel at 5 Volts.
Predicted maximum acquisition sampling speed of >100 MHz.
Analog bandwidth of >50 MHz.
Rail to rail input and output range.
Output noise of ~1 mV.
Dynamic range (single cell, 10 Mhz) of >4000:1 or >12 bits.
Non-linearity of ~1% over entire range.

Enhancements to the existing serial SCA versions are being made in conservative steps to insure success. These steps

are a natural progression of prior work, and capitalize on progress made for an SSC version of the chip.

A new pin compatible version of the serial SCA is ready for fabrication. This is aimed at completely eliminating the systematic odd-even effect noted in prior serial SCA versions. The hypothesis is that the split clock generation circuitry in the existing serial SCA versions causes an odd-even timing skew between n and p-channel switches. Newer versions have pushed all systematic and random baseline non-uniformity effects well below the mV level. Elimination of the odd-even effect in the RHIC version was difficult because of the aggressive pitch of the capacitor cells. However, a new 512 cell per channel version has completely uniform capacitor and clocking circuitry - there is no physical or logical differences between cells. Therefore, we can confidently predict an end to odd-even or other systematic effects. Baseline uniformity to approximately the 12 bit level should be achieved without any corrections being necessary.

A pitch-compatible 16 channel 12 bit ADC sub-section (Figure 3) is now in fabrication. This follows several single channel prototype fabrications that proved monotonic 12 bit conversion with about 11 bit linearity. The single slope design is flexible enough for use in less than 12 bit applications. For SSC applications, a 62 MHz digitization clock is applied for a 12 bit conversion in 32 μs. A 10 bit conversion would take 8 μs.

A clock rate of at least 125 MHz can be applied if desired, resulting in twice the conversion speed. Readout is double buffered, so digitization and readout can occur simultaneously.

An integrated SCA/ADC combination will be submitted as soon as the ADC sub-section is tested and proven.

References:

[1] G. Rai, A.A. Arthur, F. Bieser, C.W. Harnden, R. Jones, S.A. Kleinfelder, K. Lee, H.S. Matis, M. Nakamura, C. McParland, D. Nesbitt, G. Odyniec, D. Olson, H.G. Pugh, H.G. Ritter, T.J.M. Symons, H. Wieman, M. Wright, and R. Wright, IEEE Trans. on Nucl. Sci. **37**, 56 (1990).

[2] W. Buttler, A. Caldwell, C. Hayes, L. Hervas, A. Hofmann, B. Hosticka, R. Klanner, U. Kötz, P. Malecki, J. Möschen, J. Del Peso, U. Schöneberg, and W. Sippach, Nucl. Instr. and Meth. **A277**, 217 (1989).

[3] S.A. Kleinfelder, IEEE Trans. on Nucl. Sci. **37**, 1230-1236 (1990).

Figures:

Figure 1: Schematic representation of the correction capacitors

Figure2: Schematics of a shaping amplifier with correction capacitors

Figure 3: Schematics of the integrated ADC

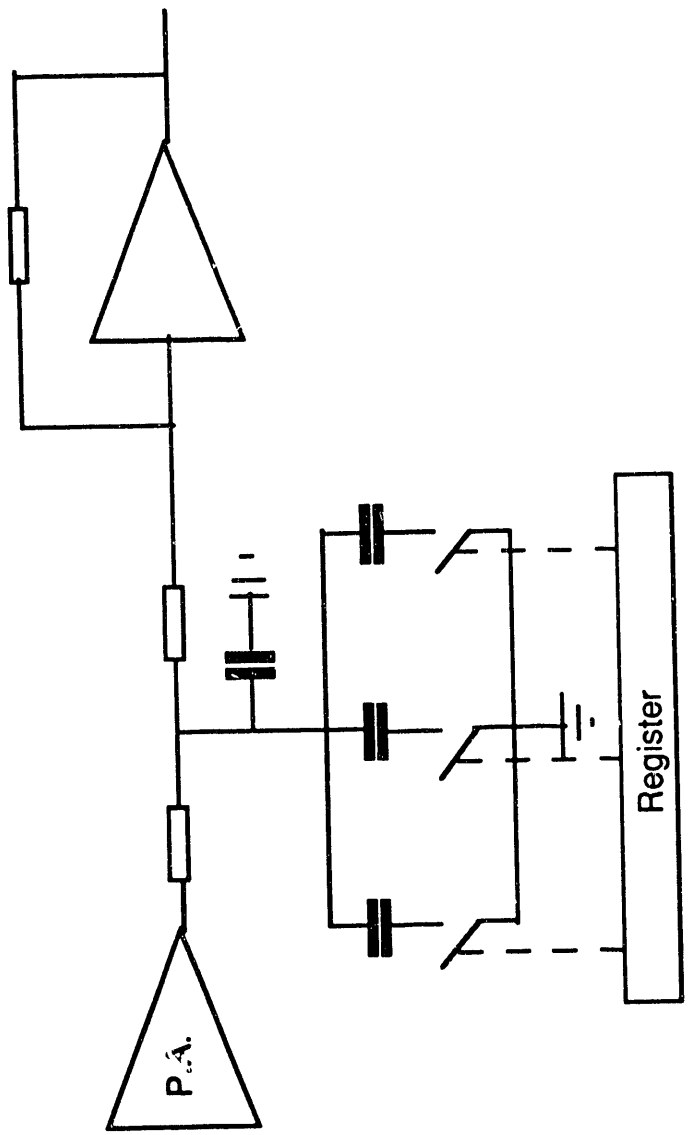

Figure 1

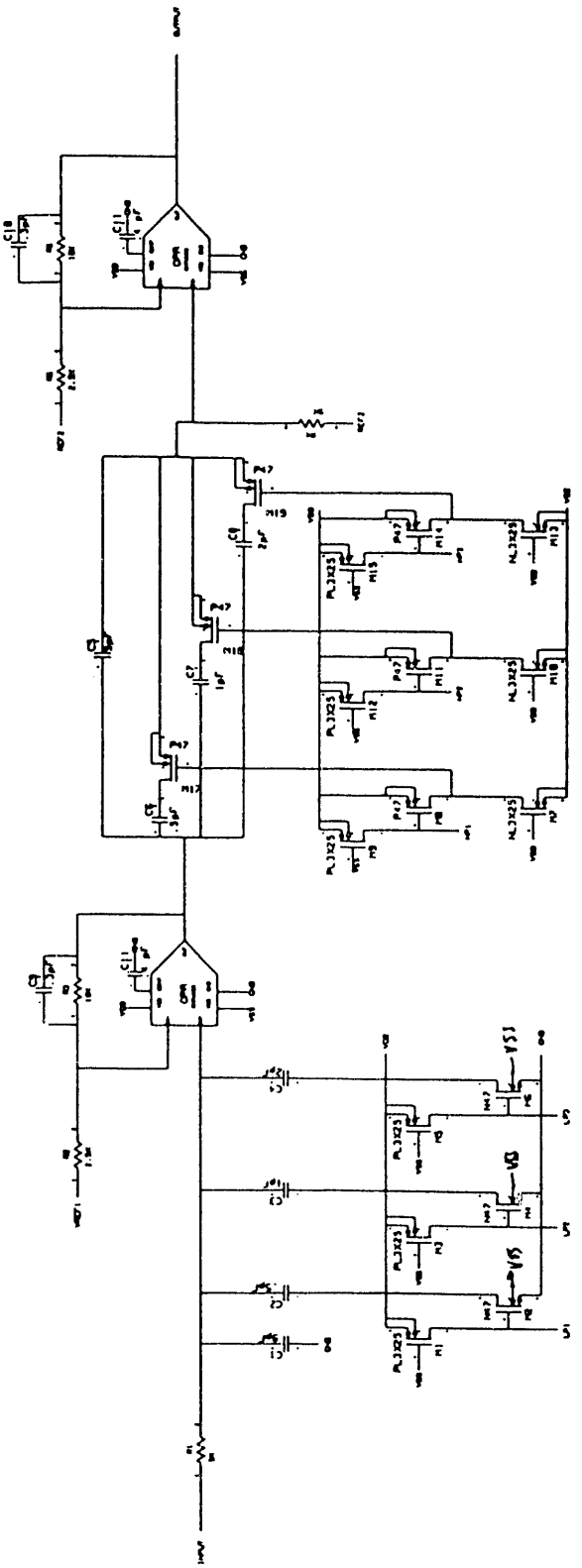

Figure 2

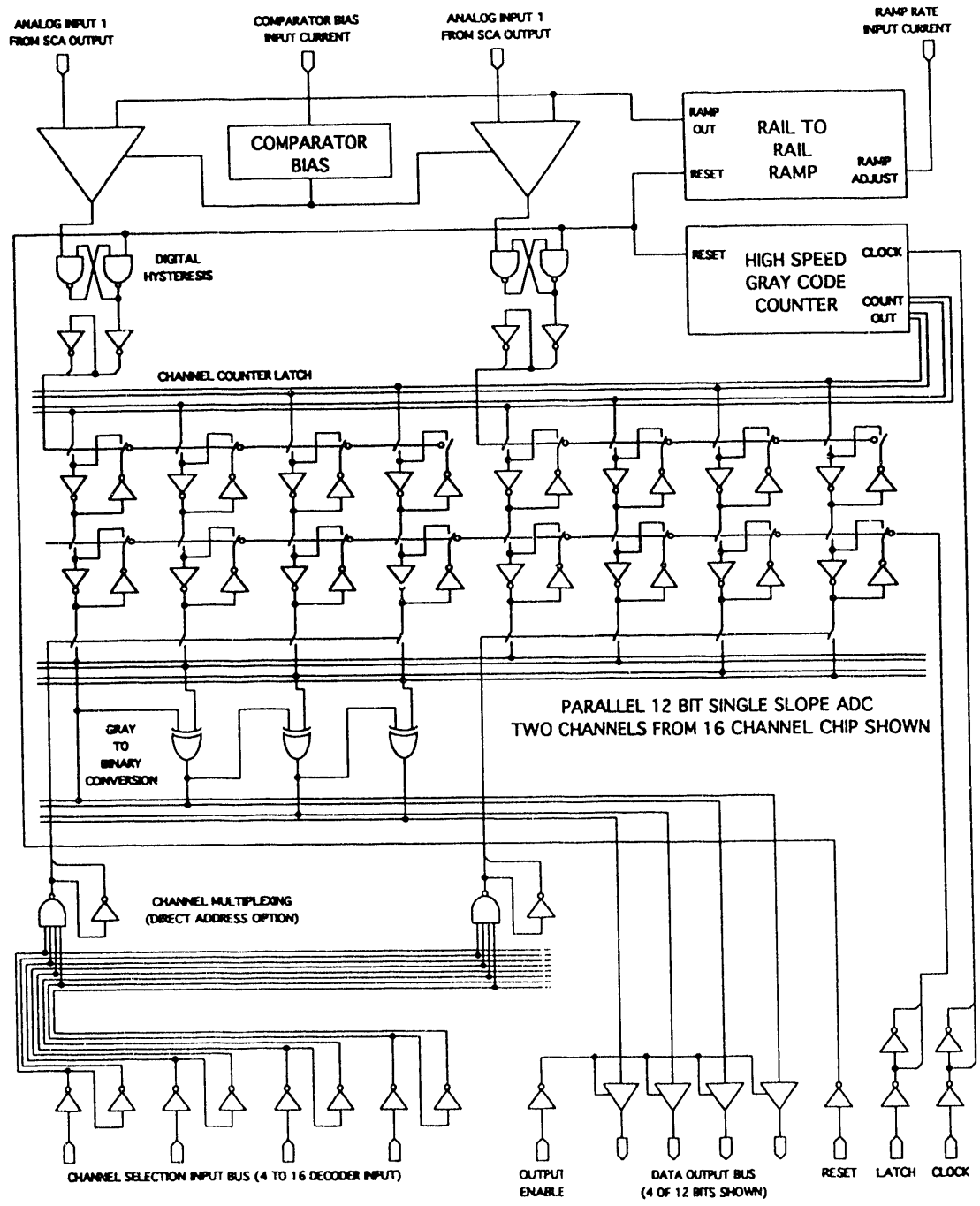
ANALOG INPUT 1
FROM SCA OUTPUT
COMPARATOR BIAS
INPUT CURRENT
ANALOG INPUT 1
FROM SCA OUTPUT
RAMP RATE
INPUT CURRENT
COMPARATOR
BIAS
RAMP
OUT
RESET
RAIL TO
RAIL
RAMP
RAMP
ADJUST
DIGITAL
HYSTERESIS
RESET
HIGH SPEED
GRAY CODE
COUNTER
CLOCK
COUNT
OUT
CHANNEL COUNTER LATCH
PARALLEL 12 BIT SINGLE SLOPE ADC
TWO CHANNELS FROM 16 CHANNEL CHIP SHOWN
GRAY
TO
BINARY
CONVERSION
CHANNEL MULTIPLEXING
(DIRECT ADDRESS OPTION)
CHANNEL SELECTION INPUT BUS (4 TO 16 DECODER INPUT)
OUTPUT
ENABLE
DATA OUTPUT BUS
(4 OF 12 BITS SHOWN)
RESET
LATCH
CLOCK

Figure 3

Monolithic Readout Circuits for RHIC

P. O'Connor, J. Harder - Brookhaven National Laboratory, Instrumentation Division

W. Sippach, Nevis Labs

Presented at the Symposium on RHIC Detector R&D October 10-11, 1991

1.0 Abstract

Several CMOS ASICs have been developed for a proposed RHIC experiment. This paper discusses why ASIC implementation was chosen for certain functions, circuit specifications and the design techniques used to meet them, and results of simulations and early prototypes. By working closely together from an early stage in the planning process, in-house ASIC designers and detector and data acquisition experimenters can achieve optimal use of this important technology.

2.0 Introduction

ASIC use in high energy physics in increasing.[1] Particularly for front end functions where density and/or cost is a constraint, ASICs' ability to trade off functionality, speed, power, and size can result in efficient detector readout. In addition, certain readout functions are very difficult to perform without custom integrated circuitry, e.g. analog pipeline delay. However, monolithic technology also imposes limitations that can restrict achievable performance, and appropriate circuit techniques must be used to get the full advantage from it.

With this in mind, a close collaboration was started between ASIC designers and data acquisition experimenters for the proposed OASIS experiment in December of 1990. We will discuss the system partitioning, and the rationale for setting priorities for ASIC designs in the next section. This will be followed by descriptions of three ASIC designs, including target specifications, key circuit issues, and approaches taken to realize the goals. Finally a brief report of progress and future plans is presented.

1. See, e.g. Proceedings of the First Annual Conference on Electronics for Future Colliders, May 22-23, 1991, LeCroy Corp., Chestnut Ridge, NY

3.0 Experiment Overview

At the outset a description was made, in functional block format, of the readout electronics for each of the seven major detectors of OASIS. The result is sketched in Fig. 1, where the detectors, readout chains, and channel counts are shown. Next, we selected certain blocks as candidates for monolithic integration; those chosen are shown as shaded boxes in Fig. 1. Since about 95% of the channels are in the transition radiation detector/tracker and liquid argon calorimeter, ASICs were considered for all blocks in their readout chains for cost reasons.As mentioned already, the LAr AMU (analog pipeline) cannot be built from commercial components. Among the other systems, the silicon pad multiplicity detector and silicon drift chambers have space constraints, again making ASICs advantageous.

While similarities exist among the front-end blocks of many systems, their requirements (for noise, dynamic range, etc.) differ at the detail level. Hence, there was not enough commonality to try to make any single ASIC fill more than one block. The eleven candidate ASICs could not all be addressed simultaneously with the resources available, so priorities were attached based on system-wide costs; this led to the selection of the three blocks shown with bold outlines in Fig. 1 for custom design. The TRD ADC RAM and L2 PIPE/DATA COMP functions could be implemented with field-programmable gate arrays (FPGA's), while the other LAr circuits could be made with hybrid technology. The three circuits chosen could all be produced in readily available CMOS technology.

4.0 TRD/Tracker

4.1 Detector and signal characteristics

The TRD/Tracker identifies electrons by detecting transition radiation which is emitted as they traverse a foam or foil radiator. In addition, particle momentum is measured for all charged particles through their ionization energy loss dE/dx. Figure 2 shows a schematic cross section of a particle crossing one layer of the TRD/Tracker along with a description of the possible anode current waveforms. For hadrons, only dE/dx charge is produced in the chamber; this drifts to the anodes and produces a current whose duration is proportional to the cosine of the angle of incidence. The current will fluctuate due to the statistical distribution of primary ionization clusters. Electrons with momenta > 0.5 Gev/c can also emit a transition radiation photon in the range of 5 - 25 keV, which has a high probability of being absorbed in the chamber gas. This produces localized ionization that results in a short current pulse of much higher magnitude than the accompanying dE/dx signal.

The characteristics of the TRD/Tracker charge and current waveforms are summarized in Table 1. The readout electronics consists of a charge-sensitive preamplifier, shaper with integration time constant matched to the average diffusive broadening of the drift chamber, and fast ADC. The 4-bit ADC has 12 levels spanning the dE/dx range and 3 levels in the TR region. It takes samples of the waveform every 20 nsec to provide good time resolution of the leading and trailing edges.

4.2 Preamp/shaper

Based on the expected characteristics of the signal waveform as described above, the specifications shown in Table 2 for the preamp/shaper ASIC were developed. The equivalent input noise charge (ENC) is about 1/20 of an LSB on the cathode strips.

Because of the high capacitance of the detector (50 pf for anode wires, 150 pf for cathode strips) and the relatively short shaping time of 70 nsec, this ENC goal is a challenge. In a well-designed preamp/

shaper, most of the noise comes from the preamp input device, so its design and biasing are critical. The following conclusions can be drawn:

- In this shaping time range, channel thermal (white) noise dominates so an NMOS device can be used.
- Minimum gate length should be used.
- An optimum gate width exists based on detector capacitance, but its value may be prohibitively large.
- Once the optimum gate dimensions are chosen, noise is a function of drain current so there is a fundamental noise/power trade-off.
- Careful attention must be paid to gate and substrate parasitic resistances.
- Reverse biasing the source-substrate junction reduces noise by reducing the body-effect transconductance g_{mb}.

It is also important to minimize the noise contributed by the bias sources in the circuit, which can contribute up to 50% of the noise. Additionally, it is important to protect the CMOS input from electrostatic discharge damage in a way that does not add noise.

Figures 3 (a) and (b) show calculated ENC (due to the input NMOS device only) as a function of W_g and I_d, for circuits made in a 2 μm n-well CMOS process. It can be seen in Fig. 3(a) that the noise minimum is a very shallow function of gate width. In Fig. 3(b) one sees that the 2500 r.m.s. e^- goal can be met for the cathode preamp ASIC, but only at the cost of several mA of drain current in the input device; in practice, this circuit will dissipate 15-75 mW per channel. The ENC goal is much easier to meet for the lower-capacitance anode wires.

The circuit of Fig. 4. was designed to meet the requirements for cathode strip readout. It consists of a folded cascode charge-sensitive loop with a long-channel PMOS device biased in the triode region for a high value DC feedback resistor. Device sizes were chosen to minimize noise while maintaining speed and stability. Simulations predict an ENC of 2560 r.m.s. e^- at 70 nsec shaping and 150 pf detector capacitance, with a rise time of 70 nsec and overall power consumption of 22 mW. A similar circuit could serve as an anode wire preamp, but with at least 10 times lower power.

4.3 Shaper

A transfer function with a zero at the origin and 5 equal-value real poles at 9.1 MHz produces a step response that peaks in 70 nsec and has adequate noise rejection. Key design issues for this circuit are:

- Provision of at least two poles per op-amp to minimize power.
- On-chip passive components used to set the time constants have wide manufacturing variations (20% run-to-run) in typical ASIC fabrication.
- The shaper's equivalent input noise voltage should be less than the preamp ENC/C_F (a few hundred microvolts in this case) to minimize its contribution to overall noise.

The circuit shown in Fig. 5[2] was chosen to implement the $1/(1+s\tau)^2$ transfer function. One open-loop pole is contributed by the capacitance at the drain of M3 in parallel with its transconductance and a second is formed by C1 and (R1+R2). In the closed loop, the poles move together to result in a transfer function:

---

2. Z. Chang, Low Noise Wide-Band Amplifiers in Bipolar and CMOS Technologies, Kluwer, 1991 pp. 186-188

$$H(s) = \frac{G_0 R1}{(1 + G_0 R1) + s(\tau_1 + \tau_2) + s^2 \tau_1 \tau_2} \quad (1)$$

where

$$G_0 = gm_3 \times \frac{(\frac{W}{L})_5}{(\frac{W}{L})_3} \quad (2)$$

$$\tau_1 = \frac{Cgs_3 + Cgs_5}{gm_3} \quad (3)$$

$$\tau_2 = C1(R1 + R2) \quad (4)$$

The desired response occurs when the closed-loop poles meet on the real axis; this is true when the condition

$$\frac{\tau_1 \tau_2 (1 + G_0 R1)}{(\tau_1 + \tau_2)^2} = \frac{1}{4} \quad (5)$$

is met. Note that this condition involves only component ratios; hence the shape of the step response should be insensitive to manufacturing tolerances. At this Q=1/2 condition the pole frequency is

$$\omega_0 = \frac{\tau_1 + \tau_2}{2\tau_1 \tau_2} \approx \frac{1}{2\tau_1} \quad (6)$$

The pole frequency is controlled mainly by the g_m/C_{gs} ratio of the NMOS device. This ratio is the most stable naturally-occurring time constant in a CMOS process, since it is nearly unaffected by oxide thickness variations and doesn't depend on NMOS-PMOS tracking. The major source of variation will be L_g which is controlled to better than 10%.

To investigate the tolerance of shaping time to process variations, Monte Carlo SPICE simulations were done. The parameters that were allowed to vary were polysilicon sheet resistance, poly1-poly2 capacitance, and NMOS and PMOS TOX, U0, VFB, CJO, CGSO, CGDO, DW, and DL. All were given uncorrelated Gaussian variations with σ = 15% of mean. Results are shown in Table 3. As expected, peaking time remains stable to within 10% of its mean value. In contrast, a shaper using Sallen-Key lowpass stages and ideal op-amps was also simulated. This design, appropriate for discrete device technology where active device variations are greater than those of passive components, relies on resistor-capacitor products to set the peaking time. Similar R and C variations result in a σ_{tp} of about 18% of the mean.

Finally, Fig. 6 presents the results of simulations of the preamp-shaper combination. Fig. 6(a) shows the input current waveform for a minimum-ionizing particle at normal incidence as generated by GARFIELD[3]. Fig. 6(b) shows the shaper output, which reproduces the major features of the current waveform with the higher frequency components removed by the lowpass filtering.

Fig. 6(c) and (d) show the input and output waveforms for a 45° minimum ionizing particle. Fig. 6(e) and (f) illustrate a 0° MIP with superimposed TR photon; note the change in vertical scale.

3. GARFIELD simulations provided by B. Yu.

In a real system, the long tail of the current waveform would be cancelled by a simple passive pole-zero compensation network which could be on- or off-chip.

4.4 Flash ADC

The resolution, accuracy, and timing goals of the FADC are shown in Table 4. As discussed earlier, the high sampling rate gives position resolution while the amplitude measurement serves to distinguish hadrons from electrons accompanied by a TR photon. In addition, accurate measurement of energy loss in the dE/dx region can improve electron/hadron separation due to the relativistic rise.

A block diagram of the FADC architecture is shown in Fig. 7. The critical subcircuits of the FADC are the input track and hold and the comparators. In the track and hold, high speed must be maintained while clock feedthrough is minimized. Fig. 8 shows three schemes for clock feedthrough cancellation. In the first (Fig. 8a), no cancellation, charge on the switch transistor's CGD and channel charge are injected on the hold capacitor when the switch turns off. In Fig. 8(b) a dummy transistor of 1/2 the width of the switch and clocked in antiphase is placed in series with the switch. Now when CLK goes high, a compensating amount of charge is withdrawn from the storage node. However, this scheme only compensates the CGD of the switch; its channel charge flows unequally due to the unequal impedance seen at its source and drain. Fig 8(c) gives a partial cancellation of this effect by incorporating two dummy switches on either side of the main switch. During turn-off, they present approximately equal impedance on each node.

SPICE circuit simulations illustrating the charge cancellation schemes are shown in Fig. 9. One can see that the first and second order techniques achieve feedthrough cancellation of 92% and 98% respectively.

The proposed latched comparator circuit schematic is shown in Fig. 10[4]. A low-offset voltage differential amplifier is cascaded with a very fast latch to achieve 4-bit resolution with 7-bit accuracy at a 40 MHz sample rate. In the differential amp, transistors have channel lengths 2-3 times minimum. This will minimize offset voltage that results from fluctuations in channel length. Layout is optimized for device matching, that is: same geometry, same orientation, same surroundings, and common-centroid configuration. P-channel input transistors are used to allow input common-mode range near ground with a single 5-V supply. Also, hot carrier instabilities are reduced with P-channel devices.

The latch uses minimum size devices for maximum speed. The preceding amplifier stage eliminates the need to minimize offset voltage in this stage.

The behavior of the latched comparator in simulation is presented in Fig. 11. As shown, a minimum set-up time of 15 nsec is achieved for 20 mV overdrive.

4.5 Analog Pipeline

Many issues at the architecture, circuit, and interface level are involved in a discussion of analog pipeline design and cannot be covered in detail here. A more complete discussion of this work can be found in the reference[5].

The function of the analog pipeline is to minimize the cost and power requirements of ADC systems needing >10 bit resolution, by buffering the encoding process to the Level 1 trigger rate (L1). The time

---

4. A. Yukawa, "A CMOS 8-bit High-SPeed A/D Converter IC," IEEE Journal of Solid-State Circuits, 20 (3), 775-779 (1985)

5. W. Sippach, "Analog Pipelines for RHIC," Nevis Laboratories note, Sept. 1991

required to form the L1 trigger determines the length of the analog pipeline. For OASIS, the largest trigger delay is about 1 μs for the liquid argon calorimeter. After the delay, the data from the pipeline can be encoded during an allowed L1 trigger deadtime of about 10 μs. Alternatively, the pipeline data can be derandomized and encoded during the average 100 μs interval between L1 triggers. The latter solution reduces the ADC bandwidth by an order of magnitude, but at the expense of a more complicated analog data-handling process. Extra buffer locations must be added on-chip for holding the data undergoing derandomization, and these locations must be able to hold for a much longer time without loss of signal from low-level leakage currents. If the buffer locations are separate from the locations used for the pipeline delay, then a deadtime must be tolerated during the transfer from pipeline to buffer. If on the other hand the buffer locations are physically commingled with the pipeline cells, then "skip" or "relabel" logic must be used to protect the buffer cells from being overwritten by data entering the pipeline. In this case the read address is not equal to the write address minus a constant offset, so a list of currently-used buffer locations must be maintained and updated each L1 and L2. In addition, the memory may need to be capable of simultaneous read and write and of resolving contention between asynchronously-arriving beam-crossing, L1, and L2 read. write, and relabel requests.

A first test chip is designed to study the switched capacitor cells and readout amplifiers (Fig. 12.) It has 4 channels of 10 independently-addressable cells each. N, P, and CMOS switches are distinguished externally and the folded cascode output amplifier (Fig. 13) can be programmed to measure either voltage or charge. Dual NMOS and PMOS versions are included.

The system is expected to have a noise floor of about 100 microvolts and a linear dynamic range of 3V operating from a 5V supply. The output amplifier has a gain-bandwidth product of about 30 MHz and settles to 0.1% in 250 nsec in simulation.

5.0 Status

A test chip for the TRD/Tracker shaping amplifier has been designed and sent to MOSIS for fabrication in the Orbit 2 μm n-well CMOS process. Completed circuits have been received and initial testing shows performance in close agreement with simulation results. Fig 14 shows an oscilloscope photograph of the step response of the shaper IC. The peaking time is about 75 nsec.

An 8-channel chip, based on the same shaper design but with devices scaled for lower power consumption, is in fabrication now and devices are expected back in late January 1992.

A track and hold and comparator circuit as described in section 4.4 on page 4 is in final layout.

A test chip for the analog pipeline (see section 4.5 on page 5) is in final layout and will be sent to fabrication shortly.

6.0 Summary

A set of CMOS ASICs were developed for the OASIS experiment. In-house ASIC designers participated in the decisions on system partitioning and technology choice during the R&D stage of the detector design. Three functions (Liquid Argon analog pipeline/derandomizer, TRD/Tracker preamp/shaper and flash ADC) were targeted for ASIC development to give the maximum impact of this technology on system performance and cost. A detailed set of baseline specifications were laid out and circuit designs have been completed for the critical subcircuits. Layout and prototyping work has begun and initial results (TRD/Tracker shaping amplifier) are quite promising. These developments are ongoing and will be adapted as necessary to meet future RHIC and/or SSC requirements.

Tables

1. TRD/Tracker charge and current.
2. TRD/Tracker preamp/shaper specifications.
3. Shaper Monte Carlo simulation results.
4. FADC specifications

Figures

1. OASIS detector readout electronics.
2. TRD/Tracker cross section and waveform characteristics.
3. (a) ENC vs. Wg for preamp; (b) ENC vs. Id for preamp.
4. Proposed preamplifier schematic.
5. Proposed shaper schematic.
6. (a),(c),(e) - GARFIELD simulations of TRD/Tracker anode current waveforms for MIP at 0°, 45°, and 0° MIP + TR photon; (b),(d),(f) - preamp/shaper output (simulated).
7. FADC block diagram.
8. Track and hold clock feedthrough cancellation schemes.
9. Track and hold clock feedthrough simulations.
10. Comparator circuit.
11. Comparator simulations.
12. Analog memory test chip.
13. Folded cascode output amplifier for analog memory test chip.
14. Oscilloscope photograph of CMOS shaping amp - vertical, 500 mV/div, horizontal, 50 nsec/div.

TABLE 1. TRD/Tracker charge and current.

	MIP	TR	Total	Unit
Anode current	**1.3**	**7-33**	**1.3-3.4**	**uA**
Duration	**0.2 - 1.5**	**~.07**	**-**	**usec**
Charge	**0.3 - 2.0**	**0.5 - 2.4**	**0.3 - 4.4**	**pC**

TABLE 2. TRD/Tracker preamp/shaper specifications.

Channels/chip	4-8
ENC	**2500 e- rms**
Shaping function	**Unipolar, semi-Gaussian impulse response**
Peak time	**70 nsec**
FWHM	**<100 nsec**
Pole-zero cancellation	**For detector tail and preamp feedback pole**
Outputs	**X1, X10 (for TR, MIP resp.)** **2 V full scale**

TABLE 3. Shaper Monte Carlo simulation results.

Quantity	Mean	St. Dev.	St.Dev./Mean(%)	Units
Step Response Peaking Time	81.1	8.14	10	nsec
DC Gain	1.0	.21		21

TABLE 4. FADC Specifications

ADCs per chip	4-8
Resolution	4 bit
Accuracy	1% of full scale
Sample Rate	40 MHz
Input bandwidth	20 MHz
Power	<100 mW/ADC

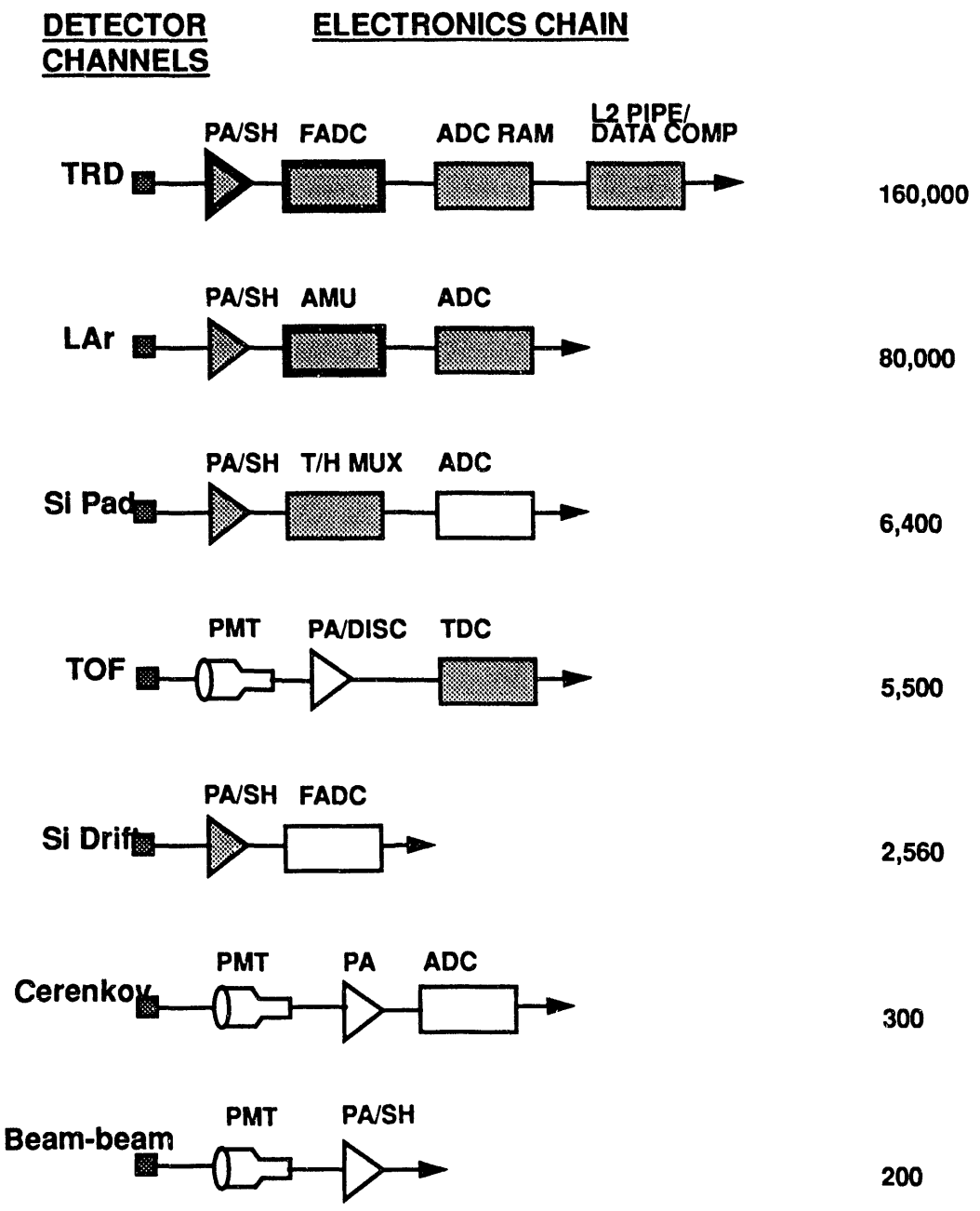
DETECTOR CHANNELS
ELECTRONICS CHAIN
TRD
PA/SH
FADC
ADC RAM
L2 PIPE/ DATA COMP
160,000
LAr
PA/SH
AMU
ADC
80,000
Si Pad
PA/SH
T/H MUX
ADC
6,400
TOF
PMT
PA/DISC
TDC
5,500
Si Drift
PA/SH
FADC
2,560
Cerenkov
PMT
PA
ADC
300
Beam-beam
PMT
PA/SH
200

Figure 1

TRD Detector and Signal Characteristics

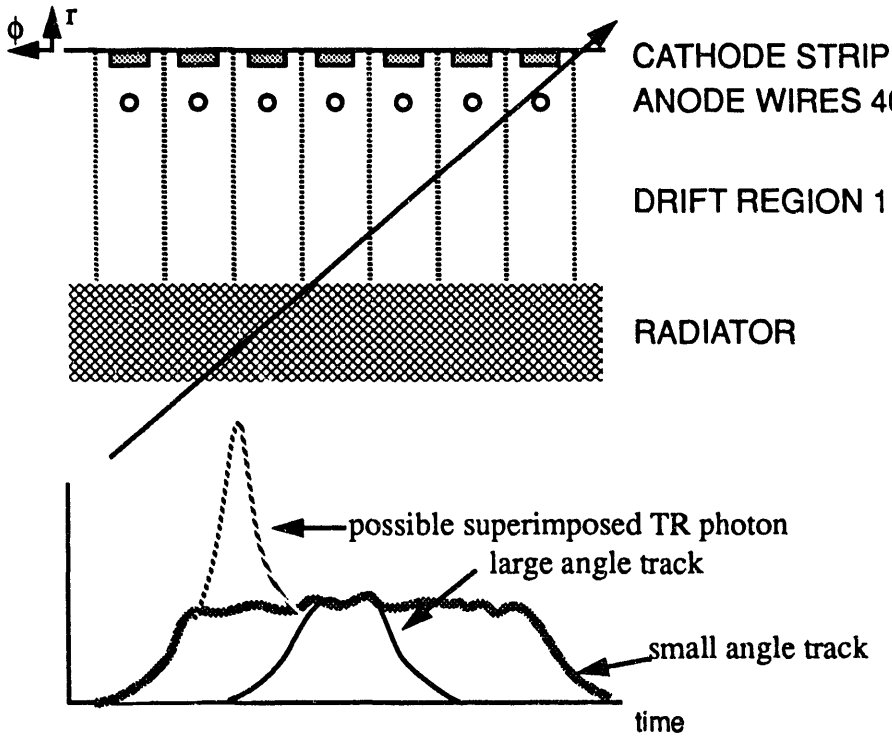

Fig. 2

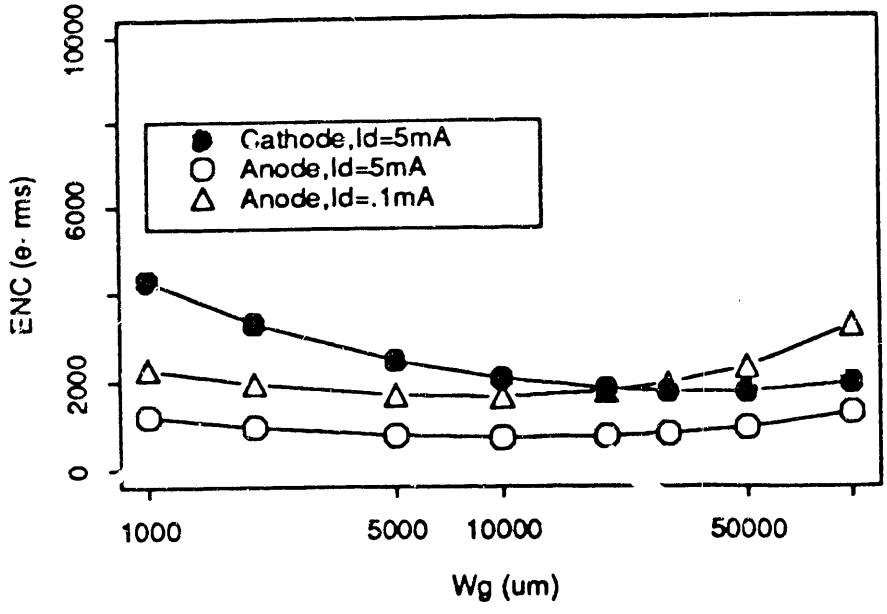

Figure 3(a)

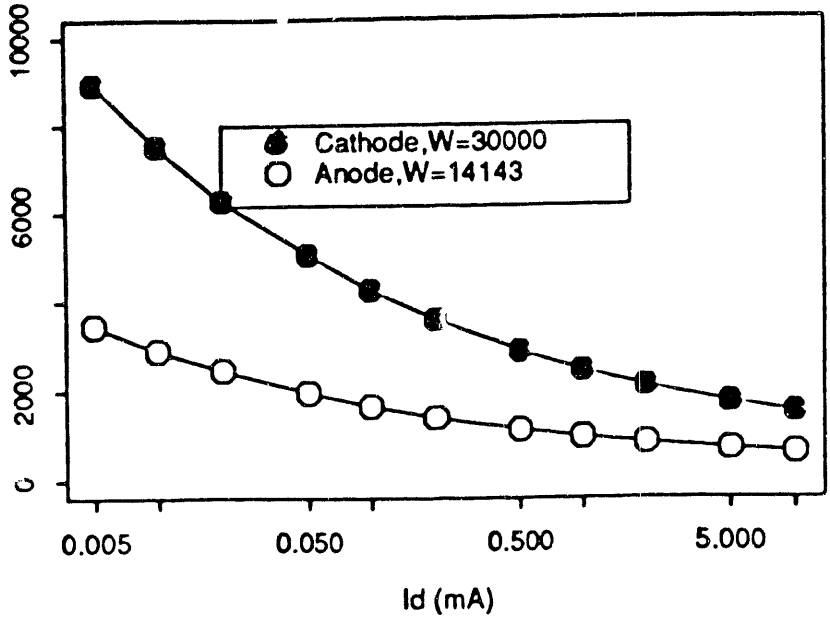

Figure 3(b)

PREAMP/SHAPER

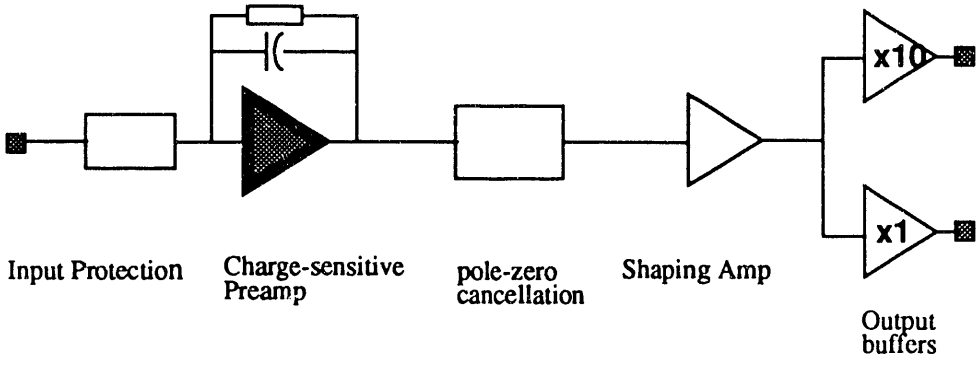

Preamp

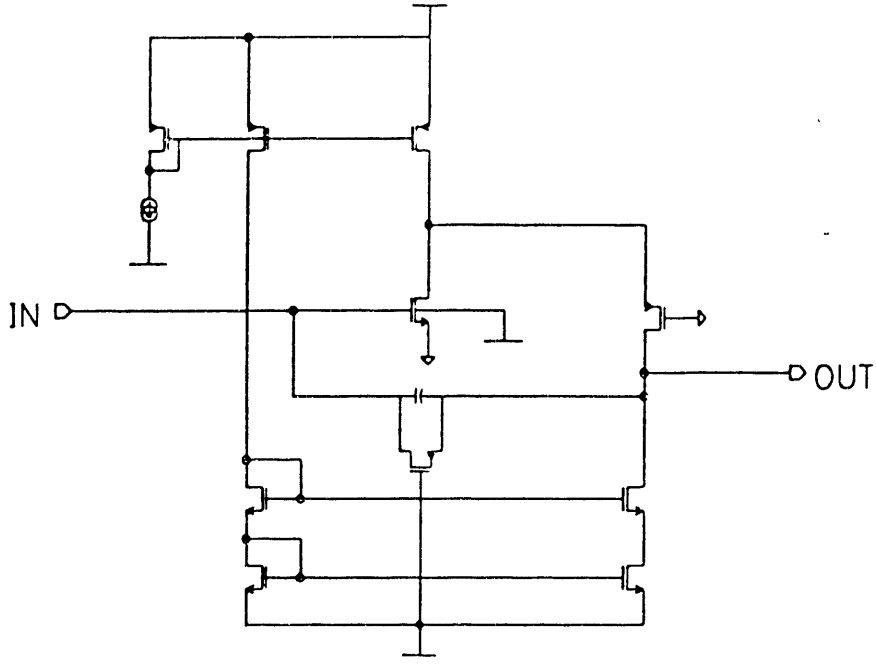

Figure 4

PREAMP/SHAPER

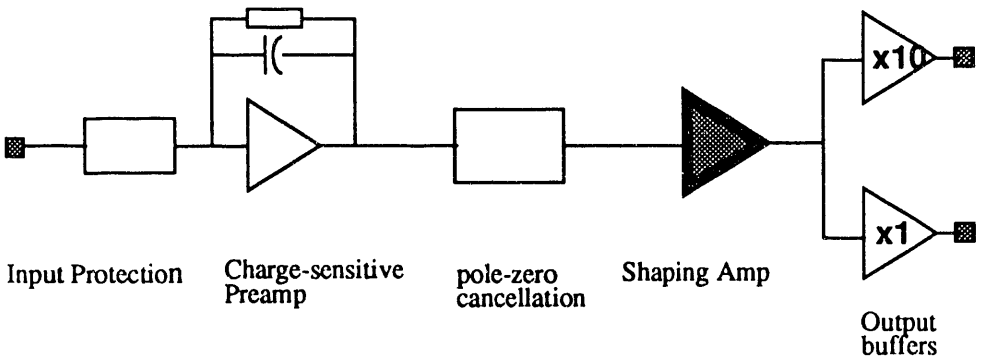

Shaping Amp - Lowpass Section

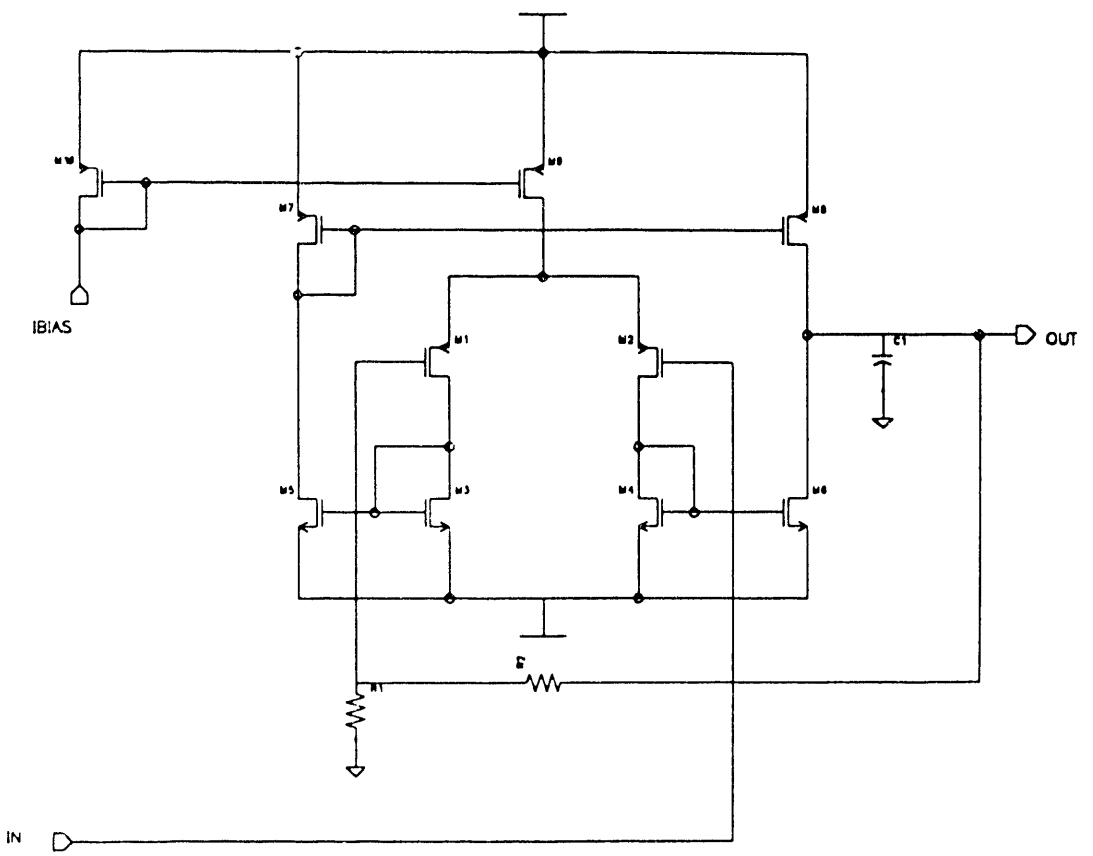

Figure 5

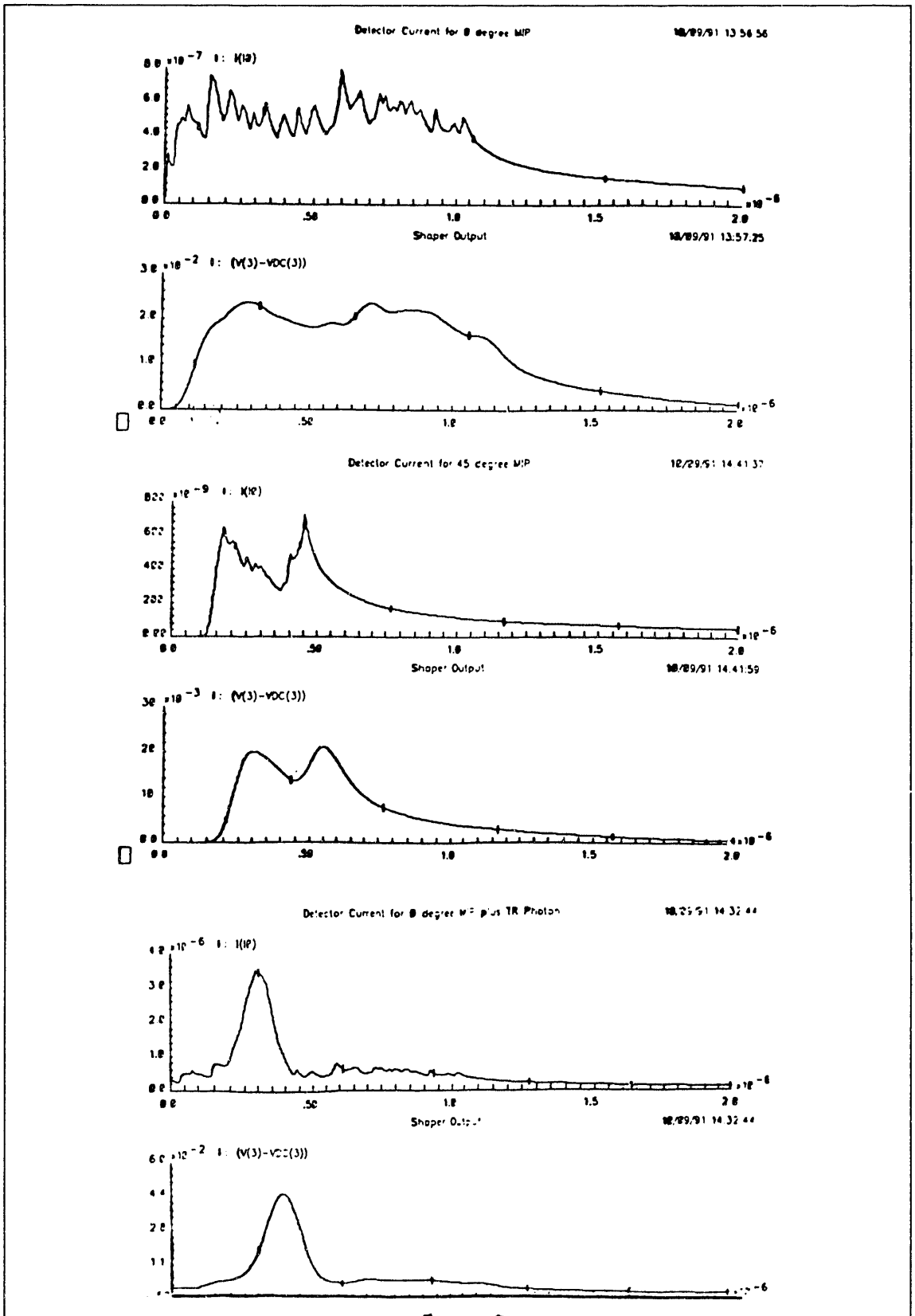
Detector Current for 0 degree MIP
Shaper Output
Detector Current for 45 degree MIP
Shaper Output
Detector Current for 0 degree MIP plus TR Photon
Shaper Output

Figure 6

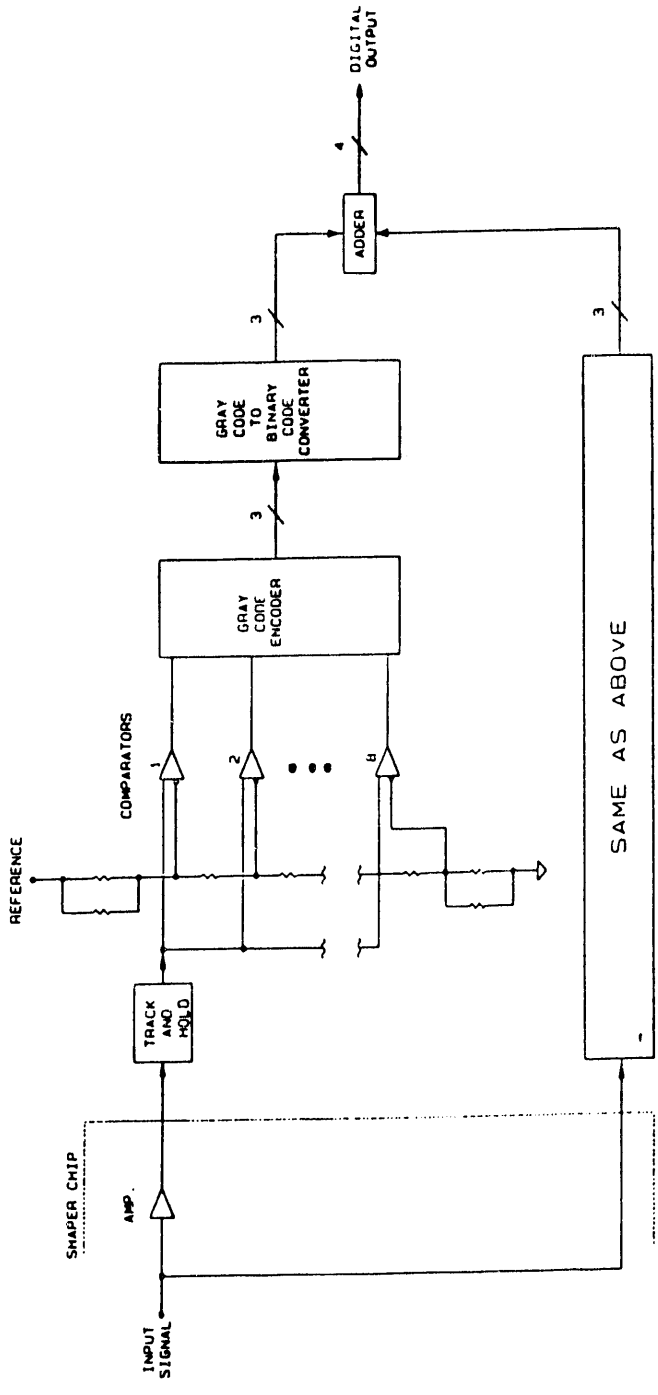

Overall architecture of the proposed ADC. The input signal is divided into high and low level components by the preceeding shaper chip. This is done to keep low level analog signals away from the noisy ADC chip and also to reduce the offset voltage requirement for the comparators. Two similar 3-bit ADC's are used to produce a 4-bit output.

Figure 7

CRITICAL SUBCIRCUITS

TRACK AND HOLD —— High speed must be maintained with minimal clock feedthrough.

a) No charge cancellation

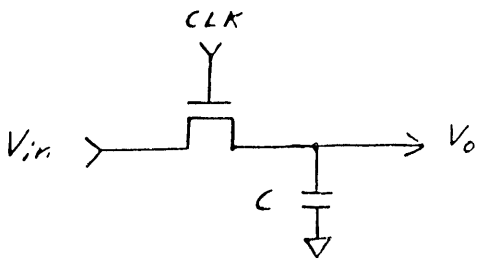

b) First order charge cancellation

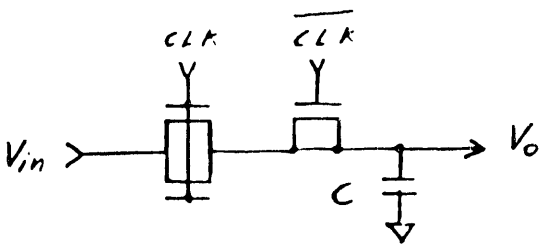

c) Second order charge cancellation

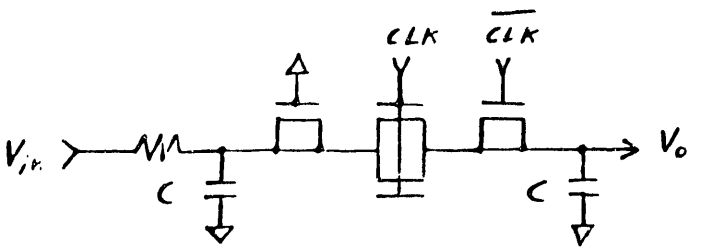

Figure 8

SIMULATIONS

- BSIM1 MOS models are used with parameter values supplied from a ORBIT 2 micron analog run.
- W/L = 3/2 (minimum geometry)
- C = 0.5 pF
- CLK is obtained as follows:

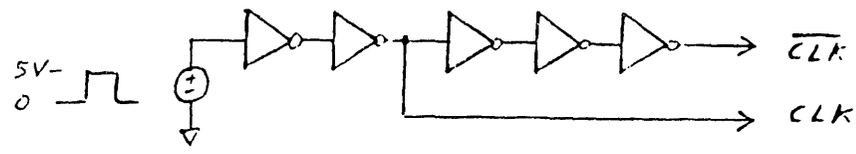

a) **No charge cancellation**

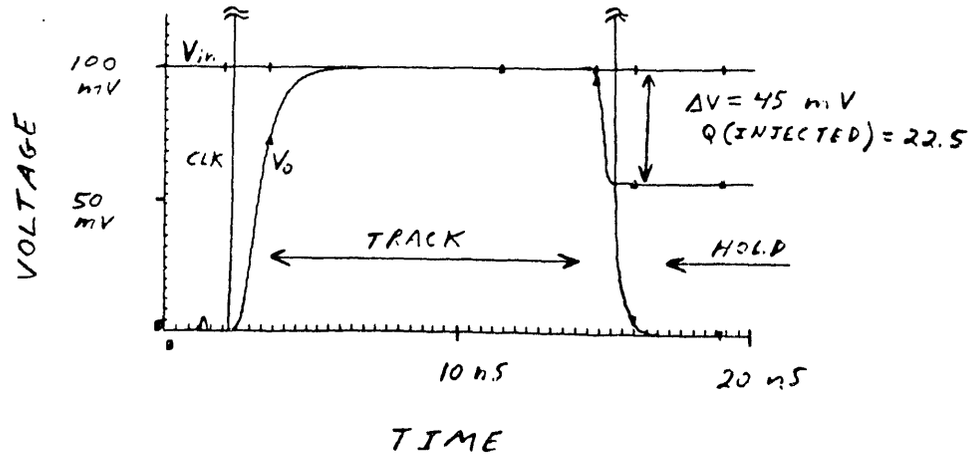

Figure 9

b) **First order charge canellation**

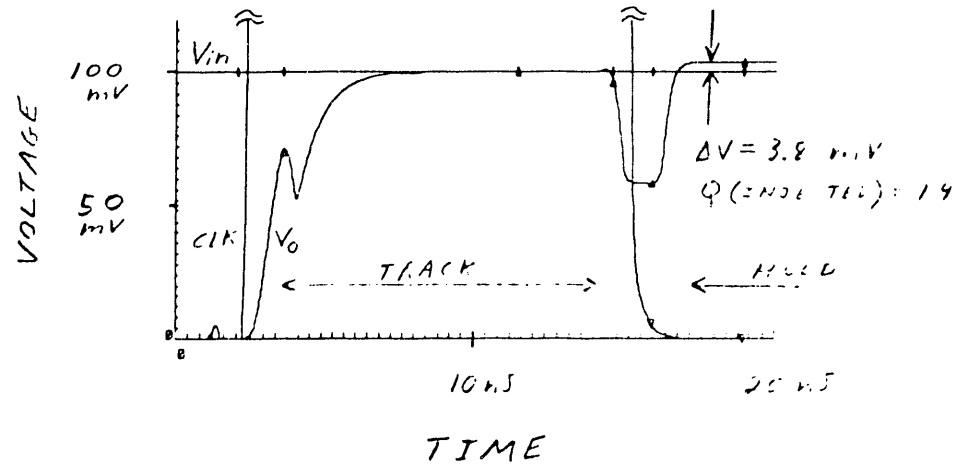

c) **Second order charge cancellation**

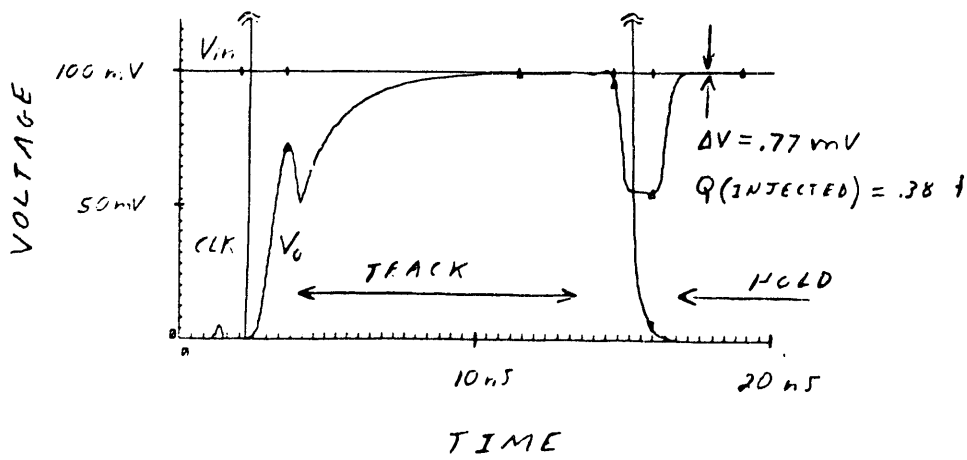

Figure 9

LATCHED COMPARATOR

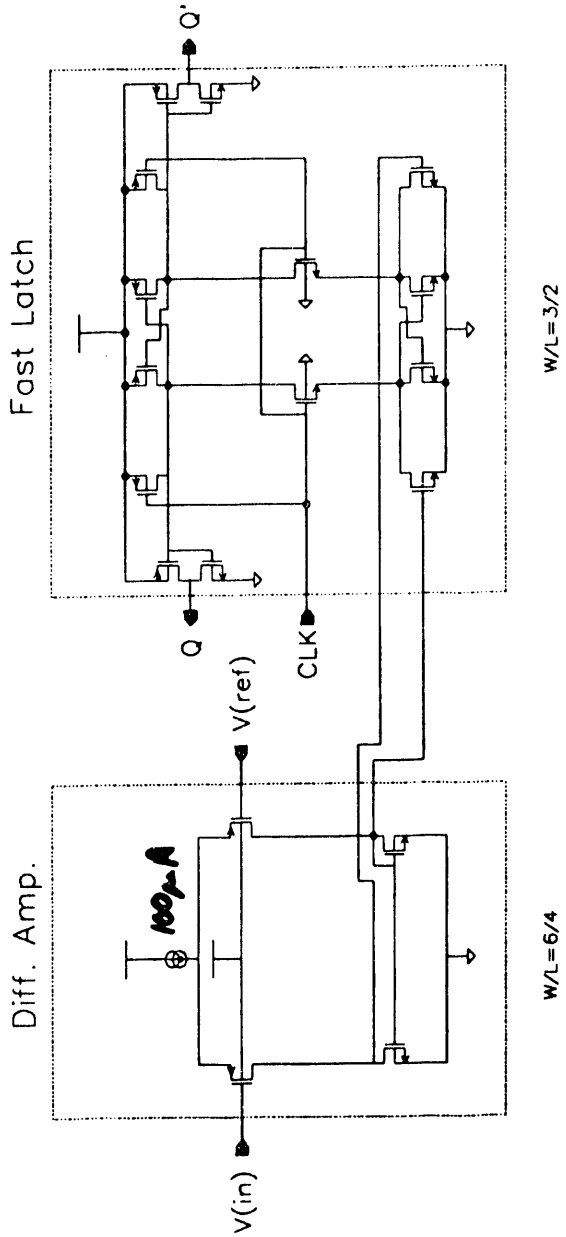

Figure 10

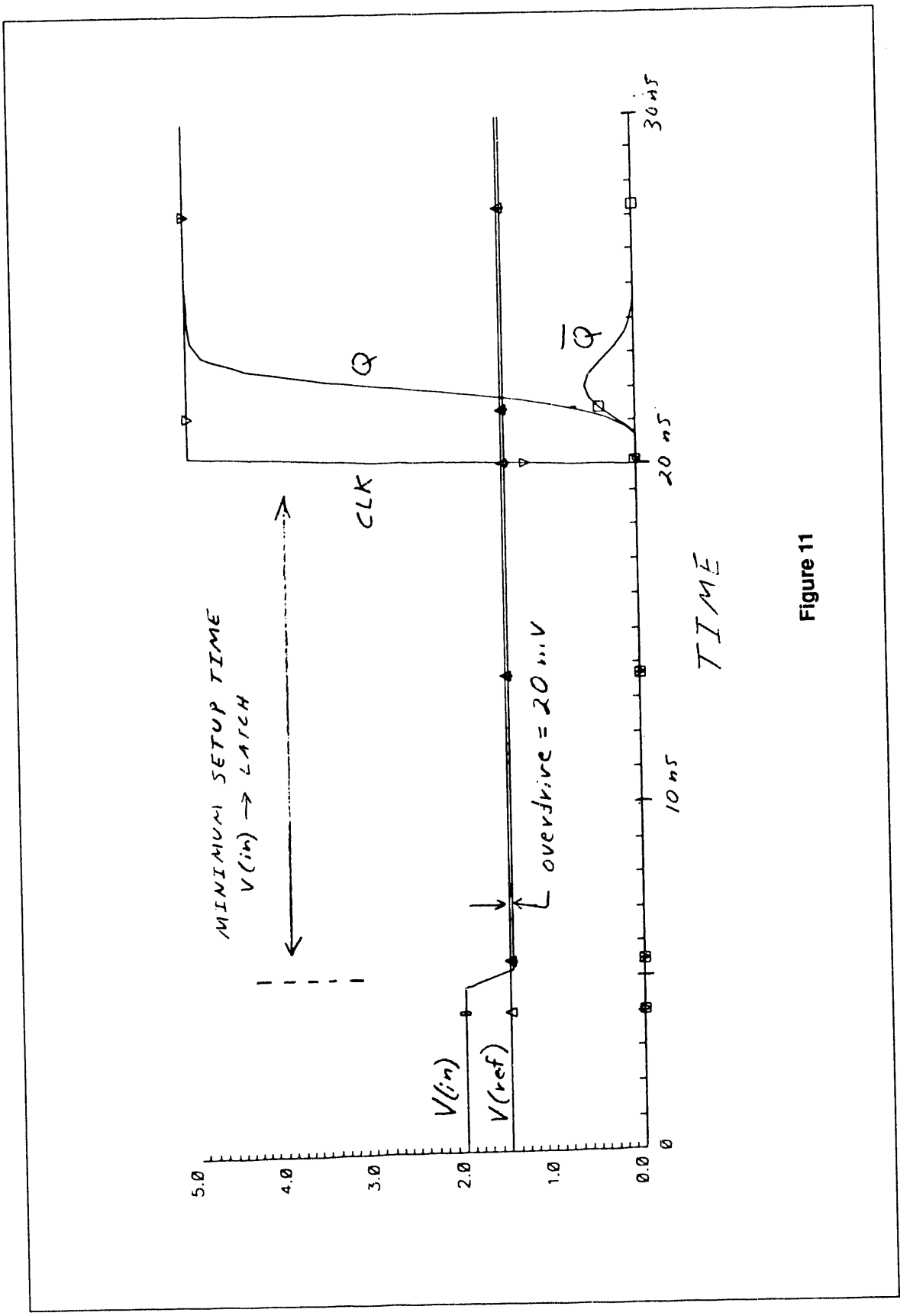
MINIMUM SETUP TIME
V(in) → LATCH
CLK
Q
$\overline{Q}$
V(in)
V(ref)
overdrive = 20 mV
TIME
0
10 ns
20 ns
30 ns
0.0
1.0
2.0
3.0
4.0
5.0

Figure 11

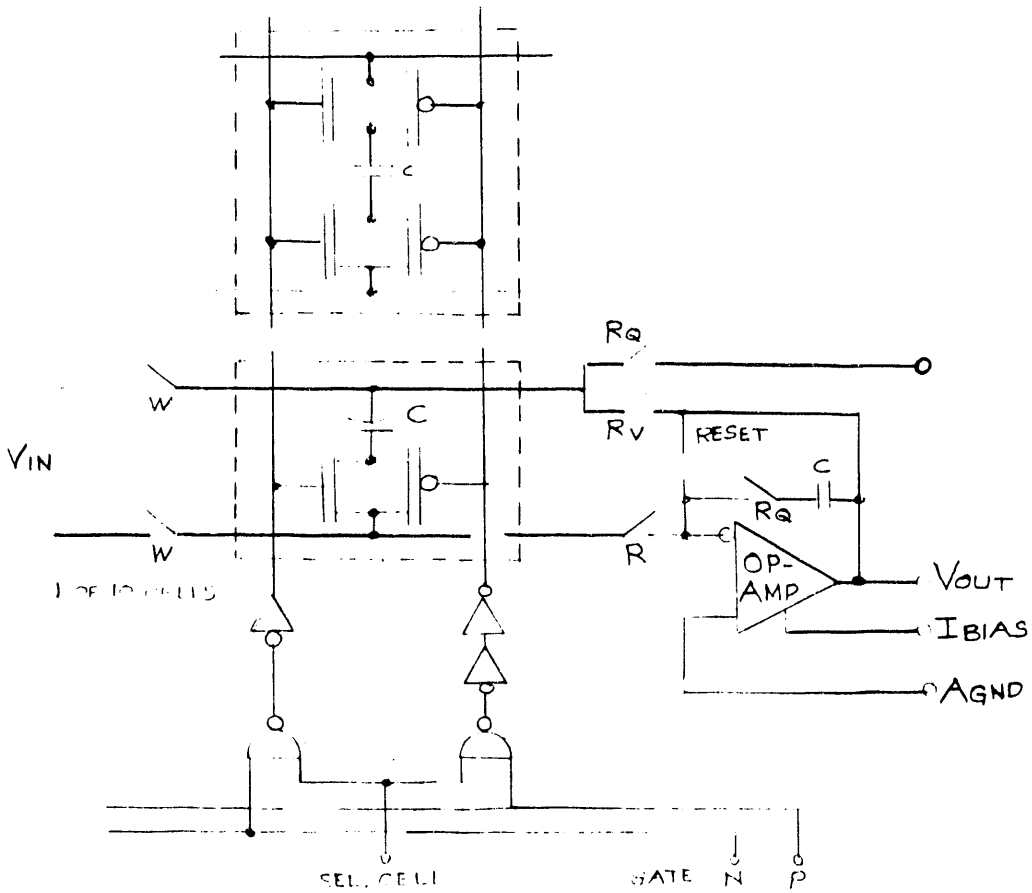

Figure 12

FOLDED CASCODE OP-AMP

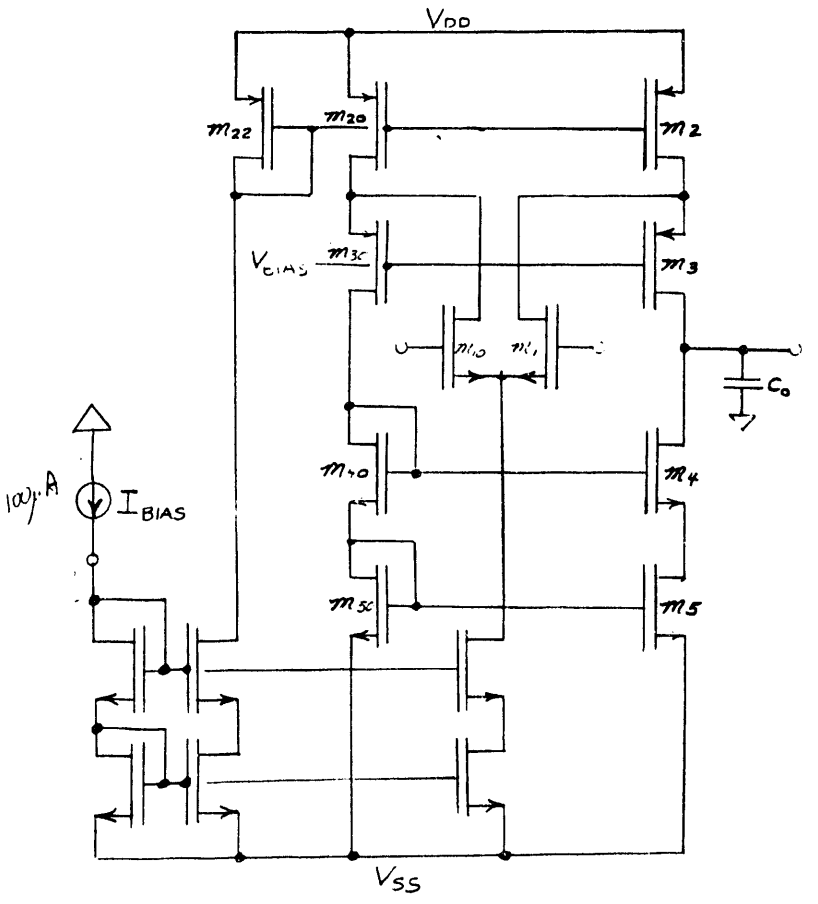

Figure 13

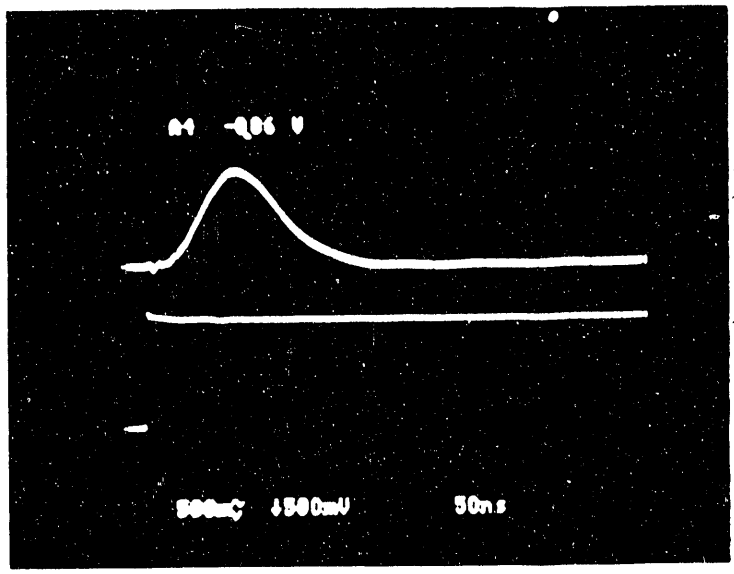

Figure 14

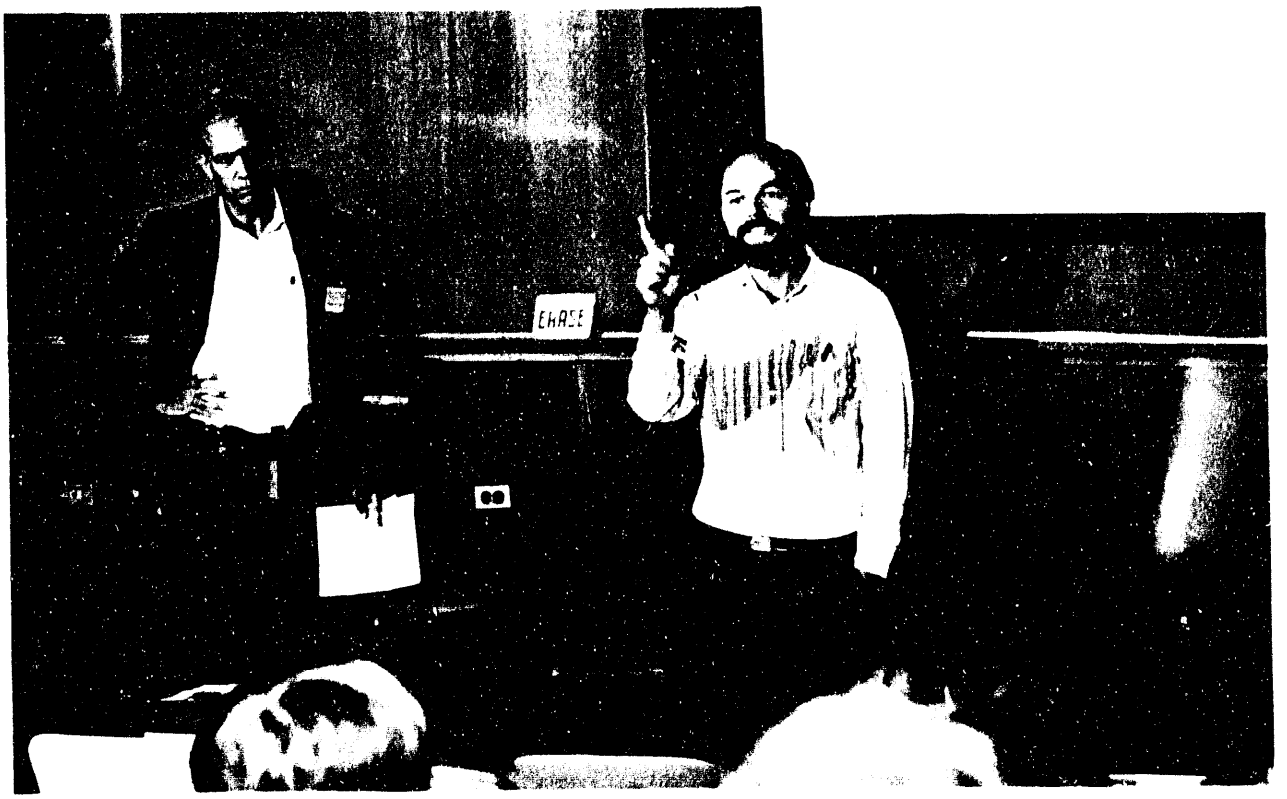
ERASE

New Methods for Trigger Electronics Development

W. E. Cleland and E. G. Stern

Department of Physics and Astronomy
University of Pittsburgh
Pittsburgh, PA 15260

ABSTRACT

The large and complex nature of RHIC experiments and the tight time schedule for their construction requires that new techniques for designing the electronics should be employed. This is particularly true of the trigger and data acquisition electronics which has to be ready for turn-on of the experiment. We describe the use of the Workview package from VIEW*logic* Inc. for design, simulation, and verification of a flash ADC readout system. We also show how field-programmable gate arrays such as the Xilinx 4000 might be employed to construct or prototype circuits with a large number of gates while preserving flexibility.

Introduction

Experiments at RHIC will be approximately as large as experiments at other colliders such as LEP, with on the order of 10^5 electronics channels. These signals have to be read out and processed in about 1 μs to keep up with the Au-Au interaction rate at RHIC. The timing requirements are even stronger for *pp* or *p*C running.

The sophisticated signal processing required for each channel, combined the large number of channels, argues for a high degree of integration in detector electronics. Since most of the circuits will be custom designed, a RHIC experiment will probably contain a large number of Application Specific Integrated Circuits (ASICs).

Industrial users of ASICs have already accumulated a large body of expertise in their use. Before the introduction of large scale system simulators, they found that even when an ASIC functions correctly on the bench in a test jig, a large fraction fail when inserted into the larger system in which they are designed to function. Also, problems may occur in interfacing signals from the ASIC with the rest of the system. Spurred by these problems, industry supported the development of simulators that could simulate an entire system including the ASIC, so that interface problems could be located and corrected before investing in fabrication in silicon.

The use of these simulators need not be limited to systems incorporating ASICs. The simulator can be of use for any large circuit which incorporates many different sorts of components. In this context, components can be small or medium scale integrated circuits, boards, or entire subsystems.

The architecture of the data acquisition system for a RHIC experiment will be pipelined to handle the large amount of data within time constraints. A logic simulator tool is ideal for verifying that a proposed design of a data acquisition system (a) functions

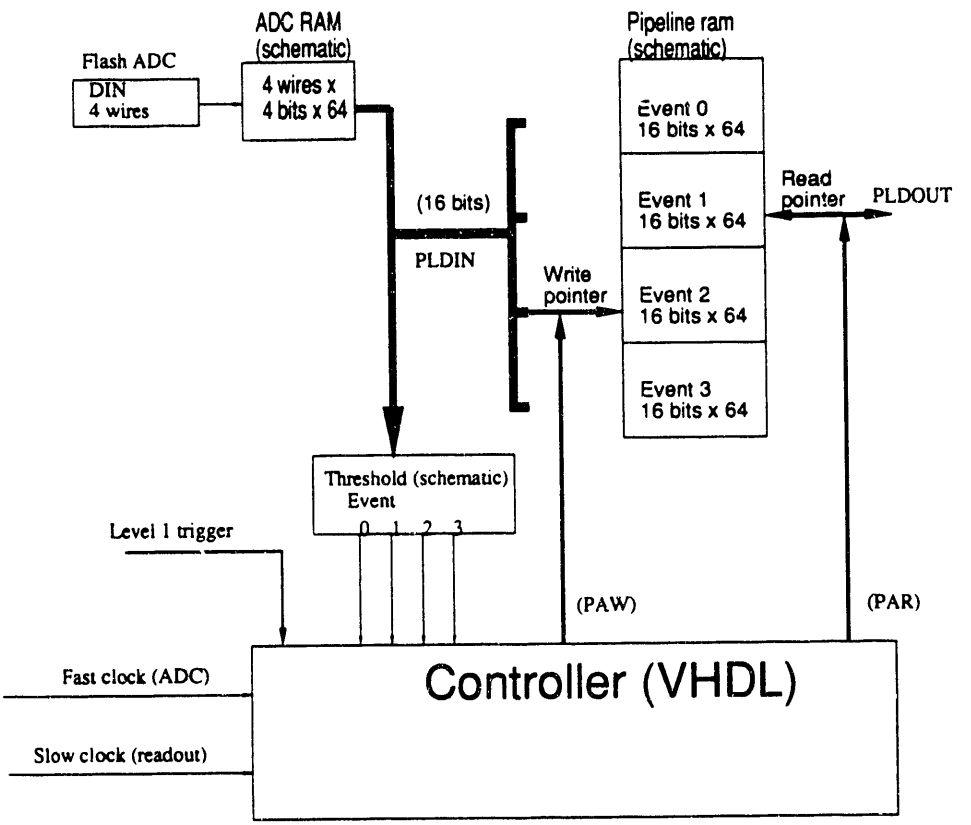

Figure 1: Block diagram of the simulated pipelined readout system

appropriately with no lockups in handshaking signals, (b) correctly handles buffer full situations, and (c) processes the full data load.

Simulator

To study the system integration needs and information flow through a pipelined data acquisition system, we acquired the Workview package of digital electronic simulation from VIEW*logic* Inc. This package supports modeling of digital electronics circuits at all heirarchical levels from gates to boards and systems. It also supports the VHDL language to model the functional behavior of electronic components whose precise structure has not been specified.

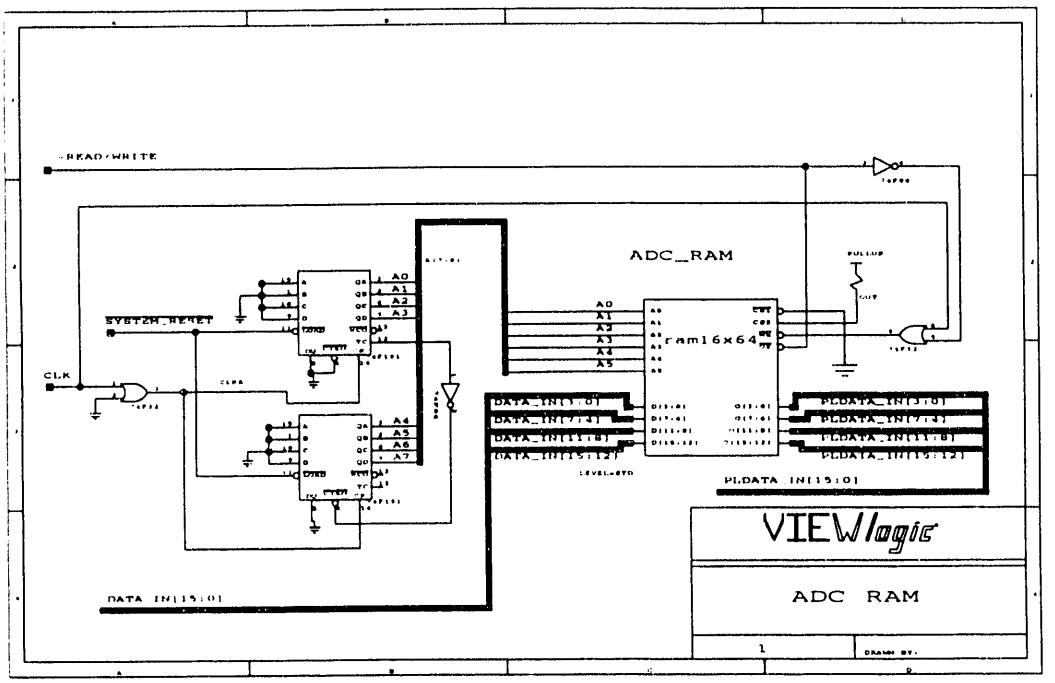

Figure 2: The gate level circuit for the ADC RAM block

As a first test of the Workview package, we have designed and simulated a system for reading data from a flash ADC system into a four event pipeline with conventional 74F gate technology. A block diagram of the readout pipeline is shown in Fig. 1. Each block marked *schematic* represents a circuit composed of 74F gates as is illustrated in Fig. 2, which is the circuit for the ADC RAM. The pipeline is driven by a simulated controller which is written in the VHDL hardware description language. Input data for the circuit is also generated by a VHDL component (not shown) which reads a data file of waveform shapes. This data file can be the output of a detailed Monte Carlo simulation such as the GARFIELD[1] chamber simulation combined with the FRITIOF[2] event generator allowing the simulation of circuit response to realistic conditions.

Data from four flash ADC's enters a 64 word RAM through line **DIN** which memorizes the waveform. At the receipt of a first level trigger, the data are transferred into one of the pipeline event buffers indicated by the write pointer **PAW** using line **PLDIN**. Simultaneously, a comparator circuit examines the data and sets a flag marking the buffer for future processing if the data exceeds the threshold for a valid waveform. Once an event enters the pipeline, the controller senses that data is available in the pipeline and will attempt to read out the buffer pointed by **PAR** through line **PLDOUT**. This readout may be interrupted by a first level trigger which always takes precendence in order to minimize the dead time. After moving data from the ADC RAM into the pipeline, readout of the pipeline resumes at the point where it was interrupted and the ADC RAM becomes available for memorizing further triggers. The ADC RAM and pipeline buffer

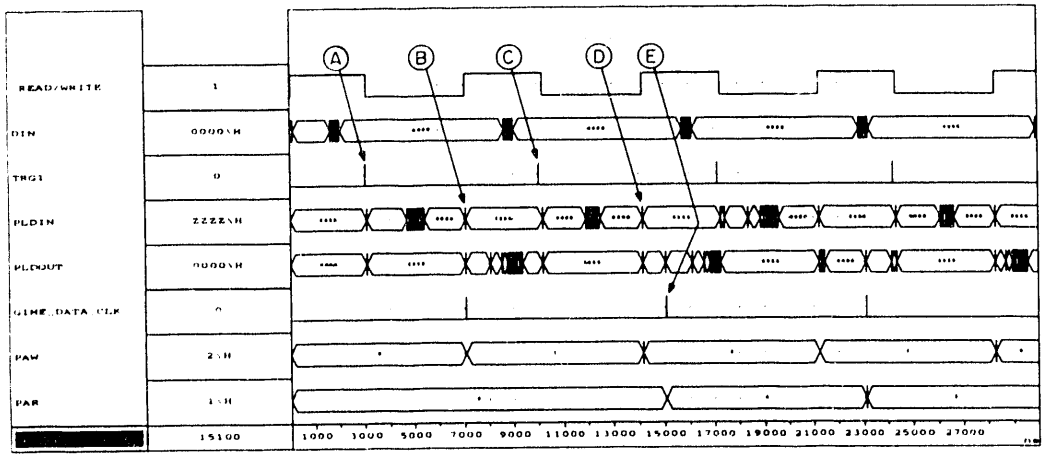

Figure 3: Timing diagram of several cycles of the readout system.

may operate at different clock speeds determined by a fast clock for the ADC and a slow clock for pipeline readout.

A timing diagram of the readout process is shown in Fig. 3. At the start of the trace, data on line DIN is being memorized in the ADC RAM. After receipt of the first level trigger (**TRG1**) at point A, the data appears on line **PLDIN** and is read into the pipeline buffer 0 (**PAW**). After the data have been transferred into the pipeline at point B, the pipeline write pointer (**PAW**) is incremented to prepare for the next event and the readout of the new event is begun (**GIME_DATA_CLOCK**). As the pipeline is read out, the data appear on line **PLDOUT**. A receipt of another first level trigger at C interrupts the pipeline readout and new data is transferred into the pipeline until D. Pipeline readout of the first event resumes until point E. At this time, readout of the second event in the pipeline commences. In this fashion, data is acquired into the ADC RAM, moves into the pipeline, and is asynchronously read out of the pipeline.

During the simulation of the flash ADC readout, several design and timing errors of the readout system were located and corrected, thus demonstrating the usefulness and efficacy of the simulation methodology.

Field Programmable Gate Arrays

An attractive option for the custom circuitry needed by a RHIC experiment is provided by the use of field programmable gate array chips (FPGAs). As in the older Programmable Logic Array (PLA) technology, FPGA chips contain a large number of configurable circuit elements, but unlike PLA's, the circuit is configured by downloading a bit stream in a special setup mode, an operation that may be performed at any time.

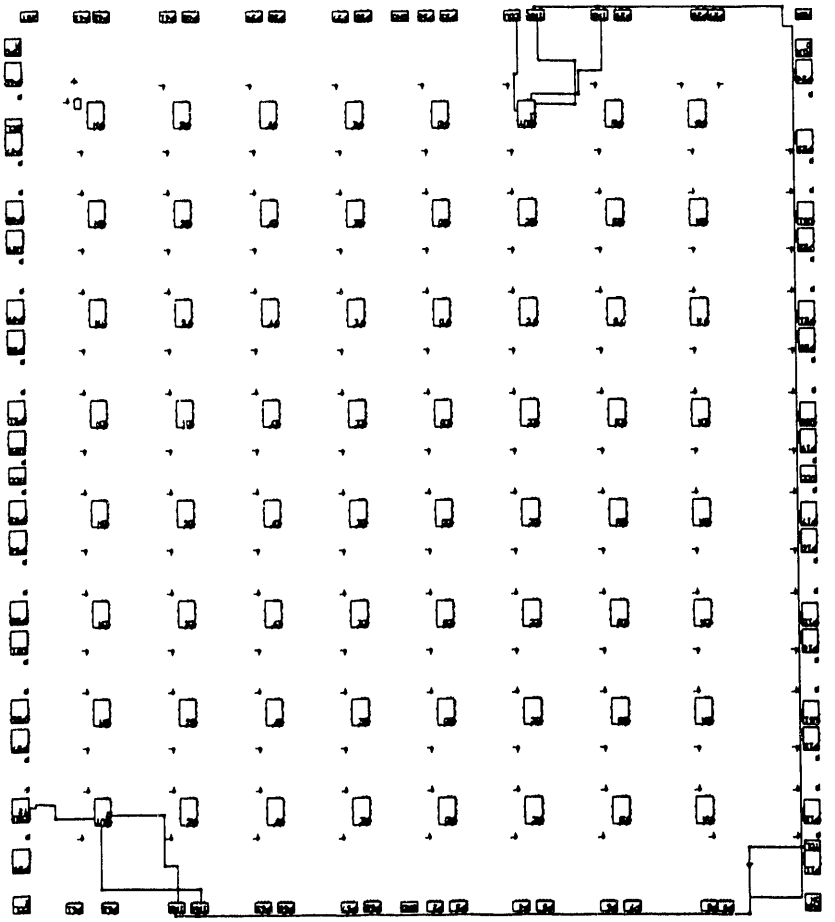

Figure 4: The layout on the Xilinx chip of a circuit to perform one AND function and one NAND function.

We have chosen to investigate the Xilinx line of FPGA chips. Xilinx chips contain arrays of configurable logic blocks (CLBs) and are available in sizes from 8×8 up to 30×30 CLBs. Signals enter and leave the chip through Input/Output Blocks (IOBs), which contain drivers/receivers, latches, and buffers for either high-current drive or tri-state bus lines. CLBs may be configured to perform a variety of functions. The capabilities of the CLB depend on particular line of Xilinx chips. A CLB in the Xilinx 4000 series (which has been announced but is not yet available) may be programmed to:

- hold 32 bits
- perform 2 independent boolean operations, each with four inputs
- contain two flip-flops.

The rated speed of the Xilinx chip is about 70 MHz.

The configuration of the Xilinx chip is developed with a set of design tools which map circuit elements on a schematic into signal routing and CLB configuration commands that are downloaded into the chip during its setup mode. The schematic for the

chip may be developed and simulated with the Workview package of tools already described. The Xilinx line has the advantage that a proven design can be easily converted into an ASIC for large scale production.

A plausible use for the Xilinx chip in a RHIC experiment might be the situation in which it is desired to require a coincidence between elements in two detector systems which project geometrically towards the interaction region. A measurement of the accidental coincidence rate could be achieved by reprogramming the Xilinx to form a coincidence between elements which do not project towards the interaction region, for instance offset by 90°.

To test the performance of the Xilinx chip, we are developing a prototype CAMAC unit with 32 inputs and 16 outputs interfaced to a Xilinx chip programmable via a downloaded program over the CAMAC dataway. The actual function of the CAMAC module will be easily modified by reprogramming the Xilinx chip to perform any combinatorial or sequential logic function with its 32 inputs.

To exercise the design tools, we laid out the design for a circuit that would perform one AND function and one NAND function, i.e., $C1 = A1 \cdot B1$ and $C2 = \overline{A2 \cdot B2}$. The layout of the circuit on the Xilinx chip is shown if Fig. 4. The 8×8 array of rectangles in the center is the array of CLBs in the chip. The rectangles along the sides are Input/Output Blocks. It is clear that the active CLBs have three lines running to IOBs. Two of these are the inputs and one is the output for the boolean function. There would be ample room for 16 binary boolean operations on this chip.

Future Developments

The VHDL language[3] already mentioned in the context of simulation, provides an alternative way of describing the function of a circuit which concentrates more on its behavioral properties than on its detailed structure. VHDL is a high-level language similar to PASCAL or ADA, with extensions for the real-time nature of electronic signals. Because VHDL is a high-level language, complicated operations that would require many gates and registers to implement in sequential logic may be compactly specified in a VHDL program. The function encoded in the VHDL program is often more obvious than the equivalent function performed by an electronic circuit.

Through a process called VHDL synthesis, a VHDL behavioral description of a circuit can be translated or mapped into an actual circuit diagram. This circuit when built will realize in hardware the functionality encoded in the VHDL program. Because it is possible to implement the same behavioral description using many different technologies, the translation of the VHDL program into a circuit design in driven by a *target technology library*.

One target techonology of particular interest is for the Xilinx chip. Using this target library offers the exciting possibility that the function of a circuit such as the CAMAC unit we are designing may be specified with a VHDL program rather than a circuit diagram. Since a VHDL program can be modified quickly without the need for hardware specialists, the function of the CAMAC unit could be tailored be meet the requirements of changing conditions.

Conclusions

We have gained experience with the Workview electronic design and simulation package from VIEW*logic* Inc. The accurate simulation of electronic circuits and systems allows rapid development of large systems with confidence that they will function correctly when constructed. The Xilinx line of field programmable gate array chips is potentially an attractive option to the problem of making complex circuits in small packages that provides flexibility as well as functionality.

Acknowledgements

We would like to acknowledge the contribution of Joe Rabel to this work for useful discussions and his circuit designs for the pipelined readout. We would also like to thank VIEW*logic* Inc. for granting us the use of their Workview software package. This work was supported in part by RHIC R&D funds.

References

1. R. Veenhof, *GARFIELD, A drift chamber simulation program*, CERN Program Library entry W5050, CERN Geneva, version 3.00, March 1991.
2. B. Anderson, G. Gustafson, T. Sjöstrand, Zeit. f. Physik, B6, 235 (1980).
3. *IEEE Standard VHDL Language Reference Manual*, IEEE Std 1076-1987, Institute of Electrical and Electronics Engineers, Inc., New York (1988).

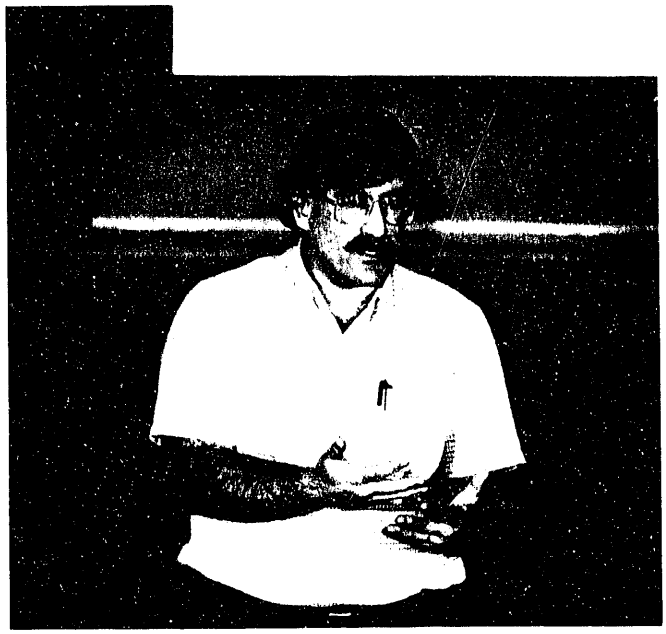

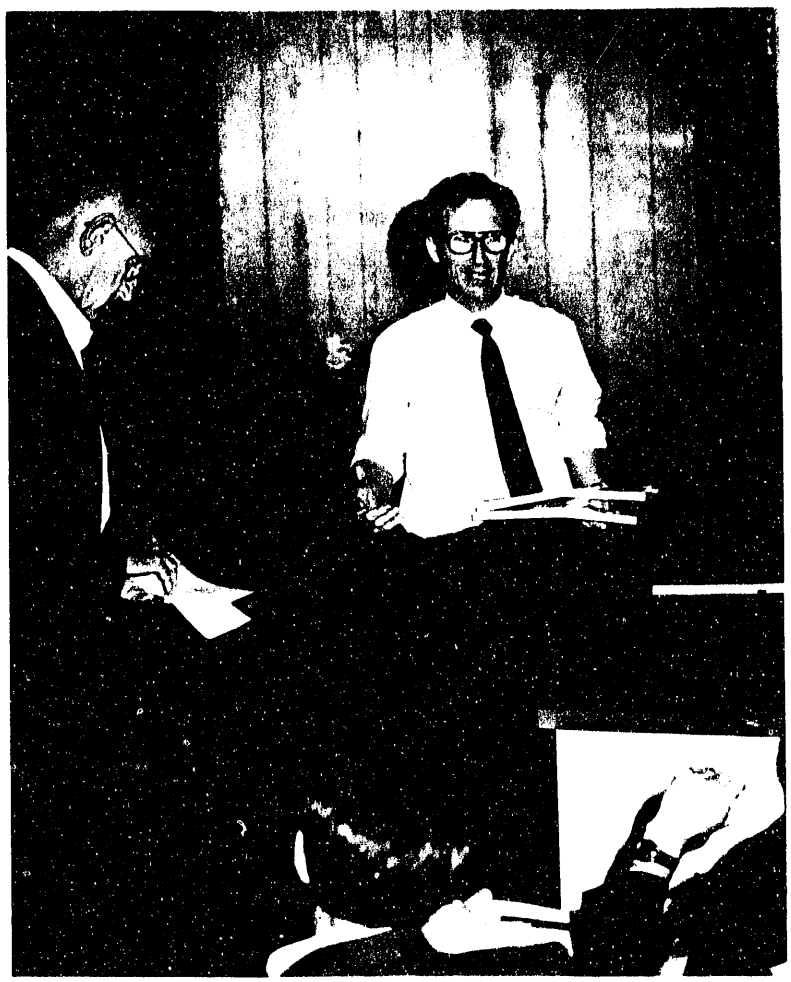

Neurocomputing Methods for Pattern Recognition in Nuclear Physics*

M. Gyulassy[1], D. Dong, and M. Harlander

Nuclear Science Division, Lawrence Berkeley Lab, Berkeley CA 94720

Abstract

We review recent progress on the development and applications of novel neurocomputing techniques for pattern recognition problems of relevance to RHIC experiments. The Elastic Tracking algorithm is shown to achieve sub-pad two track resolution without preprocessing. A high pass neural filter is developed for jet analysis and singular deconvolution methods are shown to recover the primordial jet distribution to a surprising high degree of accuracy.

1 Introduction

Experiments at RHIC will be confronted with difficult pattern recognition tasks due to the very high multiplicity of produced particles (see for example the RHIC proposals in Ref.[1]). In 1990, we initiated a generic R&D program to develop new computational strategies to help solve such problems based on numerical methods from the field of artificial neural networks[2]. One of the new results obtained was the development of a new tracking algorithm[3], Elastic Tracking (ET), that can extend tracking capabilities to much high densities than possible via conventional Road Finding or even previously proposed novel Hopfield network algorithms. This year we tested the tracking efficiency of ET on raw *unprocessed* ionization data[4]. In addition we developed a feed forward network[5] to estimate jet energies in the presence of a very high level of low frequency noise expected in nuclear collisions at RHIC energies. In this paper we review the main results obtained in the above work.

*This work was supported by the Director, Office of Energy Research, Division of Nuclear Physics of the Office of High Energy and Nuclear Physics of the U.S. Department of Energy under Contract No. DE-AC03-76SF00098.

[1]Speaker, Symposium on RHIC Detector R&D, BNL, Upton, L.I.,NY,Oct.9-10, 1991; Second Int. Workshop on Software Eng., A.I., and Expert Sys. for High En. and Nucl. Phys., L'Agelonde, France, Jan 13-18, 1992

2 Elastic Tracking

One of the physics objectives at RHIC is to measure the correlation function of identical particles in connection with pion interferometry[1]. This will require resolving tracks with very small momentum differences. To reduce effects due to Coulomb final state interactions it may be even necessary to resolve 3 or more overlapping mixed charge tracks with very small relative momenta. Present conservative estimates based on conventional Road Finding algorithms apparently limit the resolution to tracks separated by at least 3 pad widths. This limit arises because *local* tracking algorithms require a preprocessing stage in which the centroid of the local ionization density must be first determined. In Ref.[4] we demonstrated that significantly better resolution ($\sim \frac{1}{2}$ pad width track separation) is possible to achieve using the *global* strategy of the Elastic Tracking algorithm.

ET is an adaptive template matching algorithm formulated in terms of dynamical systems. In [3] we considered tracking given preprocessed ionization source densities of the ideal form

$$\rho_S(x) = -\sum_a \delta(x - x_a) \ , \tag{1}$$

where x_a are track centroids. The problem of tracking is then to identify which subsets of points a should be linked together to form tracks. For multiple crossing tracks in the presence of noise, the combinatorial explosion of possibilities creates local ambiguities that can be only resolved by applying global algorithms such as ET. In [4] we extended the analysis to much more realistic densities of the form

$$\rho_S(\mathbf{x}) = \sum_\alpha \rho_\alpha(\mathbf{x}) \ , \tag{2}$$

where the density induced by track α is expressed as

$$\rho_\alpha(\mathbf{x}) = \int d\tau q(\mathbf{r}_\alpha(\tau))\sigma(\mathbf{x} - \mathbf{r}_\alpha(\tau)) \ , \tag{3}$$

with $q(\mathbf{r}_\alpha(\tau))$ being proportional to the variable ionization charge density along the track. The finite range distribution, $\sigma(\mathbf{x})$, depends on the characteristics of the detector. On the average $\langle q \rangle$ is assumed to be proportional to the mean dE/dx of the particle. However, in physical detectors, Landau fluctuations cause large local fluctuations of q around that mean.

The α labels tracks according to the initial phase space point $\phi_\alpha = \{\mathbf{x}_\alpha, \mathbf{p}_\alpha\}$, on an allowed trajectory. We denote those trajectories by

$$\mathbf{r}_\alpha(\tau), \quad \text{where } \mathbf{r}_\alpha(0) = \mathbf{x}_\alpha, \; d\mathbf{r}_\alpha(0)/d\tau = \mathbf{p}_\alpha/m \;\; , \tag{4}$$

for a particle of mass, m, produced at vertex position, $\mathbf{x}_\alpha$, with momentum, $\mathbf{p}_\alpha$. We assume that $\mathbf{r}_\alpha(\tau)$ is either known analytically, e.g., helices in a uniform magnetic field, or computable numerically from the known equations of motion, $m dp^\mu/d\tau = eF^{\mu\nu}_{ex} p_\nu$, in the external EM field, $F^{\mu\nu}_{ex}$, within the detector.

In [4] we also generalized the template charge distributions to allow for extended distributions of the form

$$\rho_T(\mathbf{x}) = q_T \int d\tau \sigma_T(\mathbf{x} - \mathbf{r}_T(\tau)) \;\; , \tag{5}$$

where q_T is the charge assigned to that template and where $\sigma_T(\mathbf{x})$ characterizes the shape of the template distribution around the trajectory $\mathbf{r}_T(\tau)$. For M templates, the total template charge density is simply the sum over the density of each.

Tracking in ET is performed by minimizing an effective energy for the combined source and template configuration

$$\rho(\mathbf{x}) = \sum_{\alpha=1}^{N} \rho_\alpha(\mathbf{x}) + \sum_{i=1}^{M} \rho_{T_i}(\mathbf{x}) \;\; . \tag{6}$$

The ET energy or cost function, $E(t)$, is simply a generalized "Coulomb" energy

$$E(t) = \tfrac{1}{2} \int dx dx' \rho(\mathbf{x}) V(\mathbf{x} - \mathbf{x}', t) \rho(\mathbf{x}') \;\; , \tag{7}$$

where $V(\mathbf{x}, t)$ is a finite range potential with a range that decreases slowly as a function of the *iteration* time. Any convenient finite range positive definite form

can be used for the potential, e.g.,

$$V(\mathbf{x},t) \propto \exp(-x^2/2w^2(t)) \ , \tag{8}$$

with

$$w(t) = (w_0 - w_f)e^{-\gamma t} + w_f \ . \tag{9}$$

The ET energy minimization task is performed via the gradient descent equations

$$d\mathbf{p}_i/dt = -\nabla_{\mathbf{p}_i} E(t) \ , d\mathbf{x}_i/dt = -\nabla_{\mathbf{x}_i} E(t) \ . \tag{10}$$

Starting from a random initial phase space point $\{(\mathbf{x}_i(0), \mathbf{p}_i(0)),\ i = 1, M\}$, the above equations evolve the phase space point specifying the template densities to one of the nearby minima of the interaction energy.

As in all optimization methods care must be taken to avoid getting caught in one of the many *local* minima of the energy surface. The strategy adopted in ET is the introduction of a slowly decreasing range, $w(t)$, of the effective potential as in eq.(9). The initial range, w_0, should be taken to be large as compared with the average width of the measured distribution for an isolated track. The final width, w_f, should be less than that average width. The rate γ needs to be small compared to η so that (10) evolves adiabatically toward the global minimum. In the absence of fluctuations, i.e., $q(\mathbf{r}_\phi(\tau)) = \langle q \rangle$, the above algorithm always converges to the global minimum if $q_T = -\langle q \rangle$ and $\sigma_T = \sigma$.

The power of the ET algorithm is due to (1) that it utilizes all the known information about the class of allowed trajectories in a particular experimental device, (2) that no preprocessing of the measured ionization data is required, (3) that an *adaptive* non-linear χ^2 fit is automatically performed, (4) spurious minima are avoided by using a dynamical range, and (5) the output of ET is directly the quantity (x_T, p_T) of physical interest and thus no postprocessing is needed. See [6] for an alternate formulation of elastic tracking involving simulated annealing methods.

Figure 1 illustrates an application of ET to a 2D simulation of a TPC response for 2 and 3 overlapping tracks[4]. In this example, we assume a histogram form for the source $\sigma(x)$ to simulate the image charge distributions on an array of pads in a TPC like detector [7]. All distances are measured in units of the pad width, Δx. Fig. 1. illustrates the source density in a $N = 20$ row detector for different track separations, d, as defined by the source separation on the row furthest from the common origin of the tracks. As our model of the response of a TPC we assumed that the source image charge distribution on pad i of row k is given by a clipped parabolic form:

$$\begin{aligned} \rho_{ik}^{S} &= (-1 + \Delta q_{1k})[(i\Delta x - kd_1/N)^2 - w^2]_> + \\ &\quad (-1 + \Delta q_{2k})[(i\Delta x - kd_2/N)^2 - w^2]_> \ , \end{aligned} \tag{11}$$

where $[f]_> = f\theta(f)$ and $w = 1.2$. The d_i denote the crossing points of the track on row $N = 20$ and are simply related to the opening angle of the tracks ($\theta = |\tan^{-1}(d_1/N) - \tan^{-1}(d_2/N)|$). For the template density we thus take

$$\rho_{ik}^{T} = [(i\Delta x - kx_1/N)^2 - w^2]_> + [(i\Delta x - kx_2/N)^2 - w^2]_> \ . \tag{12}$$

As can be seen in Fig.1 ET is able to find the tracks even for 1/2 pad separations when local fluctuating ionization density is indeed ambiguous. The global view taken by ET is absolutely essential to resolve such local ambiguity. The average two track resolution, Δd, is shown in Fig. 2 for the case $\delta q = 0.75$ as a function of the their separation d at the outermost detector layer. The curves are labeled by the number of rows ΔN starting on row 20 toward the vertex which were taken into account in the analysis. The rapid rise of Δd for large d for the case $\Delta N = 1$ is due to an interesting phase transition as discussed in [4]. For sufficiently large number of readout layers though, Fig.2 shows that the global information is enough to achieve sub-pad resolution. Therefore we conclude that ET can extend tracking capabilities far beyond that which conventional local algorithms can achieve simply because all the measured and prior information is

used at once. It thus enables one to approach the information theoretic limit of the detector.

3 Neural Network Jet Filters

Another application of neurocomputing techniques of potential interest for RHIC experiments is to jet finding. In [5] we developed a new method of jet analysis based on high pass neural filters which are much more robust to low p_T "noise" than conventional calorimetric methods. Our motivation was two fold. First, conventional methods of jet analysis developed for pp collisions[8, 9] begin to fail in pA collisions[10] due the nuclear enhance background of low p_T particles and are expected to fail completely for future applications to nuclear collisions[1] where up to 10^4 low p_T particles may be produced per collision. Nevertheless, jet analysis may be of special interest for AA reactions as a novel tool for probing the energy loss mechanisms and infrared correlation scales in ultra-dense matter[11]. Second, recent advances in neurocomputing techniques for complex pattern recognition problems[2] suggest a novel approach to this problem.

In particular, we apply Feed Forward Network (FFN) methods to jet analysis. We show that a high pass linear neural filter can be trained using Monte Carlo event generators[11] or pp data to provide a nearly bias free estimator of the jet energy distribution even in the presence of a very high level of low p_T "noise". In addition, we show that knowledge of the neural response function allows us to deconvolute the filtered jet distribution and recover the primordial jet distribution to a surprising high degree of accuracy.

To put this problem into perspective, we recall that perturbative Quantum Chromodynamics (PQCD) predicts that in collisions of high energy hadrons or nuclei, rare high momentum transfer processes lead to a calculable primordial distribution, $\rho_0(e_0, \eta_0, \phi_0)$ of quarks and gluons with transverse energy $e_0 \gtrsim 2$ GeV and pseudorapidity, $\eta_0 = -\log\tan\theta_0/2$, and azimuthal angle ϕ_0. Those partons fragment into a jet of secondary hadrons with highly correlated momenta which

we denote by, (e_a, η_a, ϕ_a), where e_a is the *transverse* energy, η_a the pseudorapidity, and ϕ_a the azimuthal angle of hadron a.

Most of the hadrons from a jet are collimated into an angular cone[8]

$$(\phi_a - \phi_0)^2 + (\eta_a - \eta_0)^2 < R^2 \approx 0.5 \ . \tag{13}$$

The jet energy, as can be determined via a segmented calorimeter, is thus approximately given by

$$E_R = \sum_{a \in R} e_a = \sum_a e_a \, \theta(R^2 - (\phi_a - \phi_0)^2 - (\eta_a - \eta_0)^2) \ . \tag{14}$$

This is however only approximate because other processes (beam jets, pedestal effect, multiple minijets) contribute to the yield of hadrons with $e_a \lesssim E_c \sim 2$ GeV/c. Also, the jet hadronization mechanism can produce hadrons outside the angular cone R. Therefore, E_R is at best a biased estimator of the initial parton energy, e_0, and the measured distribution, $\rho_{exp}(E_R)$, can be expected to differ significantly from the true primordial distribution, $\rho_0(e_0)$ especially as the low frequency noise increases. For reactions such as e^+e^- and pp the background noise is limited to a few particles per unit pseudorapidity and thus E_R becomes an excellent estimator for $E_R \gtrsim 10$ GeV. However, in $Au + Au$ collisions[1, 11], for example, the nonperturbative background is at least 400 times greater and estimates with event simulators[11] indicate that the signal to noise ratio in (14) is on the order of unity for jets in the interesting energy range $10 \lesssim e_0 \lesssim 40$ GeV.

The aim of this work was to develop a more robust estimator of the jet energy by filtering out the low frequency noise with $e_a < E_c$. The essential idea borrowed from the field of neurocomputation is that FFN provide a powerful adaptive tool for approximating arbitrary $R^n \rightarrow R^m$ mappings[12]. An N layer FFN maps an input data array $X = (x_1, \cdots, x_n)$ into an output array $S = (s_1, \cdots, s_m)$ via

$$S = F(W_N \cdots F(W_2 F(W_1 X)) \cdots) \ . \tag{15}$$

The rectangular $n_i \times n_{i+1}$ connection matrices W_i together with response function(s) $F(Y) = (f_1(y_1), \cdots, f_k(y_k))$ define the mapping. The f_i are typically parametrized in terms of a sigmoid type functions but linear functions are sometimes sufficient for the task. The number of layers (connectivity matrices) and the block structure and dimensionality of the connectivity matrices define the architecture of the network. FFN are potentially useful because they can "learn", in principle, an arbitrarily complex mapping though a variety of simple learning algorithms[2] and because they can, again in principle, be implemented in hardware via fast, parallel, analog VLSI technology[13]. This last feature of FFN is of special interest for high energy and nuclear physics where there is a growing need for faster triggering and rapid information processing to cope with the ever increasing volume and rate of data produced by modern detectors. The adaptivity and speed of FFN has been emphasized recently in several other applications to high energy physics problems[14, 15, 16, 17].

Figure 3 shows a typical Au+Au event with two 30 GeV jets at RHIC as predicted with HIJING[11]. Plotted are the transverse energies of all produced hadrons with $e_a > E_c$ with $E_c = 0.2$ and 2 GeV/c respectively as a function of their azimuthal angle. The length of each line corresponds to its e_a. It is obvious from Fig. 3 that most of the background particles can be filtered out by setting $E_c \sim 2$ GeV/c. Therefore, instead of adding the energies of all particles within a jet angular cone as in eq.(14) it will pay to filter out first the low frequency noise. This is only possible with a detector such as a TPC since the momenta of all the particles can be determined separately. Detection of neutral particles of course also requires a highly segmented neutral energy calorimeter in conjunction with a TPC.

In [5] we concentrated on a specific aspect of this problem, namely whether the information loss due to filtering the data can be compensated for using the power of a FFN. The input to the network is the array of transverse energies within an angular cone R. The momenta and energies of produced particles are presumed

to be determined by a first stage tracking algorithm such as ET[3, 4]. The first layer of the FFN is constructed to be a simple threshold high pass filter which only passes the transverse energies of particles with $e_a > E_c$. The output of the first layer is then fed into a sorter which sorts the momenta in decreasing order. For k momenta passing the filter, the sorted vector of hadron energies is denoted by

$$\vec{X}_k = \{e_0^k, e_1^k, \cdots, e_k^k | e_0^k = 1 \text{ and } e_1^k > e_2^k > \cdots > E_c\}$$

where we refer to e_j^k as the transverse energy of the j^{th} rank hadron. The first rank hadron is the one with the largest energy in the jet cone, etc.. This vector is then passed to a second layer of neurons.

For every k we introduce a linear neuron with a connection weight vector $\vec{W}_k = \{w_0^k, w_1^k, \cdots, w_k^k\}$. The output of that neuron is used as the estimate the jet energy,

$$e_k = \vec{W}_k \cdot \vec{X}_k = \sum_{i=0}^{k} w_i^k e_i^k \ . \tag{16}$$

Note that since $e_0^k \equiv 1$ by definition, the component w_0^k acts as an external bias which physically is be related to the missing energy due to the high pass filter.

The problem then is to determine the weights given the momentum cut E_c and jet cone R such that e_k becomes an unbiased estimator of the jet energy. We note further that while (16) is formally linear, the sort operation on the input energy array, $\{e_a\}$, is intrinsically nonlinear. That sort allows us to utilize possible correlations between leading rank particles to minimize the estimation errors.

The performance of neuron k for estimating the energy of a jet of known energy e_0 is measured by:

$$\begin{aligned} \chi_k^2(e_0) &= \tfrac{1}{2}\int (e_0 - \vec{W}_k \cdot \vec{X}_k)^2 \mathcal{P}_k(\vec{X}_k, e_0) de_1^k \cdots de_k^k \\ &= \tfrac{1}{2}(\sum_{ij} w_i^k C_{ij}^k(e_0) w_j^k - 2e_0 \sum_i w_i^k A_i^k(e_0) + e_0^2 P_k(e_0)) \ , \end{aligned} \tag{17}$$

where $A_i^k(e_0) =< e_i^k >$ is the mean energy of the ith rank hadron produced from a

jet of energy e_0 when only the leading k particles pass the filter, $C_{ij}^k(e_0) =< e_i^k e_j^k >$ is the covariance of the ith and jth rank hadrons, and $P_k(e_0) = \int \mathcal{P}_k(\vec{X}_k, e_0) de_1^k \cdots de_k^k$ is the probability that only the first k rank hadrons survive the high pass filter cut. Note that P^k, A_i^k, and C_{ij}^k are determined by the jet fragmentation function $\mathcal{P}_k(\vec{X}_k, e_0)$, which depends implicitly on E_c and R.

Averaging over the primordial PQCD spectrum $I(e_0)$ of jets, a global function for neuron k is can be constructed as

$$E_k = \int de_0 I(e_0) \chi_k^2(e_0) = \frac{1}{2}(\sum_{ij} w_i^k T_{ij}^k w_j^k - 2\sum_i w_i^k F_i^k + Q^k) \,. \tag{18}$$

In contrast to P^k, A_i^k, and C_{ij}^k, the Q^k, F_i^k, and T_{ij}^k are dependent on the form of the QCD jet spectrum $I(e_0)$.

We determine the neural weights, $\vec{W}_k$ so as to minimize the global error function. Since E_k is a positive definite quadratic form, it has one global minimum, and therefore the simplest learning dynamics to train the network can be used. That minimum can again be easily found via the gradient decent equations

$$\frac{dw_i^k}{dt} = -\frac{\partial E_k}{\partial w_i^k} = -\sum_j T_{ij}^k w_j^k + F_i^k \;, \tag{19}$$

or simply solving the linear equation $TW = F$ numerically.

To train the network the jet spectrum $I(e_0)$ was calculated via PQCD[18]. The integration over the fragmentation function was performed via Monte Carlo using the LUND JETSET6.3 program. The following table shows the weights learned for $k = 1, ..., 8$ of leading particles.

k	w_0	w_1	w_2	w_3	w_4	w_5	w_6	w_7	w_8
1	2.69	0.90							
2	2.23	1.03	1.02						
3	2.67	1.01	1.02	0.96					
4	3.00	1.01	1.00	1.00	0.93				
5	3.35	0.99	1.01	0.99	0.99	0.90			
6	3.74	0.98	0.99	0.97	0.97	0.96	0.92		
7	4.43	0.96	0.97	0.92	0.94	1.08	0.92	0.85	
8	5.82	0.94	0.85	1.04	0.98	0.87	1.03	0.82	0.64

While the bias w_0^k reveals a systematic variation with k, the approximate constancy of all the weights, $w_{i\geq 1}^k \approx 1$, indicates that the global minimum in weight space is close to the point defining a simple linear high pass filter (LHPF). This is a non-trivial result of the optimization procedure. We therefore also compare results obtained with the simplest LHPF network in which all $w_{i\geq 1}^k \equiv 1$ but with biases w_0^k determined so as to minimize the global error. As a further test of the above conclusion, we also performed a hybrid network analysis in which only the leading two particles are utilized, i.e., we set $w_{i\geq 3}^k = 0$, to see how quickly the performance of the network deteriorates away from the weight space minimum.

The proximity of the global minimum to the LHPF point results from a combination of effects as demonstrated in ref.[5]. It requires that E_c is small relative to the jet energies of interest, that both charged and neutral particles above E_c are well measured, and that the noise contribution beyond E_c is small. If any of these conditions are not satisfied then the global minimum will move further away from the linear filter point.

The performance of all three networks is compared in Figure 4. Shown are the dispersion and bias of network as a function of the initial jet transverse momentum, P, of an isolated jet in units of the filter cutoff momentum, $E_c = 2$ GeV/c. The response of the network has of course a finite range. Let $R(e, P)$ be the probability that the response is e to an input jet of energy P. This response distribution is

$$R(e,P) = \sum_k \int \delta(\vec{W}_k \cdot \vec{X}_k - e)\mathcal{P}_k(\vec{X}_k, P) de_1^k \cdots de_k^k \qquad (20)$$

The bias of the network,

$$\delta_P = \int de(e - P)R(e, P) \ ,$$

measures the average shift of the estimated jet energy. The dispersion,

$$\sigma_P = \left(\int de(e - P)^2 R(e, P) \right)^{\frac{1}{2}} \ ,$$

measures the rms fluctuation around the average response.

We see that while the optimal neural filter has the overall best performance, the linear high pass filter is only slightly worse. The hybrid two particle filter leads to the worst performance. We emphasize again that the convergence of the neural network to a point in weight space close to that defining a simple LHPF is not trivial and illustrates the power of the method. We could continue to guess different hybrid weight configurations. However, the learning algorithm explores the whole error surface and converges to the true global minimum in weight space without having to make guesses. For this particular problem with this particular fragmentation function it just so happens that the minimum is not far from the high pass filter point. Training the network with real data, say from pp, may lead to a different conclusion.

Having established the parameters of the network, we turn next to the method of deconvolution for jet distribution analysis using singular value decomposition methods[19]. The output spectrum $O(e)$ of the network is a convolution of the response distribution $R(e, P)$ with the primordial input spectrum $I(P)$: $O(e) = \int R(e, P)I(P)dP$. The physics goal is to recover the primordial distribution from the distorted measured one. Binning the input and output spectra into a histogram, we can express this convolution in matrix form as

$$O_i = \sum_i R_{ij} I_j. \tag{21}$$

Naively, we would try to invert (21) by $I = R^{-1}O$. However, in general R is not symmetric and has zero eigenvectors not orthogonal to the others. Therefore, its inverse is ill-defined.

The best we can do is to determine I such as to maximize the likelihood that O is observed given R. Assuming high enough statistics is obtained experimentally that the central limit theorem applies in each bin, the best fit is obtained by minimizing the χ^2

$$\chi^2 = \tfrac{1}{2}\sum_k (O_k - N_k)^2/\sigma_k^2 \tag{22}$$

where $N_k = \sum_i R_{ki} I_i$ is the expected number of counts in bin k and $\sigma_k \approx \sqrt{N_k}$ is the expected variance of the number of counts in that bin. In the limit $N_k \gg 1$, required for the applicability of (22), a good estimate for the variance is obtained by approximating $\sigma_k^2 \approx O_k \gg 1$. Minimizing (22) with respect to I, we find that I must satisfy the following linear equation: $TI = F$, where the matrix has elements

$$T_{ij} = \sum_k R_{kj} R_{ki}/N_k \approx \sum_k R_{kj} R_{ki}/O_k \ , \tag{23}$$

and the column vector F has elements

$$F_i = \sum_k R_{ki} O_k/N_k \approx \sum_k R_{ki} \ . \tag{24}$$

The error made in the above approximation on the right hand side decreases as $O_k^{-1/2}$.

What has been gained relative to (21) is that T is symmetric and thus has a complete set of real orthonormal eigenvectors. Unfortunately, there is no guarantee that all eigenvalues are nonvanishing, and in many practical cases in fact $\det T = 0$. Hence, T^{-1} still does not exist in general. However, we can define its *pseudo-inverse*[19], $\tilde{T}^{-1}$ such that $\tilde{T}^{-1}T = 1 - P_0$, where P_0 is the projector onto the subspace of zero eigenmodes. In that case we can "solve" for I as

$$I = \tilde{T}^{-1}F + I_0 \ , \tag{25}$$

where $I_0 = P_0 I$ is an arbitrary vector in the zero subspace. Since I_0 is arbitrary we might as well take it to vanish, and thus we see that

$$I_j = \sum_{ik} \tilde{T}_{ij}^{-1} R_{ki} O_k / N_k \approx \sum_{ik} \tilde{T}_{ij}^{-1} R_{ki} \tag{26}$$

minimizes the χ^2. Note that if $\det T \neq 0$, (26) reduces to $R^{-1}O$ as expected. Numerically, $\tilde{T}_{ij}^{-1}$ is obtained by the standard singular value decomposition method[19] in which the inverse of near zero eigenvalues is set to zero. We emphasize that the above deconvolution procedure is not an on-line process but is to be performed once at the end of the experiment.

Propagation of the error during deconvolution is inevitable. Given (26) the deconvolution error is found to be

$$\sigma_{I_j}^2 = \sum_k (\sum_i \tilde{T}_{ij}^{-1} R_{ki} / N_k)^2 \sigma_{O_k}^2 \approx \sum_k (\sum_i \tilde{T}_{ij}^{-1} R_{ki})^2 / O_k \ . \tag{27}$$

This error increases as the jet energy increase because the number of counts decreases rapidly with energy. At some point this error exceeds the systematic error before the deconvolution. Beyond that point deconvolution is pointless and we have to live with the small distortions due to the network response.

Shown in Figure 5 is the optimal neural filtered jet distribution (dotted) compared the input QCD distribution (solid line). We see that below 20 GeV, the neural filter significantly underestimates the QCD distribution, but that the distortions become small above that energy. The normalization of the QCD counts is adjusted to that expected at RHIC after a year of running. The filter noise is assumed to be the square root of the number of counts. The square symbols indicate the result of deconvoluting the filter response. We see that for $P \lesssim 20$ GeV, the deconvolution method accurately corrects for the distortions caused by the neural filter. Above that energy the deconvolution method begins to fail as error propagation overcomes the accuracy of the method. Fortunately, however, by that energy the network distortions are so small that the filter response comes within 20% of the desired input.

We conclude that the neural filter deconvolution algorithm developed here[5] looks promising for application to jet finding and distribution analysis. An important point discussed in [5] is that even though the network was trained by a specific Monte Carlo algorithm, we found that it is also robust to significant changes in the primordial jet distribution. Ideally, the network should be trained on-line with real pp jet data where we know already that the PQCD jet distribution is correct from an immense body of prior experiments[8, 9]. In that case the learning dynamics may train the network to a different point in weight space to compensate for the actual efficiencies of the detector and the influence noise. The cutoff parameters, E_c and R, must eventually be determined self-consistently possibly using non-linear neurons to optimize the overall jet finding efficiency. Work on that is presently in progress.

4 Summary

New software approaches and computing algorithms will inevitably play a vital role in tracking and particle identification in high multiplicity RHIC, LHC and SSC detectors. We have shown two examples of the power of such methods in connection with tracking small relative momentum tracks in a noisy TPC and in connection with jet finding in an environment of very high beam and minijet background. Obviously many other applications can be envisioned[20]. Given unlimited resources, Mercedes or BMW type detectors can always be built with sufficient precision and efficiency that any old local information processing algorithm will suffice to process the data into useful physics. However, given finite resources, global neurocomputing optimization strategies make it possible to extract the last drop of useful information even from a VW scale experiment. In a nutshell, neurocomputing algorithms resolve locally ambiguous information by working on the global picture. Fast parallel hardware implementation of such algorithms via VLSI technology could turn even dumb apparati into smart detectors.

References

[1] Fourth Workshop on Experiments and Detectors for a Relativistic Heavy Ion Collider, eds. M. Fatyga, B. Moskowitz, BNL 52262, UC-414, July 1990; K. Kadija et al., An Experiment on Particle and Jet Production at Midrapidity, LBL-29651 (1990).

[2] J. Hertz, A. Krogh, and R.G. Palmer, Introduction to the Theory of Neural Computation, Lecture Notes Vol. 1 Sante Fe Institute (Addison-Wesley Publishing Co, 1991).

[3] M. Gyulassy and M. Harlander, Elastic Tracking and Neural Network Algorithms for Complex Pattern Recognition, Computer Physics Communications 66 (1991) 31.

[4] M. Gyulassy and M. Harlander, High Resolution Multiparticle Tracking without Preprocessing via Elastic Tracking, LBL-31276 (1991), submitted to NIM B.

[5] D. Dong and M. Gyulassy, Neural Filters for Jet Analysis, LBL-31560 (1991).

[6] A. Yuille, K. Honda, and C. Peterson, Harvard Robotics Lab preprint 90-8 (1990); M. Ohlsson, C. Peterson, A.L. Yuille, preprint LU-TP-91-27 (1991).

[7] G. Rai et al., IEEE Trans. on Nucl. Sci., 37 (1990) 56.

[8] F. Abe et al, Phys. Rev. Lett. 62 (1989) 613; PRL 65 (1990) 968; PRD 41 (1990) 1722.

[9] J. Alitti et al UA2, CERN-PPE-90-188

[10] C. Stuart, et al, PRD 42 (1990) 1385

[11] X. N. Wang, M. Gyulassy, HIJING, LBL-29390, 31036, 31159 (1991); Phys. Rev. D44 (1991) 3501.

[12] K. Funahashi, Neural Networks 2 (1989) 183.

[13] C. Mead, Analog VLSI and Neural Systems (Addison-Wesley Pub. Co., 1989).

[14] L. Lönnblad, C. Peterson, T. Rögnvaldsson, Phys. Rev. Lett. 65 (1990) 1321; Lund preprint LU TP-90-8 (1990).

[15] B. Denby et al, IEEE Transactions on Nuclear Science, 37 (1990) 248.

[16] K. S. Lackner, et al , Los Alamos preprint LA-UR 90-3774 (1990).

[17] T. Altherr and J.C. Seixas, CERN-TH.5758/90 (1990).

[18] M. Gyulassy and M. Plumer, Phys. Lett. 243 (1990) 432.

[19] W. H. Press et al, Numerical Recipes: The Art of Scientific Computing, (Cambridge Press, Cambridge, 1988)

[20] I. Tserruya and H. Specht, et al, NA45 Collab, private communication; G. Paic et al (NA35 collab) Nucl. Phys. A525 (1991) 605c.

5 Figure Captions

Fig. 1 Examples of the ionization density in a 2D simulation of a TPC like detector[7] with 20 layers and with local charge fluctuations $\delta q/q = 0.75$ at the pad level. The cases of two tracks with a separation $d = 0.5$ and 4.0 on layer 20 are shown. Top tick marks indicate location of crossing points of input tracks. The solid lines show the ET solution with a potential illustrated by the bell shaped curve on the center layer. Also an example of the response to 3 overlapping tracks is shown.

Fig. 2 Relative two track resolution of ET[4] in pad units as a function of source separation for the 2-D example in Fig. 1 and for large local charge fluctuations with $\delta q/q = 0.75$. ΔN refers to the number of detector rows below and including row 20 that were included in the analysis.

Fig. 3 A HIJING Monte Carlo[11] simulation of a 200 AGeV central $Au(197) + Au(197)$ collision producing two jets with $p_\perp = 30$ GeV together with the associated soft and minijet background. The pulse heights represent the transverse energy, E, of individual particles as a function of their azimuthal angle ϕ for $|\eta| < 1.5$. In the upper graph, all produced particles with $E > 0.2$ GeV are plotted. In the lower graph, only those that survive a high pass filter with $E > 2$ GeV are plotted.

Fig. 4 The response curves for different neural filter weight configurations. The standard deviation, and the bias of the network are plotted versus the input jet energy P in units of the cutoff energy $E_c = 2$ GeV. Three different network configurations are considered. The neural filter is the one trained for the optimal weights. The high pass filter has $w^k_{i\geq 1} \equiv 1$, and the 2 particle neural filter has $w^k_{i\geq 3} \equiv 0$.

Fig. 5 Comparison of the input QCD jet distribution (solid) to the network response distribution (dotted) and the final deconvoluted network response (boxes). Note that the errors propagating due to deconvolution begin to exceed the systematic bias of the network response beyond $P \gtrsim 20$ GeV. However, beyond that point the network response is accurate to $\sim 20\%$.

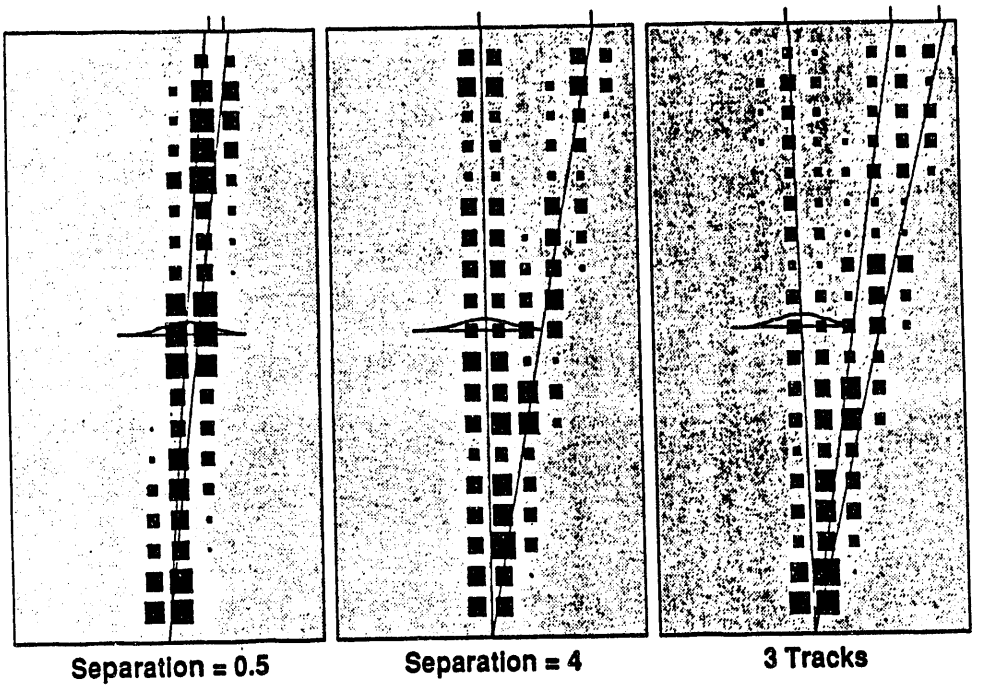
Separation = 0.5
Separation = 4
3 Tracks

Fig. 1

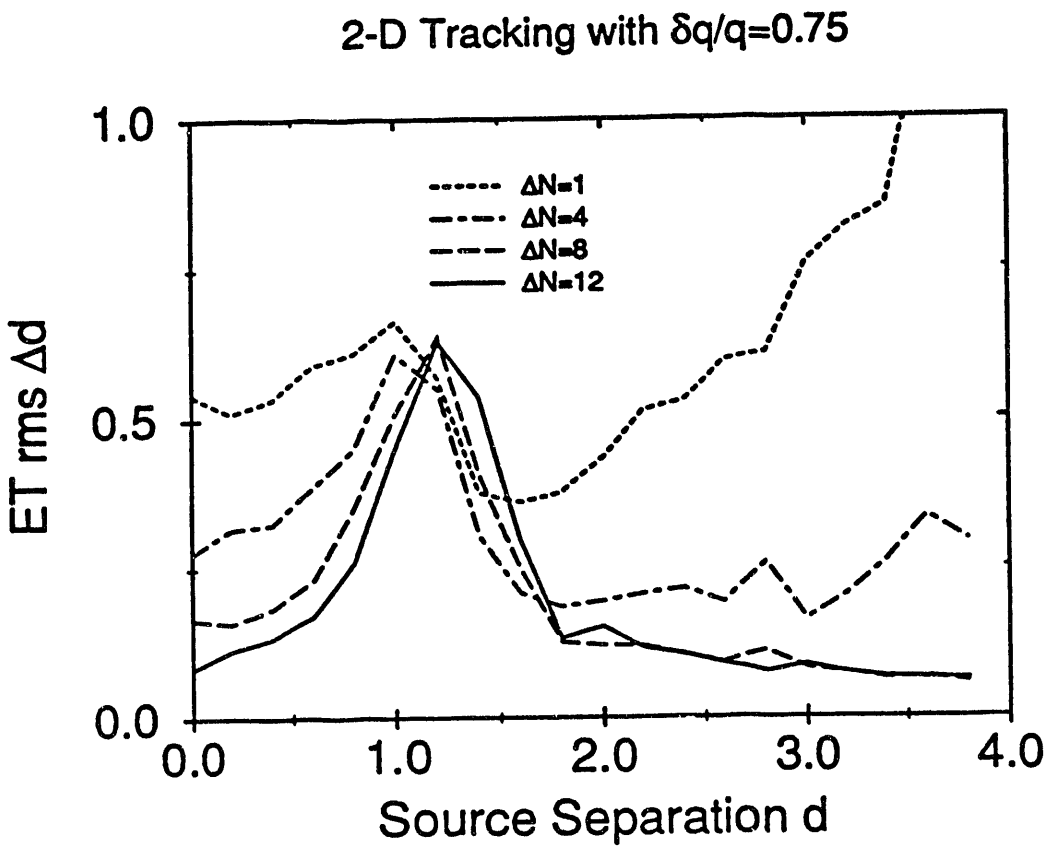
2-D Tracking with δq/q=0.75
ΔN=1
ΔN=4
ΔN=8
ΔN=12
ET rms Δd
1.0
0.5
0.0
0.0
1.0
2.0
3.0
4.0
Source Separation d

Fig. 2

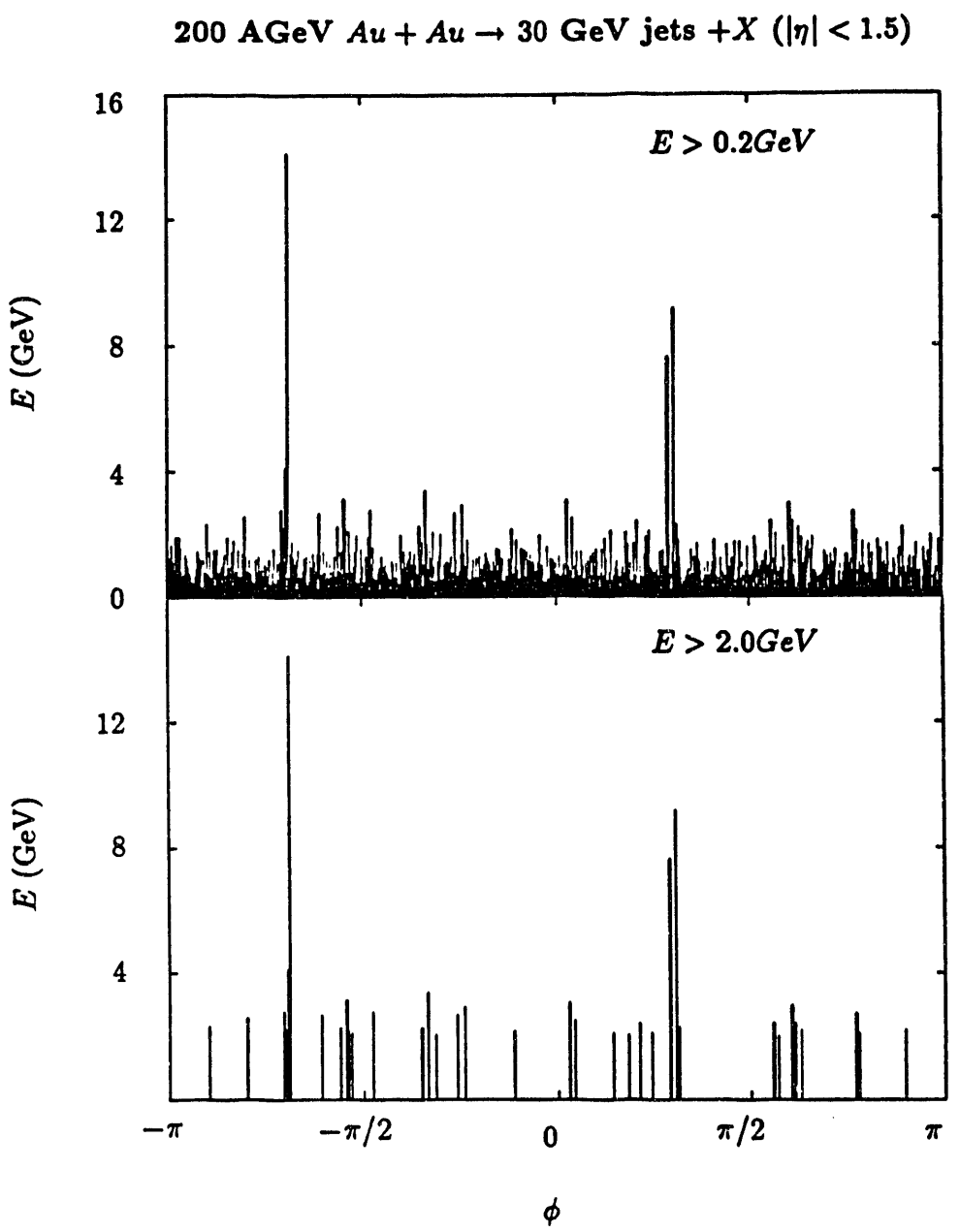
200 AGeV $Au + Au \rightarrow$ 30 GeV jets $+X$ ($|\eta| < 1.5$)
$E > 0.2GeV$
$E > 2.0GeV$
E (GeV)
16
12
8
4
0
$-\pi$
$-\pi/2$
0
$\pi/2$
π
ϕ

Fig. 3

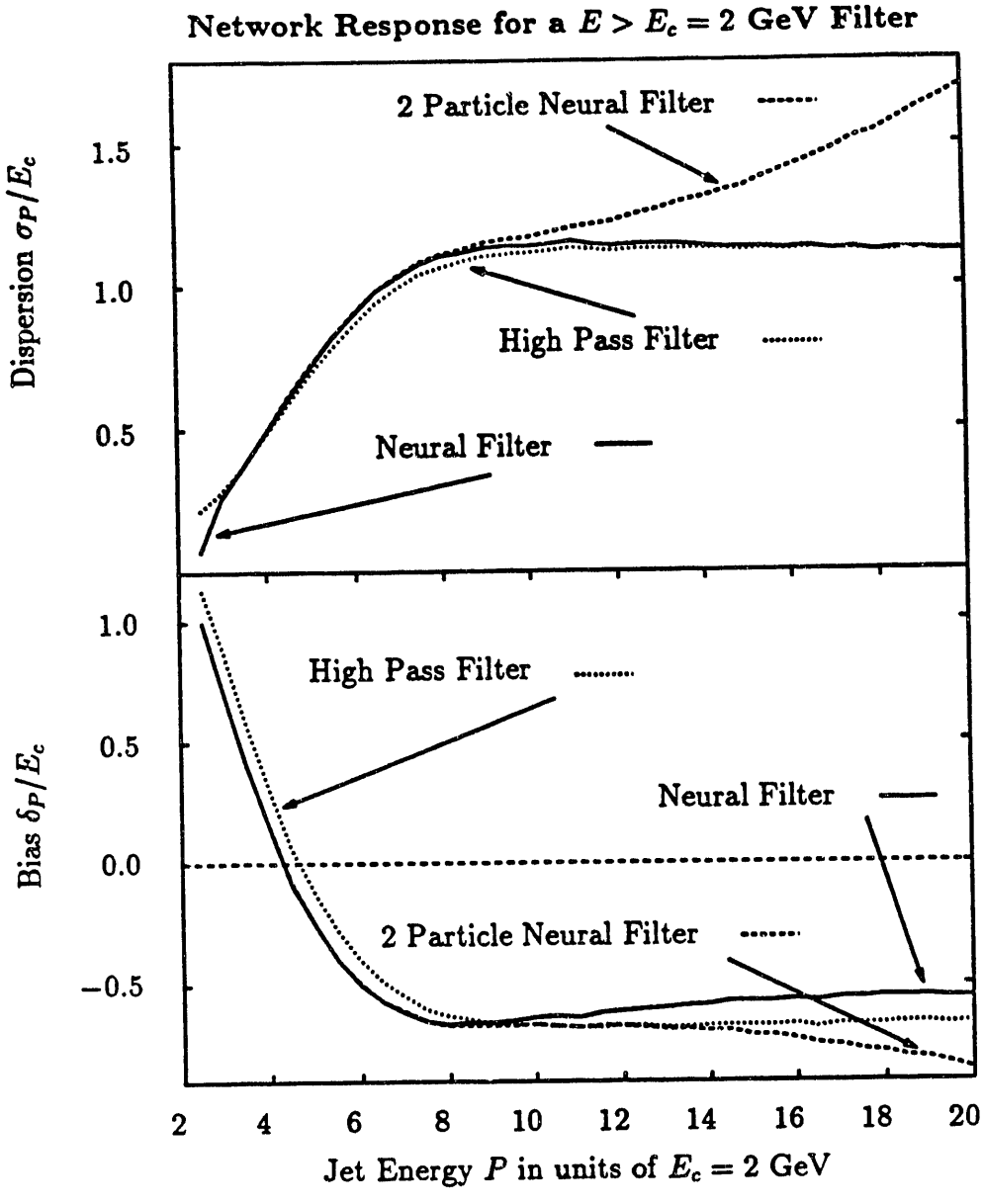
Network Response for a $E > E_c = 2$ GeV Filter
2 Particle Neural Filter
High Pass Filter
Neural Filter
Dispersion σ_P/E_c
1.5
1.0
0.5
High Pass Filter
Neural Filter
2 Particle Neural Filter
Bias δ_P/E_c
1.0
0.5
0.0
−0.5
2
4
6
8
10
12
14
16
18
20
Jet Energy P in units of $E_c = 2$ GeV

Fig. 4

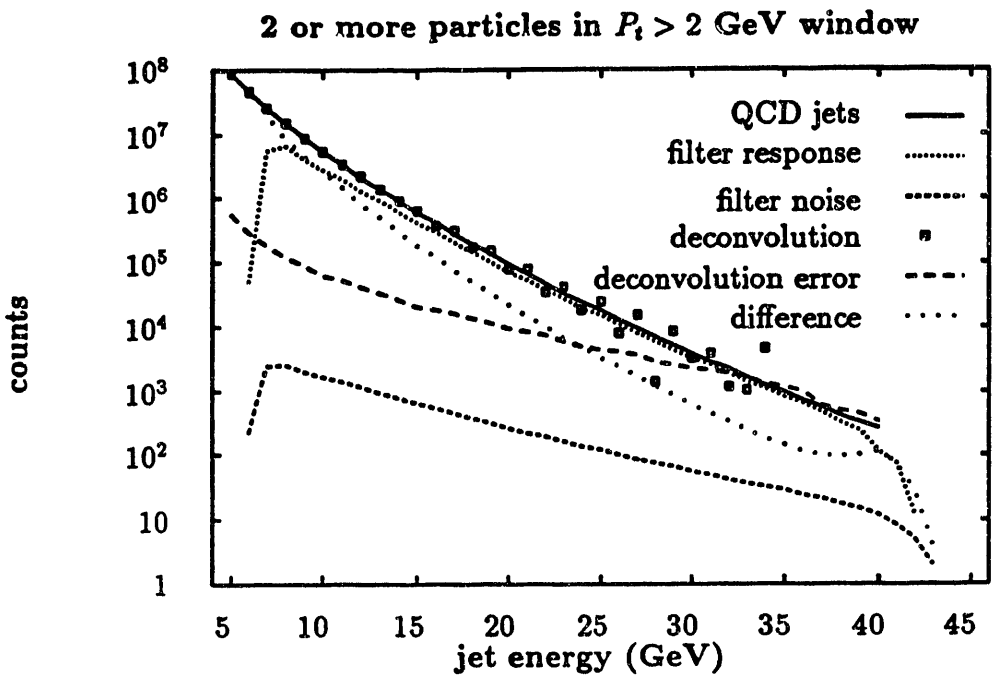
2 or more particles in $P_t > 2$ GeV window
counts
10^8
10^7
10^6
10^5
10^4
10^3
10^2
10
1
5
10
15
20
25
30
35
40
45
jet energy (GeV)
QCD jets
filter response
filter noise
deconvolution
deconvolution error
difference

Fig. 5

THE DEVELOPMENT OF A SILICON MULTIPLICITY DETECTOR SYSTEM

C. A. Pruneau

for the OASIS Silicon Multiplicity Detector R&D Group

J. Barrette[2], R.H. Beuttenmuller[1], S.R. Borenstein[4], J. Hall[2], H.W. Kraner[1], D.Lissauer[1], D. Makowiecki[1], S.K. Mark[2], V. Polychronakos[1], C.A. Pruneau[2], V. Radeka[1], J. Sondericker[1], D. Stephani[1], D. Wolfe[3]

ABSTRACT

The physics program and the design criteria for a Silicon Pad Detector at RHIC are reviewed. An end cap double sided readout detector configuration for RHIC is presented. Its performance as an on-line and off-line centrality tagging device is studied by means of simulations with Fritiof as the event generator. The results of an in-beam test of a prototype double-sided Si-detector are presented. Good signal-to-noise ratio are obtained with front junction and the resistive back side readout. Good separation between one and two minimum-ionizing particle signals is achieved.

1) Brookhaven National Laboratory, Upton, N.Y. 11973
2) McGill University, Montréal, Québec, Canada
3) University of New Mexico, Albuquerque, New Mexico 87131
4) York College-CUNY, Jamaica, N.Y. 11451

1. INTRODUCTION

In the study of heavy ion collisions, such as Au + Au, at RHIC, one will need some event characterization to estimate the number of participating nucleons and the energy density attained in the collisions. To fulfill this purpose, past and ongoing experiments at CERN and at the AGS have used some form of combination of mainly three observables. They are the produced multiplicity of charged particles (N), the transverse energy production (E_T), and the measure of zero degree energy (E_0). In fact, various experiments have noted a strong correlation between these three observables[1]. Thus, unless one is specifically interested in the study of fluctuations and/or correlations, a measurement of one of these observables alone may be sufficient to characterize the events. The measurement of zero degree energy appears somewhat inconvenient in a collider geometry. Also, unless a calorimetric coverage over a substantial solid angle is available, measuring N instead of the transverse energy is the most practical and less expensive alternative to determine the collision centrality and estimate the energy density. In this report, we present the design work we have done for an "end caps" multiplicity detector at RHIC and describe the results of a recent in-beam test of a double sided Si pad detector prototype. The design work described was originally performed for the OASIS detector. However, all our R&D work on the detector technology and readout electronics is easily adaptable to most detector systems used in the RHIC environment.

This report is divided in four sections. In the first section, we briefly review the physics program of a multiplicity detector and discuss the criteria driving the design of a Si-multiplicity detector in the RHIC environment in general, and in the context of the OASIS experiment as a specific example. The use of charged particle multiplicity or the total energy loss of charged particles in a Si detector, as centrality tags, are discussed in Section two. The proposed detector is etched on thin Si wafers with a front and back readout capability. The front side of the Si-detector has a fine segmentation allowing an accurate determination of the multiplicity. The opposite side of the detector, to be read independently, has a coarser segmentation to be used to provide approximate on-line estimates on the collision centrality. Prototype Si-pad detectors with a double sided readout have been fabricated at BNL. The results of an in-beam test of one of them is reported in Section 3. Finally, the problems remaining to be solved and subject to R&D are discussed in the last section.

1. Introduction

The observables measured with a Si multiplicity detector can be summarized as follow:

- Total charged particle multiplicity in a given rapidity range (N)
- $dN/d\eta$
- $dN/d\phi$
- Correlation functions and multiple factorial moments.

Essentially, the physics goals are: 1) to establish the presence or absence of a plateau in the $dN/d\eta$ distribution at mid-rapidities. 2) to determine "event by event" with a reasonable accuracy (5%) the collision centrality, 3) to estimate the energy density produced in the central A+A collisions and 4) search for potential "intermittency effects". Physics goals 1 and 2 imply a multiplicity detector should have a wide rapidity range and a full azimuthal coverage in order to verify the existence of a plateau in the dN/dy distribution and to maximize the number of particles detected for any collision centrality, therefore minimizing the effect of fluctuations in the determination of collision centrality.

Perhaps the most stringent criterion in the design of a Si pad detector for a RHIC experiment is the extremely large particle multiplicity expected for Au+Au central collisions. It can be estimated by means of Monte Carlo event generators such as HIJET, VENUS or FRITIOF to be as large as 1000 charged particles per unit of rapidity at mid-rapidity in central Au+Au collisions at $\sqrt{s}$=200 GeV/u (Ref 2).

Usually, segmentation of Si-pad detectors were designed to permit an average pad occupancy not in excess of 5 to 10%. At RHIC energy, a similar 10% occupancy requirement would easily lead to a detector with 10000 pads per unit of rapidity covered. The implementation of a detector with such a large number of pads would be impractical and costly. An alternative approach would be to let the occupancy probability increase to a high value and then unfold the signals from each pad in an off-line analysis. This approach is illustrated by the energy loss spectrum, shown in Figure 1, measured with a 300 μm Si pad detector by the HELIOS collaboration at the CERN SPS in the study of O + W collisions with a high transverse energy trigger. Clearly, Landau fluctuations are small enough in Si to permit a reasonable separation of single and double minimum ionizing particle (MIP) signals for average pad occupancies

of the order of 45%. The charged particle multiplicity can then be determined by counting the number of MIP in each pad and is subject to a small statistical correction only. The use of such a "high occupancy" technique appears to be suitable for RHIC applications. It will allow a significant reduction of the number of pads and readout channels without a deterioration of the physics capabilities of the detector. However, a 50% occupancy probability will still require about 2000 pads per unit rapidity coverage and would necessitate the use of very large scale integrated circuit techniques for the readout electronics.

At RHIC, the high luminosity of the machine will be achieved partly by operating at high frequency. With the nominal design, there will be one beam crossing every 114 ns. Although the actual rate for Au+Au collisions is about a few 1000 events, the experiment trigger will have to be capable of rejecting or selecting events down to one per second. Obviously, trigger decisions cannot be made in 114 ns so the data will have to be pipelined. Moreover, in the study of high rate A+A collisions, it will be desirable to select the events according to their centrality. Such a trigger selection could be based on the charged particle multiplicity, which can be done quickly so as to avoid unnecessary analog to digital conversion of the data in the pipeline and the associated dead time. However, it would be difficult to handle 10000 pads at once. A simple solution is to reduce the number of pads to be handled for a fast trigger decision by having a parallel readout of the detector with a much coarser segmentation. We propose to do this by using a double sided Si-detector readout. On one side of the detector, the junction side, we propose to use a fine segmentation to provide an accurate measure of multiplicity to be determined in the off-line analysis. On the resistive side, one could use a very coarse segmentation which would essentially provide a measure of the energy losses of all particles traversing the detector.

2. A MULTIPLICITY DETECTOR FOR RHIC

To investigate that a double sided multiplicity detector such as the one outlined above might be used both on-line and off-line to provide a measure of collision centrality, we present in this section simulations performed for the OASIS multiplicity detector.

The conceptual design of the OASIS detector, shown in Figure 2, is designed around a large dipole magnet whose field is parallel to the beam axis. The beams enter the interaction region through center bore of both magnet poles. The multiplicity detector is

located close to the interaction region as illustrated in Figure 3. The detector consists of four identical disks positioned symmetrically about the magnet gap at ±23 cm and ±95 cm. The disks have inner and outer radii of 10 and 26 cm, respectively. The pad detectors were kept out of the flight path of the charged particles emitted in the central rapidity region in order to minimize the probability for secondary interaction and multiple scattering. The detectors are made of a mosaic of 40 smaller sub-detectors of trapezoidal shape cut out of 4 inch wafers currently available from the industry (see Figure 4). These in turn, are segmented in small pads on their junction side in such a way as to insure an average pad occupancy of roughly 50% for central Au+Au collisions. There are 2300 pads per disk for a grand total of 9200 pads. On the resistive side, the segmentation was not finalized but one could envision having roughly 600 back side pads to be handled at the trigger level.

The pseudo-rapidity coverage of the four detectors as a function of the vertex location is shown in Figure 5. Roughly speaking, if one neglects the extreme vertex positions, the rapidity coverage is more or less uniform for all vertex positions between ±20 cm. For a given collision impact parameter, one can then expect the multiplicity to be fairly independent of the vertex position and the measured multiplicity should be a sensible measure of the collision centrality. This is presented in Figure 6, giving the total multiplicity of charged particles hitting the four detectors as a function of the collision impact parameter for Au+Au at $\sqrt{s}$=200 GeV/u. 2000 FRITIOF events were used to generate this plot. Each event was used 10 times, each time with a new vertex location randomly selected between ±23 cm to study the effect of the finite diamond size. Clearly the correlation between the multiplicity and the impact parameter is preserved in spite of the large diamond size and the limited angular coverage of the detectors. There is, however, a non negligible distortion of the correlation caused by a weak dependance of the multiplicity on the vertex position as shown in Figure 7a). Such a dependance can of course be studied and corrected for off-line in the analysis of the data.

For on-line impact parameter selection, one would like to use the total energy loss of the particles in the detectors. As seen from Figure 6b), the correlation between this quantity and the impact parameter is very strong and in fact even better than that with the actual multiplicity. (No noise effects were included in this plot. It is likely that the inclusion of noise would manifest by a weak dependance of the width of the distribution as a function of the impact parameter.) Such a strong correlation comes about because the particle yields at a given location on the detector goes as the cosine of

the incidence angle of the particles, whereas the energy loss of the particles is proportional to the multiplicative inverse of the cosine of the same angle, giving rise to total energy loss more or less independent of the vertex position as seen in Figure 7b). Thus, the energy loss sums would provide a fast and sensitive on-line centrality tag for the events.

3. IN-BEAM TEST OF DOUBLE SIDED DETECTOR PROTOTYPES

Three detector prototypes have been fabricated in the last year or so in the Instrumentation Division at BNL. Figure 8 shows a pad layout of both their resistive and junctional sides. There are 512 pads on the junctional sides whereas the back side is divided into 16 petals. The detectors are based on n-type Si wafers 300 μm thick with a diameter of 3 inches. The silicon has a resistivity of 3000 to 4000 Ω-cm; the detectors are fully depleted with a bias of about 50 v. The back side petal-to-petal insulation is achieved on the first two prototypes fabricated by means of a p-channel stop as illustrated in Figure 8c), whereas a field plate technique was used for the yet untested third prototype.

The detector is mounted on a small G10 board whose layout is shown in Figure 9a). The pads are connected through holes in the G10 board to copper traces on the opposite face of the board by means of thin wires ultrasonically bonded to the pads. The small board is itself mounted as illustrated in Figure 9b) on a larger multilayer board which hosts the readout electronics. Good electrical connections between the boards is achieved by employing a thin sheet of a polymer electrically conducting only in a direction perpendicular to the surface. This polymer is made by Sinetsu Corporation in Japan.

For the purpose of testing the prototypes, the back plane petals were read out with hybrid preamps and timing filter amplifiers operated with a shaping time of 200 ns. The junction side readout was accomplished with AMPLEX chips[3].

A schematic diagram of the AMPLEX chip is shown in Figure 10, together with a table describing the main characteristics of the chip. There are 16 identical channels per chip. Each channel consists of a preamplifier stage followed by a shaping amplifier with a peaking time of 750 ns and a switched capacitor. The 16 capacitors are read out by an on-board multiplexing circuit on a single output line. One detector board was

equipped with 32 chips permitting a full readout of the prototype front pads. The multiplexing circuit of the AMPLEX was triggered and controlled externally. For this purpose, we used the DRAMS electronics modules developed at CERN by E. Chasi.

The DRAMS electronics consist of one controller and one or multiple receiver cards. A schematic diagram of a receiver card is shown in Figure 11. Multiplexed output signals from the AMPLEX are digitized by an 8 bits flash ADC whose output is then compared to a threshold value fetched from a 1K word threshold stack by an Arithmetic Logic Unit (ALU). If the digitized signal happens to be above the threshold for the given channel, a pedestal value is also fetched from the stack and subtracted from the signal which is then stored into a data stack. Otherwise the output of the signal for the particular channel is suppressed. Each receiver card has two such circuits. Each of these can handle sequentially up to 512 channels. The pedestal subtracted signals stored in the data stack, together with a corresponding geographical address, are finally read through CAMAC. A dedicated high speed front panel bus line is also available on the DRAMS. The data were acquired with a PC and were written to 1.4 Mbytes floppy disks.

The first detector fabricated was tested at the BNL-AGS with a Si-beam. Although MIP signals were observed to be clearly separated from the noise for the front pads, the signal-to-noise ratio was found to be somewhat poor (~5). Moreover, the response of the back side petals was found to be extremely noisy. However, the experience thus gained permitted us to identify the various problems with the electronics board and the Si detector itself. A second detector was then fabricated. Careful attention was given, in particular, to the mask quality. The backside response of this detector was studied on a bench with a ^{106}Ru source, as a source of minimum ionizing particles.

The signal-to-noise ratio S/N of back side petals was found to increase rapidity with the detector bias and levelling off at a value around 8.5 for twice the full depletion bias. This corresponds approximately to an ENC of 3000 electrons: a reasonable S/N ratio given the somewhat large capacitance of the back side petals (approx 100 pF). This was a substantial improvement compared to the disappointing results obtained with the first prototype. It was, however, legitimate to ask how the detector would behave in a real "noisy" experimental environment. The prototype was then taken to CERN for an in-beam test.

The test was performed in mid-august as a parasitic experiment on the H6 beam line at the CERN SPS which was setup for an extensive TRD test[4]. Our prototype detector was mounted in front of the TRD setup. We utilized the same beam definition system and trigger as the TRD. A target was optionally put in front of the detector. A low intensity (100 or so particles/spill) 200 GeV/c pion beam was incident directly on the detector.

Figure 12a) shows a spectrum of the typical response of front side pads exposed to the pion beam. The threshold setting capability of the DRAMS receiver card was used to partially suppress the pedestals and permit a significant reduction of the volume of data written to disk. A clean separation of the MIP signal from the pedestal is obtained and the measured signal-to-noise ratio, about S/N=8, corresponds to an ENC of 3000 electrons. Although acceptable in a low occupancy environment, such a performance is not quite as good as one may expect with the AMPLEX readout of the small front side pads. A major contributing factor to the noise was due to low frequency oscillations on the multiplexed output line caused by an incomplete insulation of a level shifter operational amplifier driving the track and hold (T/H) circuit of the AMPLEX chips. The level shifter circuit, located on the readout board, is currently redesigned and one expects an improved S/N of 12 or so.

The typical response of "good" petals is also shown in Figure 12. The energy loss spectrum shown in b) was obtained with a "beam trigger", i.e., with only one pion traversing the detector at a time. The separation between the MIP signal and the pedestal peak is excellent. Petals were found to have MIP S/N ratio ranging from 7 to 9, which is a satisfactory response in view of the large capacitance of the pads. The E-loss spectrum shown in Figure 12c) was measured with a "high multiplicity trigger". A target was placed right in front of the detector. The signals of four petals exposed to the beams were summed and fed into a discriminator set to require a large pulse height. Multiplicities ranging from 2 to 4 MIP particles could be selected. Double hits in one detector back side petal are clearly seen in Figure 12c). This confirms the result shown earlier (Figure 1) and demonstrates that Si pad detectors can be used for charged particle multiplicity measurements, even with high occupancy probability per pad and with pads as large as 2 cm^2.

Finally we consider how the front and back side response of the detector correlates in Figure 13, which shows a plot of the sum of pulse height (pedestal suppressed) of

front side pads matching one back side petal as a function of the signal strength in that petal. Clearly, although the detected multiplicities were rather limited and the correlation has a finite width, there are indications of good linearity between the two side responses. The charge collection efficiency of the back side petals was tested explicitly by feeding a known charge in the petal preamp channels. Within the accuracy (approx. 10%) of the measurement permitted by poor statistics and the equipment available the charge collection was found to be maximal for all tested petals.

4. FUTURE PLANS

The feasibility of using a double sided Si pad detector readout for multiplicity measurements has been demonstrated for the first time. A good energy resolution can be achieved with back side pads as large as 2 cm^2. Also, AMPLEX chips were used successfully to perform the front pad readout of the prototype detectors. Such chips, although not suitable for RHIC application because of their long shaping time and lack of pipelining, nevertheless constitute a good model and potential building block for RHIC readout electronics. Given the feasibility of double sided detector readout, a fast triggering scheme such as the one devised for OASIS and outlined in section 2 appears quite promising for large RHIC detectors. We emphasize that the proposed "end caps" geometry allows, at low cost, a good centrality tagging both on and off line without any deterioration of tracking resolution of particles emitted at central-rapidities.

The research and development work on double sided readout detectors is not completed and is still in progress. A Field Plate prototype detector has been fabricated and will be tested. Also, although a good mask quality was shown to be essential for the fabrication of a detector with a reasonable response, the back plane response of the tested detector was not found to be uniform. Some petals were found to be extremely noisy. These are in part due to bad front side pads. A good petal response could be restored, in some cases, by disconnecting the noisy front pads. However, not all noisy petals could be eliminated. The source of noise has to be studied further. In particular, one must build a few more detectors and determine how reproducible the results discussed in this report are and whether it is possible to produce detectors that are 100% active, i.e. with no dead pads.

REFERENCES

1. See for instance P. Giubellino et al., NIM **A275** (89) 89 or J.R. Hall in Proceedings of the Workshop on Heavy-Ion Physics at the AGS-BNL, Ed. O. Hansen, March 1990.
2. See for instance F. Videbeak and T. Throwe, Fourth Workshop on Experiments and Detectors at RHIC.
3. P. Jarron et al., CERN, Private Communication.
4. B. Dolgoshein et al., RD6, CERN

FIGURE CAPTIONS

1. Energy loss spectrum of minimum ionizing particles in a 300 μm thick Si-pad detector measured by the HELIOS experiment at the CERN-SPS.
2. Conceptual design of the OASIS detector system.
3. The interaction region and the multiplicity detector.
4. Schematic layout of one Si-detector.
5. Pseudorapidity coverage of the Si-detector.
6. (a) Total multiplicity of charged particles hitting the four detectors and b) total particle energy loss as a function of the collision impact parameter for Au+Au at $\sqrt{s}$ = 200 GeV/u averaged over all vertex positions.
7. (a) Total multiplicity and b) total energy loss as a function of the vertex position for central Au+Au collisions.
8. Layout of a double-sided readout prototype Si-detector.
   (a) Junction side pad segmentation
   (b) Resistive side
   (c) Illustration of the p-channel stop tecnnique.
9. (a) Detector Mother Board layout
   (b) Mounting scheme
10. Schematic of the AMPLEX chip
11. Block diagram of a DRAMS receiver card.

12. (a) Front pad energy loss spectrum.

(b) Back side E-loss spectrum for 200 GeV/c pions.

(c) Ibid with a target positioned upstream and operated with a "high" multiplicity trigger.

13. Contour plot showing the correlation between the sum of energy losses in the front pads and the energy loss in one back side petal.

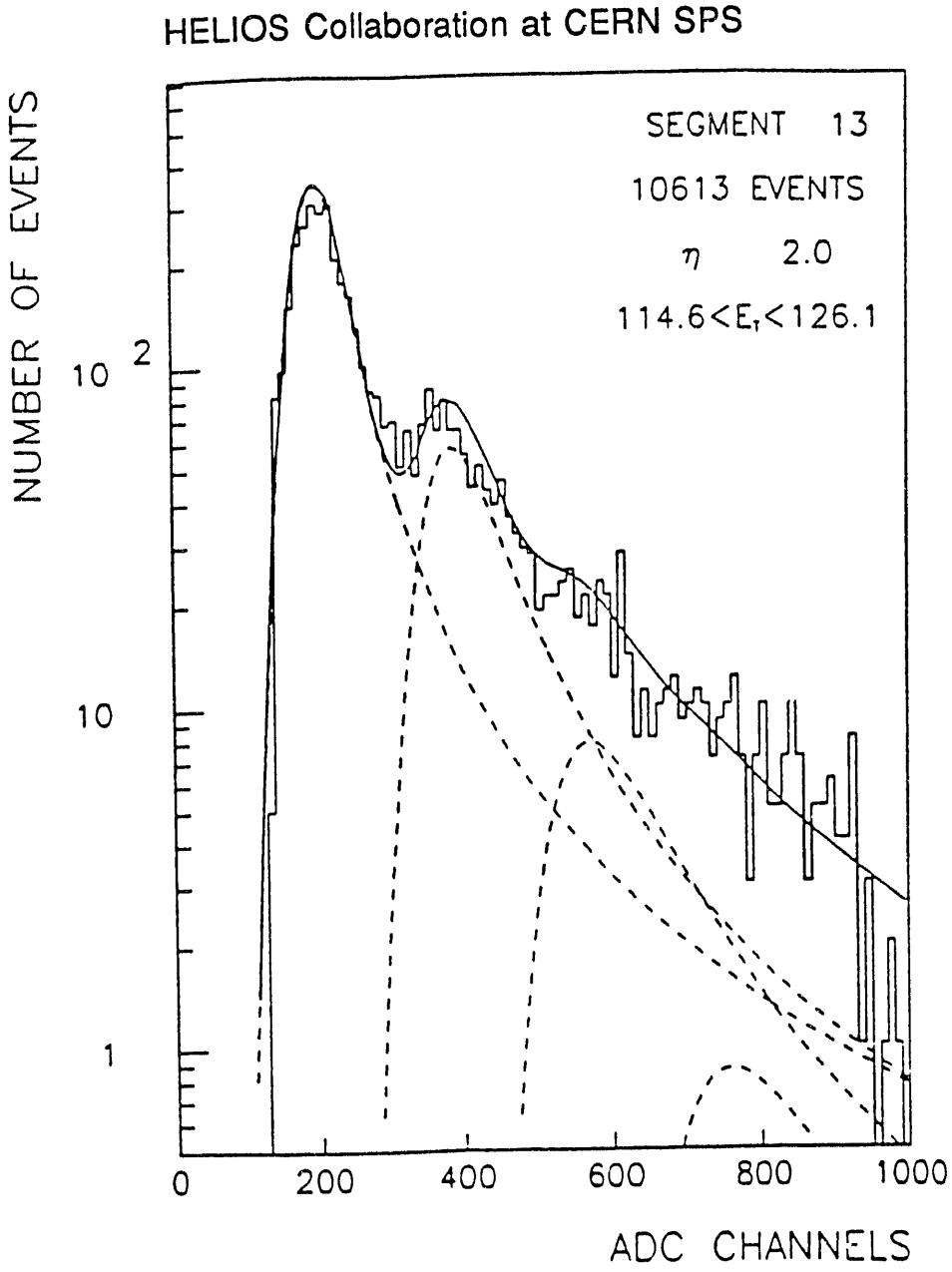
HELIOS Collaboration at CERN SPS
SEGMENT 13
10613 EVENTS
η 2.0
114.6<E_T<126.1
NUMBER OF EVENTS
10 2
10
1
0
200
400
600
800
1000
ADC CHANNELS

Figure 1

Overview of the OASIS detector.

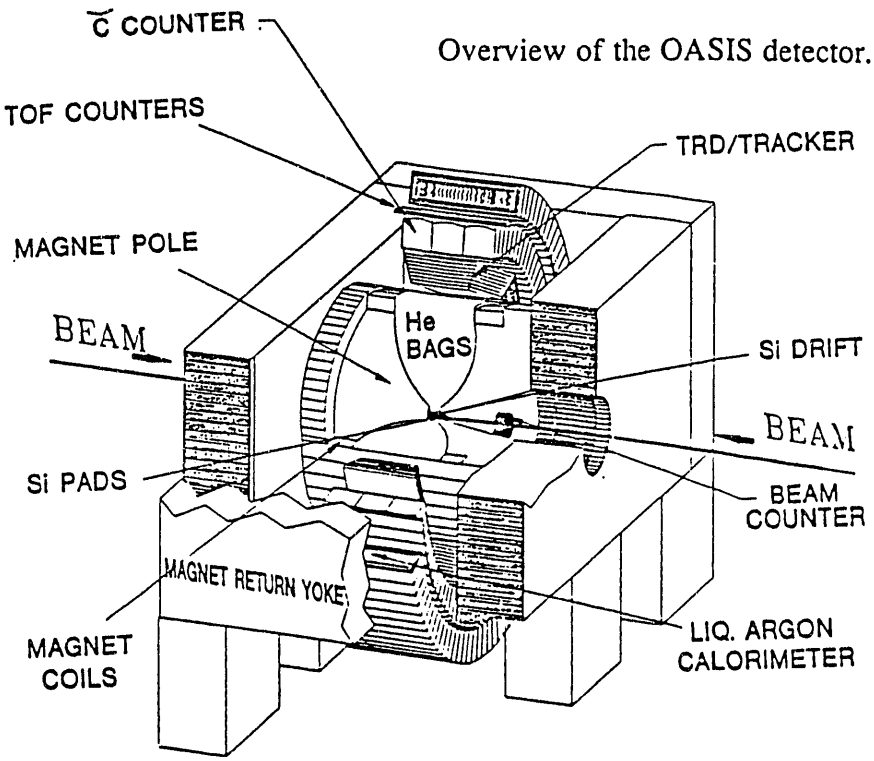

Figure 2

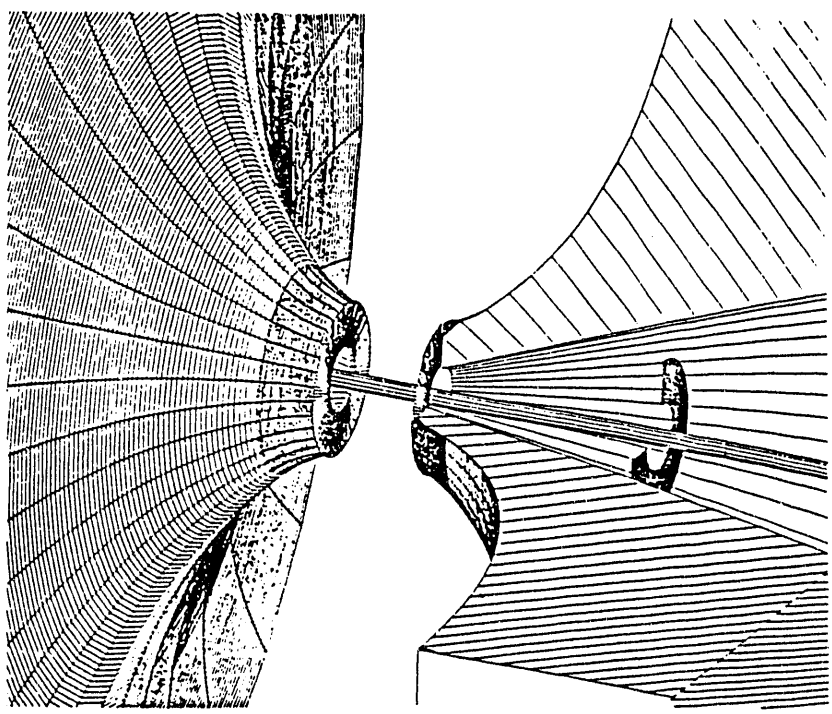

Figure 3
OASIS Multiplicity Detector Layout

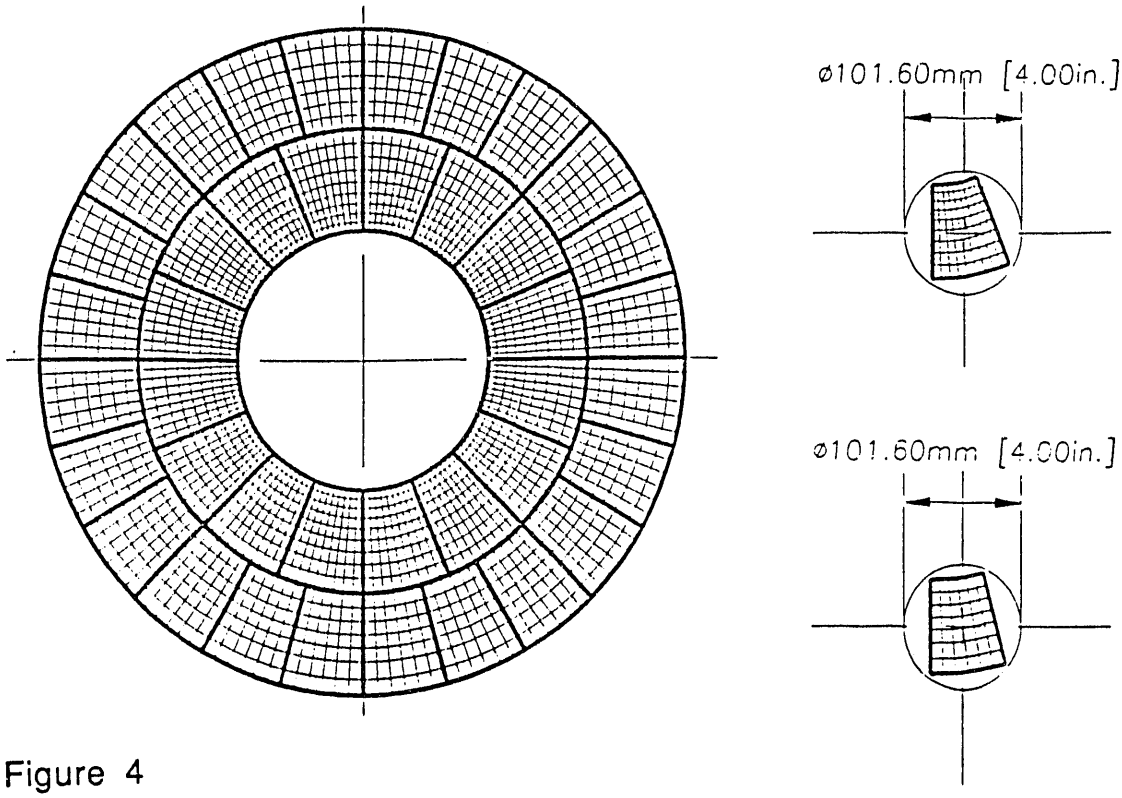

Figure 4

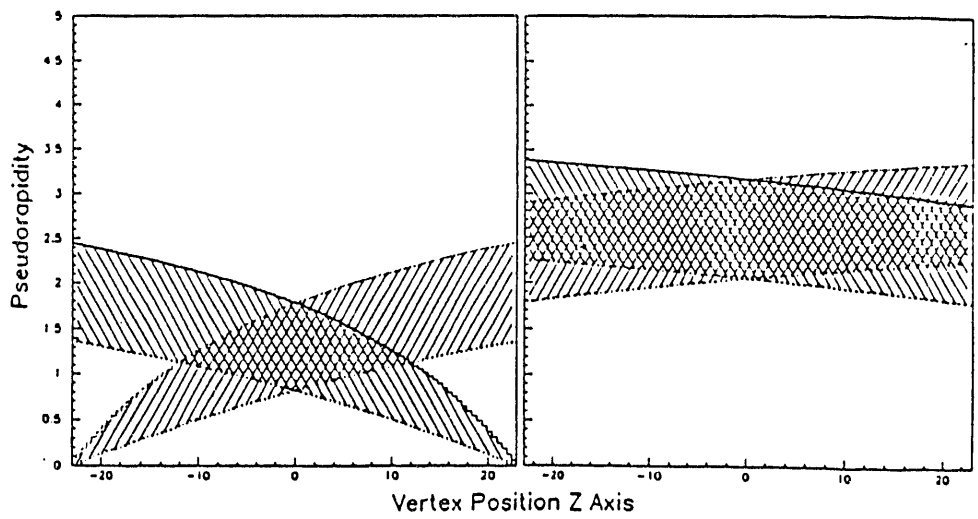

Figure 5

Rapidity coverage of the Si multiplcity detectors as a function of interaction vertex position measured from the center of the magnet field gap.

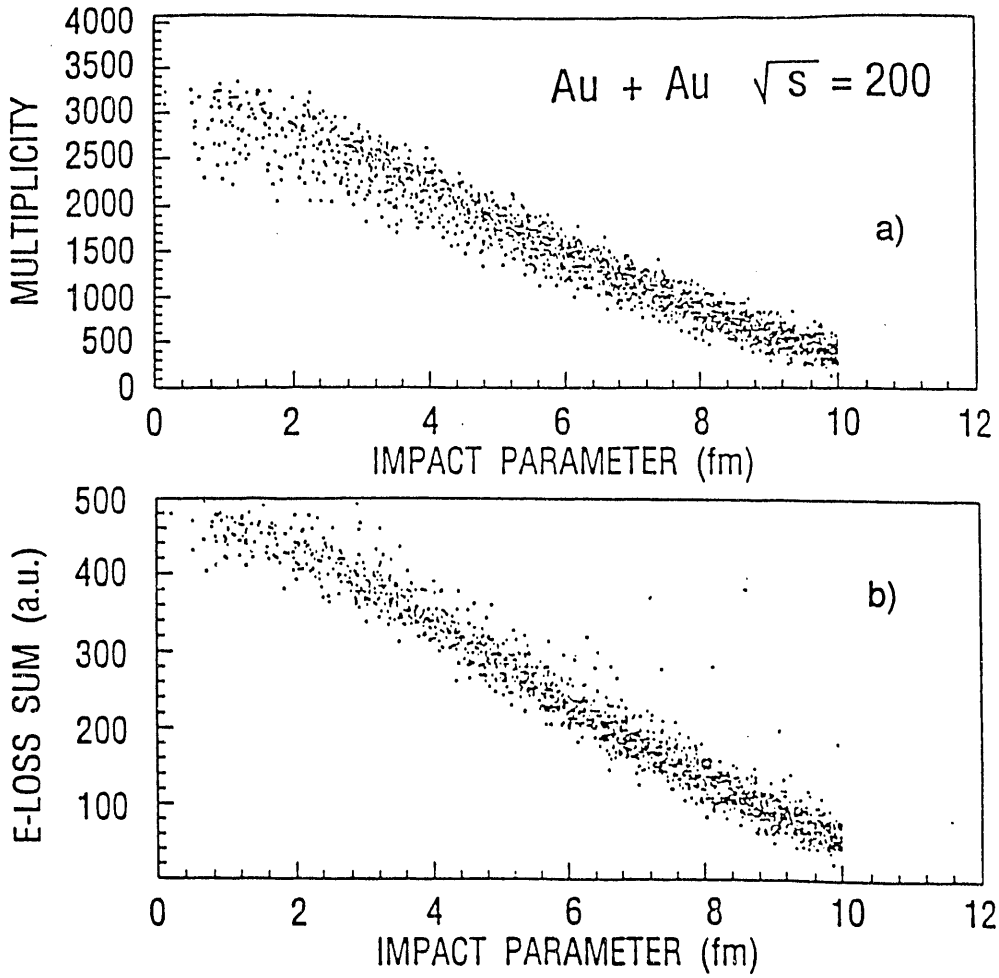
Au + Au √s = 200
a)
MULTIPLICITY
4000
3500
3000
2500
2000
1500
1000
500
0
0
2
4
6
8
10
12
IMPACT PARAMETER (fm)
b)
E-LOSS SUM (a.u.)
500
400
300
200
100
0
2
4
6
8
10
12
IMPACT PARAMETER (fm)

Figure 6

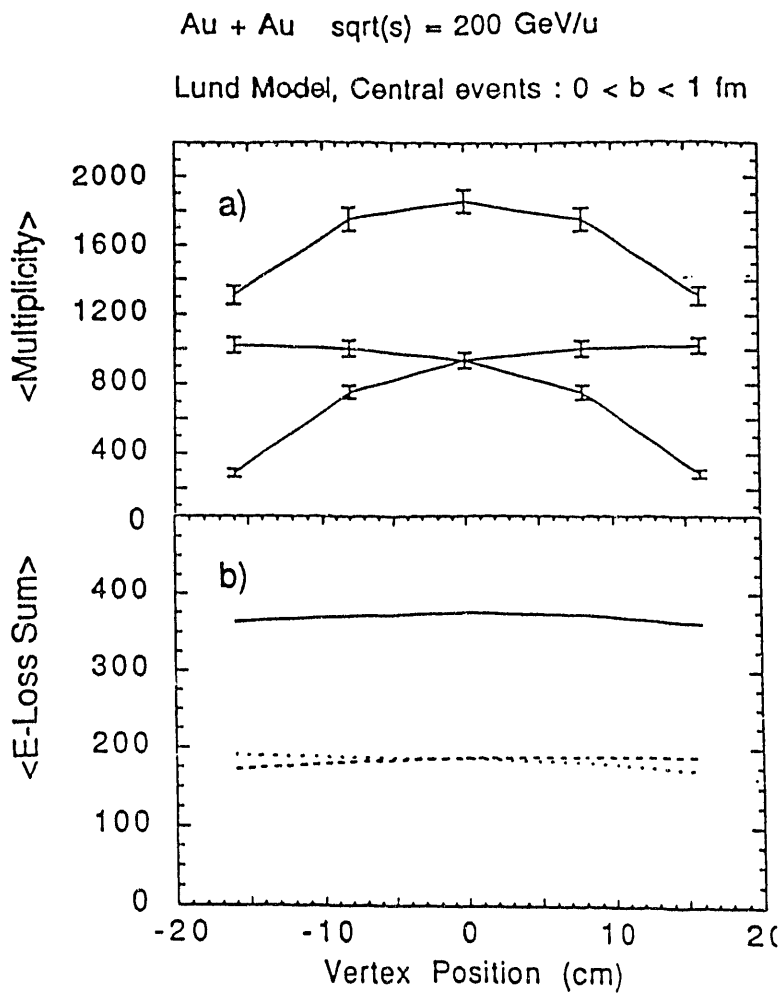
Au + Au sqrt(s) = 200 GeV/u
Lund Model, Central events : 0 < b < 1 fm
<Multiplicity>
2000
1600
1200
800
400
0
a)
<E-Loss Sum>
400
300
200
100
0
b)
-20
-10
0
10
Vertex Position (cm)

Figure 7

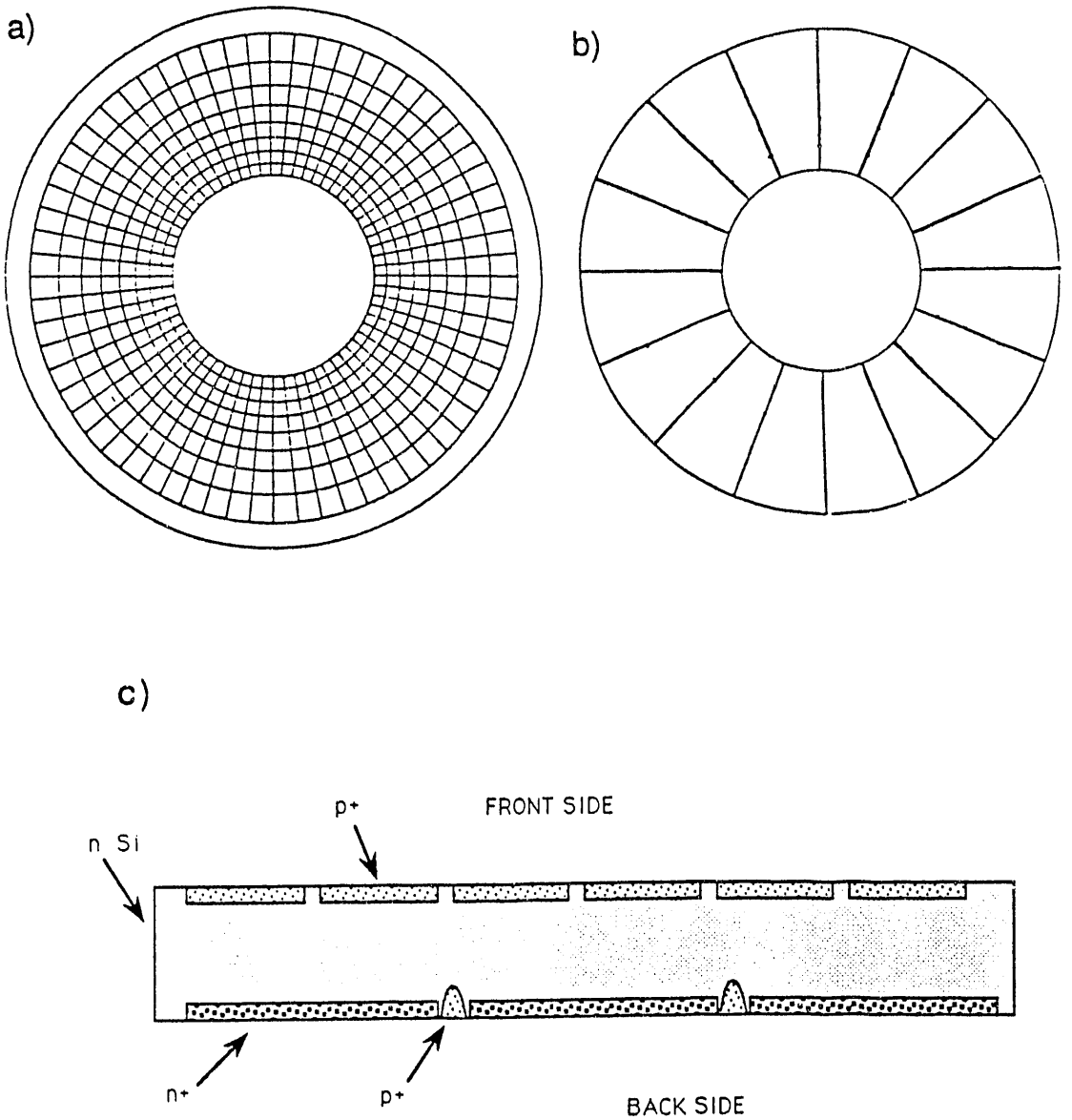

Figure 8

a)

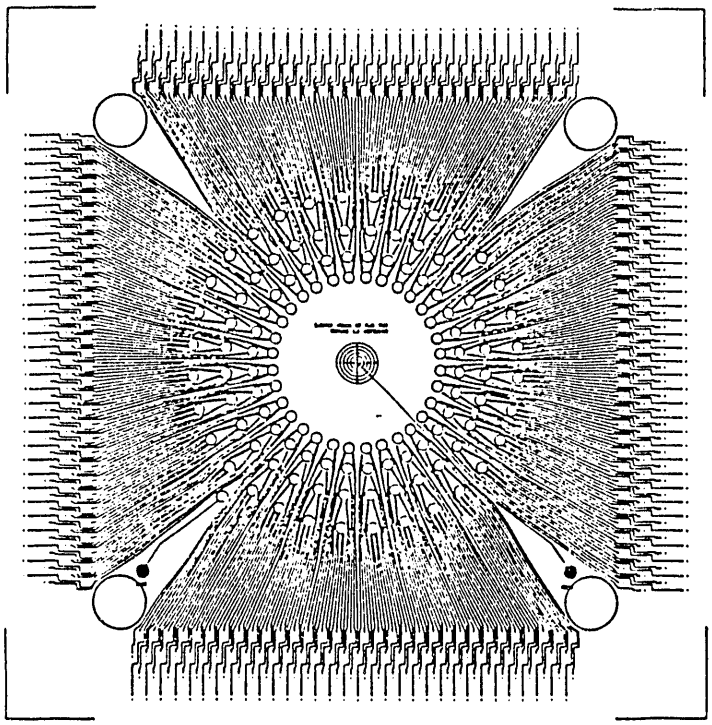

b)

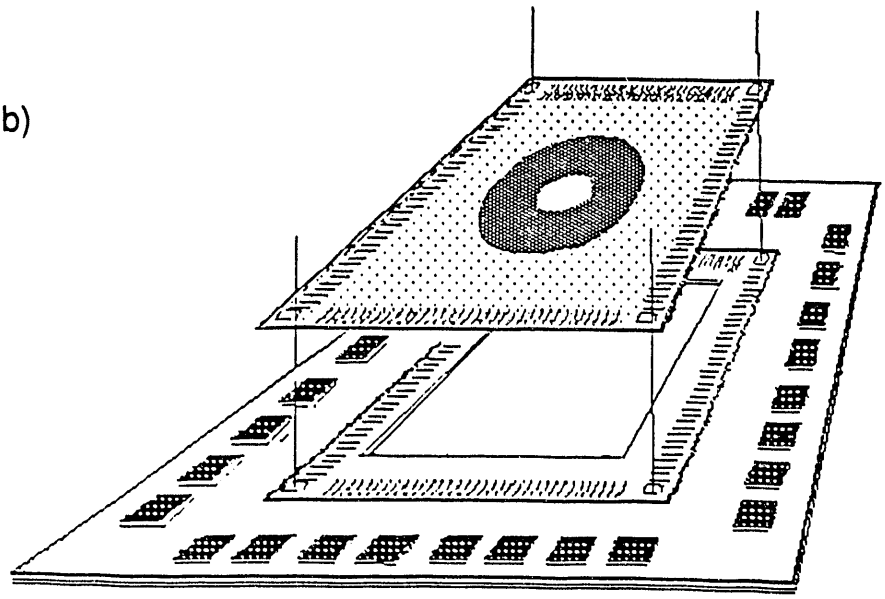

Figure 9

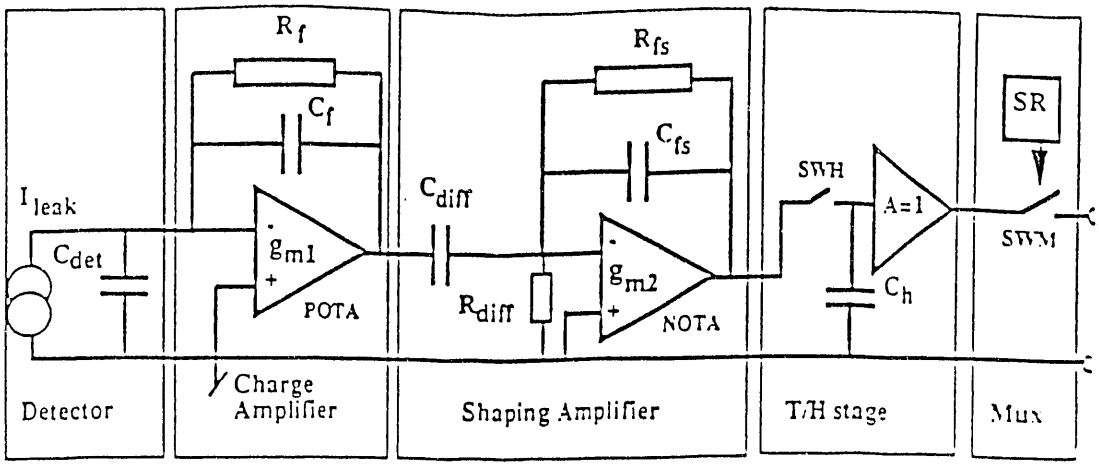

Schematic of AMPLEX circuit.

Gain	5 mV/fC for C_{det} = 20 pF 18 mV/min. ionizing part. in 300 µm Si detector (MIP)
Gain uniformity	2% within chip, 5% from chip to chip
Gain versus C_{det}	0.6% gain decrease per pF
Noise	ENC 1000 r.m.s. electrons for C_{det} = 20 pF
Linearity	Better than 2% integral up to 70 fC input charge (corresponds to ~ 20 MIP)
Output DC offset	+ 15 mV
Offset spread	± 10 mV
Maximum acceptable detector leakage current	450 nA
Power consumption	1.1 mW per channel for biasing conditions: $I_{bias\ (POTA)}$ = 50 µA, $I_{bias\ (NOTA)}$ = 10 µA
Peaking time	750 ns

Summary of characteristics of AMPLEX

Figure 10

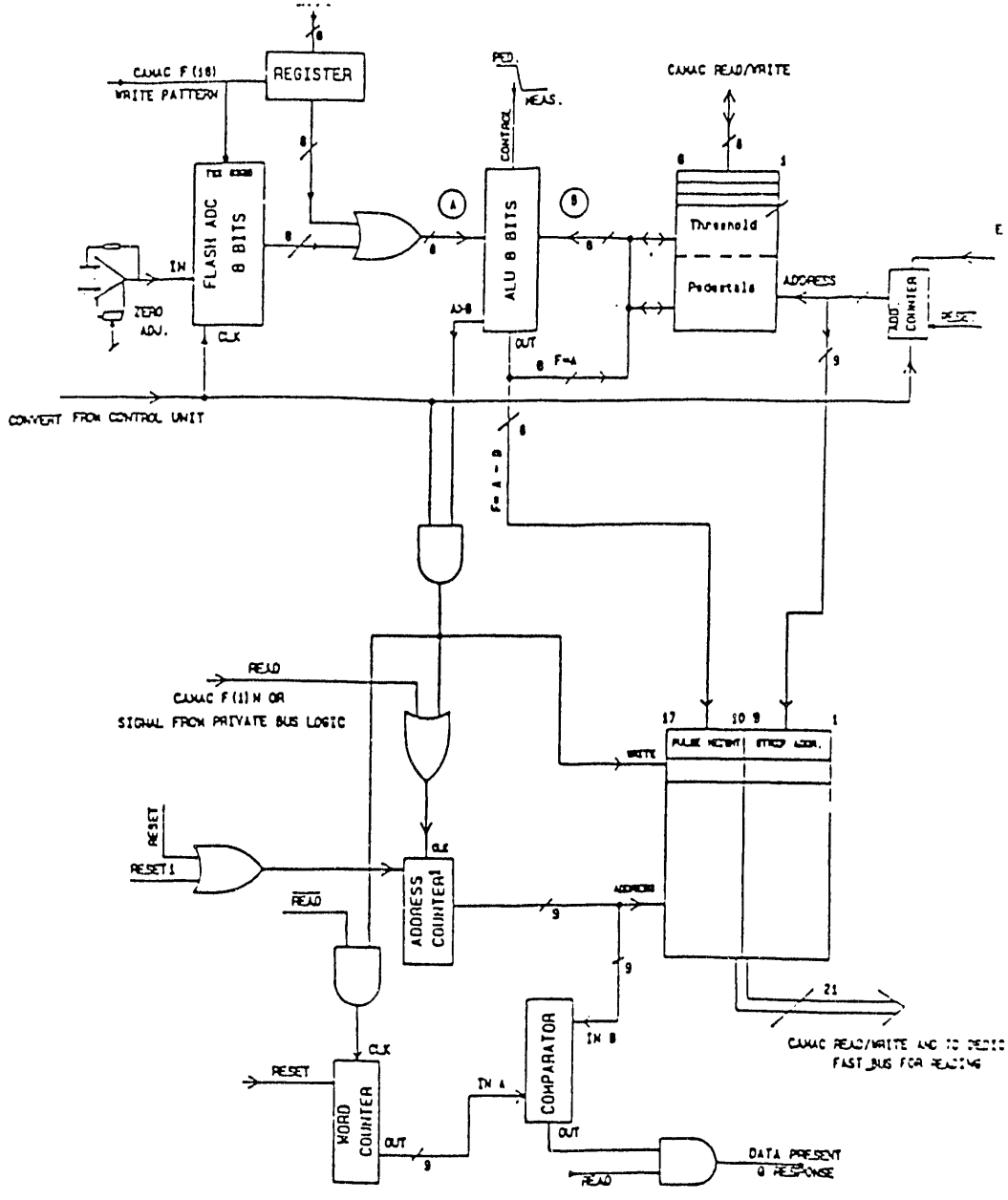
REGISTER
FLASH ADC 8 BITS
ALU 8 BITS
Threshold
Pedestals
ADDRESS
ADD. COUNTER
CONVERT FROM CONTROL UNIT
READ
RESET
ADDRESS COUNTER
WORD COUNTER
COMPARATOR
DATA PRESENT

Figure 11

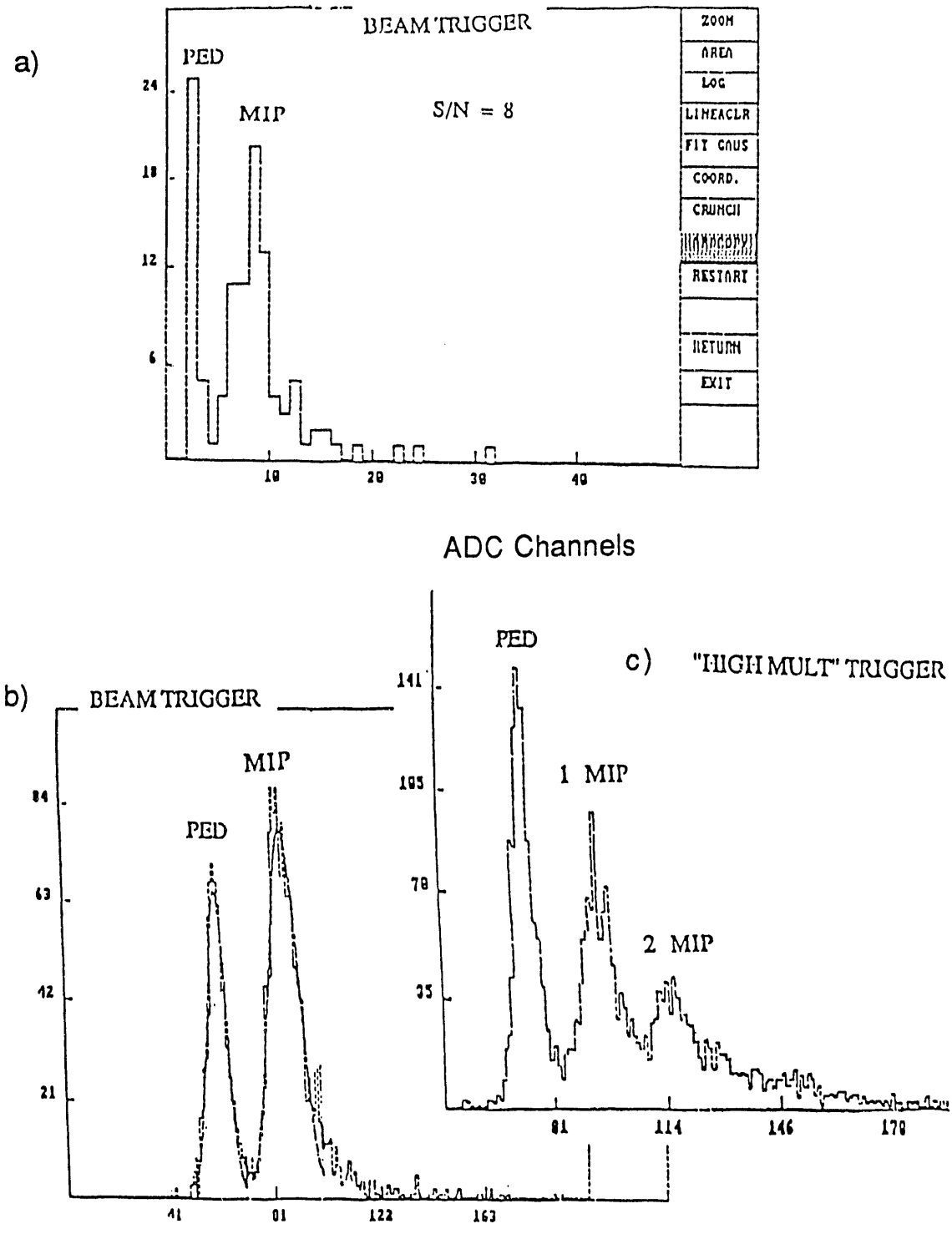
a)
BEAM TRIGGER
PED
MIP
S/N = 8
ZOOM
AREA
LOG
LINEARLR
FIT GAUS
COORD.
RESTART
RETURN
EXIT
ADC Channels
b)
BEAM TRIGGER
PED
MIP
c)
"HIGH MULT" TRIGGER
PED
1 MIP
2 MIP
ADC Channels

Figure 12

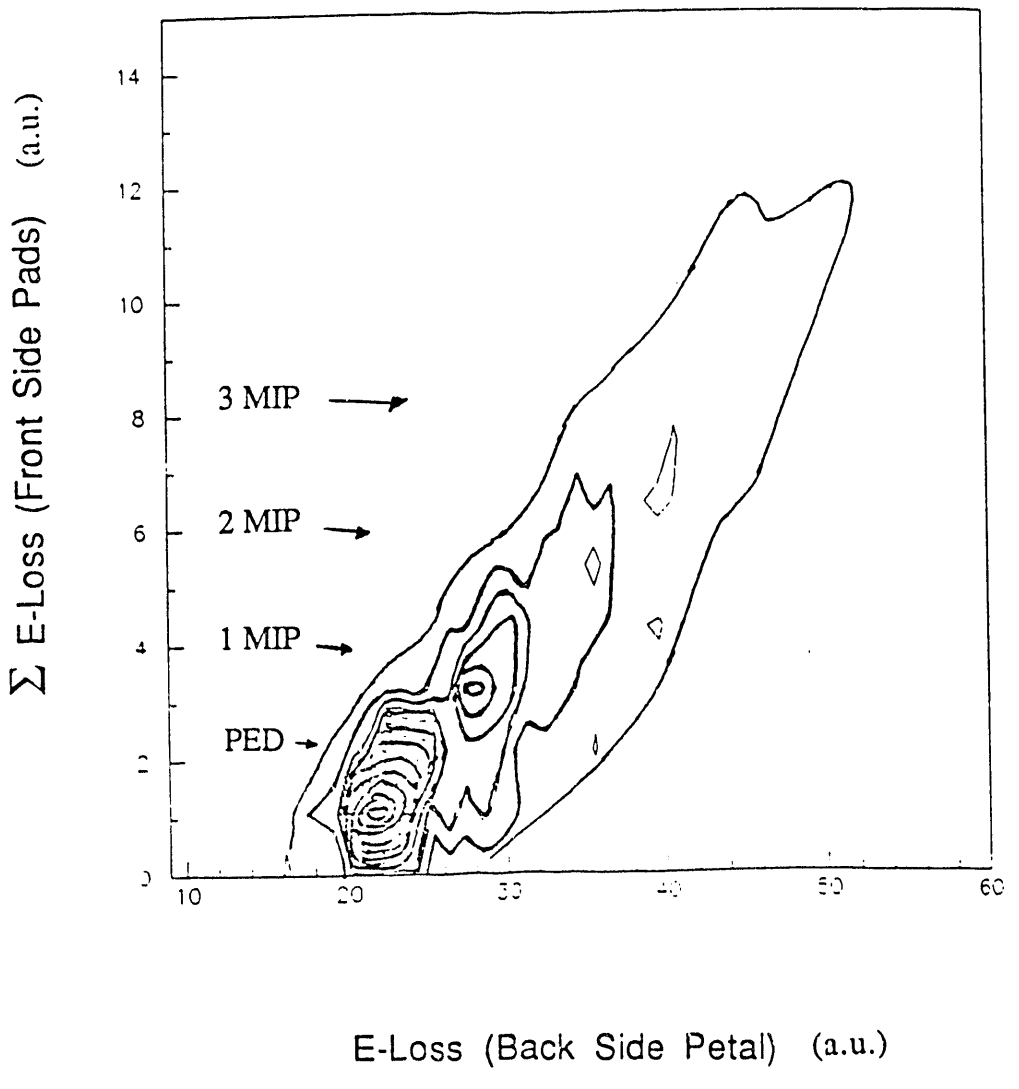
Σ E-Loss (Front Side Pads) (a.u.)
14
12
10
8
6
4
2
0
3 MIP
2 MIP
1 MIP
PED
10
20
30
40
50
60
E-Loss (Back Side Petal) (a.u.)

FIGURE 13

THE VERTEX DETECTOR FOR THE LEPTON/PHOTON COLLABORATION

J. P. Sullivan, J. G. Boissevain, D. Fox, H. van Hecke
B. V. Jacak, J. S. Kapustinsky, M. J. Leitch,
P. L. McGaughey, J. M. Moss, W. E. Sondheim
Physics Division, MS D456
Los Alamos National Lab
Los Alamos, NM 87545

Abstract

The conceptual design of the vertex detector for the Lepton/Photon Collaboration at RHIC is described, including simulations of its expected performance. The design consists of two concentric layers of single-sided Si strips. The expected performance as a multiplicity detector and in measuring the pseudo-rapidity (η) distribution is discussed as well as the expected vertex finding efficiency and accuracy. Various options which could be used to reduce the cost of the detector are also discussed.

1 Introduction and Design Assumptions

A vertex detector, based on silicon strips[1], was designed for the lepton/photon spectrometer collaboration[2]. The purposes of the vertex detector were to measure the number of charged particles per unit pseudo-rapidity ($dN/d\eta$) and their multiplicity in addition to finding the vertex. A large part of the R&D that went into this design should be useful for any RHIC experiment.

In order to cover the central rapidity ($\approx \eta$) region, the $dN/d\eta$ measurement should cover η from $\approx$ -3 to +3. The total charged particle multiplicity must be available for the first level trigger. When the multiplicity is low, an accurate measurement requires a detector which covers a large fraction of the total solid angle. For central Au+Au collisions at RHIC the expected[3] number of charged particles in the range $-3 < \eta < 3$ is around 5000. If the occupancy is to be kept

to 10% or less, this implies that the detector will need at least 50K channels in each layer.

Finally, the vertex detector must find the vertex. This should be done approximately (to within $\approx$ 1cm) at the trigger level, with a more accurate determination ($\approx$ 1mm) offline. Any vertex finding algorithm requires several charged particles in the detector, which is not a serious constraint for Au+Au collisions. However, in order to consistently find the vertex position for p+Au and p+p collisions, where the charged particle multiplicities can be much lower, a large fraction of the total solid angle must be covered.

2 Vertex Detector Conceptual Design

The conceptual design of the vertex detector was based on two concentric, approximately cylindrical, barrels of single-sided 300μm thick silicon strips with 100μm pitch[2]. Fig. 1 shows schematic views. Half of the strips in each barrel are oriented parallel to z (the beam direction) and half orthogonal to z. The parallel and perpendicular strips are sometimes called "r-ϕ" and "z" strips, respectively.

The inner and outer detectors should not move relative to one another; details of these constraints are discussed in a later section. The detector should be constructed from "ladders" which maintain accurate relative positioning of the inner and outer detector wafers in each azimuthal segment. Each ladder will be constructed from Rohacell® foam[4], which is a very light (reduces multiple scattering) but rigid foam whose coefficient of thermal expansion is close to that of Si. Using a ladder-like structure, rather than a solid piece of foam, further reduces the mass of the support structure and permits better airflow for cooling. Based on the expected power dissipation of the chips, preamps, and transmitters, the assembly will be air-cooled.

The ladders fit into a graphite/epoxy mechanical structure with a small coefficient of thermal expansion. The thermal expansion of the different pieces of the detector must be considered to maintain position accuracy. A large mismatch in the coefficients of thermal expansion of the detector wafers and the support structure could also result in severe damage to the detector. The modular construction of the detector allows some azimuthal segments to be removed if necessary.

A series of simulations of the detector were performed, using a nearly realistic model. The model was a pair of cylinders, whereas the "real" detectors[2] have a hexagonal cross-section. The "real" detector has dead areas around the edges of the chips, but in the simulations, the chips are assumed to be active even at their edges. Table 1 summarizes the number of channels assumed in the simulations of the vertex detector. For the chips containing strips parallel

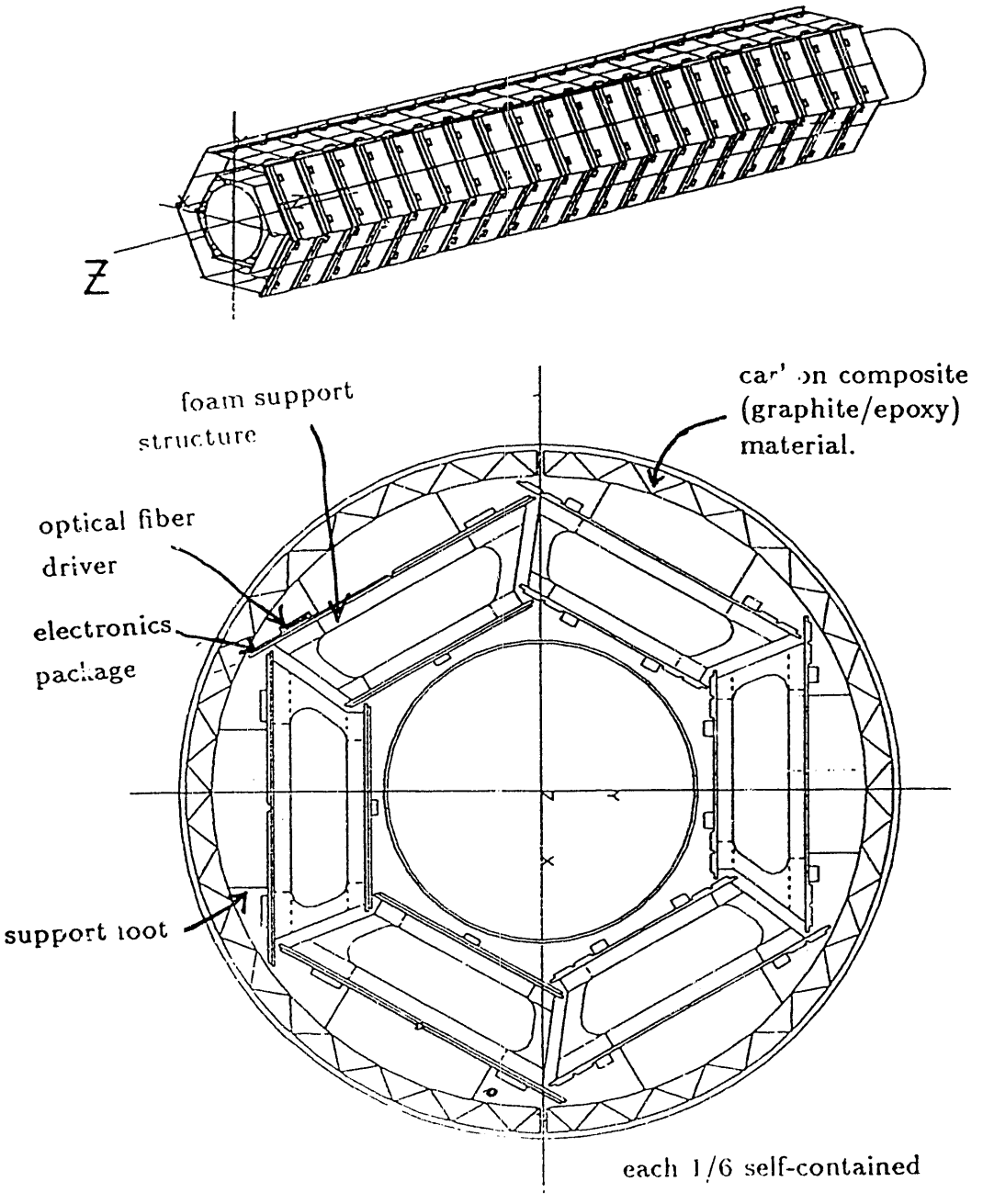

Figure 1: The conceptual design of the vertex detector. The bottom part shows the view along the beam line. The top part shows a 3D perspective view.

barrel	strip type	R (mm)	wafer size (mm x mm)	ϕ segments	# of wafers	strips/ wafer	total strips
inner	$\parallel$	61.1	64 x 50	3	20	640	38400
inner	$\perp$	61.1	32 x 50	3	40	480	57600
outer	$\parallel$	91.7	96 x 50	3	40	320	38400
outer	$\perp$	91.7	48 x 50	3	40	480	57600
Totals					140		192000

Table 1: Summary of the number of channels in the simulation of the vertex detector. The shape is approximated by a cylinder, whose radius is given. Pitch=$100\mu m$ except parallel strips in the outer barrel, where $150\mu m$ is assumed

to the beam, there are some further differences between the simulations and a realistic design. The simulations assume $150\mu m$ pitch for parallel strips in the outer barrel, with $100\mu m$ pitch in the rest of the detector. This assumption is convenient because it means that the parallel strips in the inner and outer barrel each occupy the same $\Delta\phi$.

The total number of channels per barrel shown in table 1 is about a factor of two larger than the estimate in the introduction. This was necessary because the distribution of particles along the length of the detector is not uniform, and because single particles can hit more than one strip — a serious problem for strips perpendicular to the beam.

The particle distributions in the simulations all come from Fritiof[3]. These simulations were done for p+p, p+Au, and Au+Au collisions assuming 100GeV/nucleon beams. The average charged particle multiplicities from these calculations are shown in table 2. The vertex position was assumed to always be on the central axis of the vertex detector. The z position was varied assuming a Gaussian distribution whose tails were cut off so that all interactions were assumed to take place within ±50cm of the center of the vertex detector. The Gaussian distributions assumed[5] σ_I =20, 16, and 5.7cm, for Au+Au, p+Au, and p+p collisions, respectively.

System	$< F >$ = fraction of particles which hit detector	$< N_{total} >$ No. charged particles
Au+Au (central)	0.64	5894
p+Au (min-bias)	0.55	50
p+p	0.56	21

Table 2: The average fraction of the particles which hit both layers of the vertex detector and the average total number of charged particles produced. Based on Fritiof[3] for 100GeV/nucleon beams.

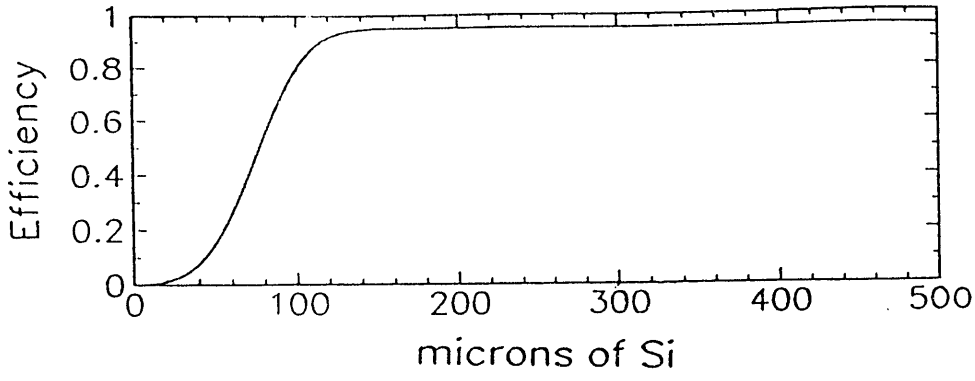

Figure 2: Assumed efficiency as a function of μm of Si traversed in a cell.

Each charged particle produced in the simulation was tested to see if it would hit the vertex detector; uncharged particles were ignored. If a particle entered the vertex detector, the program calculated which parallel and perpendicular strips would be hit. Multiple scattering of charged particles in the inner barrel of the vertex detector was included. To approximately account for the support structure and electronics, the multiple scattering calculation assumed that the inner barrel of the vertex detector was twice its real thickness. Particles were allowed to hit more than one strip. When a particle hit a detector barrel, the program calculated how much silicon a particle would pass through in each strip of the detector. A minimum-ionizing particle (mip) will lose an average of 116 keV in $300\mu m$ of Si. The result of this was an array giving the amount of Si (approximately equivalent to the energy loss) that particles passed through in a strip.

The array giving the amount of Si traversed in each strip is used to generate a pattern of "hits" in the strips. This is done using the efficiency function shown in fig. 2, which shows the efficiency as a function of the amount of Si traversed in a strip. The maximum efficiency[6] was assumed to be 95%. A "threshold", corresponding to $\frac{1}{4}mip$ (or 75μm of Si here) was assumed. A noise level, which was varied from 0.1% to 0.01% was included in the efficiency function — this means that a strip which was not hit has a small probability (P_{noise}) to be "on". If a strip was "on" then each of the adjacent strips were assumed to have a 10% probability to be "on" too — introducing some charge sharing effects into the simulation. This final array holds the pattern of strips that were "on" or "off" — no analog information is used in the analysis of the events. The array was then used as input to algorithms to find the vertex, $dN/d\eta$, and the multiplicity.

The inner barrel has a "radius" of $R_1 = 6.1$cm, constrained by the beam pipe radius of 5 cm. If η is to be measured out to ± 3, the length of the detector must be $\approx \pm R_1/tan(6°) = \pm 58$cm. A length of 50 cm has been chosen. The

variation in the vertex position means that for some events the coverage will extend above (below) $\eta = 3$ in the forward direction with a compensating decrease (increase) in the coverage around $\eta = -3$. The "radius" of the outer barrel is $R_2 = 1.5 \times R_1 = 9.2$cm.

In the following sections some discussion of the loss in performance expected from a modified design has been included along with the discussion of the detector described above. In these discussions, the conceptual design described here is compared to the vertex detector described in the Tales/Sparhc Letter of Intent[7], which covers only 1/3 of the azimuthal angle with strips perpendicular to the beam and is 64cm long instead of 100cm.

3 The problem of the angle of incidence

Particles entering the detector far from the vertex have incident angles nearly parallel ($\approx 7°$) to the surface of the vertex detector. Consequently, a single particle will pass through many strips if the strips are oriented perpendicular to the beam axis. The number of hit strips as a function of z is $N_{strips} \approx (300\mu m \times z)/(100\mu m \times R) \approx 3 \times z/R$,
where z is the distance from the vertex and R is the radius of the barrel. At the ends of the detector, about 25 strips are hit in the inner barrel, for discriminator thresholds at $\frac{1}{4}mip$, as in E789 at Fermilab[6]. This threshold represents the highest threshold for full efficiency for normally incident particles; Landau fluctuations allow the energy loss in 300μm of Si to be as small as 1/2 of the average energy loss. If this signal is split equally between two strips, then the signal in each will be 1/4 of the mean. Particles incident nearly parallel to the surface would give about 1/3 of the signal ($\approx \frac{1}{3}mip$) expected from a particle at normal incidence ($\approx 1mip$). So all 25 strips could register hits — drastically increasing the apparent occupancy. Realistically, considering Landau fluctuations in the energy loss in a thin layer, a threshold at $\frac{1}{4}mip$, compared to a signal of about $\frac{1}{3}mip$ would probably give some strips which would be "on" and some which would be "off". This situation would make accurate measurements of the multiplicity and $dN/d\eta$ extremely difficult.

One solution to this problem is to turn the strips parallel to the beam direction. In this case, a particle at a nearly parallel incidence angle would give a large signal ($\approx 10mip$), essentially all in one strip. This eases the measurements of $dN/d\eta$ and multiplicity, but increases the dynamic range needed in the electronics.

4 Analysis of Monte Carlo Events: Multiplicity

The total multiplicity (N_{total}) and the detected multiplicity (N_{meas}) are related via $\langle N_{meas} \rangle = F \langle N_{total} \rangle$, or $N_{total} \approx N_{meas}/F$, where F and N_{total} are given in table 2. The uncertainty on N_{total} due to statistical fluctuations[8] in the number of particles in the detector is:

$$\frac{\sigma_{total}}{N_{total}} \approx \sqrt{\frac{1-F}{(N_{total})F}} \tag{1}$$

Using the numbers in table 2 with eq. 1 allows the value of σ_{total}/N_{total} to be estimated as 1%, 13%, and 19% for Au+Au (central), p+Au (min-bias), and p+p, respectively. These fluctuations in the fraction of the particles detected set limits on the performance of the detector as an event-by-event multiplicity detector.

The performance of the detector will introduce further uncertainties in the multiplicity measurement. The important factors included in the simulations which affect the multiplicity measurement are the efficiency of the individual strips (see fig. 2), noise, the number of strips "hit" by a single particle, and multiple hits on a single strip. However, corrections for all of these effects can be made.

When[6] $P_{noise} = 10^{-3}$, the average number of hits due to noise in the parallel strips will be 38.4 per barrel. This is not an important correction for central Au+Au collisions, but is significant for p+p and p+Au. In these cases, this (pessimistic) noise level is frequently greater than the number of real hits in the inner barrel. Therefore, it will be important to both minimize and understand the noise in the detector.

Eq. 1 gives an estimate of the loss in performance from a reduction in the coverage of the vertex detector. Given the large multiplicity in a central Au+Au collision, a sightly smaller detector would give a good measurement of the multiplicity. However, the reduced coverage of the vertex detector described in the Tales/Sparhc letter of intent[7] would further degrade the already marginal accuracy of the p+p and p+Au multiplicity measurements. Although the solid angle coverage of such a detector would be sufficient to measure the multiplicity for central Au+Au collisions, its use of parallel alone strips could complicate the measurement.

5 Analysis of Monte Carlo Events: dN/dη

The problems associated with the dN/dη measurement are similar to those of the multiplicity measurement. The major additional complication is the

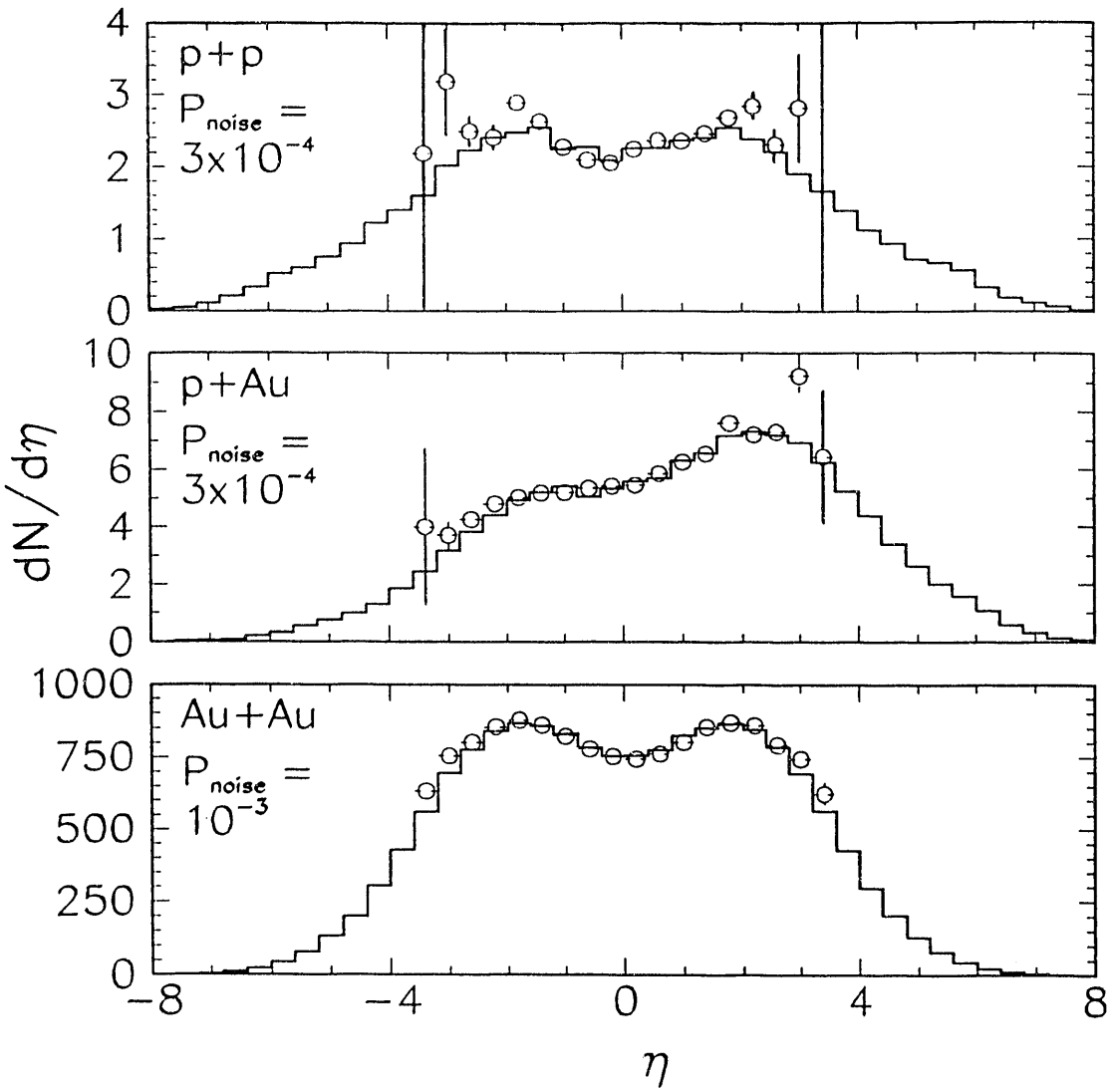

Figure 3: "Real" (histogram) and measured dN/dη distributions (circles with error bars) for p+p, p+Au, and Au+Au. Only the inner barrel was used to get "measured" distributions. $P_{noise} = 3 \times 10^{-4}$ was assumed for p+p and p+Au.

determination of the vertex to allow calculation of the pseudo-rapidity ($\eta = -\ln(\tan(\frac{\theta}{2}))$). dN/d$\eta$ measurements are generally averages for many events. Statistical fluctuations in the average over many events are therefore less important than the event-by-event fluctuations in the total multiplicity. Consequently, $dN/d\eta$ measurements should be possible for p+p, p+Au, and Au+Au.

First, the vertex position must be found, this is discussed in the following section. Next, the range of η occupied by each chip is calculated. Because the chips with strips parallel to the beam give more reliable information on the number of hits, only those are used to calculate the number of hits (N_{hit}) in each range of η. Corrections for the efficiency, noise, double hits, and charge sharing are made. The "measured" dN/dη value is the average of $N_{hit}/\Delta\eta$ over many events.

Fig. 3 compares the "real" and "measured" dN/dη distributions for p+p, p+Au, and Au+Au events. The shapes of the "measured" distributions are always close to the "real" distributions. Since the distributions are calculated using the vertex found by the pseudo-tracking algorithm, which does not always find the correct vertex, some of the differences may be from events with an incorrect vertex position used in the calculation.

As with the multiplicity measurements, noise complicates the dN/dη measurements. The number of particles which hit each chip is much smaller near the edges of the detector, but noise causes a constant fraction of the strips to be "on". This means that the signal/noise ratio is much worse (factor of $\approx$ 10) at the largest $|\eta|$ values. For p+Au, even with the optimistic assumption that $P_{noise} = 10^{-4}$, the signal and noise will be comparable around $\eta = \pm 3$, resulting in larger statistical uncertainties on the points around these η values. This noise problem will be worse for p+p collisions where the multiplicity is lower, but unimportant for central Au+Au events.

6 Analysis of Monte Carlo Events: Vertex Finding

The vertex detector must also be able to find the vertex. As an aid in understanding this process, figs. 4-5 show the number of hits on the vertex detector vs. z for a p+p event and for a Au+Au event. Hits on the parallel strips (left side) and perpendicular strips (right side) and on the inner barrel (top) and outer barrel (bottom) are shown separately. For perpendicular strips the number of clusters of adjacent hits vs. z is shown — not the raw number of hits. The real vertex positions are marked. By looking at these figures, it is clear that the distribution of hits on the parallel strips can be used to estimate the vertex position for Au+Au, but for p+p the small number of hits, coupled with the noise, makes it difficult to find the vertex from this information alone.

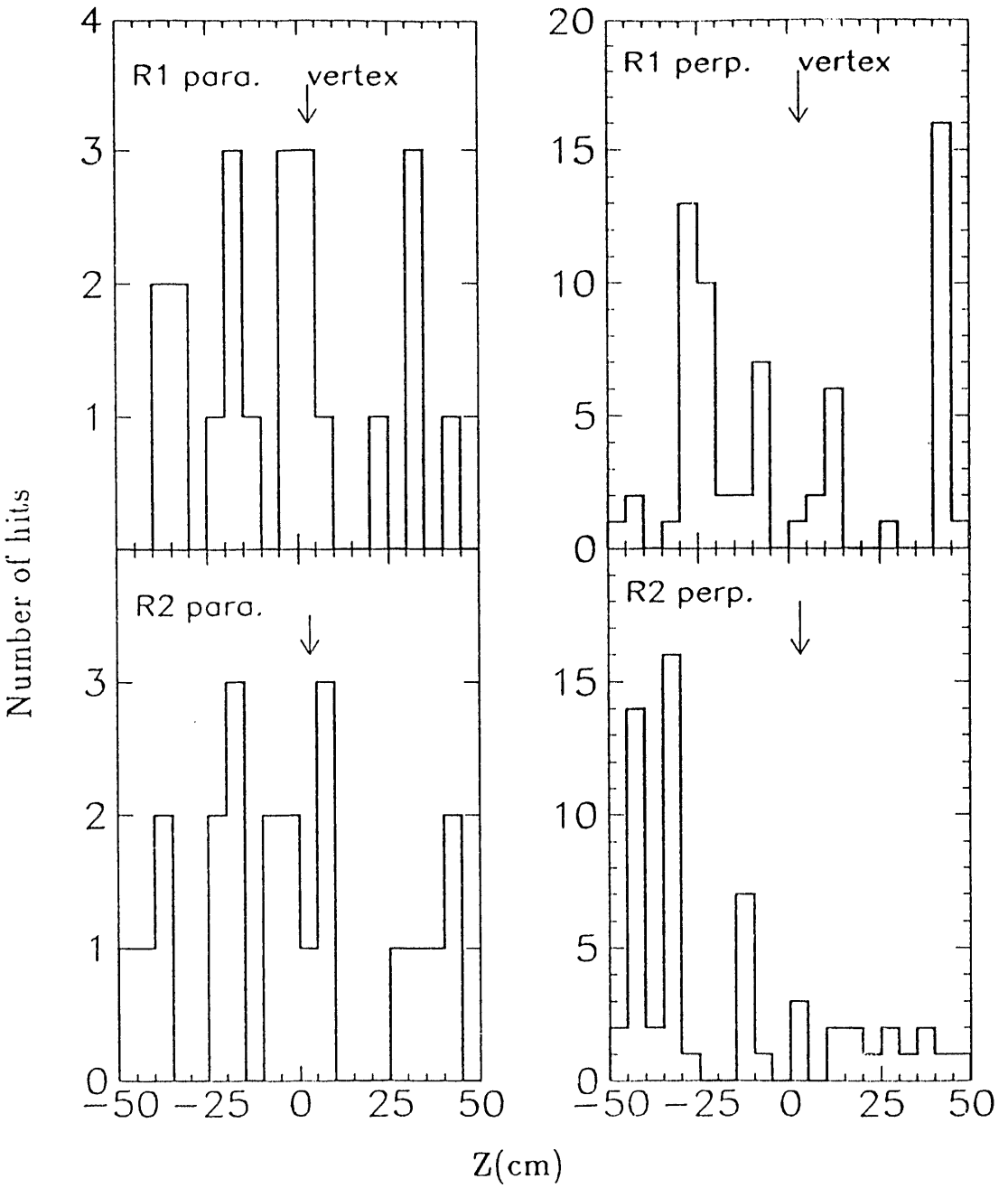

Figure 4: p+p — a sample event. The left side shows the number of hits vs. z (the beam direction) for parallel strips. The right side shows the number of hits vs. z for perpendicular strips. The top half shows hits on the inner barrel (R1) and the bottom half shows hits on the outer barrel (R2). The arrows mark the vertex position.

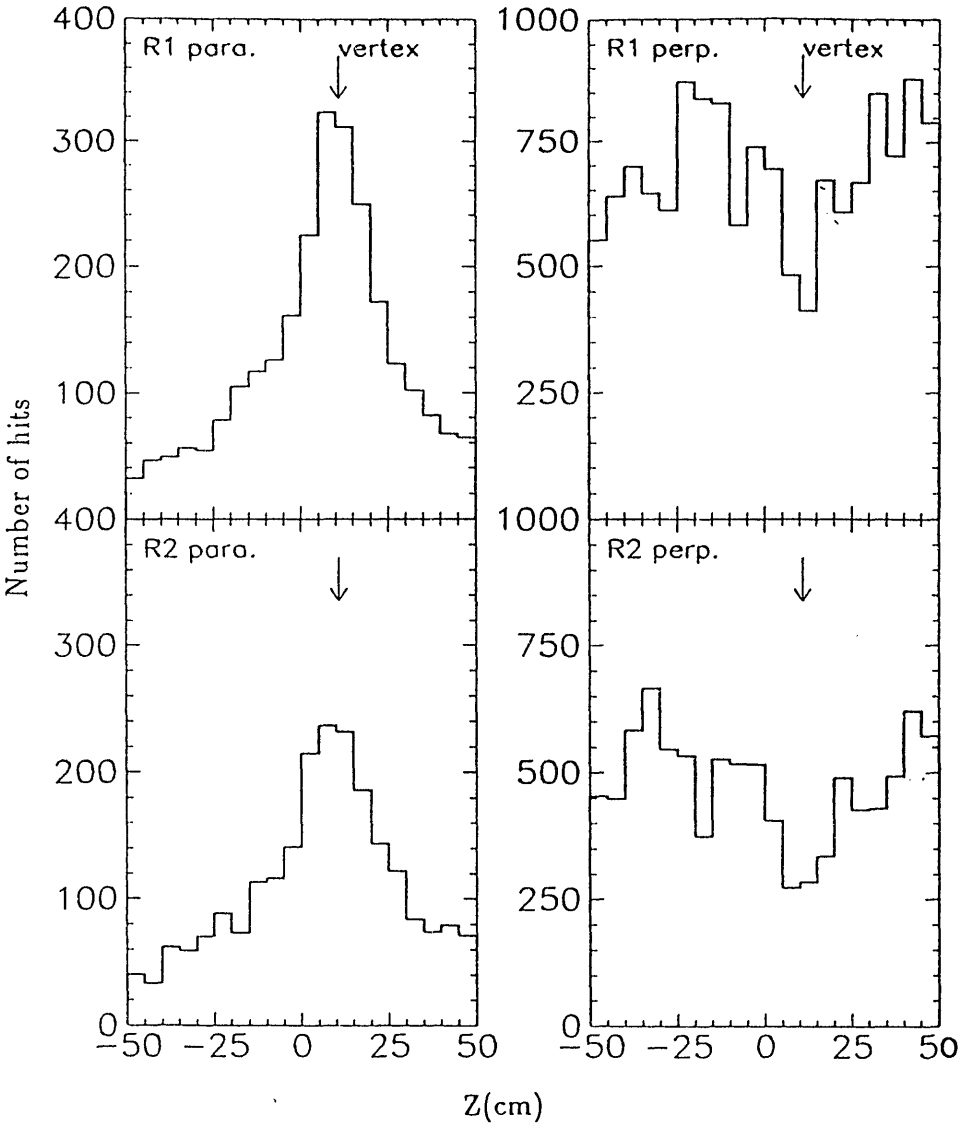

Figure 5: Au+Au — a sample event. The left side shows the number of hits vs. z (the beam direction) for parallel strips. The right side shows the number of hits vs. z for perpendicular strips. The top half shows hits on the inner barrel (R1) and the bottom half shows hits on the outer barrel (R2). The arrows mark the vertex position.

6.1 Vertex from Center of Gravity

The simplest algorithm to find the vertex in a symmetric collision would be to find the center of gravity (CG) of all hits. It is not clear how well this should work in the asymmetric case of p+Au. However, by taking the difference between the CG in the inner and outer barrels, if could be possible to project towards the vertex in this case. Information from parallel strips only was used to find the vertex from the CG, using two iterations. First, the whole hits distribution (see the left sides of figures 4-5) was used. Then an equal number of channels above and below this initial CG were used to improve the vertex position measurement.

There is a statistical limit to this method. The minimum uncertainty on the vertex position is $\approx$(rms width)$/\sqrt{N}$ $\approx$0.4cm for central Au+Au collisions, which is below the vertex resolution required at the trigger level ($\approx$ 1cm), but insufficient for the offline analysis ($\approx$ 1mm). The actual vertex resolution found using the CG method was σ=2.1cm for Au+Au. For p+p and p+Au, the number of hits on the vertex detector is much smaller and the statistics do not allow a sufficiently accurate estimate of the vertex position using the CG only, especially when random hits due to noise are included.

6.2 Vertex from Pseudo-tracking

Another method used to find the vertex is based on "pseudo-tracking." This method treats all pairs of hits in the inner and outer barrels as potential tracks and calculates a vertex position from them. The real vertex appears as the most probable value of the vertex position.

There are two stages in the pseudo-tracking vertex search. First, only the parallel strips are used, obviating the need to test all pairs of hits as each parallel strip covers a small $\Delta\phi$ (azimuthal angle). Particles from the central axis of the vertex detector have the same ϕ at each barrel, except for small variations due to multiple scattering. Fig. 6 shows a distribution of the change in the strip number hit in the outer barrel due to multiple scattering in the inner barrel; most particles hit the outer barrel within $\pm$2 strips of the expected position. For each hit in the outer barrel, all hits in the inner barrel which are within $\pm$2 strips are used to calculate a possible vertex position. The top part of fig. 7 shows the resulting distribution of vertices for a sample Au+Au event. An estimate of the event vertex appears as a peak. The peak height gives the number of particles hitting both barrels of this half of the detector. The background comes from random pairs of hits. Limiting the hits tested to $\pm$2 strips reduces the number of pairs that must be tested by a factor of $\approx \frac{5strips}{640\times3} = \frac{1}{384}$. This reduces the background in the histograms shown in the upper half of fig. 7 by $\frac{1}{384}$ while only reducing the counts in the peak by about 12% (see fig. 6).

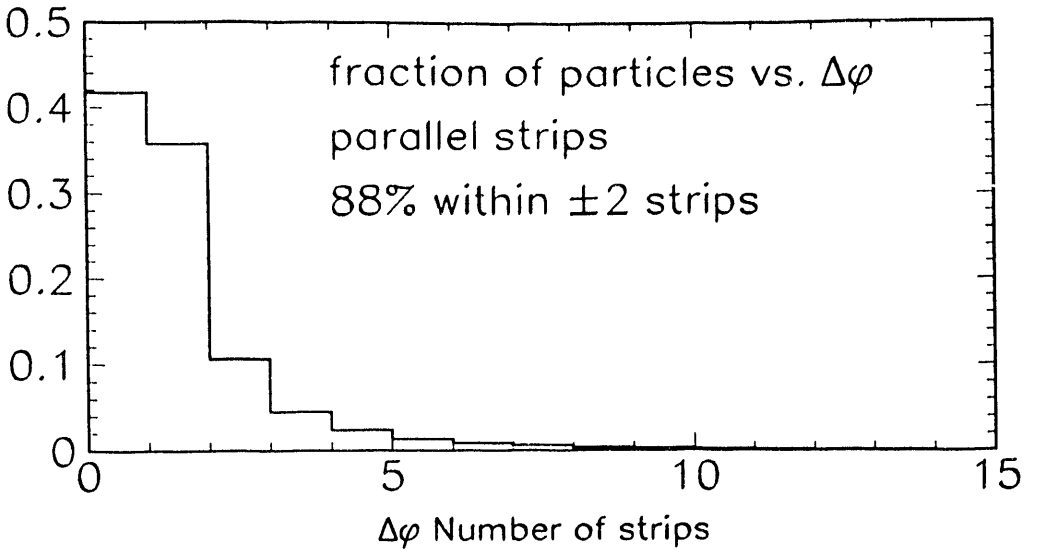

Figure 6: Probability vs. the difference in the parallel strip in the outer barrel which was hit and the strip that would have been hit with no multiple scattering. All charged particles which hit both barrels are included.

Because the peak found using pseudo-tracking with parallel strips is broad, the vertex position is estimated by taking the center of gravity of three bins around the maximum. Because the strips are long (5cm) in the z direction, this method can not give very good vertex resolution. Fig. 8 shows the vertex resolution for p+p, p+Au, and Au+Au using pseudo-tracking with parallel strips only. For p+p and p+Au, this method gives better resolution than the center of (CG) and is much less noise sensitive. However, pseudo-tracking with parallel strips alone still does not give a vertex resolution for p+p which is significantly better than the variation in the vertex position itself[5].

This first stage using parallel strips is used to estimate a vertex position. The second stage of the vertex search uses perpendicular strips which are short in the z direction (100μm), and determine the vertex much more accurately. Beginning with an approximate vertex reduces the range of vertex positions to be searched and increases the speed of the algorithm. The second stage of the vertex search is similar to the first, but as each perpendicular strip occupies a large $\Delta\phi$, the number of pairs of hits that must be tested is about $N_1 N_2/3$, where 3 is the number of different azimuthal segments with perpendicular strips and N_1 and N_2 are the number of hits on the perpendicular strips in the inner and outer barrels, respectively. For central Au+Au events, this number is large, so the algorithm is slow. The vertex from the first stage of pseudo-tracking is used to restrict the pairs of strips which are tested; for Au+Au, only those pairs of strips which point to a vertex position within ±5cm of the vertex found in

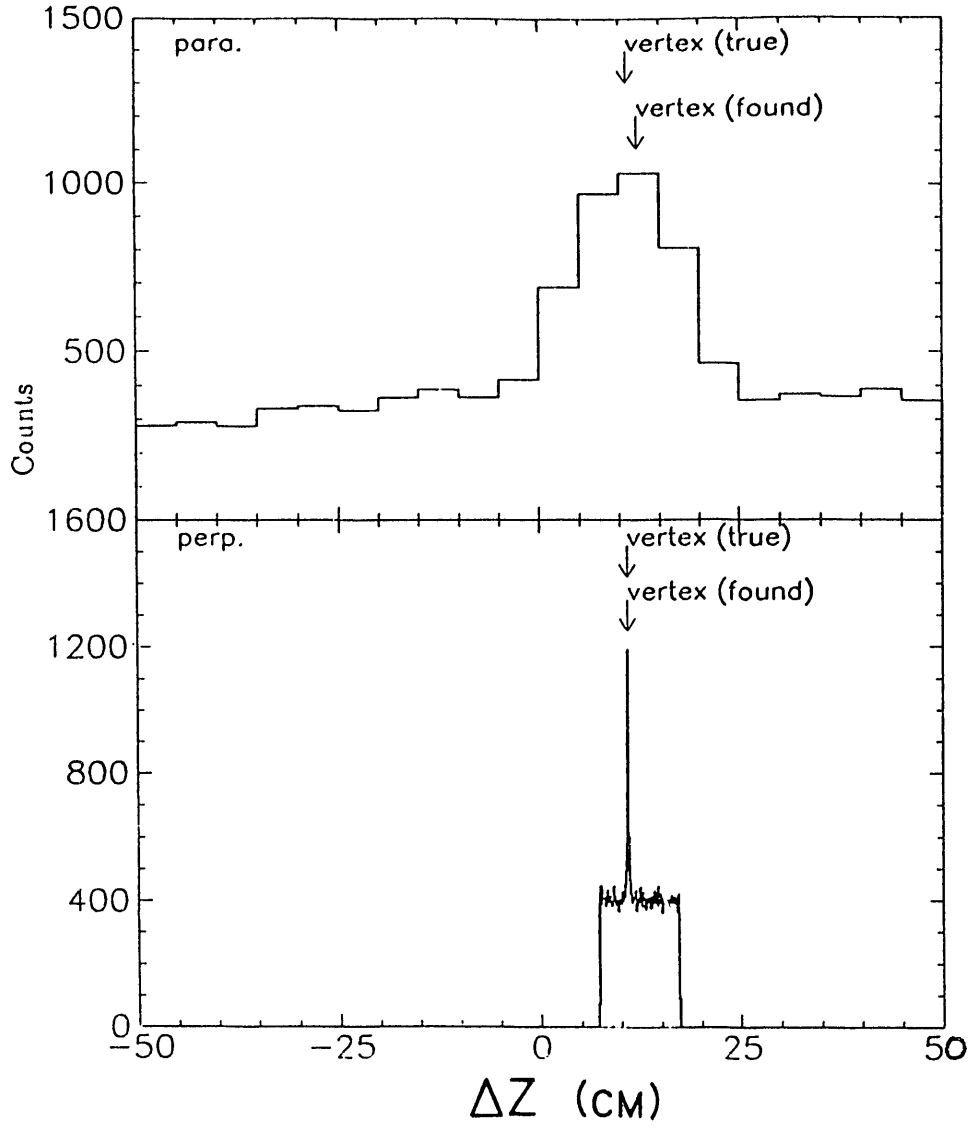

Figure 7: Au+Au — pseudo-tracking example. Top shows the distribution of vertices using parallel strips only. Bottom shows the distribution of vertices using the perpendicular strips. Arrows mark the true vertex and the vertex found in each stage.

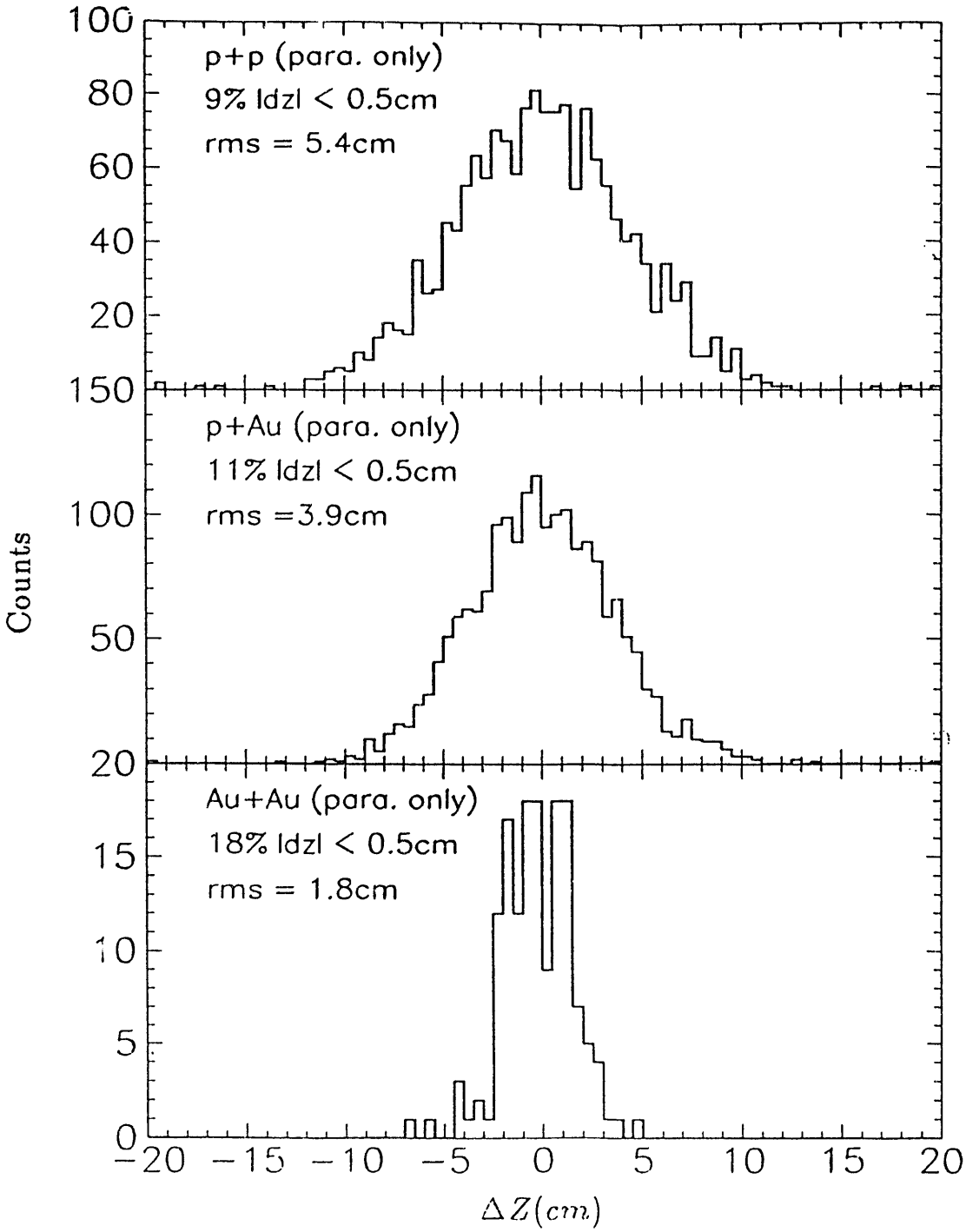

Figure 8: The vertex resolution using pseudo-tracking with parallel strips only for p+p, p+Au minimum bias, and Au+Au central. The horizontal axis is the difference the true vertex and the vertex found.

the first stage of pseudo-tracking are tested. For p+p and p+Au, this range is expanded to ±10cm. A histogram of vertex positions is calculated from the pairs of hits. An example of one of these histograms is shown on the bottom part of fig. 7. The vertex position appears as the peak in this distribution.

Fig. 9 shows the vertex resolution using both stages of pseudo-tracking. The correct vertex is found in all events tested for central Au+Au collisions. For p+p and Au+Au the correct vertex is usually found. Table 3 summarizes the efficiency of pseudo-tracking vertex search for different assumed levels of noise for the three systems. "Total events" and "triggers" are the total number of Monte Carlo events and the number of those that satisfied the "trigger" condition — at least two charged particles hitting both cylinders of the vertex detector. The column labeled "% of triggers" gives the efficiency of the vertex search algorithm — the fraction of the events for which the vertex found was within 5mm of the true vertex. The last column gives the resolution of the vertex finding algorithm based on the widths of the peaks in fig. 9. These widths are upper limits due to the size of the bins used in the pseudo-tracking algorithm. Especially for p+p collisions, noise has a significant effect on the vertex finding efficiency.

system	P_{noise}	Total events	Triggers	% of triggers	σ (mm)
p+p	0.0001	2000	1699	91%	$\leq$0.4
p+p	0.0003	2000	1699	86%	$\leq$0.4
p+p	0.0010	2000	1699	71%	$\leq$0.4
p+Au	0.0001	2000	1921	97%	$\leq$0.3
p+Au	0.0003	2000	1921	94%	$\leq$0.3
p+Au	0.0010	2000	1921	90%	$\leq$0.3
Au+Au	0.001	150	150	100%	$\leq$0.2

Table 3: Efficiency of pseudo-tracking vertex search vs. assumed level of noise for p+p, p+Au, Au+Au. Interaction diamond assumes $\sigma_I = 5.7, 16, 20$cm for p+p, p+Au, Au+Au, respectively. See text for explanation of columns.

Fig. 10 demonstrates one source of problems with the pseudo-tracking vertex search — when the multiplicity is very low, the probability of finding the vertex is also low and this probability gets smaller for higher noise levels. Higher noise levels have a significant effect on the vertex finding efficiency at low multiplicity (below ≈10), but the efficiency reaches ≈100% in each case for sufficiently high multiplicity. In an ideal case, with no noise, 100% efficiency, and no multiple scattering, the algorithm would work for even one charged particle hitting both layers of the detector.

A vertex detector like the one described in the Tales/Sparhc letter of intent[7]

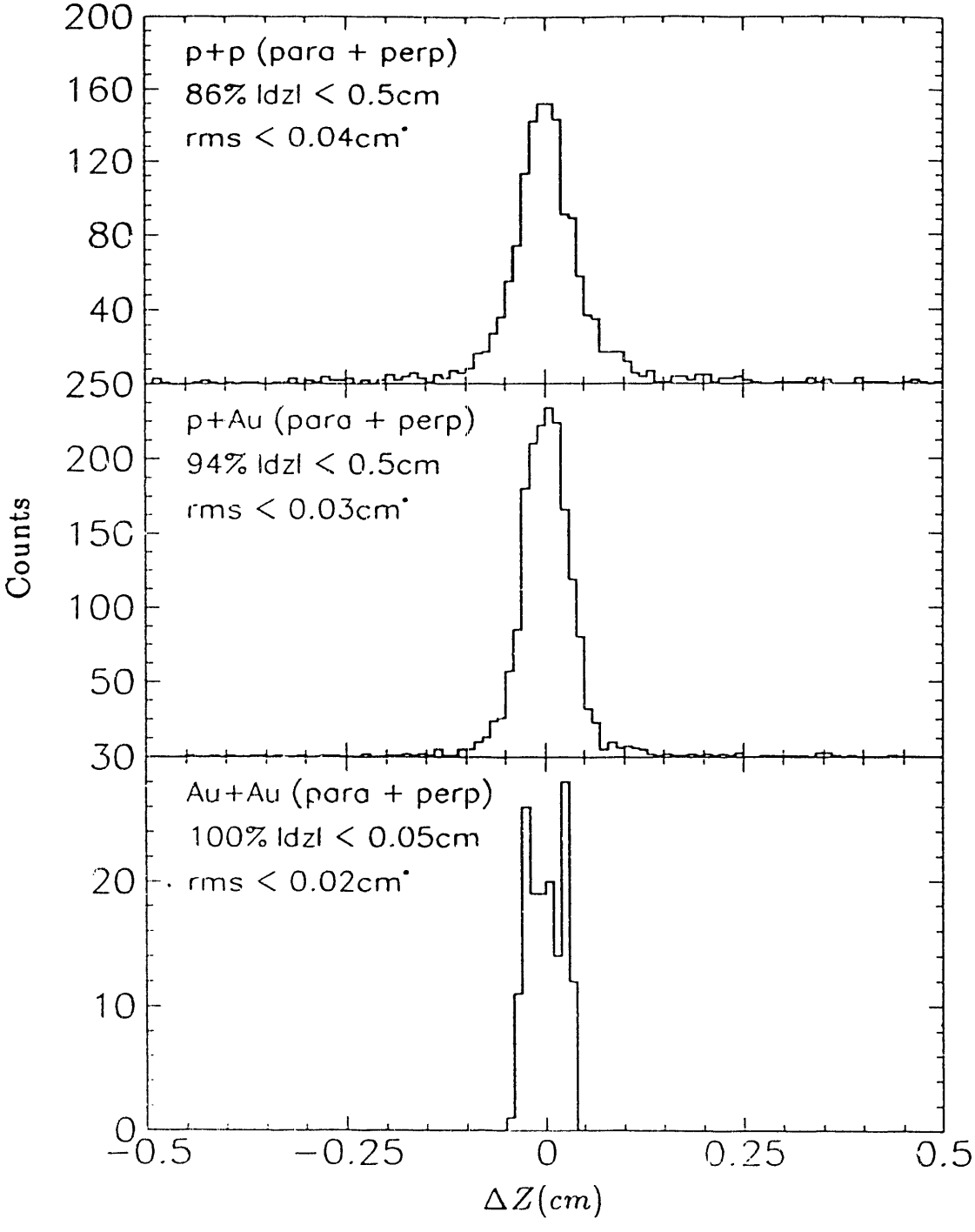

Figure 9: Notice the difference in scale from fig. 8. The vertex resolution using pseudo-tracking with both parallel and perpendicular strips for p+p, p+Au minimum bias, and Au+Au central. * Due to the bin size used, the RMS deviations are upper limits.

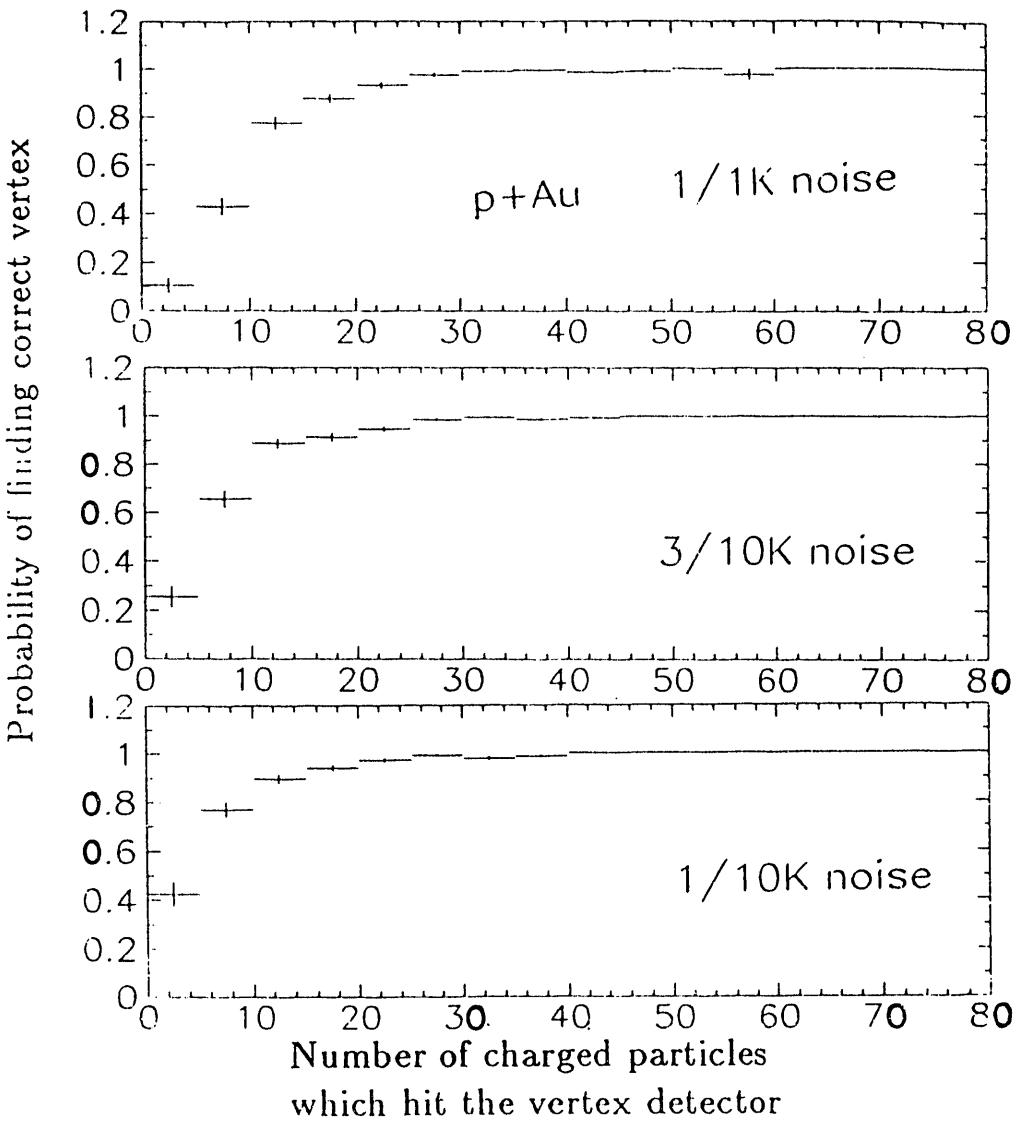

Figure 10: p+Au minimum-bias events from Fritiof. The probability that the correct vertex will be found vs. the number of charged particles that hit both layers of the vertex detector for three assumptions about the noise level. Notice the differences in efficiency for the lowest multiplicity, where the effects of noise are most important

system	P_{noise}	Total events	Triggers	Vertex correct	% of Triggers
p+p	0.0003	2000	1699	1228	72%
p+Au	0.0003	2000	1921	1662	87%
Au+Au	0.001	150	150	150	100%

Table 4: Efficiency of pseudo-tracking vertex search for p+p, p+Au, Au+Au with only 2 azimuthal segments of perpendicular strips used and a length of 64cm. Interaction diamond assumes $\sigma_I = 5.7, 16, 20$cm for p+p, p+Au, Au+Au, respectively. Compare this to table 4, using the full detector.

which had only 2 azimuthal segments of strips perpendicular to the beam, instead of 3, and was 64 cm long, instead of 100cm, could still find the vertex, but with reduced efficiency. Table 4 shows the expected vertex finding efficiency for this detector configuration. The efficiencies are smaller (compare to table 3), especially for p+p, but if the cost savings are large enough, the efficiency loss may be acceptable. Some efficiency is lost when the vertex is outside the shorter detector. However, tests with the full detector configuration show that the pseudo-tracking algorithm can find the vertex in central Au+Au collisions in 94 out of 100 events even when it is 50cm outside of the detector (100cm from the center of the detector), although the resolution falls to $\sigma \approx 2$mm.

6.3 Vertex from the Correlation Method

The most interesting of the vertex finding methods tested here is based on correlations between the pattern of hits on the inner and outer detectors. This method uses a single row of chips on the inner barrel and the corresponding coverage on the outer barrel, or 1/6th of the total circumference.

When an interaction occurs, tracks project outward from the vertex, producing a pattern of hit strips on the inner and outer barrel. To first order, the pattern on the outer barrel is equal to that on the inner barrel except that all distances between hit strips are increased by a factor of (R_2/R_1). If we take the pattern on the outer barrel, and shrink it by a factor of R_1/R_2, we would be able to take this new pattern, and slide it along the inner barrel until there is a perfect match between the hit patterns on the two barrels. We search for the match by forming the correlation function between the patterns as a function of relative position z. For any z we multiply ("and" in hardware) the value of the strip on the inner barrel (1=hit, 0=no hit) by the value of the overlying strip of the outer barrel, and sum these values for all strips. For a randomly chosen relative offset this sum will be small (to first order equal to the multiplicity in the segment of the outer barrel tested times the occupancy of the inner barrel), but when the patterns match, the sum will be equal to the multiplicity in the

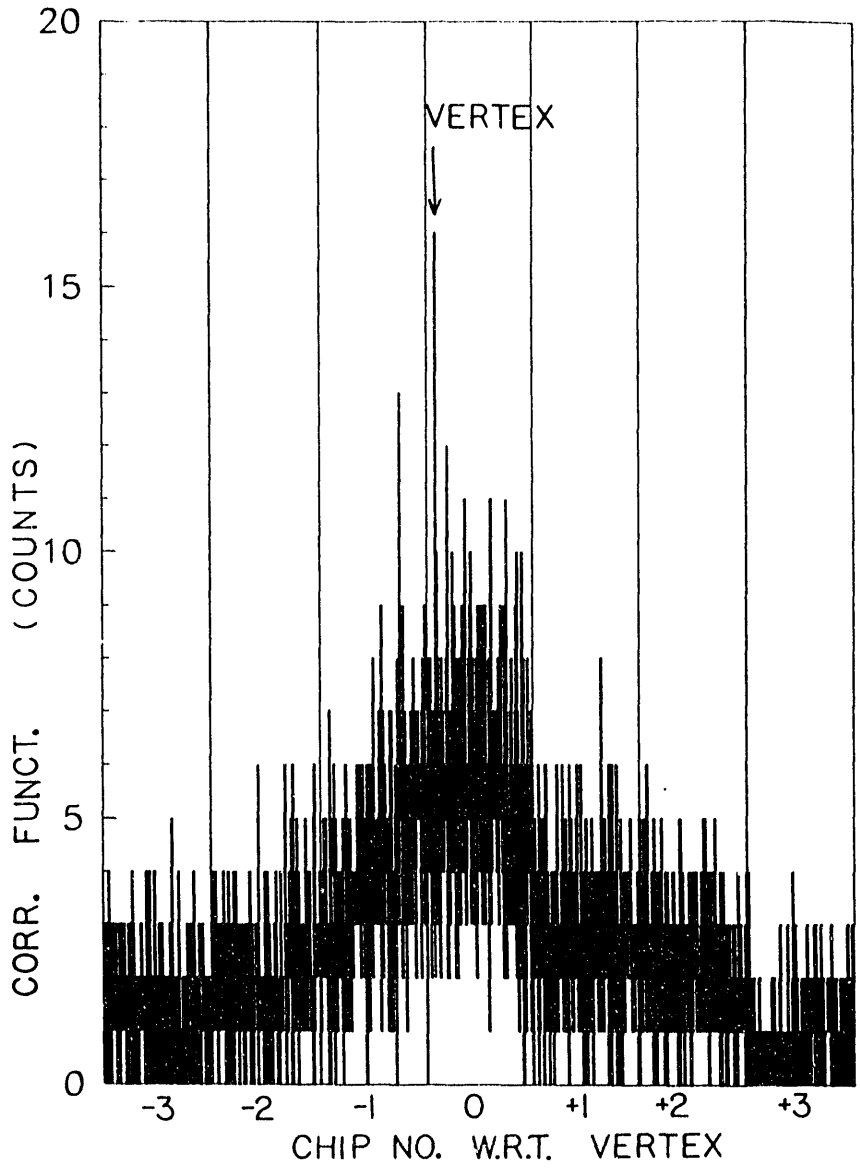

Figure 11: Correlation function for 7 adjacent chips in the vicinity of the vertex. Realistic case — multiple strips turned "on" by slanting tracks, multiple scattering on, R2/R1 = 1.5. The peak now occupies more than one channel, but it is still easily found.

ideal case. The value of z in this case translates directly into the event vertex position with a resolution equal to one strip width.

A hardware implementation to deliver this vertex position would execute the calculation described above on each pair of inner/outer chips in parallel. Thus one of the 20 pairs finds the vertex, all others turn up null answers. This algorithm works for central Au+Au events, but for the lower multiplicities of p+p and p+Au collisions, there are not enough hits per chip to reliably find the vertex. However, offline the algorithm could be extended to use all hits in all chips, and the method would also work for p+Au and p+p collisions. In this limit the algorithm's efficiency would be similar to that of pseudo-tracking.

A series of tests were done for R_1 = 6cm and R_2 = 12cm. Using central Au+Au events for the ideal case where each track turns on only one strip and ignoring multiple scattering, the algorithm finds the correct vertex in 20/20 events with a (peak)/(average background) ratio of about 3/1. Allowing each track to turn on multiple strips due to its angle of incidence increases the apparent occupancy far from the vertex, and the algorithm never finds the vertex in this case. However, when clusters of contiguous hits were replaced by a single hit, the algorithm finds the vertex in 20/20 cases again, still assuming no multiple scattering. The peak/background ratio remained around 3/1. Including multiple scattering spreads hits across neighboring strips, and reduces the signal without changing the background. In this case the algorithm found the correct vertex 17/20 times with a typical (peak)/(average background) ratio of about 2/1. The last step was to reduce the radius of the outer barrel to $R_2 = 1.5R_1$, which matches the current detector design. This reduces the effect of multiple scattering, and the correct vertex is found in 19/20 cases with a typical (peak)/(average background) ratio slightly larger than 2. An example of the resulting correlation function is shown in fig. 11, for 7 chips centered on the chip over the vertex. The channel corresponding to the vertex appears as the maximum value. Increasing the number of adjacent channels used to calculate the correlation function would improve the peak to background ratio.

The correlation method is much faster than the pseudo-tracking method. However, because it requires the patterns of hits to line up exactly in the two barrels, it is more sensitive to multiple scattering than the pseudo-tracking method. The on-line version of the correlation method requires at least a few tracks going into the chip over the vertex, which does not generally happen for p+p and p+Au events. The offline version of the correlation method, using all strips, found the correct vertex in 18/20 events for p+Au, which is similar to the efficiency of the pseudo-tracking method.

7 Alignment requirements

We have assumed that the vertex needs to be known to better than 1mm in z. In the plane transverse to the beam, the definition is already equal to the beam size (σ_T ≈0.45mm for Au+Au[5,9]). Some chip placement aberrations result in a track ending up in a strip neighboring the expected one, reducing the peak value of the correlation function. Preventing this kind of error defines most of the constraints on placement of the chips in 3 directions, z (along the beam axis), R (radial), and s (circumferential, or R*dϕ), plus the 3 rotations around these axes. The chips lie at radii R_1 and R_2, which are assumed to be 6 and 9 cm in the calculations below. The size of a chip in the z-direction (Z_{chip}) is taken to be 5cm, and the detector "cylinders" have a hexagonal cross-section.

The correlation method is only concerned with the relative placement of chip pairs, one chip on the inner cylinder and the corresponding chip(s) on the outer cylinder. Here, one example of the determination of the alignment constraints is given. The other constraints are determined similarly and are summarized in table 5.

Consider the displacement in R (ΔR) of one of the cylinders relative to the other. When scaling the outer pattern by the nominal R_1/R_2, a radial displacement would result in a pattern that is improperly scaled. A calibration procedure could find the actual R_1/R_2, but the nominal ratio will presumably be a ratio of integers, hard-wired in a fast vertex finder. In order to limit the error such that in the worst case, a track is displaced by 1 strip (100μm),

$$100\mu m = \frac{R_1}{R_2} \times \frac{Z_{chip}}{R_2} \times \Delta R \qquad (2)$$

This is satisfied if radial displacement of the outer chip is less than ≈0.3mm.

axis	max. error in relative position	max. error for relative rotation about this axis
z (beam)	0.5mm	0.15°
R (transverse)	0.3mm	0.1°
s (circumference)	0.5mm	0.3°

Table 5: Summary of tolerances in placement of inner/outer chip pairs relative to each other from correlation method

These tolerances, summarized in table 5, are between inner/outer chip pairs only. Suppose that a chip pair is joined such that they meet these tolerances. There are further constraints on the positions of chips pairs relative to the beam. Again, consider one example. There is a constraint in R, which leads to a limit of:

$$dR \times \frac{R_2 - R_1}{R_2} \times \frac{Z_{chip}}{R_2} \times \frac{R_1}{R_2} = 100\mu m. \qquad (3)$$

The pair must be placed at a radial distance which is known better than dR ≈0.8mm. This should be compared to the size of the Au+Au beam in the transverse direction[5,9], σ_T ≈0.45mm. Table 6 summarizes the constraints on the positions of pairs of chips relative to the beam. These constraints are not as stringent as those on the relative positions of the chips.

axis	max. error	max. error for rotation about this axis
z	5.0mm	1°
R	0.8mm	37°
s	∞	4°

Table 6: Summary of tolerances on the placement of chip pairs relative to the beam from correlation method, where each pair of chips are positioned relative to each other within the tolerances given in table 5.

The correlation method of vertex finding leads to the limits given in tables 5 and 6. The pseudo-tracking method combines a hit on any of the inside chips with a hit on any of the outer chips, which may pose limits on the relative placement of all chips simultaneously, not just in pairs. In order for this method to work, all pairs must be able to point to the same vertex. This implies relative placement requirements between any pairs of chips similar to those in table 5. However, this is an offline method, and the positions of chips may be calibrated using tracks reconstructed from other detectors. Such calibrations would work for all aberrations except rotations around r and z. However the tolerances imposed on these angular placements by the correlation method are much more stringent than anything needed to define a vertex to 1mm. Thus the pseudo-tracking method imposes no further restrictions.

8 Electronics Requirements

There are several important constraints on the design of the electronics for the vertex detector. The size and mass must be minimized to prevent space conflicts with other detectors and to minimize multiple scattering and production of secondary particles. The electronics system must produce as little heat as possible; if the power consumption can be kept to the order of ≈1mW/channel, then forced-air cooling should be possible. If air cooling is not possible, a complicated and potentially expensive cooling system will be required, which would add significant mass in the vertex region. The shaping time of the preamplifier must allow individual beam crossings (every ≈ 200ns) to be distinguished. Since the vertex detector multiplicity is expected to form part of the first level trigger, a system which moves this information "into the pipeline" at this rate is

needed. This time constraint, combined with the power consumption constraint eliminates most of the presently available electronics components.

There are several Si strip vertex detectors currently being designed (for instance for GEM and SDC at the SSC), and some already in operation[6,10-15]. As a result, some components are available. However, none of these components can be considered completely "off-the-shelf" items. Even in those cases where a similar component has been made before, some modifications will be necessary. For example, the Si strip detector wafers similar to the ones needed for this detector have been constructed by a number of vendors[16-20]. However, in order to purchase them for use with this detector, a new set of masks must be made for the appropriate strip pitch and length. Then the detectors must be manufactured and tested. Quality control is time-consuming, but vital, as is working closely with the vendors. A well-defined and complete set of quality-control parameters must be agreed upon with the venor. For a project of this scale, automated testing on a probe station will probably be necessary. A custom probe card and some of the related software would have to be provided. Our experience suggests that this process typically takes $\approx$18 months (or more) before all of the detector elements are in hand.

The first part of the electronics system is the connection of the detector strip to the preamplifier. Although some work is being done to integrate the front-end electronics and the detector strips[19,20] on a single wafer, we expect to have a separate front-end integrated-circuit chip which will be wire-bonded to the detector strips. Here, the 100μm pitch is advantageous since machines exist for wire-bonding at this pitch. The front-end electronics chip would consist of a preamplifier, shaper, discriminator, and latch. An LED-based optical fiber readout system, for high speed ($\approx$100MHz) and low local power consumption will probably be used. In order to simplify the mechanical design, the electronics packages would be supported on the Si detector chips.

The simulations have shown that it is possible to satisfy all of the vertex detector's design criteria without using ADC's on the individual strips. This would simplify the system and reduce the volume of data produced. However, a single analog output for each detector chip would be useful for triggering. Due to the angle of incidence problems, a simple sum of the analog signals from each chip would not give the multiplicity without first determining the vertex position. For a multiplicity to be used in the trigger, a sum of discriminator outputs from the strips parallel to the beam (where $\approx$ 1 strip per particle would be "hit") is needed. A sum of the analog signals from all strips on a chip might be useful; if $dN/d\eta$ is constant over the length of the vertex detector (based on Fritiof calculation, this is true at the $\approx$15% level — see fig. 3), then the total energy loss in each detector would be proportional to $dN/d\eta$ independent of the z position relative to the vertex. This is similar to an observation in the Oasis Letter of Intent[21], although that vertex detector geometry was much

Source	Description	Available now?	Where used or to be used	Approx. peaking time (ns)	Power use (mW/ chan)
FNAL[6,10]	bipolar	Yes	E789	10	$\geq$50
LBL[11,24]	SVX-D: shaper, disc.,latch., digital circuits, Some rad. damage problems	Yes	CDF (SVX-I)	$\approx$700	$\approx$1-2
FNAL/ ORNL[25]	R&D: CMOS preamp, shaper prototype (now), more later	Yes*	BVX(D0), RHIC?	$\approx$200	
LBL[26]	SVX-H: rad. hard CMOS, shaper,disc., latch,digital circuits	Yes*	CDF (SVX-II), L3	$\approx$500	$\approx$1-2?
LBL[27]	CMOS preamp, shaper,disc,latch, analog sum?, no buffering	No	SDC	15?	
Santa Cruz[28]		No	SDC		
Ikeda[19]	R&D: combined Si strip detectors & front-end	Yes*	SDC		7
SDI[20]	R&D: BiCMOS combined Si strip detectors & front-end	No			

Table 7: Selected sources of front-end electronics for Si strips vertex detectors. The last two columns gives the approximate peaking time and power dissipation. * indicates that only prototypes are available.

different. This quantity could also be useful in triggering. Knowing $dN/d\eta$ implies knowledge of the multiplicity only if the vertex position is known — so if the multiplicity is needed for the first level trigger, the need for parallel strips remains.

More work is needed to design, manufacture, and test suitable front-end electronics components. Some work on this subject has been reported at this conference[22,23]. This important work should lead to front-end electronics systems which are fast enough and have low enough power consumption. A summary of selected electronics systems for Si strip detector appears in table 6. None of the currently available components satisfies the combined power dissipation and speed limitations for this detector. In addition, it is crucial to integrate the components into a system as soon as possible. It would be unwise to start construction of an expensive and complex detector system without careful tests of all of the components together. Some of this integration work is already being done by the P2 group in Los Alamos. Prototype CMOS preamplifiers[25] have been acquired and will be combined with an OPAL-type strip detector[17], using a locally developed hybrid circuit. Tests of this system will take place in early 1992, with tests of other systems[26] following shortly.

The electronics development can take place using either CMOS or bipolar processes. CMOS circuits are easier and cheaper to develop, but are not suitable for long strips, which have large capacitance — this is not a limitation in the current design, but could be for other designs. It will be easier to develop circuits with less than 100μm pitch using a bipolar process than with CMOS — but the current design assumes 100μm — eliminating this advantage. In general, bipolar circuits use less power for the same performance as CMOS.

The radiation damage to a cylindrical vertex detector caused by charged particles from the primary reaction can be estimated[1] by assuming that $dN/d\eta$ is constant over the length of the vertex detector. Assume that a "RHIC year" is 10^7sec long at a Luminosity[29] of $2 \times 10^{26} cm^{-2} sec^{-1}$ with $\sigma_{tot} = 6.13$b. For central Au+Au collisions assume that $dN/d\eta$ for charged particles is constant at $\approx$800 in the central region (see fig. 3). For minimum-bias Au+Au events this would be reduced to $\approx$200. With these assumptions, the radiation damage per "RHIC year" can be estimated:

$$\frac{Dose}{time} \approx \frac{125 Gy/year}{R_\perp^2}, \tag{4}$$

where $R_\perp$ is the radius of the cylinder in cm and $1Gy = 100Rad$. This is a factor of $\approx$3000 less than at the SSC and should not cause a serious problem if radiation hard electronics are used. For example, tests with the CDF SVX-I detector[11], without radiation hard electronics, showed a doubling of the electronic noise for a dose of 20Krad. At RHIC, a dose of $\approx$350Rad per "RHIC year" would be expected — far below this limit. Therefore, radiation damage

should not be a problem at RHIC. Neutral particles and the presence of a magnetic field around the vertex could increase this dose, but the estimate suggests that it will not be important.

9 Conclusions

The simulations show that a vertex detector like the one described here will be able to measure the charged particle multiplicity except for very low multiplicity events, where statistical effects in the sampling of the distribution limit the measurement. The detector will be able to measure $dN/d\eta$ in all cases studied as long as the noise is understood. The noise will be an important factor in the multiplicity and $dN/d\eta$ measurements for p+p and p+Au.

On-line vertex finding with high efficiency is possible using the correlation method for central Au+Au events. Offline, the pseudo-tracking method should have ≈100% efficiency in this case. The correlation method can not determine the vertex on-line for p+Au or p+p because the multiplicities are too low but the pseudo-tracking method finds the vertex in 90% or more of the p+Au events and 70% or more of the p+p events. The pseudo-tracking method breaks down for charged particle multiplicity less than ≈10, and is affected by the noise in the detector.

A vertex detector with reduced coverage[7] would make the already marginal measurement of the multiplicity in p+p and p+Au worse, but a trigger-level multiplicity may not be needed for these collisions. For an easily interpretable multiplicity measurement, at least one segment of strips parallel to the beam should remain in the system, as the angle of incidence of the particle makes it difficult to extract meaningful multiplicities (or $dN/d\eta$) from the perpendicular strips. The last 14% in vertex finding efficiency that comes with the more complete vertex detector for p+p and 8% for p+Au (compare tables 3 and 4) may not be worth the extra cost of an extra azimuthal segment. However, it is the η coverage out to $\approx \pm 3$ and the correlation method for finding the vertex which constrain the length of the detector. Reducing the length of the detector will make the correlation method fail more often, eliminating the possibility of a high-resolution high-efficiency on-line vertex reconstruction. For comparison, a 100cm long detector covers 97.7% and a ±32cm detector covers 85.4% of the Au+Au interaction diamond. If the inefficiency at the ends is acceptable, a shorter length for the azimuthal segments with perpendicular strips could be used. For 100cm long azimuthal segments with parallel strips, the η coverage is maintained.

Another potentially valuable feature of the parallel strips is finding the vertex position in the transverse direction. The transverse size of the beam should be very small ($\sigma \approx 0.45$mm[5,9] for Au+Au), but the ability to measure the beam

position in the transverse direction could be extremely useful in the alignment of the detector.

There are still some problems with the vertex detector that require further study. Thermal expansion and contraction of the detector (and its support structure) are important and related to the power dissipation by the electronics. These effects are being studied and will constrain the electronics design. A study of electronics components with low power dissipation is underway. Some sample detectors and electronic components have been acquired and are in the process of being tested as a system.

10 REFERENCES AND NOTES

1. For a brief summary of the characteristics of Si strip detectors see: Particle Data Booklet, 1990 edition, pg 131; M. Aguilar-Benitez, *et. al.*, Phys. Lett. **B239**, 1 (1990).

2. S. Aronson et.al., "A Lepton/Photon Spectrometer for RHIC, Measurements of Lepton Pairs, Vector Mesons, and Photons," letter of intent: July 15, 1991.

3. B. Nilsson-Almquist and W. Stenlund, Comput. Phys. Commun. **43**, 387 (1987); the calculation here used: Standard lund parameters, $\sqrt{s}$ = 200.0GeV. Fritiof version 1.7, Jetset version 6.3.

4. ROHACELL is a registered trademark. Available from Rohm Tech Inc. 195 Canal St. Malden, MA 02148. It is a polymethyacrylimide foam.

5. D. Beavis, *eta. al.*, **Fourth Workshop on Experiments and Detectors for a Relativistic Heavy Ion Collider**, BNL report # 52262, 235 (1990), M. Fatyga and B. Moskowitz, eds.

6. P. L. McGaughey, private communication. The vertex detector used in E789 at Fermilab is based on 50μm pitch Si strips. This (currently operating) detector has $\geq$90% efficiency for an individual strip with about 1/1000 strips "on" due to noise.

7. TALES/SPARHC Letter of Intent for a RHIC Experiment, P. H. Zhang et. al. July 1991.

8. A binomial distribution is appropriate if the probability that a particle will hit the vertex detector is the same for each particle and independent of the others.

9. RHIC Bulletin, BNL, Vol. II, No. 3, Oct. 1991.

10. D. Christian, *et. al.*, IEEE Trans. on Nucl. Sci., NS-36, 507 (1989).

11. CDF vertex detector: W. C. Carithers, *et. al.* , Nucl. Inst. Meth. **A289**, 388 (1990).

12. Delphi vertex detector: H. Dijkstra, *et. al.* , Nucl. Inst. Meth. **A289**, 400 (1990); Delphi Collaboration, Nucl. Inst. Meth. **A303**, 233 (1991).

13. Fermilab E687 vertex detector: G. Bellini, *et. al.* , Nucl. Inst. Meth. **A305**, 395 (1991).

14. Mark II vertex detector: C. Adolphsen, *et. al.* , SLAC Report No. SLAC-PUB-5543, 1991 (unpublished); (to be published).

15. Brief descriptions of some existing vertex detectors appear in: Nucl. Inst. Meth. **A305**, 621 (1991).

16. Hammamatsu Photonics K.K. Solid State Division, US address: Hammamatsu Corp. 360 Foothill Road, P.O. Box 6910, Bridgewater, NJ, 08807-0910.

17. Micron Semiconductor Inc., Lancing, England.

18. CSEM, Neuchatel, Switzerland.

19. Ikeda, Japan.

20. L. Van der Have, Silicon Dynamics Inc., Ames, Iowa.

21. Oasis Collaboration, RHIC Letter of Intent, R. Debbe *et. al.* , July 1991.

22. B. Wadsworth, MIT, this conference.

23. C. Britton, ORNL, this conference.

24. S. Kleinfelder *et. al.*, Proc. IEEE NSS Symp. 1987; *ibid*, 1989.

25. G. T. Alley, C. L. Britton, E. J. Kennedy, P. Skubic, ORNL; T. Zimmerman and R. J. Yarema. Some details presented at IEEE Nuc. Sci. Symp., Santa Fe, NM (1991).

26. S. Kleinfelder, LBL, Berkeley, CA. private communication. To be manufactured by UTMC, Colorado Springs, CO.

27. H. Spieler, LBL, Berkeley, CA.

28. D. Dorfan, S.C.I.P.P., Santa Cruz, CA.

29. S. Ozaki, Nucl. Phys. **A525**, 125c (1991).

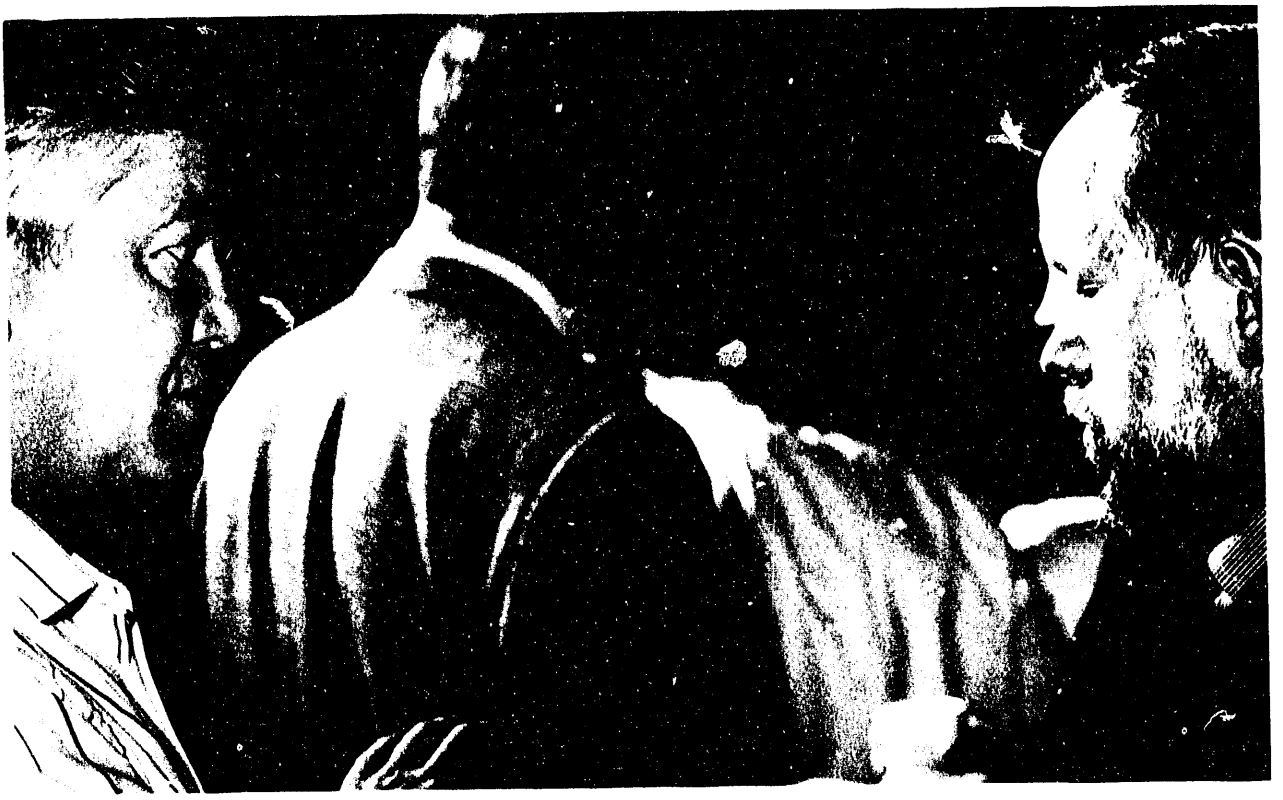

SIMULATIONS OF SILICON VERTEX TRACKER FOR STAR EXPERIMENT AT RHIC

G.Odyniec, D.Cebra, W.Christie, D.Liko*, S.Margetis**, C.Naudet, L.Schroeder, W.Wilson
Lawrence Berkeley Laboratory,
Berkeley, CA 94720

J.Cramer, D.Prindle, T.Trainor, W.Braithwaite***
University of Washington,
Seattle, WA 98195

ABSTRACT

The first computer simulations to optimize the Silicon Vertex Tracker (SVT) designed for the STAR experiment at RHIC are presented.

1.INTRODUCTION

The physics goals [1,2] and the expected complexity of the events at RHIC dictate the design of a tracking system for the STAR experiment. The proposed tracking system will consist of a silicon vertex tracker (SVT) to locate the primary interaction and secondary decay vertices and to improve the momentum resolution, and a time projection chamber (TPC), positioned inside a solenoidal magnet, for

---

* Institut fur Hochenenergiephysik, Vienna, Austria.

** University of Frankfurt, Frankfurt, Germany.

*** University of Arkansas, Little Rock, AR

continuous tracking, high momentum resolution, and particle identification. The extremely high position resolution required of the SVT detector is particularly important for the measurement of strangeness and charm production.

However, it must be noted that, although the strange quark density in the quark-gluon plasma phase is much higher than in the hadronic gas phase, the total content of strange quarks is less enhanced in a quark-gluon plasma than in a fully equilibrated hadronic gas at constant total energy or entropy. This is because the volume associated with the hadronic gas is much larger due to the smaller number of available degrees of freedom at fixed energy [3]. Therefore, the observables which depend on the total strangeness abundance, such as Λ, $\bar{\Lambda}$, K^0 yields or K/π ratio should not be considered as direct signatures of quark-gluon plasma formation. On the other hand, the observables depending on enhanced strangeness density, such as baryons with multiple strangeness or possibly correlations between strange particles, benefit from higher (near equilibrium) strangeness density reached in the quark-gluon plasma. Their relative independence of final state effects makes them much more characteristic signatures of quark-gluon plasma formation [4]. The STAR SVT, with its excellent vertexing, will allow for studying multistrange baryon production at RHIC.

It has been argued [5] that the enhancement of the final total open charm, which is mainly due to pre-equilibrium production, could be used as a measure of the thermalization time of the dense partonic system. The SVT capability of open charm detection is currently under investigation.

During FY'91 simulations of SVT performance in the high multiplicity environment at RHIC have been carried out in collaboration with the University of Washington. The goal was to obtain an initial SVT design.

This note is divided into 8 sections. The second section contains a brief description of the detector layout. The third section explains the simulation procedure and lists the various hit densities for central Au+Au FRITIOF events. Sections 4 and 5 deal with reconstruction of primary and secondary verticies. Section 6 describes the effectivness of the SVT-TPC matching algorithm and possible improvements. Section 7 is devoted to Kalman filtering and presents some preliminary results. Finally, section 8 contains a summary.

2. SVT LAYOUT

Fig.1 shows the STAR experimental configuration with the SVT placed in the center of the detector. Fig.2 shows SVT layout presently used in the simulations.

Individual detectors are grouped into ladders. Each ladder holds a row of 6 silicon drift detectors (SDD). The ladders are arranged in three concentric barrels around the interaction at radii of 5, 8, and 11 cm (containing approximately 36K channels of information). Each barrel is about 40 cm in length, to nearly cover the diamond size. Each SDD is 6.5 cm in length and is made from a 4-inch diameter wafer. The thickness of a wafer is 300 microns which appears to be a good compromise between signal strength (24K electrons are created by minimum ionizing particle) and acceptable values of multiple scattering and secondary particle production for particles traversing the detector. Choice of SDD as the basic component of the SVT system was dictated by the excellent performance of these detectors, in particular: outstanding tracking precision (~10 microns), very good two-track resolution (few hundred microns), no dead time, low number of electronic channels, and the ability to monitor and calibrate the system [6,7,8].

3. SIMULATION PROCEDURE

The FRITIOF event generator was used to create Au+Au central events at E_{beam} = 100 GeV/N. The events were then filtered through the STAR detector systems using GEANT. The spatial resolution used in simulations was σ=25 microns for SVT and σ=250 microns for TPC. Interactions with all materials in the present STAR design were taken into account. Multiple scattering, energy loss, secondary interactions, and all other physics processes in GEANT were included.

A typical central Au+Au FRITIOF event at RHIC energies gives rise to about 2900 charged particles that leave at least 20 hits in the TPC. There are about 2400 hits in SVT layer 3 (at 11 cm), 2800 hits in layer 2 (at 8 cm) and 3600 hits in layer 1 (at 5 cm). The average hit densities are 0.71 hits/cm^2, 1.2 hits/cm^2 and 2.3 hits/cm^2 in layer 3, layer 2 and layer 1, repectively.

4. MAIN VERTEX

Fig.3 shows the capability of locating the primary vertex along the beam axis (z axis) with and without the SVT. Tracks can be associated with their correct vertex from events whose vertices are separated by 2 mm, as seen in Fig.3b. The precision of finding the main vertex position in the perpendicular directions (x and y) is significantly better than along the beam axis.

5. SECONDARY VERTICES

5.1 Singly strange particles: K^0, Λ, $\bar{\Lambda}$

The K^0, Λ and $\bar{\Lambda}$ produced in FRITIOF Au+Au events were used to evaluate the efficiency of detection of neutral strange particles decays. About 25% of K^0 and 20% of Λ and $\bar{\Lambda}$ are within the overall detector acceptance. The majority of losses are due to non-charge decays and the acceptance of STAR. To reduce the high density of potential crossing tracks near the primary vertex, a minimum track length of 1 cm for K^0 and 2 cm for Λ and $\bar{\Lambda}$ was applied (this is in effect a lifetime cut). In addition, the parent particle reconstructed from the two secondaries ($K^0 \rightarrow \pi^+ + \pi^-$, $\Lambda \rightarrow p + \pi^-$, $\bar{\Lambda} \rightarrow \bar{p} + \pi^+$) was required to point back to the primary vertex within 2 mm. Fig.4 shows the effective mass distributions for reconstructed events. Sharp peaks at the correct masses are obtained above a flat background. Approximately 2/3 of the accepted secondary neutral decays are reconstructed.

5.2 Charged Hyperons : Ξ^-, Ω^-

Among the multistrange particles only $\Xi^- \rightarrow \pi^- + \Lambda$ and $\Omega^- \rightarrow K^- + \Lambda$ decays can be studied at STAR. The 15000 Ξ's (+ 13000 $\bar{\Xi}$'s) and 300 Ω's (+300 $\bar{\Omega}$'s) produced in 4000 FRITIOF Au+Au events were analyzed. Note that the considered Ξ and Ω decays have the same topology, as shown on Fig.5. As a consequence of the very short lifetime (down to 10^{-13} s), the decaying particle track is straight and its momentum cannot be determined. A 3 constraint fit (3C) with the assumed mass of the decaying particle, or a 2 constraint (2C) fit with the

mass calculated must be performed. All measured quantities (e.g. for $\Omega^- \rightarrow K^- + \Lambda$; momenta of K^- and Λ) are then fitted to give the best solution [9] and the probability for the correctness of the hypothesis is calculated. To optimize the signal to background ratio, a number of cuts were imposed (analogous to those for Λ, $\bar{\Lambda}$ and K^0): tracks which miss the main vertex by less than 2 cm for Ξ's and 1 cm for Ω's were excluded, a reconstructed hyperon was required to point back to the main vertex within 1.5 mm, and the distance of closest approach for the Λ decay products in all three directions should not exceed 5 mm. Overall about 15% of multistrange baryons which were within STAR acceptance were reconstructed (which corresponds to ~5.5 % of all Ξ's, $\bar{\Xi}$'s, Ω's and $\bar{\Omega}$'s produced produced in full phase space). The bulk of the losses (~ 85%) are due to the limited acceptance of STAR and, for Ω's, due to the branching ratio (67% for $\Omega^- \rightarrow K^- + \Lambda$). Fig.6 a and b show the invariant mass distribution ('ideal' case, without accounting for momentum resolution) for Ξ's reconstructed in STAR TPC (a) alone and TPC with the SVT (b). The SVT eliminated the background almost completely, whereas TPC alone could only provide marginal information on Ξ production, even in the so called 'ideal' case with the perfect momentum measurements. Fig. 7 shows the invariant mass of Ξ (TPC + SVT) for a TPC momentum resolution of $\delta p/p=1\%$ taken to the account. The peak is slightly broader, but the signal is still very strong (note: different vertical scales on Fig. 6 and 7).The arrows indicate the correct masses of hyperons.

Similar results were obtained for $\bar{\Xi}$'s, Ω's and $\bar{\Omega}$'s. As an example, the invariant mass plot for omegas is shown on Fig.8.

6. MATCHING SVT HITS WITH TPC TRACKS

The results of the previous sections were based on the assumption that a perfect assignment of SVT hits with tracks identified in the TPC was possible. An algorithm to examine how well this assignment can be justified was developed. Au+Au events, generated by FRITIOF, were used as described before. A track was required to have 20 points left in the TPC to ensure good tracking information, and three SVT hits (do not confuse acceptance with matching efficiency). A helix was fitted to 20 GEANT points and its parameters were used to calculate the expected hit position in SVT layer 3. The expected multiple scattering of the track was calculated and used to define a 3σ 'search' area. The deviation between the

expected position and the actual position is well described by multiple scattering calculation and the chosen 3σ area contain the correct hit over 98 % of the time. Over one third of the time there is only one hit in the search area. All candidates in layer 3 were tested by adding them (one at a time) to the TPC points and re-doing the helix fit. Using the improved helix parameters, extrapolation to the layer 2 was made, and subsequently to the SVT layer 1.

After this procedure, sets of three candidate points for each track were found. Normally there is only one possible helix. When there is more than one helix the one with the lowest χ^2 was chosen. The helix is defined as being 'correct' when all three SVT points and the TPC points come from the same GEANT track. A measure how well matching is done is expressed by ratio of 'correct' helices to the number of times the attempt to find the track was made. This efficiency as a function of p_t is plotted in Fig.9. The overall average efficiency, for a p_t cutoff at 100 MeV/c, is 91%. For p_t cutoff of 200 MeV/c matching efficiency is over 97%.

For tracks with lower p_t there are serious problems with multiple scattering. There are two obvious software improvements to make. The first is the use of KALMAN filter techniques. The second is to assign the tracks to a vertex and use this as a constraint. Regardless of software optimizations, FRITIOF predicts a significant number of tracks at low enough p_t such that the track parameters are altered before they are measured in the TPC. To make the SVT-TPC match for low p_t tracks one would need to start tracking in the TPC closer than 50 cm or add a 4-th layer to the SVT at ~ 20 cm radius. Conversely, one could use the SVT information alone to determine the track parameters of these tracks. Adding a fourth layer to the SVT would make the device an independent tracker for low p_t particles and enlarge the STAR acceptance significantly. This problem is currently under study.

7. KALMAN FILTER METHOD

The Kalman Filter, a method derived from system theory, has been recently proposed as a novel approach to the reconstruction of charged tracks and vertex fitting [10].

Concerning the reconstruction of charged tracks - it combines the advantages of the former methods, especially if the tracks are fitted with breakpoints [11], and adds a new concept for identification of outliers[12].

The vertex fit by means of the Kalman Filter is equivalent to traditional methods based cn LSM estimators. However, an advantage is gained by an easy and fast method of outlier identification that allows reconstruction of a primary vertex in the presence of a large number of tracks.

The Kalman Filter method was implemented for the purpose of reconstructing charged tracks with the STAR SVT and TPC. Results from the comparison of the performance of the TPC alone and the TPC combined with the SVT are shown on Fig.10, 11, and 12. Fig.10 shows the momentum resolution obtained in the STAR TPC. Adding the SVT hits improves resolution significantly. The impact parameter resolution (accuracy of extrapolation in the vertex region) is dramatically improved. Fig.11 shows the comparison of impact parameters with and without SVT. In Fig.12 the extrapolation is shown as a function of transverse momentum.

Implementation of the Kalman Filter method to include the primary vertex fitting is currently in progress. As a next step, a Kalman Filter algorithm is going to be incorporated into a reconstruction of secondary vertices, particularly D^+ and D^- finding.

8. SUMMARY

Our investigations and simulation studies have shown that the STAR SVT, together with the TPC, will identify very well the secondary and primary vertices. The overall track momentum resolution is significantly improved. We conclude that the SVT is the only detector capable of measuring multistrange hyperons at RHIC and perhaps allows the study of open charm production.

References:

1. Kadija at al., "An Experiment on Particle and Jet Production at Midrapidity", LBL-29651.
2. The STAR Collaboration, "Update to the RHIC Letter of Intent for an Experiment on Particle and Jet Production at Midrapidity", LBL-31040.
3. L.McLerran, Nucl.Phys. A461,245c(1987),
   K.Redlich, Z.Physik C27,699(1985)
4. P.Koch,B.Muller,J.Rafelski, Phys.Rep.142,167(1986).
   J.Rafelski,A.Schnabel, "Intersections Between Nuclear and Particle Physics", AIP Proceedings No.176(1988),p.1068 and references therein.
5. B.Muller and X.Wang, Duke University Preprint DUKE-TH-91-29.
   E.V.Shuryak, Phys.Lett.78B(1978)150.
   T.Matsui and H.Satz, Phys.Lett.178B(1986)416.
   A.Shor, Phys.Lett.B215(1988)375 and Phys.Lett.B233(1989)231,
6. P.Rehak et al., NIM A248(1986)367.
7. E.Gatti, P.Rehak and M.Sampietro, NIM A274(1989)469.
8. P.Rehak and E.Gatti, NIM A289(1990)410.
9. B.Ronne, CERN/TC, "Kinematical Analysis".
10. R.Fruhwirth, NIM A262(1987)444.
11. R.Bock, H.Grote, D.Notz and M.Regler (ed. by M.Regler) - Data Analysis Techniques in High Energy Physics Experiments, Cambridge Univ. Press, Cambridge (UK), 1990.
12. R.Fruhwirth, Ph.D. Thesis, Univ. of Technology, Vienna, 1988; HEPHY PUB-516/88.

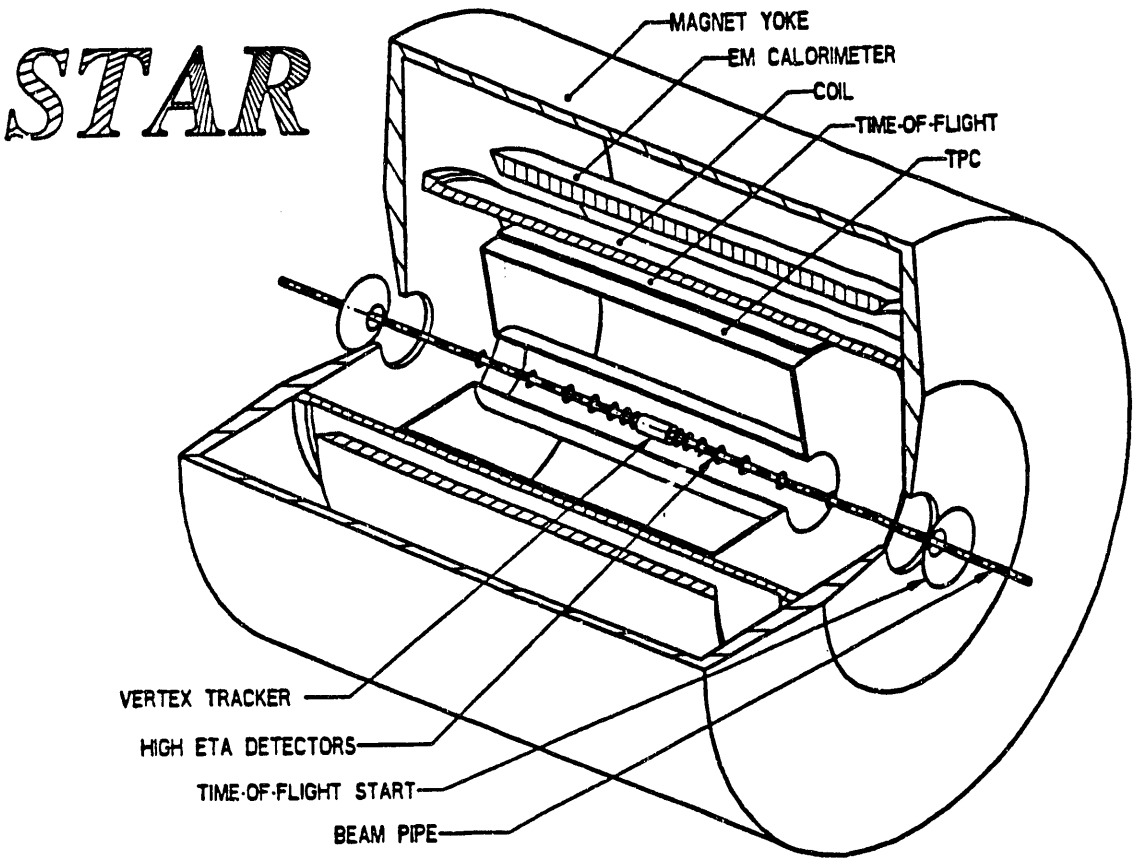

Fig.1 STAR experimental configuration.

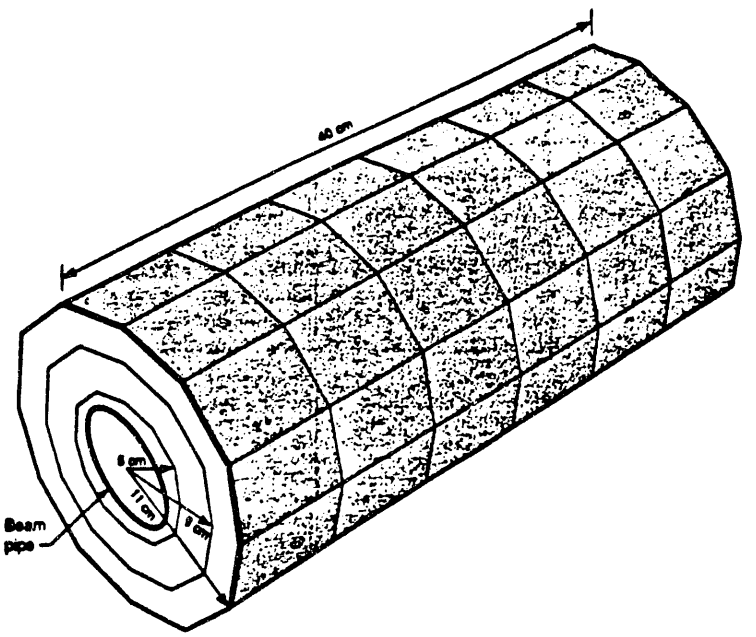

Fig.2 SVT layout used in the present simulations.

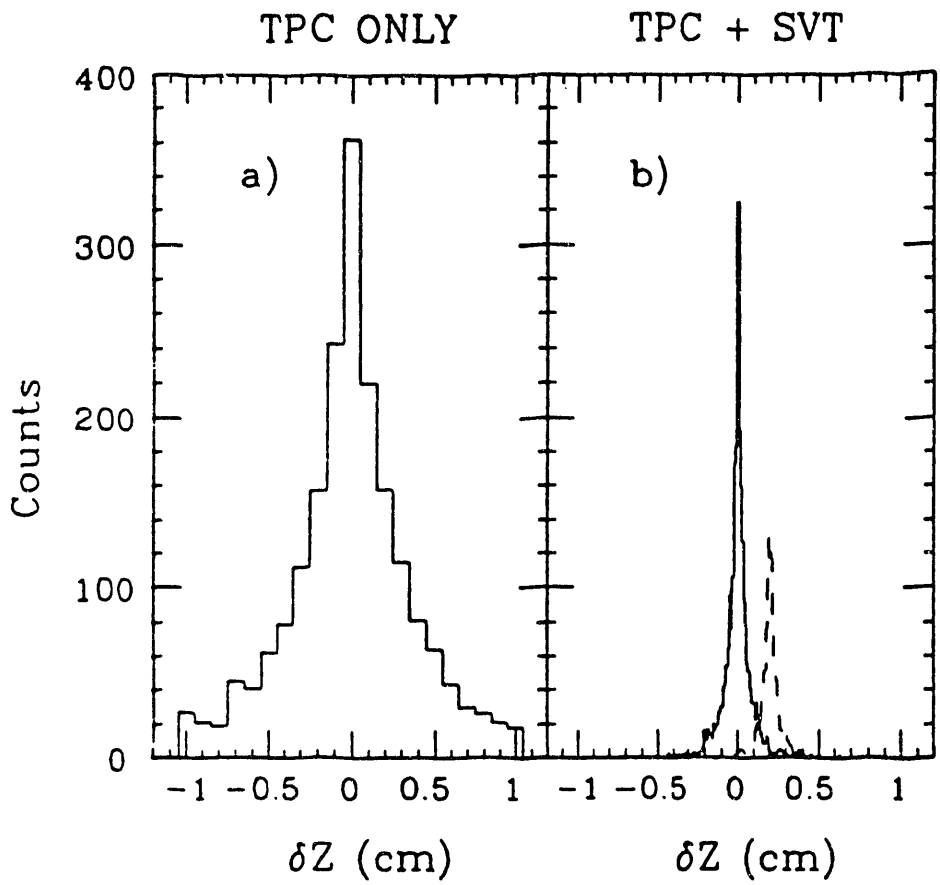

Fig.3 Primary vertex resolution (along beam direction) using: TPC tracking only (a) and TPC+ SVT tracking(b).

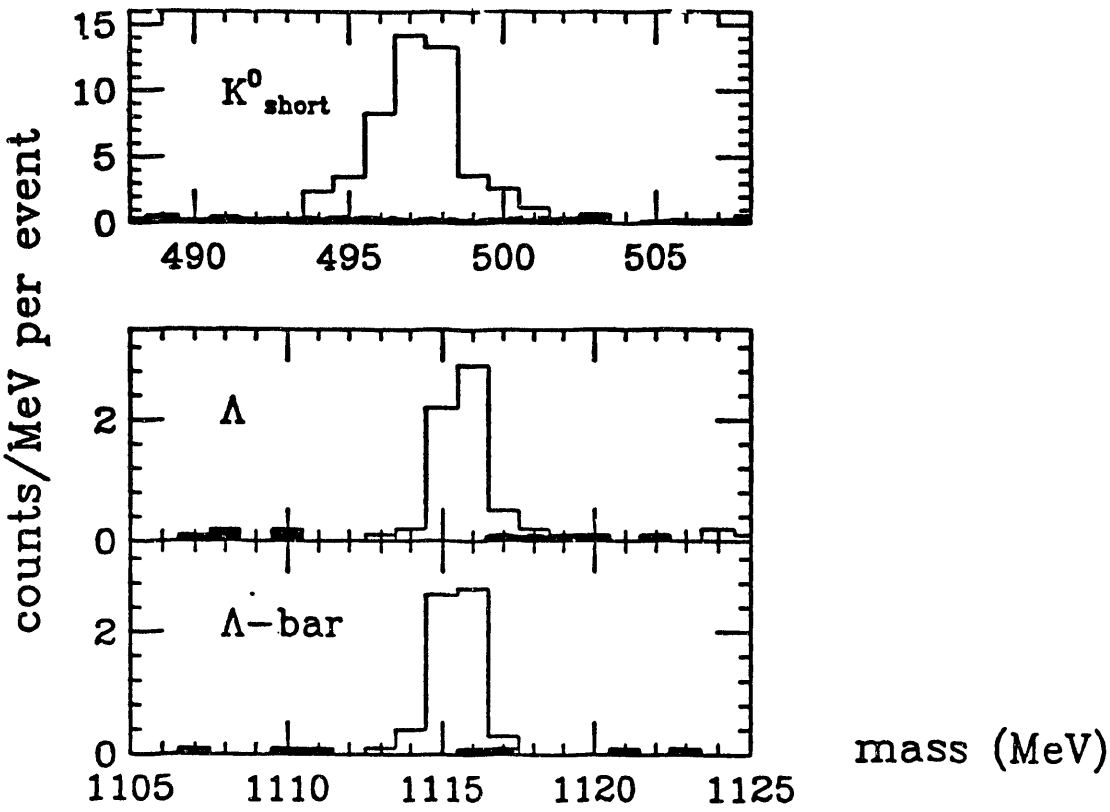

Fig.4 Invariant mass plots for Λ, $\bar{\Lambda}$ and K^0 reconstructed from 10 full FRITIOF/GEANT Au+Au events. Shaded areas represent the contribution from random background.

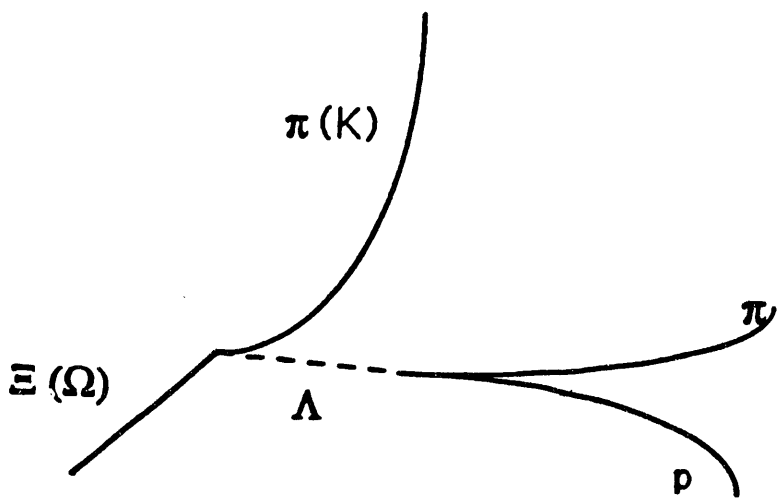

Fig.5 Topology for Ξ and Ω decays.

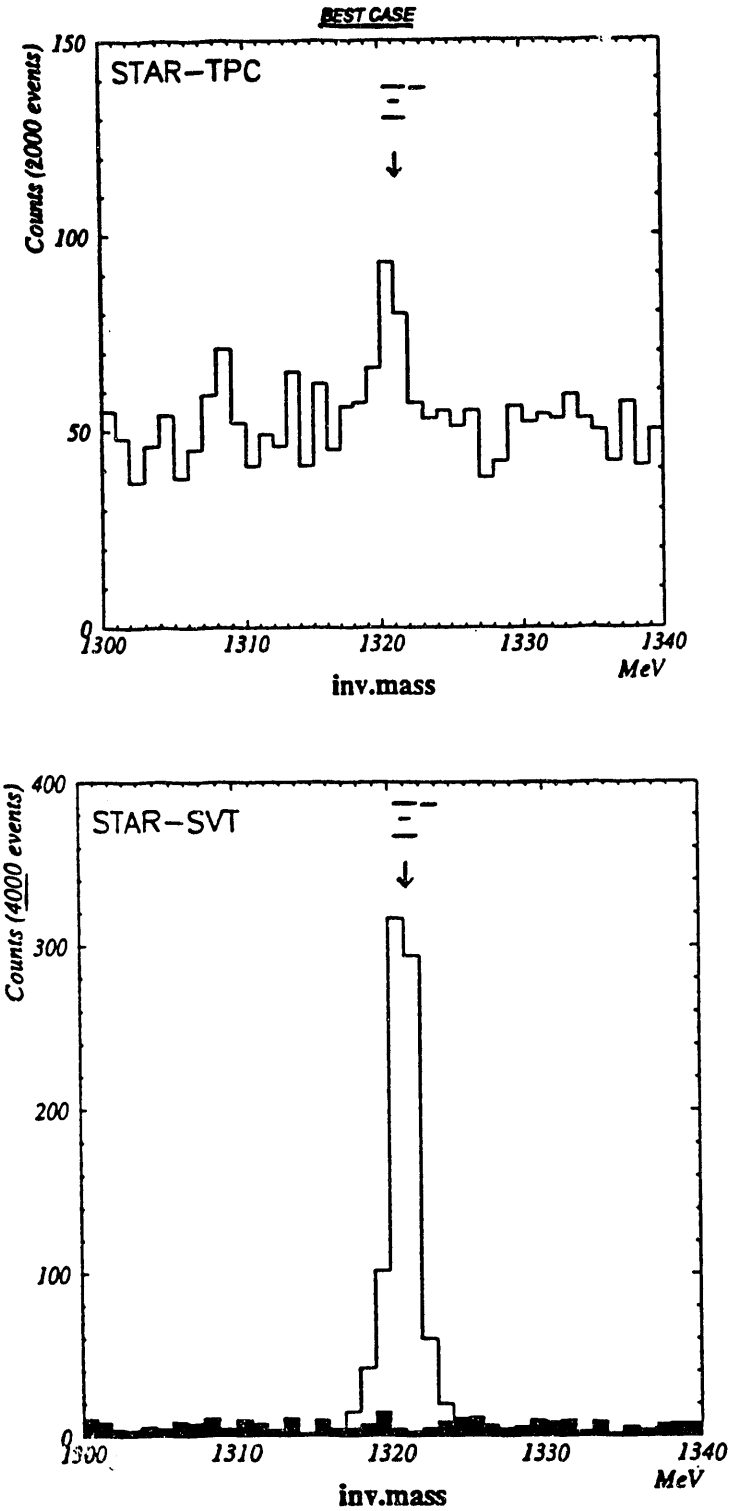

Fig.6 Invariant mass distributions ('ideal' case) for Ξ's reconstructed in STAR TPC (a) alone and TPC with the SVT (b). Shaded areas represent the contribution from random background.

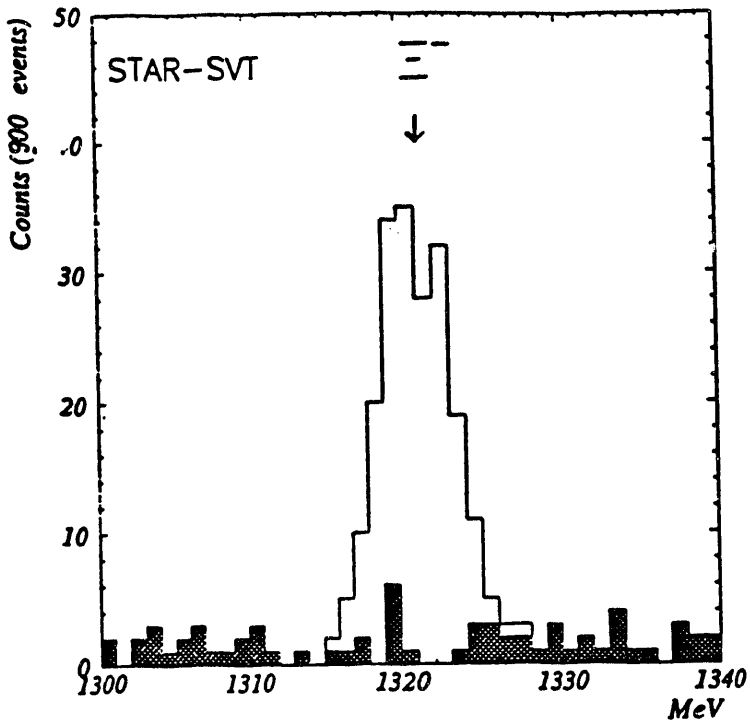

Fig.7 Invariant mass distribution of Ξ (TPC+SVT) with TPC momentum resolution taken to the account. Shaded areas represent the contribution from random background.

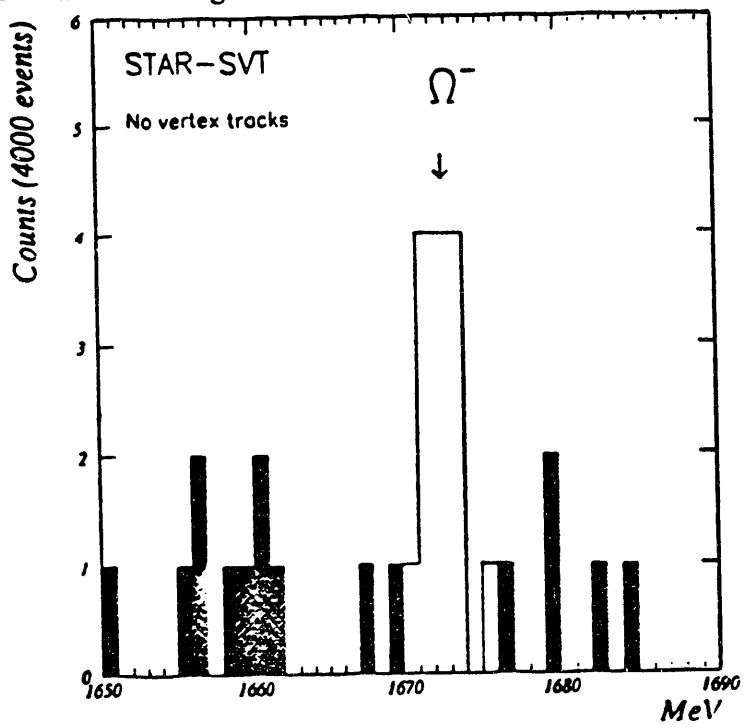

Fig.8 Invariant mass distribution of Ω reconstructed in STAR SVT and TPC. Shaded areas represent the contribution from random background.

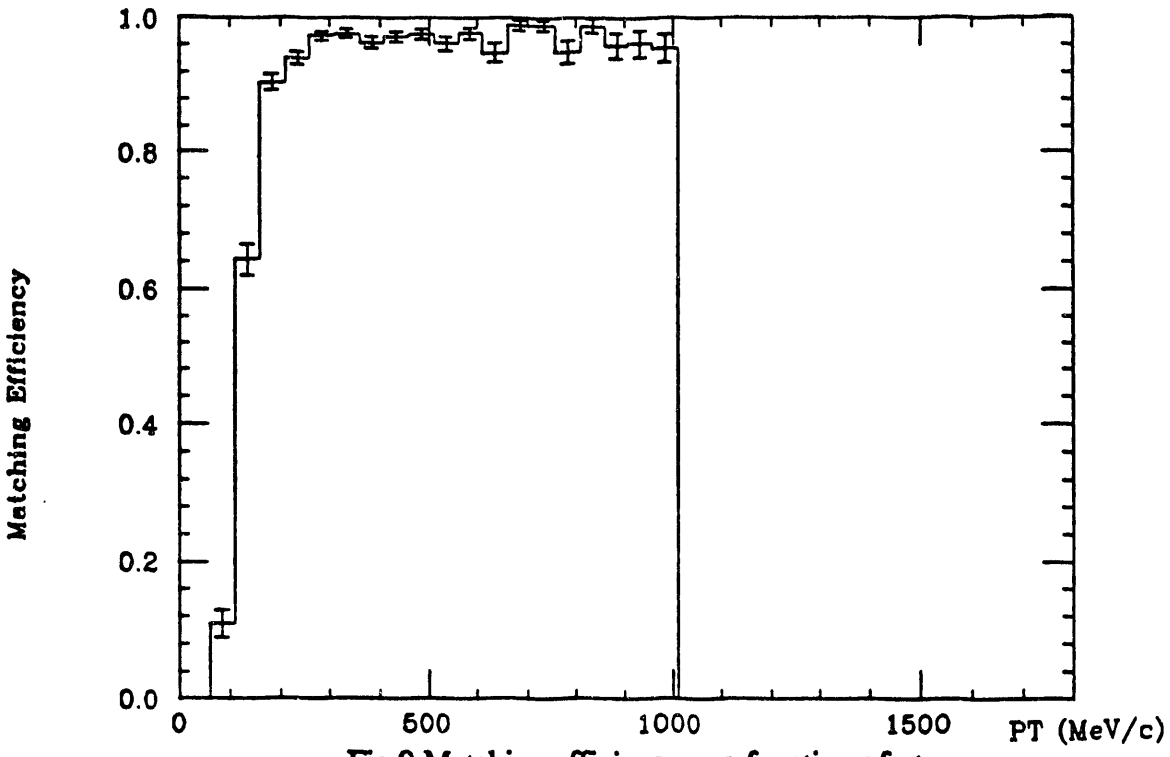

Fig.9 Matching efficiency as a function of pt.

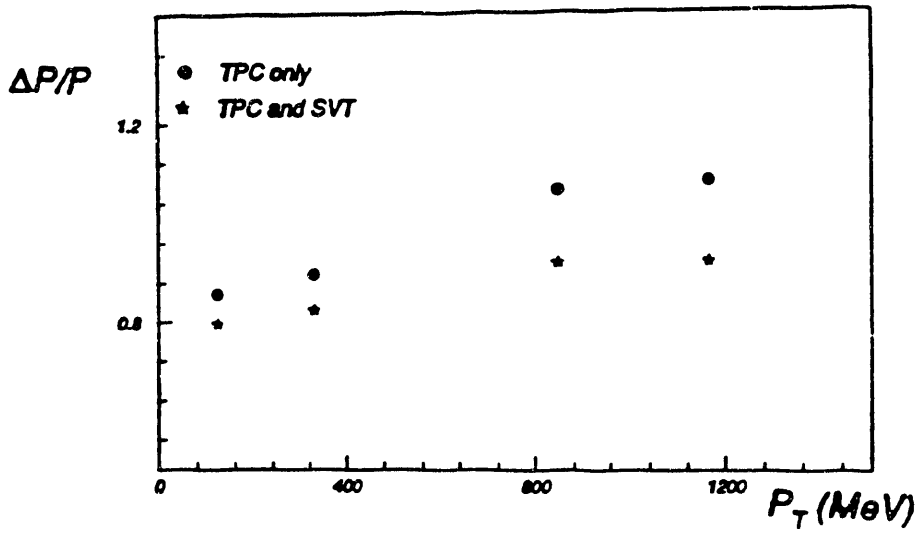

Fig.10 Momentum resolution for tracks reconstructed by TPC hits alone and by TPC hits and SVT hits. The same track sample has been used to derive these numbers.

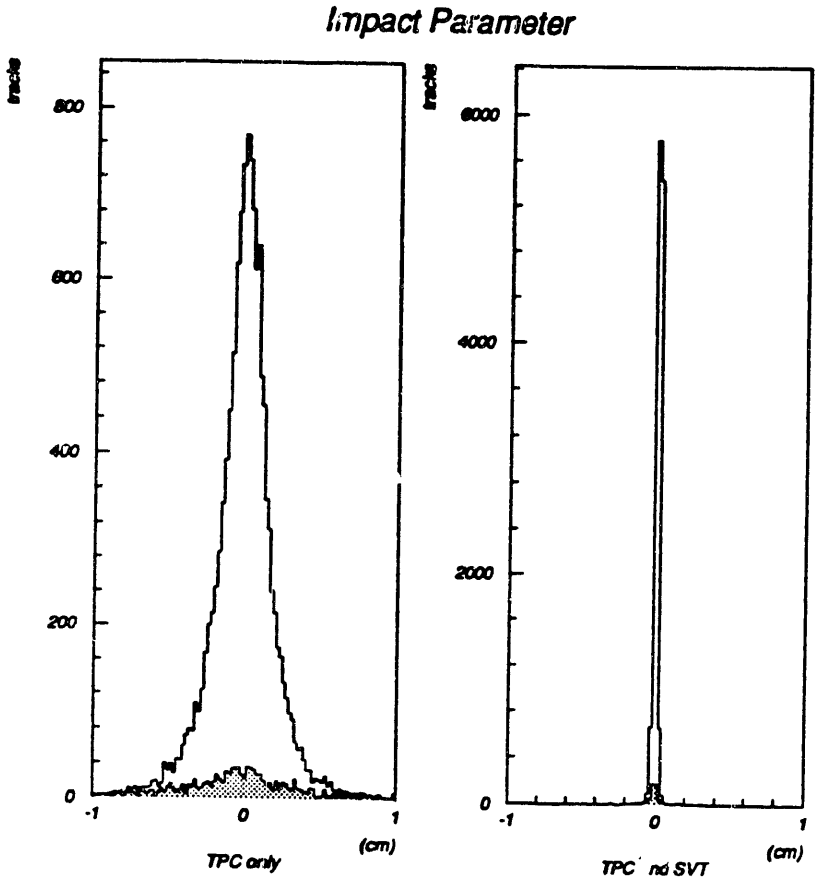

Fig.11 Impact parameter distribution of reconstructed primary tracks. For comparison the impact parameter distribution of secondary tracks is shown in the shaded area.

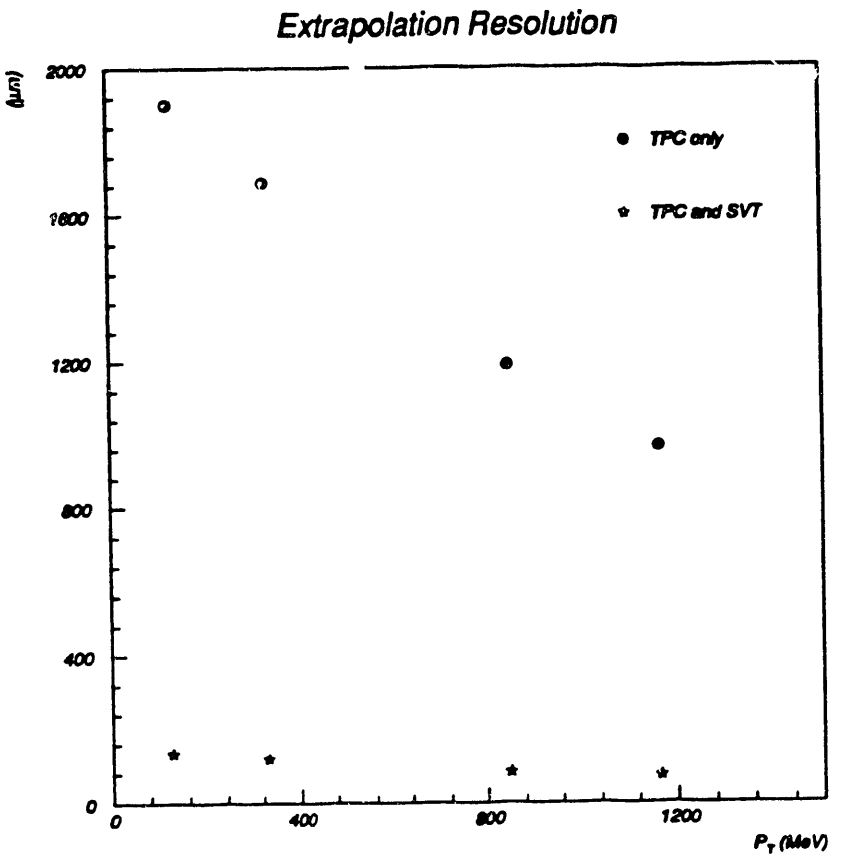

Fig.12 Extrapolation resolution to the vertex region for tracks reconstructed by TPC hits alone and by TPC hits and SVT hits. The same track sample has been used to derive these numbers.

CALORIMETER/ABSORBER OPTIMIZATION FOR A RHIC DIMUON EXPERIMENT (RD-10 PROJECT)

S. H. Aronson, M. J. Murtagh, M. Starks
Brookhaven National Laboratory, Upton, NY 11973

X. T. Liu, G. A. Petitt, Ziyang Zhang
Georgia State University, Atlanta, GA 30303

L. A. Ewell, J. C. Hill, F. K. Wohn
Iowa State University, Ames, IA 50011

J. B. Costales, M. N. Namboodiri, T. C. Sangster, J. H. Thomas
Lawrence Livermore National Laboratory, Livermore, CA 94550

A. Gavron, L. Waters
Los Alamos National Laboratory, Los Alamos, NM 87545

W. L. Kehoe, S. G. Steadman
Massachusetts Institute of Technology, Cambridge, MA 02139

T. C. Awes, F. E. Obenshain, S. Saini, G. R. Young
Oak Ridge National Laboratory, Oak Ridge, TN 37831-6372

J. Chang, S.-Y. Fung, J. H. Kang
University of California, Riverside, Riverside, CA 92521

J. Kreke, Xiaochun He, S. P. Sorensen
University of Tennessee, Knoxville, TN 37916-1200

E. C. Cornell, C. F. Maguire
Vanderbilt University, Nashville, TN 37235

ABSTRACT

The RD-10 R&D effort on calorimeter/absorber optimization for a RHIC experiment had an extended run in 1991 using the A2 test beam at the AGS. Measurements were made of the leakage of particles behind various model hadron calorimeters. Behavior of the calorimeter/absorber as a muon-identifier was studied. First comparisons of results from test measurements to calculated results using the GHEISHA code were made

INTRODUCTION

The RD-10 project was begun in late 1989 in order to study the properties of candidate hadron absorbers for a proposed dimuon/photon experiment at RHIC[1, 2]. The physics of interest at RHIC is rather "soft" compared to that normally studied at large hadron-hadron colliders. In particular, the invariant masses and rapidities of interest dictated that a novel approach involving relatively thin hadron absorbers be developed for measuring muon pairs in a collider geometry in order to maintain sufficient dynamic range and mass resolution in a RHIC dimuon experiment. Existing collider experiments typically have 6-10 interaction lengths of steel preceding any muon-tagging sections of the detector, thus restricting the muon measurements to transverse masses of 6-7 GeV/c^2 or higher. The softness of the spectrum of hadrons emitted at RHIC suggested using a much thinner hadron absorber. This could be of the order of 2-3 interaction lengths at y=0, increasing to 6 interaction lengths at y=3. This would be followed by the main tracking section of the experiment, which in turn would be followed by an active hadron absorber, or "muon-identifier", used to identify muons by their different behavior compared to that of hadrons upon penetration of 5 or more interaction lengths of steel or concrete.

Information is needed concerning the leakage of particles, particularly hadronic shower secondaries, through such thin hadron absorbers. Fixed target muon experiments typically use much thicker absorbers and deal with incident particle momenta 10-100 times higher. Little information is available, and none below 4 GeV/c. Information is also needed about the behavior of the final-stage "muon-identifier" of the experiment, as data on this are also not readily available. It was realized that by using a hadron absorber that was constructed as a calorimeter, both sets of information could be obtained together using the 1-10 GeV/c particles available in the A2 test beam of the AGS. As an added benefit, the behavior of the absorber as a calorimeter could be studied, adding to the knowledge of hadron behavior in different types of hadron calorimeters.

The resulting information can be used to benchmark hadron-shower codes such as GHEISHA or LAHET at energies below 10 GeV. It is further expected that this information will be used in the near future in designing the PHOENIX experiment for RHIC.

The following sections describe the layout of the test apparatus on the A2 line, preliminary results concerning particle leakage as a function of calorimeter/absorber thickness and composition and as a function of incident particle momentum and type, and the behavior of one particular arrangement of the calorimeter/absorber as a muon-identifier.

DESCRIPTION OF THE RD-10 SETUP

The method used in RD-10 to make the above-mentioned measurements is to install an active calorimeter/absorber (hereinafter called the "calorimeter") downstream of a number of beam defining elements. The calorimeter is followed by two x-y hodoscopes for particle tagging and triggering. These hodoscopes sandwich a set of tracking chambers used for trajectory measurement as well as counting the number of hits that would be seen in a wire chamber. Downstream steel and concrete walls followed by additional hodoscopes serve to tag penetrating

particles, including muons. The settings of the beam-line magnets and collimators in A2 are used to select momentum and polarity of the incident particles.

The general layout of RD-10 on the A2 line is shown in Fig. 1. The counters

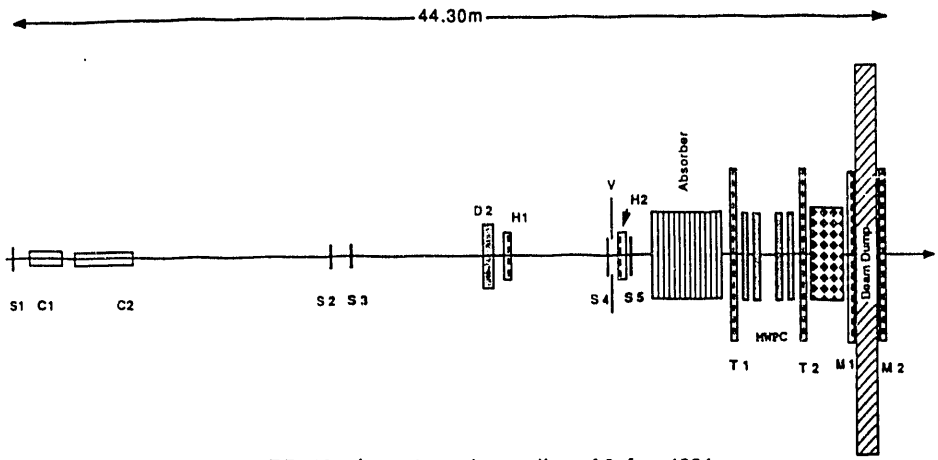

Figure 1: Layout of RD-10 experiment on A2 beam-line at the AGS.

marked S1 through S5 are single-element timing scintillators used to define the accepted beam envelope and provide π/p discrimination via time of flight. They also serve to select only those particles traversing the hole in the center of the 1-meter-long lead collimator used by other experiments sharing the A2 beam line and located between S2 and S3. This is essential in order to provide a beam of reasonable transverse dimensions by the time the downstream end of A2 is reached. The A2 beam-line magnetic elements include only a single quadrupole doublet, which precedes the single dipole on the line. All these magnets are upstream of the S1 counter and do not appear on Fig. 1. These quads serve to define a central momentum and momentum "bite" at the horizontal collimator following the dipole. However, the beam has no further magnetic focussing elements and can be limited in spatial extent only by use of three further collimators. One each is located just before and after the shield wall at the entrance to the A2 zone. The third is located just upstream of the tracking RICH of Nemethy et al. This last collimator has a square aperture of roughly 1.8 cm x 1.8 cm opening and serves to recollimate the beam seen by downstream experiments. This is necessary because the beam has grown to a transverse size of σ=15 cm by the entrance to this collimator. Even with this collimator, the beam has a transverse size of σ=2.5 cm by the time it reaches S5 in the RD-10 setup.

The C1 and C2 counters are gas-filled Cerenkov counters used to tag electrons and pions. Typically C1 was operated with a few atmosphere of Freon-12 to provide π/p separation at the momentum selected, and C2 was operated with N_2 at 1 atmosphere or less to provide e/π separation. H1 and H2 are finger hodoscopes made of plastic scintillator. They consist of an x- and y-plane each, with 10 fingers per plane in H1 and 16 per plane in H2. The slats are 10 mm wide, and neighboring slats are overlapped by 1 mm to give good efficiency. The incident direction of a given beam particle can be determined to 3 mrad. These hodoscopes,

together with S1 through S5, are used to guard against multiple particles incident simultaneously on the calorimeter.

The calorimeter layout is shown in Fig. 2. It consists of a number of planar

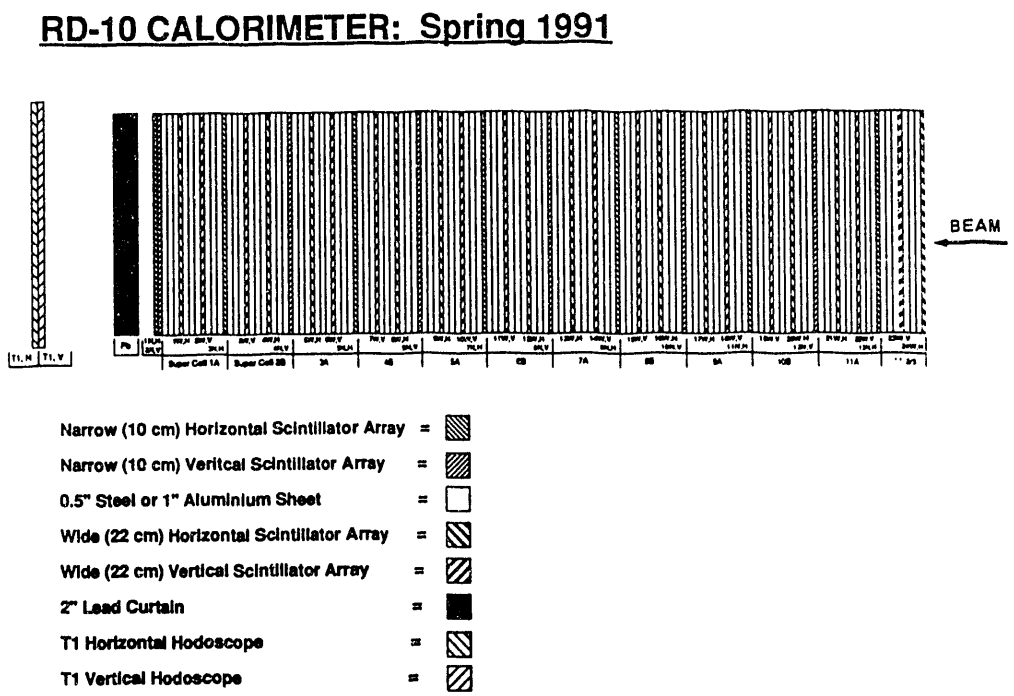

Figure 2: Detailed layout of the calorimeter in the RD-10 experiment.

"supercells" placed on edge on a steel framework so that they are perpendicular to and centered about the nominal beam centerline. Each supercell is comprised of 3 alternating layers of metal and scintillator. The overall calorimeter thickness is varied by installing different numbers of supercells. A variable-position press with a lead-screw is used to keep the entire calorimeter under compression. This provides mechanical stability and ensures that no dead spaces occur between metal and scintillator layers. The calorimeter composition is varied by changing the metal used in the supercells. The metal layers are made of either 3 sheets of 120 cm x 120 cm x 1.27 cm thick steel sheet or 3 layers of 120 cm x 120 cm x 2.54 cm thick aluminum sheet, so that a supercell includes a total of 9 metal plates. The scintillator layers are of two types. Both are 120 cm x 110 cm x 1 cm thick in size and are called "arrays." The "narrow-slat" type is comprised of 11 scintillator (Polycast type PS15A) "slats" of 120 cm x 10 cm x 1 cm thickness which are read out on each end using Amperex S2212A photomultiplier tubes previously used in E734. The "wide-slat" type is comprised of 5 scintillator slats of size 120 cm x 22 cm x 1 cm thickness which are read out on each end using PMTs previously used in either E734 (Amperex S2212A) or in E845 (RCA 8575). The slat arrays alternate between vertical and horizontal in their orientation perpendicular to the beam axis. The metal thicknesses were chosen so that both types of supercell, the "steel" type and the "aluminum" type, would be about the same number of interaction lengths thick while using readily available plate thicknesses. The steel supercells are 0.72 λ thick and the aluminum supercells are 0.62 λ thick.

The PMTs are connected via 70 meter long RG58 delay cables to LeCroy Model 1882 FASTBUS ADCs. A charge-integration gate of 75ns has been found to be adequate for strobing these ADCs.

One plan of the RHIC Dimuon/Photon experiment was to use a hadron absorber of very low average Z in order to minimize the multiple scattering per unit interaction length experienced by muons traversing it and also to minimize the low-momentum "tail" due to energy loss straggling of the muons. Both problems are exacerbated by using high-Z materials. The use of a low-Z material to alleviate these problems leads to a new problem, namely that primary electromagnetic radiation (such as π^0 decay photons) and the electromagnetic components of hadron showers are not absorbed efficiently in thin low-Z hadron absorbers because the radiation length, X_0, is a large fraction of the hadronic interaction length, λ. The ratio X_0/λ is 1/33 for uranium and 1/10 for copper but only 1/4 for aluminum and nearly 1 for beryllium. To counteract this, a 10-15 X_0 thick lead shield was proposed to surround the outside of the absorber in the Dimuon/Photon experiment. This is modelled in the RD-10 setup by a pair of 5 cm thick (9.1 X_0) lead shutters which are 120 cm square and can be installed or removed separately at a position just downstream of the calorimeter. The lead shutters are expected, based on EGS and GEANT simulations, to remove over 98% of the electromagnetic radiation present at the exit of the calorimeter. This is particularly valuable in removing few MeV electrons, which serve only to contribute to the background in the tracking chambers.

Four x-y hodoscope stations are installed downstream of the calorimeter. These are marked T1, T2, M1 and M2 in Fig. 1. The first two, T1 and T2, are installed just before and after the tracking chambers. T1 is located 40-cm downstream of the end of the calorimeter and consists of 15 each x and y scintillator slats of dimensions 8 cm x 120 cm x 1 cm thick. These are read out on one end using a single PMT. T2 is located 2.5 meters downstream of T1. It consists of 24 vertical slats of the same construction as in T1. It has 30 horizontal slats arranged in two groups of 15. These abut in the center of T2, on the ends which do not have PMTs. The active area of T2 is rectangular, 120 cm tall and 240 cm wide. These hodoscopes are used to determine an initial estimate of the multiplicity of leakage particles, to define roads for the tracking chambers, and to form the primary on-line "leakage" trigger for the experiment. This leakage trigger consists simply of "or" circuits firing on any hit in T1 and/or T2.

The last two hodoscopes, M1 and M2, are used to tag penetrating particles. M1 is similar to T1, being an x-y scintillator hodoscope that is 12 x 12 slats in area. It is located behind 20 cm ($\approx$ 1.2 λ) of steel; this corresponds to $\approx$250 MeV kinetic energy loss for minimum ionizing particles, meaning M1 does not tag the very soft components of leakage from the calorimeter. M2 consists of a single layer of 9 slats of 100 cm x 20 cm x 5 cm thick scintillator read out on each end by PMTs. All the slats in M2 are oriented horizontally. M2 is located behind the A2 area beam dump. This dump consists of 1 meter of steel followed by 1 meter of shielding concrete blocks. M2 thus only sees particles of $\geq$3-4 GeV (depending on the thickness of the calorimeter for that particular run). Its main function is to tag penetrating muons which are used to check basic operation of the setup and to serve as a calibration of the multiple scattering induced by the calorimeter.

Four stations of wire chambers are located between T1 and T2. Two stations are placed near T1 and two near T2. Each station consists of 4 planes of drift chamber organized in an x-x′-y-y′ pattern. These chambers plus preamplifiers and discriminator cards were recuperated from E780/845. In order to reduce the number of TDCs required for their readout, the anode wire spacing was increased from the original 3 mm to 9 mm by removing the appropriate 2/3 of the anode and field wires from the anode planes. Cathode planes were not altered. The chambers were read out into LeCroy FASTBUS type 1879 multihit pipeline TDCs. The chambers' function is to give a measure of the number of particles exiting the calorimeter which would cause a tracking chamber to fire, and to measure the direction cosines and trajectory of the observed leakage particles. This latter function is used to determine the number of exiting particles which would be accepted by an angle/vertex cut designed to allow for multiple scattering of muons but reject the wider-angle secondaries characteristic of hadronic showers.

The setup was operated with 3,5,7,9 and 11 "aluminum" supercells (the "aluminum calorimeter setup"), 3,5,7 and 9 "steel" supercells (the "steel calorimeter setup"), and one special "mixed" arrangement consisting of 4 upstream aluminum supercells and 5 downstream steel supercells (the "mixed calorimeter setup"). The first arrangements (aluminum calorimeter) modelled the barrel region of the proposed RHIC Dimuon/Photon experiment, the steel calorimeter gave a point of contact to data in the literature, which tend to be dominated by measurements made with steel calorimeters, and the mixed calorimeter was used to simulate the proposed forward hadron absorber for the RHIC Dimuon/Photon experiment. Data were taken for all these setups with 0 and with 2 lead shutters in place; data were also recorded for a subset of the setups with one lead shutter in place. Positive beams of 1 - 7 GeV/c were used. The flight path from the "A" production target to the RD-10 setup is sufficiently long that typically more than 20% of pions decay. Therefore, positive beams were chosen in order to measure results for protons incident in order to have at least one type of incident hadron not subject to muon contamination.

Four principal triggers were employed. The first was a "raw beam" trigger, requiring a time overlap of hits in all start counters plus at least one particle seen in each of the four beam hodoscope planes. This trigger was used for calorimeter studies, muon-ID studies and overall normalization checks for the leakage studies. The second, "leakage" trigger required at least one slat in T1 or T2 to fire. This trigger was used for the bulk of the running. The third trigger required one slat in M1 or M2 to fire and was used to tag a sample of muon events. It was usually run in parallel with the leakage trigger. The fourth trigger, operated out of spill, was a pulser trigger used to monitor pedestals and noise problems. Other specialized triggers included electron triggers, requiring C2 to fire, to study the (e/h) response of the calorimeter.

The data acquisition system consisted of a DEC microVAX-II responsible for run control, overall data collection, readout of FASTBUS, recording to 6250 bpi magnetic tape, and distribution to analysis stations. Data in CAMAC crates were read out by local PDP11 processors which transferred data to the microVAX-II via Ethernet links. Typical events include a total of 1900 ADC, TDC and other parameters. No zero suppression was done. The event length varied due to the variable number of hits recorded in the FASTBUS TDC system used to read out

the drift chambers. On-line spectrum generation was done on a VAXstation 2000 connected to the microVAX-II via Ethernet. Event packets were transmitted to it by the microVAX-II and analyzed on a time-available basis. The on-line software served as a kernel for the offline analysis package. Results presented here were obtained using the offline software analysis routines.

Typical runs involved recording of 1-2 x 10^4 triggers onto magnetic tape. The usual running sequence can be described as a set of 5 nested loops, which in order were :

1. vary the calorimeter composition ("outer loop")
2. vary the calorimeter thickness
3. vary the lead shutter position
4. vary the beam momentum
5. vary the trigger switch settings ("inner loop")

Data for a given calorimeter composition were typically collected over a period of three weeks of A2 running. A total of some 460 runs were recorded on tape.

RESULTS ON PARTICLE LEAKAGE BEHIND THE CALORIMETER

The Updated Letter of Intent (ULOI) for the proposed RHIC Dimuon/Photon experiment noted that the flux of charged particles emitted in central Au+Au collisions at $\sqrt{(s)} = 200 \cdot A$ GeV must be reduced by a factor of 30-40 at y=0 and a factor of 100 at y=3 in order to satisfy desired occupancy levels of 5% or less in the main tracking chamber sections. The initial photons emitted are removed by 12 radiation lengths of Al_2O_3 (alumina) followed by 18 radiation lengths of Pb at y=0, and by 12 radiation lengths of Al_2O_3 followed by 30 radiation lengths of steel and then by 18 radiation lengths of Pb at y=3, so they cause no problem. The 18 radiation length thick lead cap is also needed to damp out "secondary" photons resulting from π^0 and other mesons created in hadron showers as well as to absorb soft e^+ and e^- exiting the alumina and steel.

The charged particles emitted at y=0 are quite soft and are largely removed by dE/dx energy loss in the inner absorber (that is, they tend to stop.) One absorption length corresponds to 150-220 MeV kinetic energy loss for a minimum-ionizing particle, and this of course increases as $1/\beta^2$ for slower particles. Approximately 80% of the particles emitted at y=0 thus *stop* due to dE/dx through the 3.5 λ of material at y=0. Most of the remaining particles react ("shower" is too strong a word for particles of 0.5 GeV kinetic energy), resulting in soft secondaries that also stop. The few particles above 1 GeV start to make well-developed showers and are responsible for much of the secondaries and particle leakage that would be observed. The result of such considerations is that one needs to reduce the leakage from incident particles above 1 GeV/c by a factor of 6 in order to reach the goal in the Dimuon/Photon ULOI of removing $\geq$ 97% of the primary charged particles at y=0. One primary analysis is then the study of the number and distribution of leakage particles as a function of incident momentum and calorimeter thickness.

An example of the distribution of leakage particles observed behind a thin aluminum calorimeter is shown in Fig. 3. The distribution of the number of

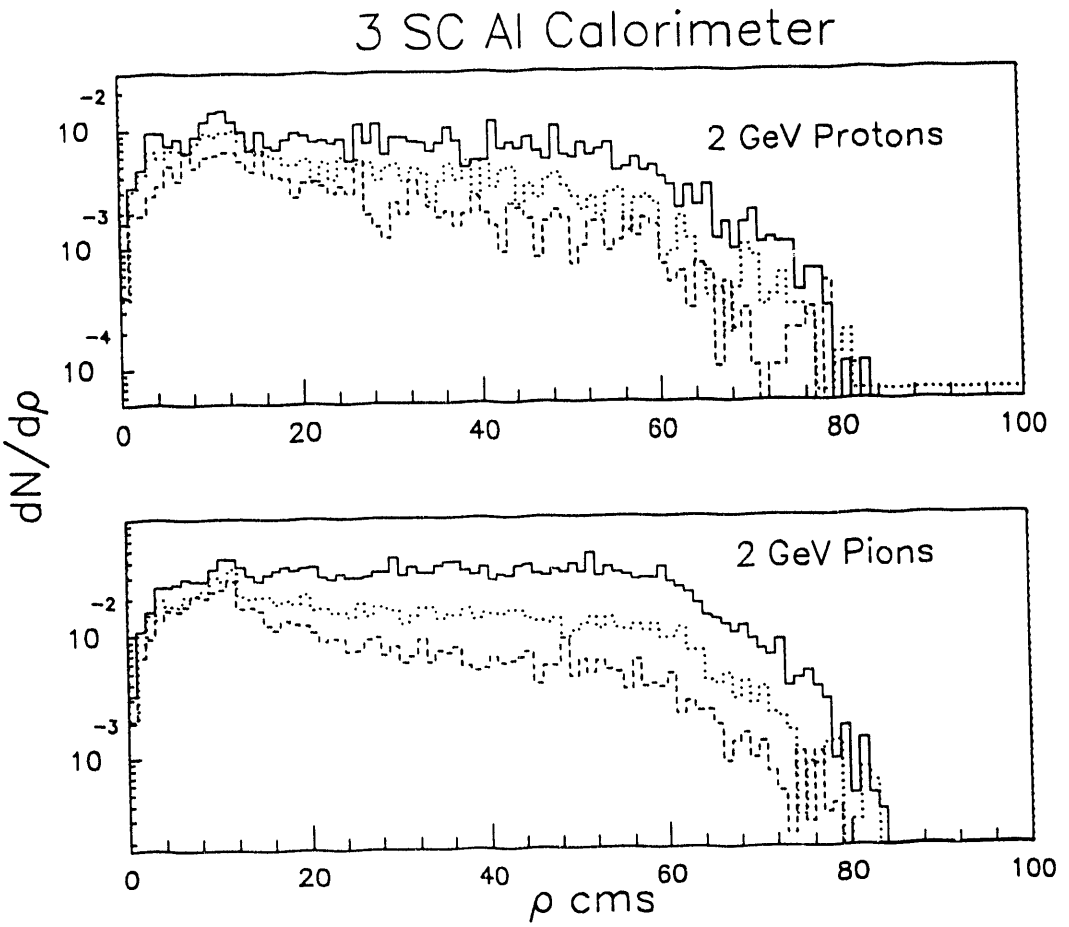

Figure 3: Distribution of $dN/d\rho$ vs. ρ for 2.0 GeV/c protons and π^+s incident on a 3 supercell aluminum calorimeter, for the three possible lead shutter configurations. The lead shutter can be 0,9, or 18 radiation lengths thick, corresponding to 0 (solid line), 1 (light dashed line) or 2 (heavy dashed line) layers being "in."

particles per unit transverse radius ρ is shown as a function of ρ for 2 GeV/c protons and π^+s incident on a 3 supercell (2 λ) thick aluminum calorimeter for 0,1, and 2 layers of lead (corresponding to 0,9 and 18 radiation lengths of lead) following the calorimeter. The lead shutter is seen to cause a factor of 5 or more reduction of leakage at large values of ρ for the π^+ and more than a factor of 3 at all values of ρ for the protons.

The small ρ region for the pions will be contaminated with muons. Separation of these muons from the pions is discussed in the following section where the operation of the calorimeter as a muon-identifier is discussed. In future rounds of the analysis, we will implement an algorithm based on the muon-identifier type analysis in order to tag probable muon events and remove them from the class of pion events considered for the leakage analysis. The proton identification is quite clean at these momenta, meaning the protons can be used as a control for this procedure.

The distribution in exit polar angle of the leakage particles observed behind the 3 supercell aluminum calorimeter is shown in Fig. 4, for 1.5 GeV/c protons and π^+ incident, and for 0,1 and 2 lead layers present. Angles were determined using the T1 hodoscope data. This distribution is found to be rather broad.

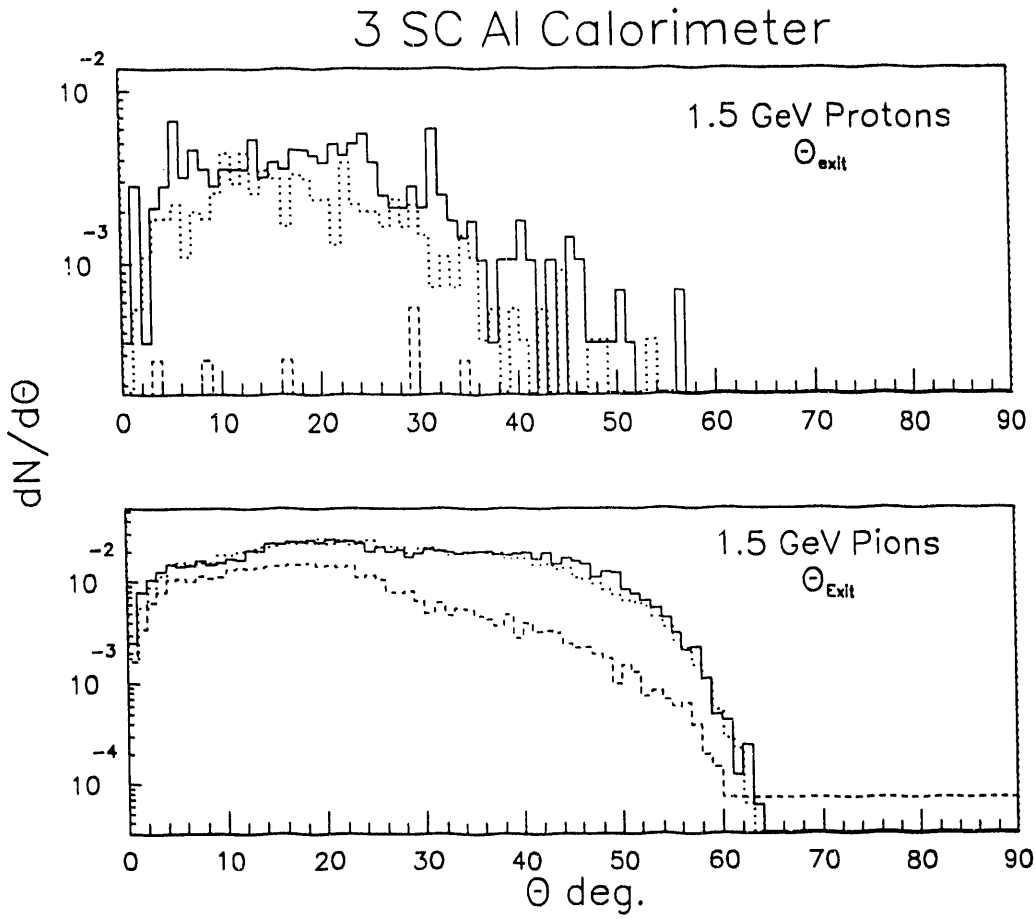

Figure 4: Distribution of charged particles as a function of polar angle, $dN/d\theta$, vs. polar angle θ_{exit}, for 1.5 GeV/c protons and π^+s incident on the 3 supercell aluminum calorimeter, for 0,1, and 2 lead shutters "in." (Symbols as in the previous figure.)

This is what is hoped for, because a strong cut to discriminate against leakage from incident hadrons is an exit-angle cut that allows for 2 or 3 sigma of the multiple-scattering that would be experienced by a muon. For comparison, the rms scattering angle for a 1.5 GeV/c muon incident on 3 supercell (2 λ) aluminum calorimeter is 1.9°, making allowance for the $\approx$ 350 MeV energy loss experienced by the muon during traversal of the calorimeter. (Note, however, that the slats at T1 subtend $\approx \pm 6°$ relative to the calorimeter downstream end.)

The multiplicity of exiting particles in a single event is also a key parameter of interest, as a large number of particles confuses and overloads the tracking section. One wants to be in a situation where the mean exit multiplicity is quite low (preferably zero!). The multiplicity of leakage particles for the 3 supercell aluminum calorimeter with no lead and 1.5 GeV/c protons and π^+s incident is

shown in Fig. 5. The multiplicity is plotted as the product of the number of

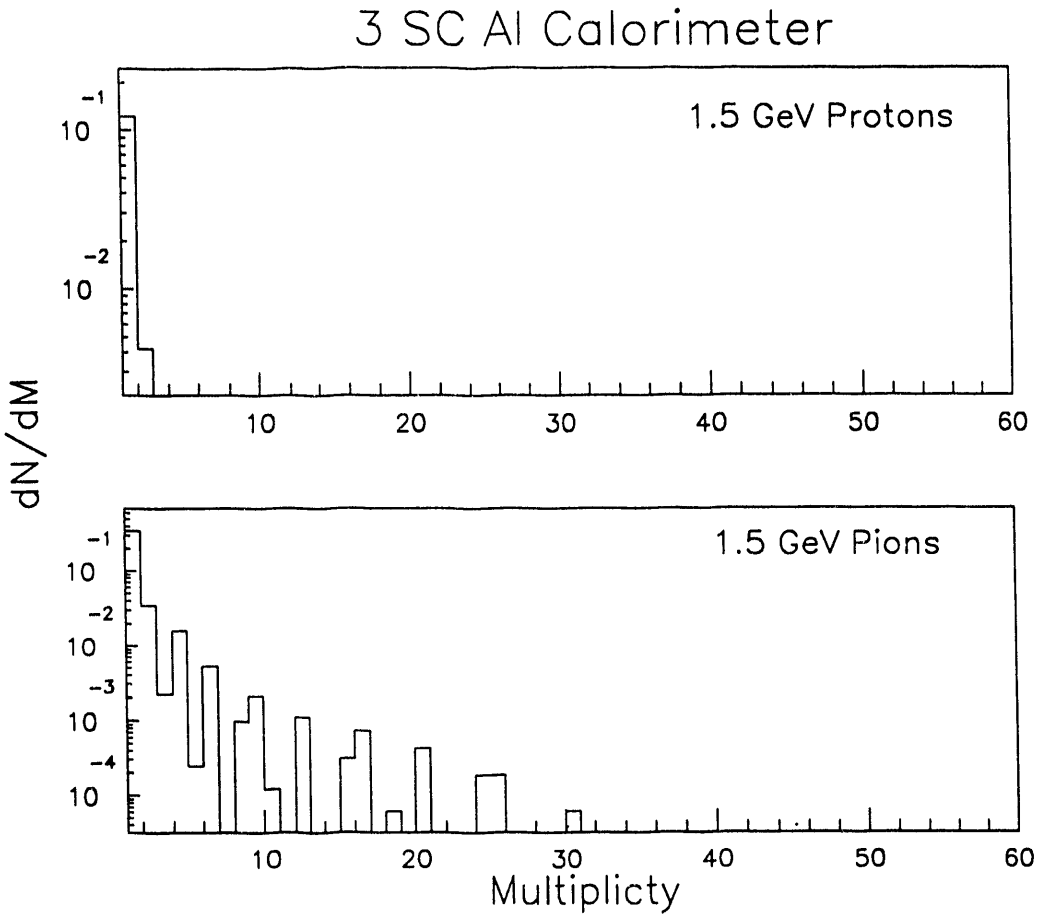

Figure 5: Multiplicity of exiting particles for 1.5 GeV/c protons and π^+s incident on the 3 supercell aluminum calorimeter with no lead in place. The multiplicity is expressed as the product of the number of "fired" vertical and horizontal slats, $N_H \times N_V$, in hodoscope T1.

"fired" horizontal slats in the T1 hodoscope times the number of fired vertical slats in that same hodoscope, denoted as $N_H \times N_V$. The proton data are almost entirely at a value of $N_H \times N_V$ of 1x1, while the π^+ data show a strong peak at that value but with (much) smaller peaks at 2x2, 3x3, 4x4, and 5x5. A few other combinations, such as 2x3 = 6 appear, signaling either inefficiency of a slat or two particles traversing the same slat in one dimension.

Preliminary results of a set of calculations using the GEANT 3.13 Monte Carlo code (with the GHEISHA hadron-shower interface) are presented in Fig. 6 through Fig. 11. Fig. 6 shows calculated distributions of $dN/d\rho$ for all charged particles exiting the calorimeter and with various thicknesses of lead installed. In this case these distributions are given for the positions of the T1, T2, M1 and M2 hodoscopes. These calculations were done for the 3 supercell steel calorimeter and for 2 GeV/c π^+s incident.

Fig. 7 shows calculated distributions, again expressed as $dN/d\rho$ (also called dN/dR) for all charged particles exiting the calorimeter and reaching T1 for the

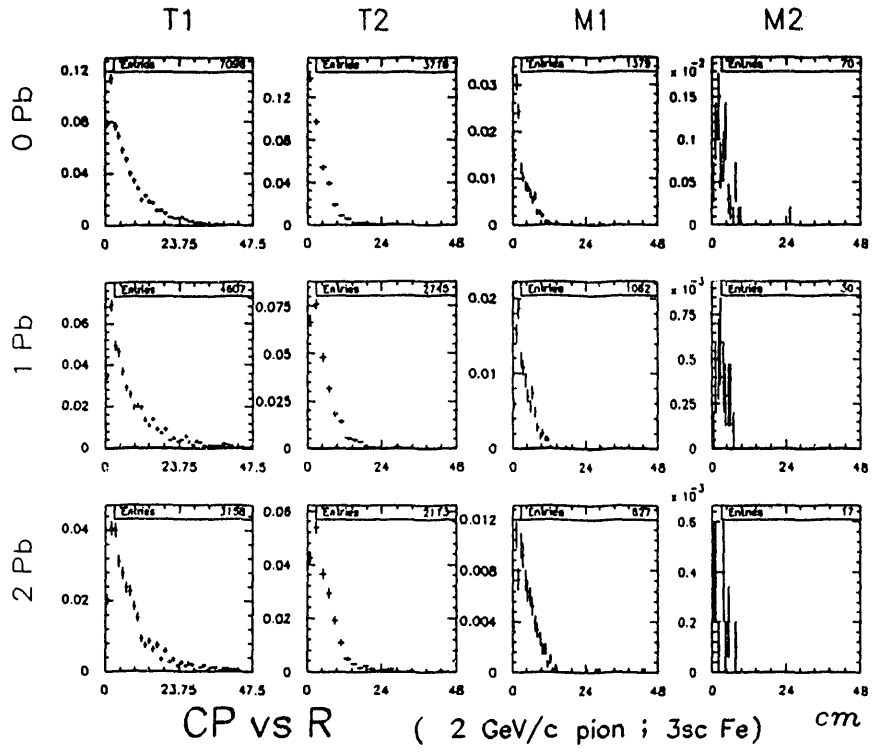

Figure 6: Results of preliminary GEANT 3.13 calculations for the number of charged particles observed per unit transverse radius, dN/dR (here $\rho \equiv$ R.) The distributions seen by the T1, T2, M1 and M2 hodoscopes are shown for the case of 2 GeV/c π^+ incident on a 3 supercell steel calorimeter, for 0,1 and 2 lead layers "in."

case of 2 GeV/c protons and π^+s incident on the 3 supercell aluminum calorimeter. We take advantage of the fact that a Monte Carlo code is being used to

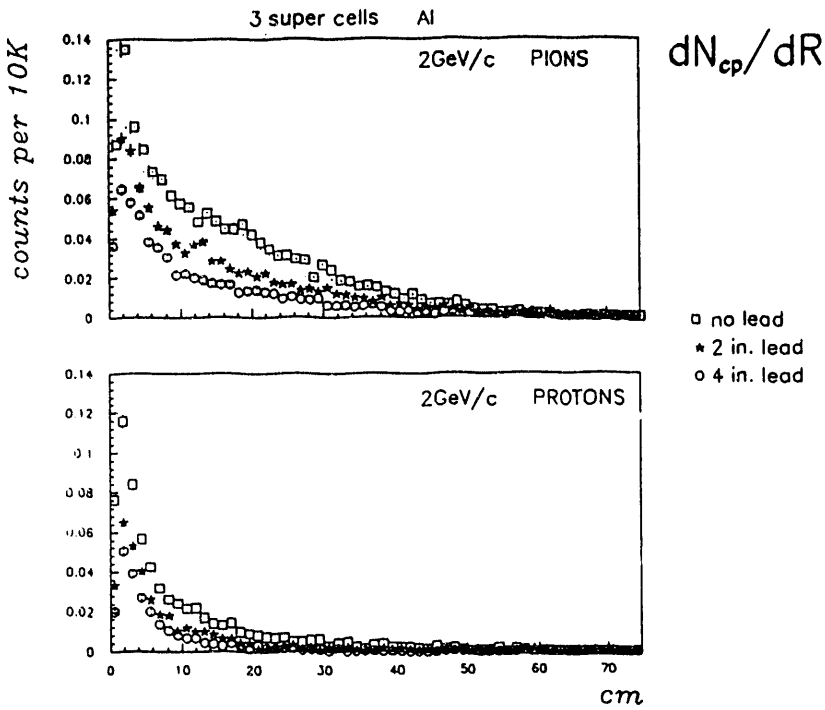

Figure 7: Preliminary results of GEANT 3.13 calculations of dN/dR for all charged particles reaching T1 for 2 GeV/c protons and π^+s incident on a 3 supercell aluminum calorimeter, for 0 (squares), 1 (stars), and 2 (circles) lead layers "in", for 10,000 events.

determine the distributions in order to calculate not only the distribution at T1 for all charged particles exiting (Fig. 7) but also for exiting electrons (Fig. 8), protons (Fig. 9), muons (Fig. 10) and pions (Fig. 11). We note that muon and pion distributions only show significant activity for π^+s incident and the proton distributions only show significant activity for protons incident. The large peak near R=2-4 cm in Figs. 9, 10, and 11 appears to be a leading particle effect. It is also seen that only the electrons are affected in any major way by the lead, as expected, and that they account for 40% of the leakage in the case of π^+s incident but only 10% or so for protons incident.

We caution that all these results are preliminary. The cuts and normalizations used for the data analysis are evolving. The Monte Carlo results need to be "smeared" to account for the finite sizes of the hodoscope slats. Both these efforts are continuing and need to progress further before meaningful comparisons of results of the data analysis and the Monte Carlo calculations can be made.

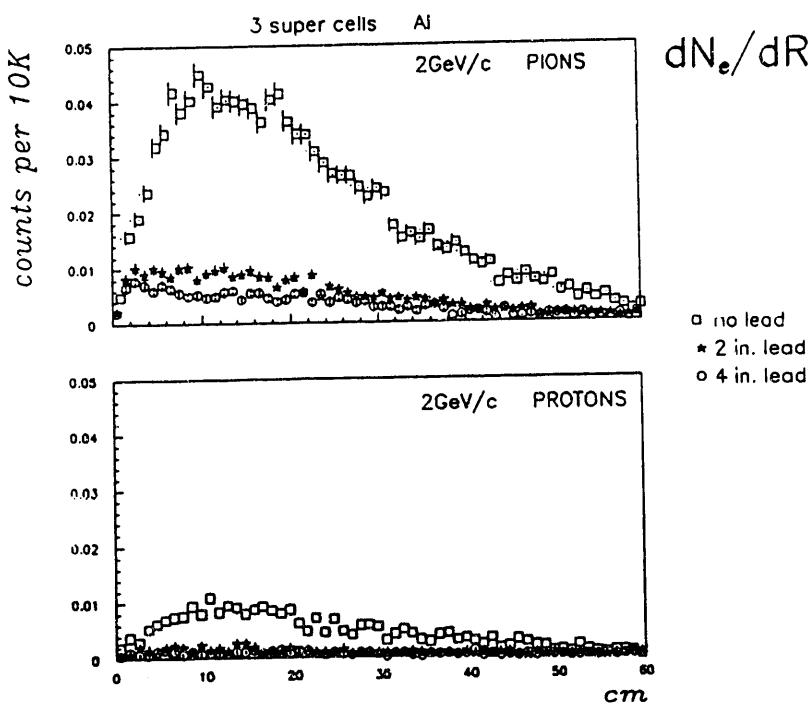

Figure 8: Preliminary results of GEANT 3.13 calculations of dN/dR for electrons and positrons reaching T1 for 2 GeV/c protons and π^+s incident on a 3 supercell aluminum calorimeter, for 0 (squares), 1 (stars), and 2 (circles) lead layers "in", for 10,000 events.

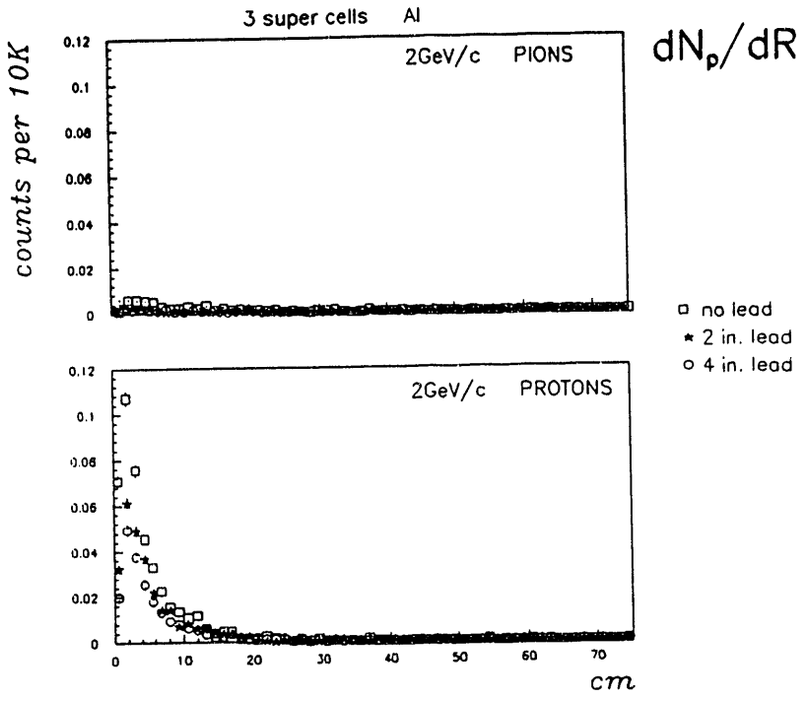

Figure 9: Preliminary results of GEANT 3.13 calculations of dN/dR for protons reaching T1 for 2 GeV/c protons and π^+s incident on a 3 supercell aluminum calorimeter, for 0 (squares), 1 (stars), and 2 (circles) lead layers "in", for 10,000 events.

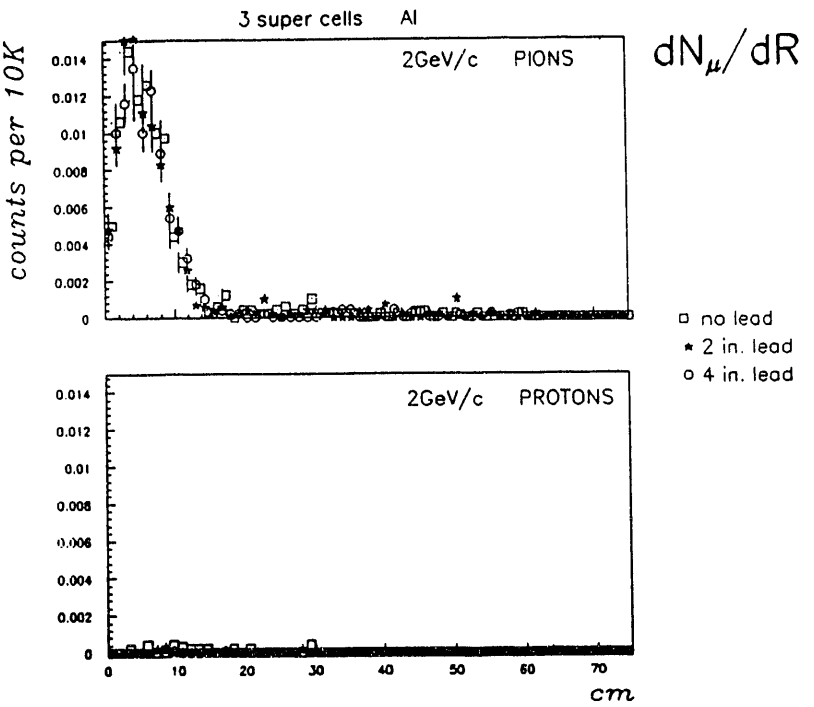

Figure 10: Preliminary results of GEANT 3.13 calculations of dN/dR for muons reaching T1 for 2 GeV/c protons and π^+s incident on a 3 supercell aluminum calorimeter, for 0 (squares), 1 (stars), and 2 (circles) lead layers "in", for 10,000 events.

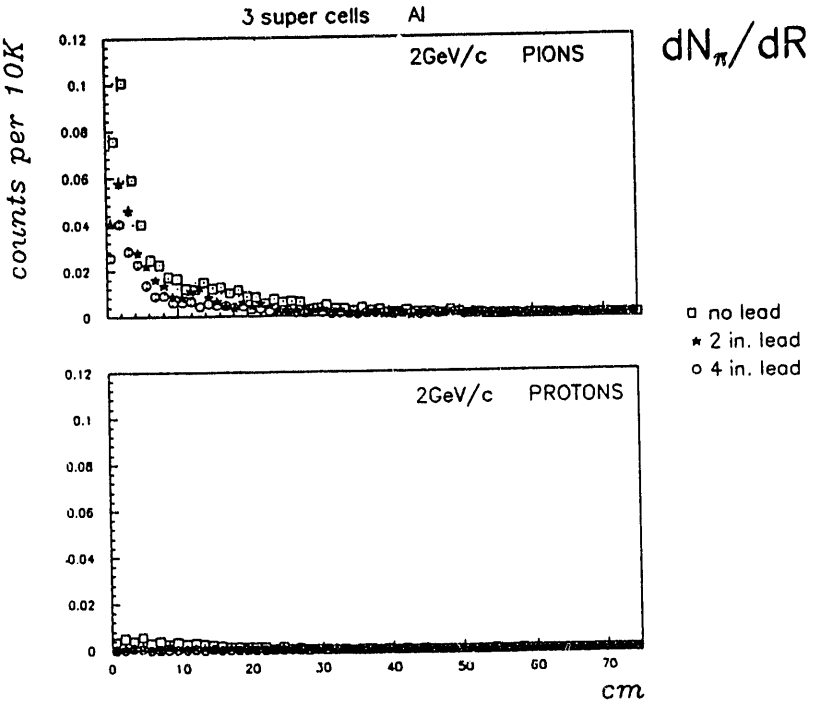

Figure 11: Preliminary results of GEANT 3.13 calculations of dN/dR for pions reaching T1 for 2 GeV/c protons and π^+s incident on a 3 supercell aluminum calorimeter, for 0 (squares), 1 (stars), and 2 (circles) lead layers "in", for 10,000 events.

RESULTS ON PERFORMANCE OF THE CALORIMETER AS A MUON-IDENTIFIER

The calorimeter is segmented in depth as well as in the transverse direction, although this latter segmentation is only projective. It is thus possible to examine the data from the calorimeter for differences in the hit distributions created by incident muons and by incident protons or π^+s. This is in large measure a pattern recognition problem. Muons tend to pass through the calorimeter nearly undisturbed, firing only 1 slat per scintillator layer, experiencing multiple Coulomb scattering, and reaching the last scintillator layer. Protons or π^+s usually will interact, creating secondaries which stop and spread out transversely by a large amount. Several slats per scintillator array will fire, and the distribution of fired arrays usually does not extend to the downstream scintillator arrays, instead usually stopping several arrays short even for a 9 supercell (6 λ) thick calorimeter.

This is the basis for analyses studying the calorimeter as a rough prototype of the muon-identifier needed as the last muon-detection element in the Dimuon/Photon ULOI. We call it a rough prototype because the segmentation presently is projective in nature while the proposed muon-identifier had several planes instrumented with pad readout, thus providing 3-D segmentation. The analysis performed here looks at the means and covariances of several variables. The response of the algorithm for analyzing the calorimeter data for muon/proton or muon/pion discrimination is "trained" with particles of known momentum and type. The response is then tested with other particles of known type and momentum. (To perform both functions for a fixed particle type and momentum, we split the data runs into halves with the first used for training and the second used for testing.) We then determine what percentage of protons (or pions) can be identified and thus rejected. This is determined as a function of the percentage of muons which would be kept and also as a function of the segmentation used for the readout. The offline data analysis can vary the number of depth segments of readout included in the analysis as well as chose between the two sizes of slat (10 cm wide vs. 22 cm wide.) This last step is quite important in deciding how much (or rather, how little) instrumentation of the muon-identifier is needed for it to function at the $\geq$ 99% level for rejecting hadrons.

The difference in hit patterns for muons and protons is shown schematically in Fig. 12 and Fig. 13. These show horizontal and vertical views of the calorimeter. The metal sheets are not drawn for reasons of clarity. The fired scintillator slats are shown in the appropriate view (a cut through the vertical slats in the plan view and a cut through the horizontal slats in the elevation view.) The basic difference in pattern is readily apparent. The discriminant analysis attempts to quantify this difference.

The analysis proceeds by first determining the distributions for hadron or muon events as a function of several different variables. The variables chosen are ones likely to exhibit useful differences between their distributions for hadrons and for muons. Some choices are of course much better than others. Fig. 14 shows the distribution for the number of the last scintillator array hit for the three cases of 3 GeV/c protons incident, 2 GeV/c protons incident, and 3 GeV/c muons incident on the mixed calorimeter. (The mixed calorimeter has 4 upstream aluminum/scintillator supercells and five downstream steel/scintillator supercells.

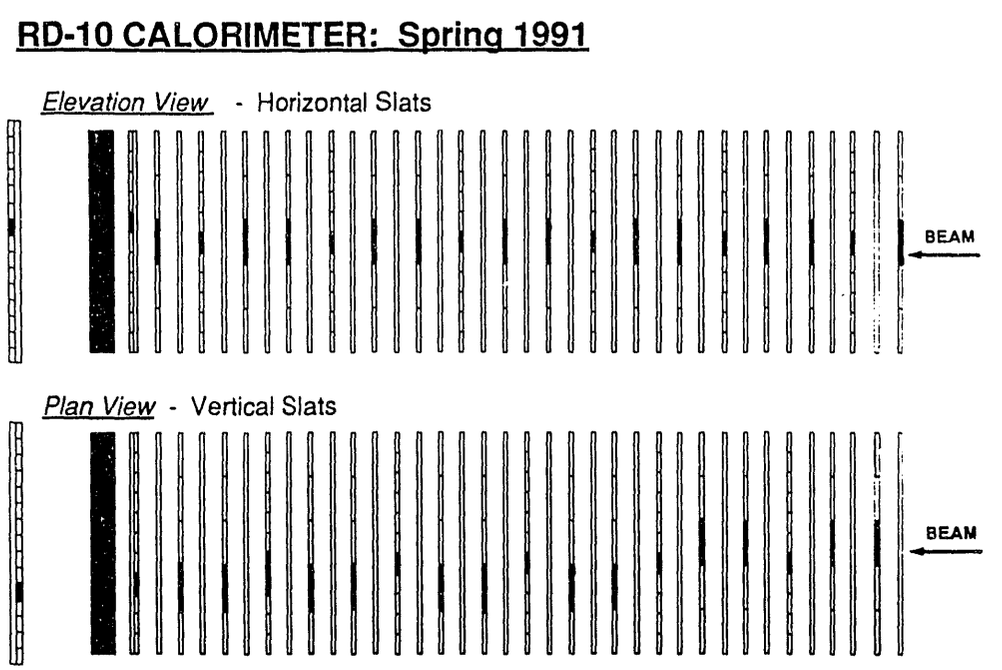

Figure 12: Schematic plan and elevation views of muons traversing the 9 supercell mixed calorimeter. Projections of the hits in horizontal (vertical) slats are seen in the elevation (plan) view.

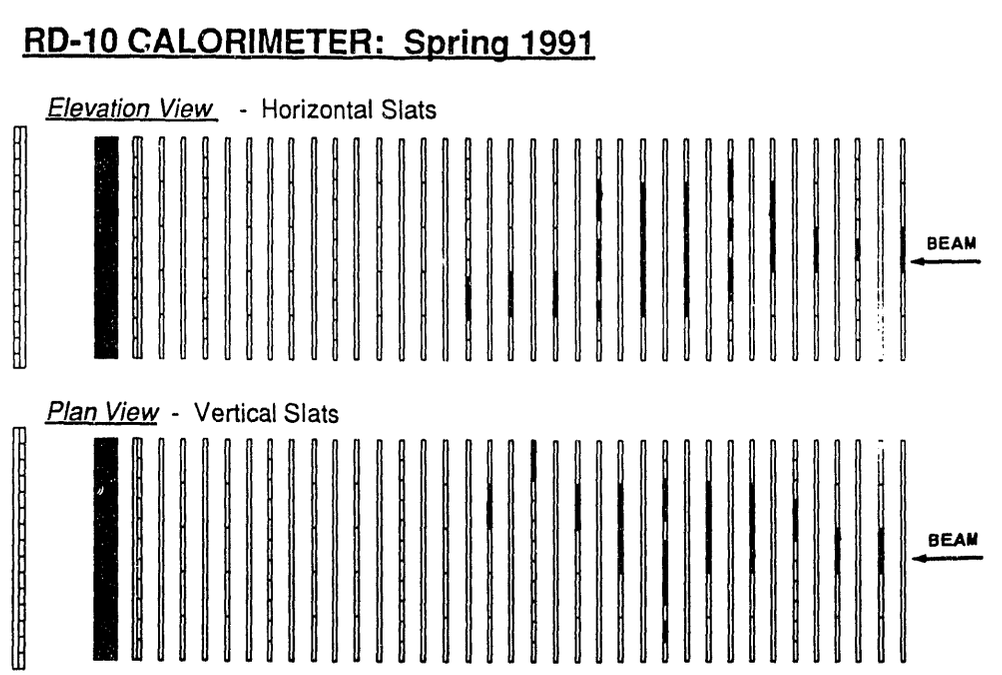

Figure 13: Schematic plan and elevation views of protons traversing the 9 supercell mixed calorimeter. Projections of the hits in horizontal (vertical) slats are seen in the elevation (plan) view.

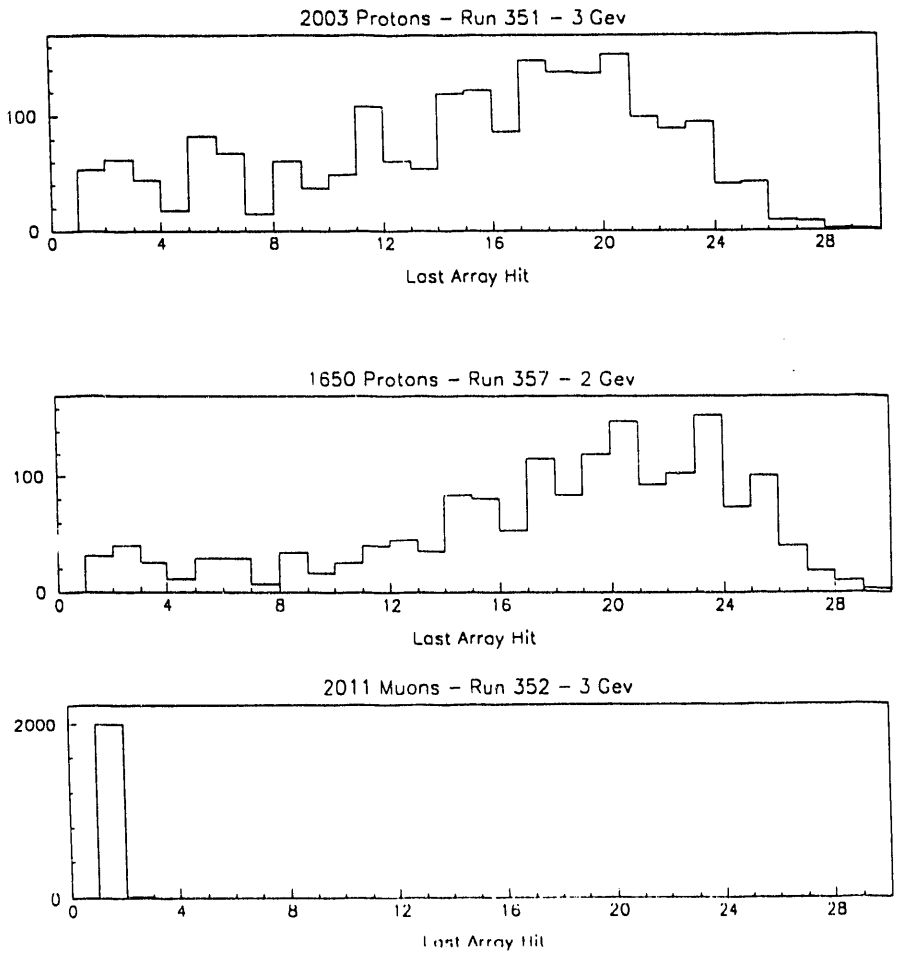

Figure 14: Distribution of the number of the last scintillator array fired as a function of array number, for 3 and 2 GeV/c protons and 3 GeV/c muons incident on the 9 supercell mixed aluminum/steel calorimeter. Note that array 29 is the upstream end of the calorimeter.

These same three choices of particle incident on the mixed calorimeter will be used in Figs. 14 through 18 and the following discussion.) We note that the scintillator array numbering is such that array 29 is at the upstream end of the calorimeter and array 1 is at the downstream end. Therefore muons penetrating the full array will fire all arrays from 29 through 1, with 1 the last array hit. Hadrons tend to produce hit distributions that are much shallower. The 2 GeV/c protons produce hit patterns that penetrate no deeper than array 18 or so, or barely one-third of the calorimeter thickness. The distributions are seen to differ markedly in both mean and width.

Fig. 15 shows distributions that differ markedly in width but not mean. This figure shows the distribution of the number of hits (i.e. number of slats

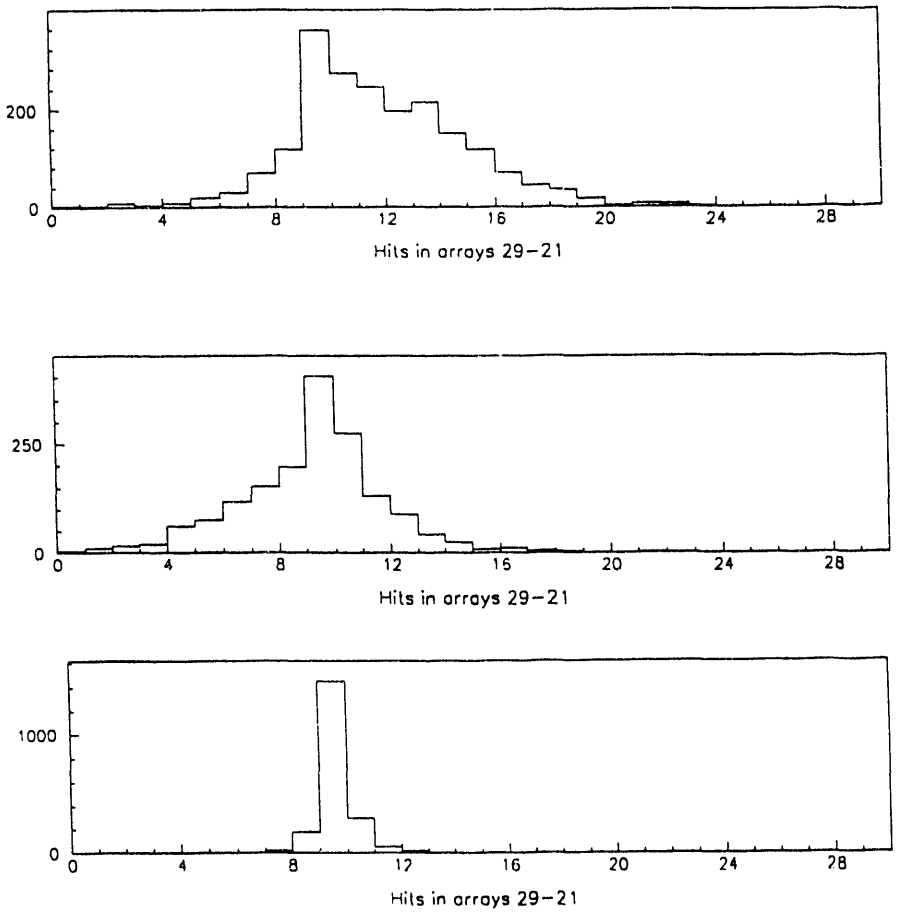

Figure 15: Distribution of the number of hits in the *first* 3 supercells (first 2 λ) of the 9 supercell mixed aluminum/steel calorimeter, for 3 and 2 GeV/c protons and 3 GeV/c muons incident.

with pulse-height exceeding pedestal by 3 sigma) in slats in the upstream third of the mixed calorimeter. Fig. 16 shows the corresponding distribution for the downstream third of the mixed calorimeter; again, a good separation is seen, although this is expected for the downstream third of the mixed calorimeter based on the information in Fig. 14.

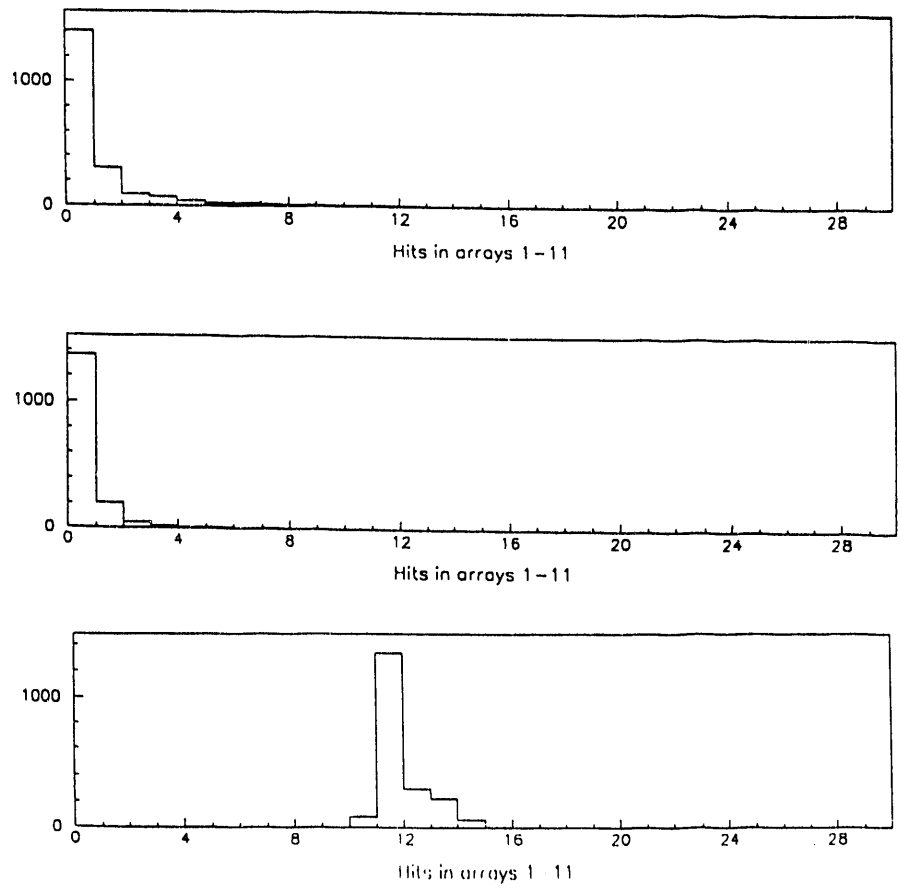

Figure 16: Distribution of the number of hits in the *last* 3 supercells (last 2 λ) of the 9 supercell mixed aluminum/steel calorimeter, for 3 and 2 GeV/c protons and 3 GeV/c muons incident.

Fig. 17 shows the distributions of the total number of hits in the mixed calorimeter. The protons produce many more hits in the scintillator arrays fired by

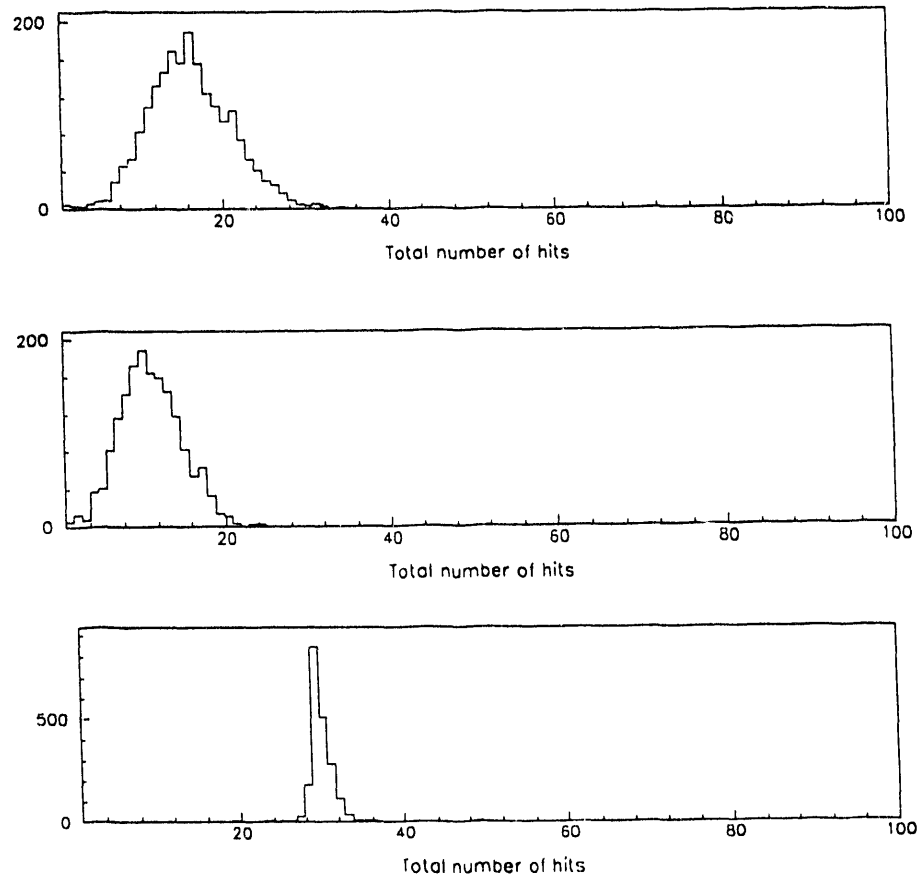

Figure 17: Distribution of the *total* number of hits, for *all* supercells of the 9 supercell mixed aluminum/steel calorimeter, for 3 and 2 GeV/c protons and 3 GeV/c muons incident.

their showers. However, the muons penetrate so many more arrays that they yield more hits overall. It is also possible to record the pulse-height in each scintillator, normalized by that for a minimum-ionizing particle. Fig. 18 shows the distribution corresponding to Fig. 17, but now expressed as total pulse-height observed in the struck scintillators. This distribution clearly offers less discrimination power than that in Fig. 17 due to the much larger width for the pulse-height distribution than for the number of hits distribution.

The "discriminant function" analysis [3] described in the Dimuon/Photon ULOI is then carried out. The covariance matrix of the selected distributions is constructed, inverted and used to determine the range of values expected for the discriminant function for hadrons and for muons. The discriminant function resulting from an analysis using a restricted range of variables is shown in Fig. 19. The variables used were:

1. last scintillator array fired

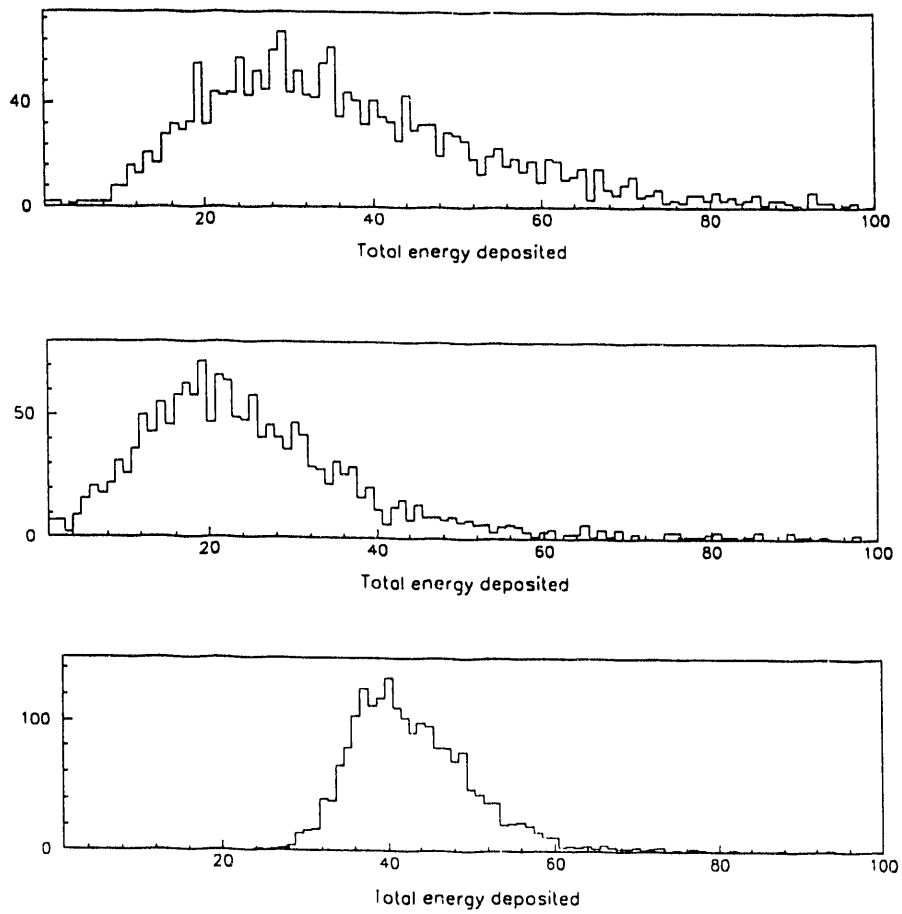

Figure 18: Distribution of the total *pulse height*, normalized to that for minimum-ionizing particles, for *all* supercells of the 9 supercell mixed aluminum/steel calorimeter, for 3 and 2 GeV/c protons and 3 GeV/c muons incident.

2. total number of fired scintillator arrays

3. total number of fired scintillator arrays in arrays 1-11 (i.e. the downstream end of the mixed calorimeter)

4. the number of the mean array fired, weighted by the number of fired slats in each array

5. total number of fired scintillator arrays in arrays 1=11, weighted by the normalized (to minimum-ionizing particles) pulse-height recorded by slats in that array

6. the number of the mean array fired, weighted again by normalized pulse-height

As can be seen in the figure, the separation between muons and protons is encouraging even for such low momentum muons.

A further analysis was carried out using all fourteen of the discriminant variables listed in the Dimuon/Photon ULOI. This analysis was carried out using the information from all slat arrays in the calorimeter and then again using either only the narrow (10 cm wide) slats or only the wide (22 cm wide) slats. For all these cases, the analysis was also carried out either using all 9 supercells present in the mixed calorimeter or using only the 7 upstream supercells present. The results are summarized in Table 1 as a function of the efficiency for keeping muon events. The symbol $\geq$ signifies that more than 99.5% of the protons analyzed could be identified correctly while keeping the specified fraction of the muons. There are two types of wide slat (differing in light-guide type and thus light-collection efficiency). The results presented below for "wide" slats are a mean (of quite similar results) of the analyses using these two types of wide slats. The conclusion is that it is possible to reject more than 99% of the protons using just the narrow slat array information while maintaining better than 98% efficiency for the muons. The proposed muon-identifier would be expected to have somewhat better performance if only because the proposed segmentation would be truly 3-D, not projective as is the case for the scintillator slats available for the present analysis.

CONCLUDING REMARKS

The first look at the particle leakage rates provided by these data for low incident momenta and thin calorimeters is quite encouraging. The indications are that the leakage rates specified in the Dimuon/Photon ULOI will be attained or bettered. The addition of a lead shutter helps reduce the leakage rates, particularly of particles emitted at large exit angles, which would be quite troublesome for the tracking chambers in a heavy-ion experiment.

The muon ID capability of the calorimeter was demonstrated. This gave results suggesting that a muon-identifier of some 6 λ thickness and instrumented only every $2/3\lambda$ with readout of 10 cm or even 22 cm granularity would be adequate for identifying muons of 1-4 GeV/c momenta. Further analysis will examine whether the instrumentation in the upstream part of the calorimeter is actually necessary to attain the good values of hadron rejection observed to date.

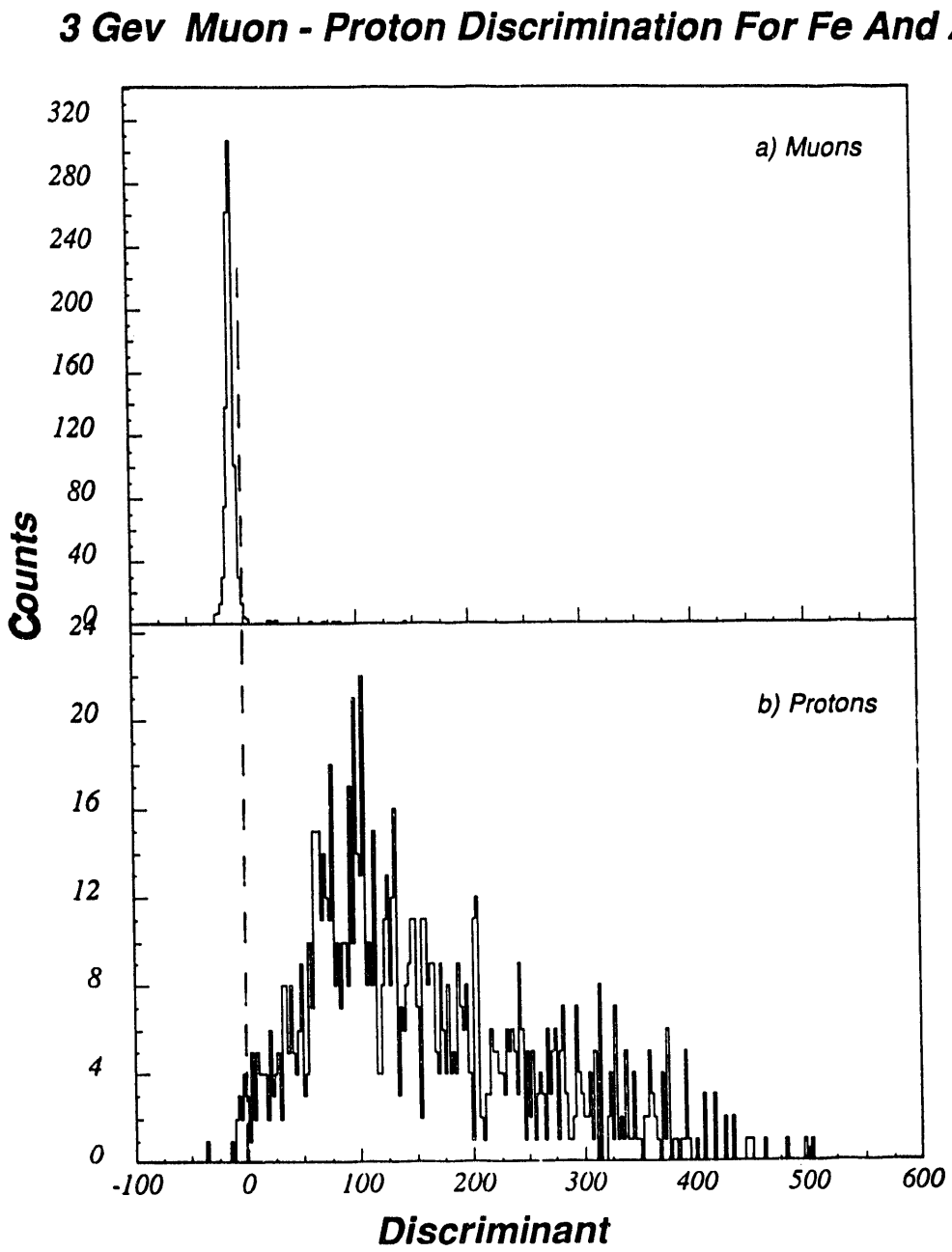

Figure 19: Discriminant function using the six discriminant variables listed in the text. Both training and test data were taken from the data recorded for 3 GeV/c muons and protons incident on the 9 supercell mixed aluminum/steel calorimeter.

Arrays Used	No. of SC	90%	95%	98%	99%	99.5%
All	9	$\geq$	$\geq$	$\geq$	$\geq$	$\geq$
	7	98.4	98.0	97.5	94.7	94.0
Narrow	9	$\geq$	$\geq$	$\geq$	99.1	97.7
	7	97.7	97.3	95.5	94.0	88.4
Wide	9	$\geq$	$\geq$	99.4	98.7	98.5
	7	97.5	97.0	95.0	91.8	90.5

Table 1: Results of Discriminant Function analysis, using all 14 discriminant variables from the Dimuon/Photon ULOI, for 3 GeV/c muons and protons incident on the 9 supercell mixed aluminum/steel RD-10 calorimeter. The column headings for the rightmost 5 columns give the efficiency for retaining muons. The symbol "$\geq$" means $\geq$99.5% of the protons are identified at that level of muon efficiency.

Further analysis is in progress to quantify matters better. The full range of momentum for which we have data will be analyzed, as will be the full set of absorber thicknesses, compositions and lead shutter positions. Further data-taking will include obtaining drift chamber info for the aluminum calorimeter setup, filling in missing data points, improving statistics, particularly for low incident particle momentum, and examining thick ($\geq 6\lambda$) steel calorimeter setups, the better to match possible forward-angle dimuon setups that might be built as a part of the PHENIX experiment at RHIC.

The Monte Carlo effort needed is underway. General trends of the data are reproduced. Effort on understanding absolute normalizations has begun. Comparisons of GHEISHA with LAHET will continue. It is expected that final comparisons will concentrate on using LAHET.

ACKNOWLEDGEMENTS

We acknowledge the assistance provided by D. Dayton of the AGS staff and the extensive technical work performed by R. Morgret of LLNL, by R. Cumby of ORNL, and by S. Marino, J. Yelk and M. Lenz of the Omega Group in the BNL Physics Department. In particular we thank Bill Morse for his loan of the E780/845 drift chambers and of many dozens of light guides and photomultiplier tubes. We thank the staff of the AGS for the good running conditions in the SEB run this past spring. All institutions acknowledge support from the U.S. Department of Energy. M. Starks acknowledges support from the U.S. Department of Energy's Division of University and Industry Programs, Office of Energy Research, as a Science and Engineering Research Semester (SERS) Program participant. Research at Oak Ridge National Laboratory is sponsored by the U.S. Department of Energy under contract DE-AC05-84OR21400 with Martin Marietta Energy Systems, Inc.

References

[1] S. H. Aronson et al., "A Dimuon Spectrometer for RHIC: Measurements of Muon Pairs, Vector Mesons and Photons", RHIC LOI-4, submitted September 28, 1990.

[2] S. H. Aronson et al., "A Lepton/Photon Spectrometer for RHIC Measurements of Lepton Pairs, Vector Mesons and Photons, RHIC LOI-12, submitted July 15, 1991.

[3] G. Capon, Nucl. Instr. and Methods **A276**, 58 (1988).

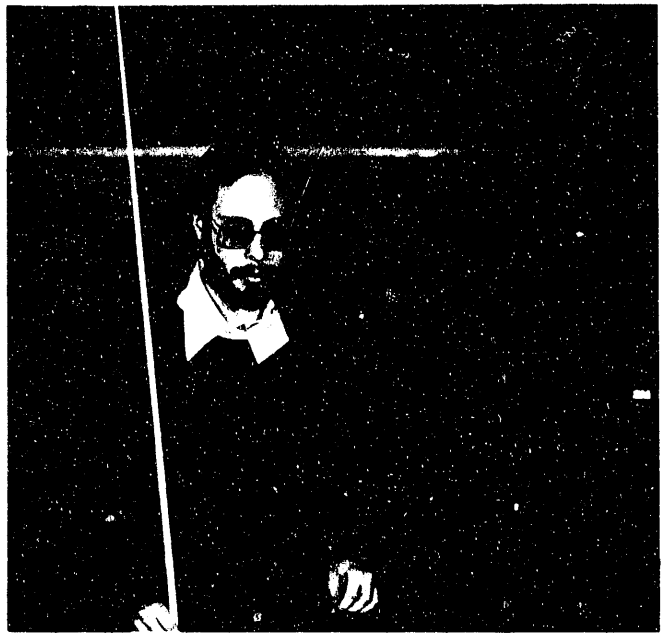

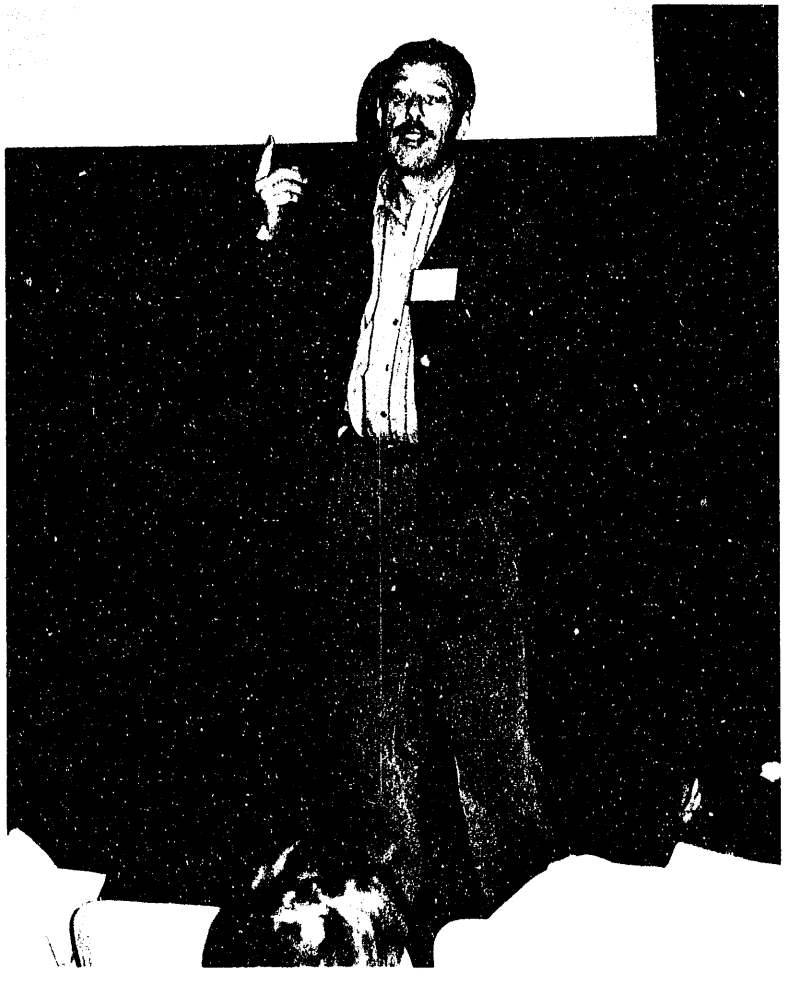

APPLICATIONS OF THE LAHET SIMULATION CODE TO RELATIVISTIC HEAVY ION DETECTORS

Laurie Waters, Avigdor Gavron
Los Alamos National Laboratory, Los Alamos, New Mexico 87545

ABSTRACT

The Los Alamos High Energy Transport (LAHET) simulation code has been applied to test beam data from the lead/scintillator Participant Calorimeter of BNL AGS experiment E814. The LAHET code treats hadronic interactions with the LANL version of the Oak Ridge code HETC. LAHET has now been expanded to handle hadrons with kinetic energies greater than 5 GeV with the FLUKA code, while HETC is used exclusively below 2.0 GeV. FLUKA is phased in linearly between 2.0 and 5.0 GeV. Transport of electrons and photons is done with EGS4, and an interface to the Los Alamos HMCNP3B library based code is provided to analyze neutrons with kinetic energies less than 20 MeV. Excellent agreement is found between the test data and simulation, and results for 2.46 GeV/c protons and pions are illustrated in this article.

INTRODUCTION

In the design of detectors for relativistic heavy ion experiments, response to hadrons with kinetic energies less than 4-5 GeV must seriously be considered. For central Au + Au collisions at RHIC, predictions from the LUND event generator show that nearly all protons and neutrons emitted in the central region, $-1 < \eta < 1$, and 30% of those in the forward region $| \eta | > 1$ have kinetic energies less than 4 GeV. Corresponding figures for pions are 100% and 78%. In addition, the effect of primary and secondary very low energy (less than 100 MeV) neutrons on detector response must also be carefully considered, since reactions such as $^{12}C+n$ may produce visible signals in scintillators and wire chamber gasses. It is essential that well tested simulation codes be available to model detector response to such particles.

Recent improvements to the Los Alamos High Energy Transport (LAHET) code[1] are designed to further enhance its performance at such energies. Figure 1 illustrates the code organization. Transport is available for protons, neutrons, pions, muons, photons and electrons. For hadrons with kinetic energies less than 2.0 GeV, the Los Alamos version of the Oak Ridge HETC[2] code is used. The user may chose between the Bertini and Isabel/Vegas intra-nuclear cascade models, also between several fission and evaporation codes. The LAHET Users Guide[1] contains detailed references for the various models. For hadrons with kinetic

energies from 2.0 to 5.0 GeV the FLUKA[3] code is phased in linearly, and FLUKA is used exclusively above 5.0 GeV. All photons and electrons are transported with the EGS4[4] code. The combined HETC-FLUKA-EGS4 package is referred to as SUPERHET.

All neutrons with kinetic energies less than 20 MeV are written to a separate file for processing with the library based monte carlo code HMCNP3B[5]. The output of this code is combined with the results of the SUPERHET analysis through a simple interface. Particular attention is paid to ensuring the accuracy of n+^{12}C and H(n,n) reactions down to 0.1 MeV in both codes, which is especially important in the analysis of scintillator light output.

The output of all codes is written to a standard format and various routines are available to the user for analysis. In addition, the routines may be linked to standard CERN library packages such as PAW. SUPERHET and HMCNP3B are supported on VAX/VMS and UNIX.

SIMULATIONS OF THE E814 PARTICIPANT CALORIMETER

One element of Brookhaven AGS Experiment E814 is a lead/scintillator sampling calorimeter known as the Participant Calorimeter (PCAL). Figure 2 shows the construction of this device[6]. The PCAL consists of four identical quadrants arranged around the beam (fig. 2a). Each quadrant is subdivided into four "pie" shaped slices of 22.5° each, and each pie is further divided radially into eight towers. Each tower is read out by a scintillator plate with the signal carried by a scintillating fiber coupled along the edge of the plate. Longitudinally, the calorimeter consists of alternating layers of the 0.3 cm thick scintillator and 1.0 cm lead absorber plates. The scintillator plates lie in 0.1 cm polypropylene trays. The PCAL is divided into 4 segments (fig. 2b); the first electromagnetic (EM1) consisting of 6 Pb/sci sections, the second electromagnetic (EM2) consisting of 6 Pb/sci sections, the first hadronic (HAD1) with 24 Pb/sci sections and the second hadronic (HAD2) with 23 Pb/sci sections. Each of the four segments is further separated by 1.6 cm steel plates for support. The PCAL contains a total of 4 hadronic interaction lengths.

The PCAL has been tested and calibrated with various beams at the BNL AGS[7]. In this article, we present the results of the LAHET simulations with 2.46 GeV/c momentum pions and protons. The beam is incident on the face of the PCAL as indicated in figure 2. Data for 1160 incident protons and 1670 pions were obtained, and these same number of events were simulated so that the results of the simulations could be directly compared to the data. Particles were subject to tracking thresholds of 0.1 MeV for hadrons, and 0.5 MeV for photons and electrons. The light output response of the scintillators was modelled in two ways. The standard Birks formalism weights incremental energy deposition by a factor of $1.0/(1.0 + a \cdot (de/dx) + b \cdot (de/dx)^2)$, where $a = .0126\ g/MeV \cdot cm^2$

(.0072 $g/Mev \cdot cm^2$ for alphas), and $b = 9.6 \times 10^{-6}\ g^2/Mev^2 \cdot cm^4$. In addition, the formalism of the TRACE[8] code has been tested. Figure 3 shows the total energy contained in the PCAL for protons and pions, using both the Birks and TRACE methods. The simulated energy deposition has been scaled in the same manner as the PCAL calibration[7]. Note a closer agreement is obtained when the TRACE method is used.

The effect of the low energy neutrons is illustrated in figure 4. Here, the total energy in the PCAL is compared to the results of SUPERHET alone and with the output of the HMCNP3B analysis added in. The effect of adding in the response of neutrons with kinetic energies less than 20 MeV is to increase the energy deposition upward by about 10%. The simulations shown in this figure use the TRACE response functions.

Energy deposition is shown within the various segments in figures 5 and 6. The tails of the distributions are well reproduced, and no renormalization at all is required to match the data. Figures 7 and 8 show the radial energy deposition. In the simulation, the energy per unit area deposited in concentric rings of 4 cm width centered around the beam axis is shown. The points are joined with a solid line to guide the eye. Again, the simulations are in good agreement with the data.

CONCLUSION

The extended LAHET code, SUPERHET is now being extensively benchmarked against various data relevant to the expected RHIC environment. Work with the E814 PCAL is only a beginning; extensive analysis and simulation of the RHIC R&D project RD10 is now underway. In addition, further improvements to the code are being made. The number of particles for which tracking is available is being extended. Tracking in magnetic fields is being implemented and improvements in energy straggling and delta ray formation are being made. The code is extensively supported at Los Alamos to provide RHIC users with a package which includes the most accurate physics processes now available.

REFERENCES

1. R. E. Prael and H. Lichtenstein, "User Guide to LCS: The LAHET Code System", Los Alamos National Laboratory (Sept 15, 1989)

2. Radiation Shielding Information Center,"HETC Monte-Carlo High-Energy Nucleon-Meson Transport code", Report CCC-178, Oak Ridge National Laboratory (1977)

3. P. A. Aarnio, et. al.,"FLUKA89", issued by CERN

4. W. R. Nelson, H. Hirayma and D. W. O. Rogers,"The EGS4 Code System", SLAC-265, December 1985

5. J. F. Breismeister, ed., "MCNP - A General Monte Carlo Code for Neutron and Photon Transport", LA-7396-M Rev. 2, Los Alamos National Laboratory (1986)

6. J. Simon-Gillo, et. al.,"The Design and Construction of a Pb/Scintillator Sampling Calorimeter with Wavelength Shifter Fiber Optic Readout", submitted to Nucl. Instr. & Meth.

7. D. Fox, et. al., "Response of the Participant Calorimeter to 1.5-6.8 GeV/c Electrons and Hadrons", submitted to Nucl. Instr. & Meth.

8. W. C. Sailor, R. C. Byrd and Y. Yariv, "TRACE: A Monte Carlo Code for the Efficiency of Multi-Element Neutron Scintillator Detectors", Los Alamos report LA-11348-MS (1988), unpublished.

SUPERHET
Interaction & Transport Code

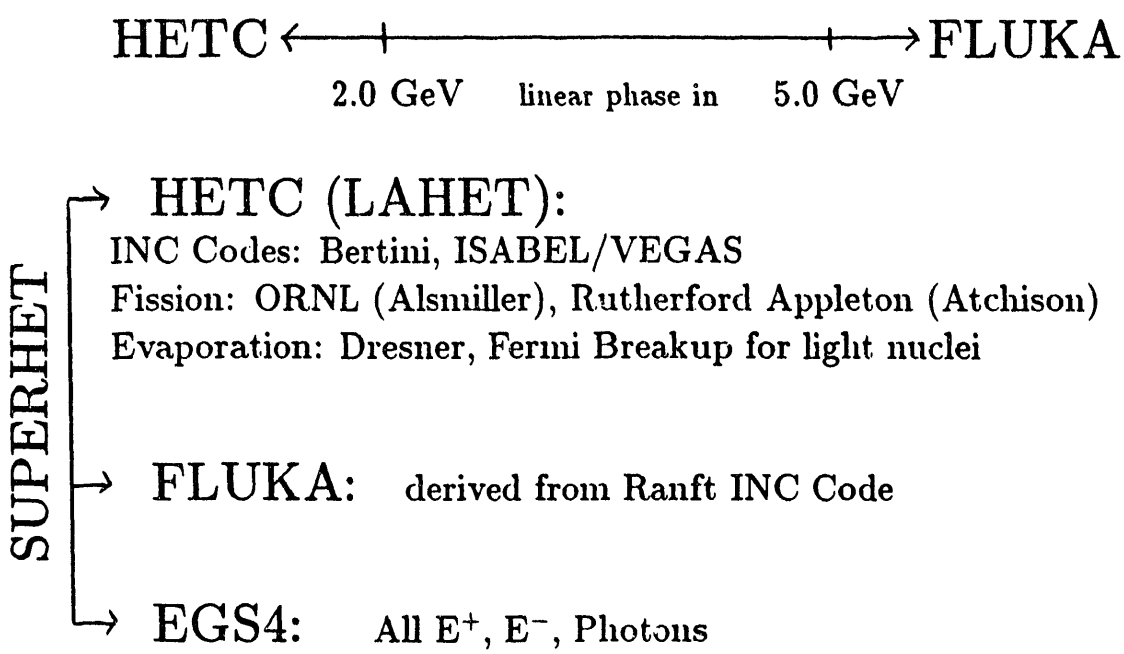

FIGURE 1: Organization of SUPERHET code

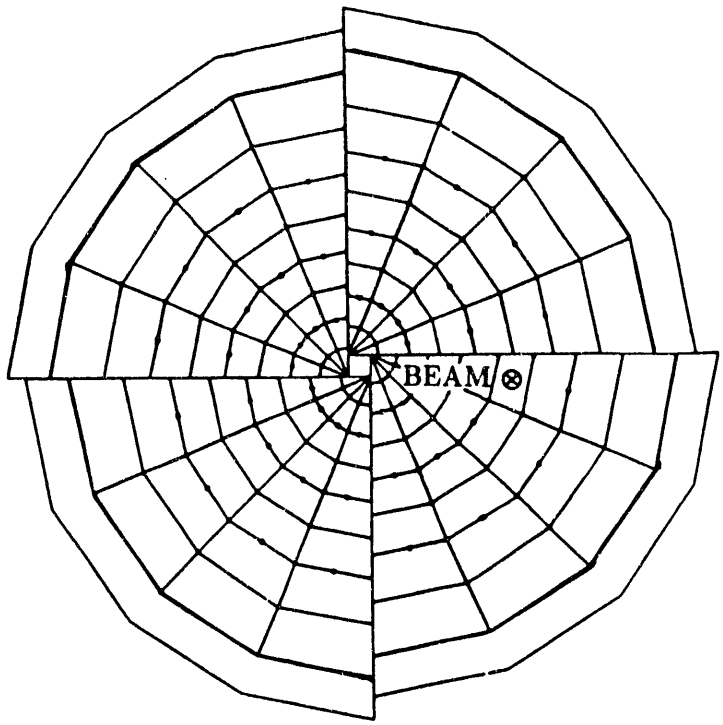

2a

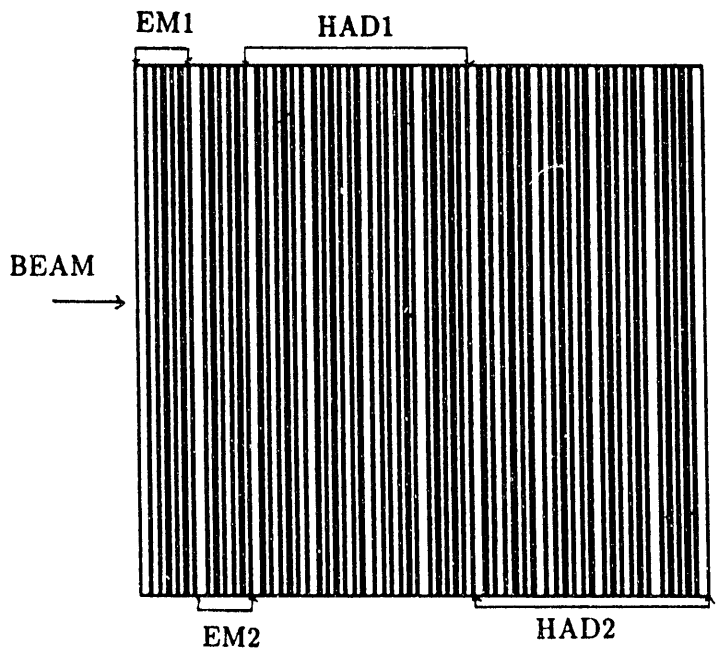

2b

FIGURE 2: E814 Participant Calorimeter
a) downstream view
b) longitudinal view

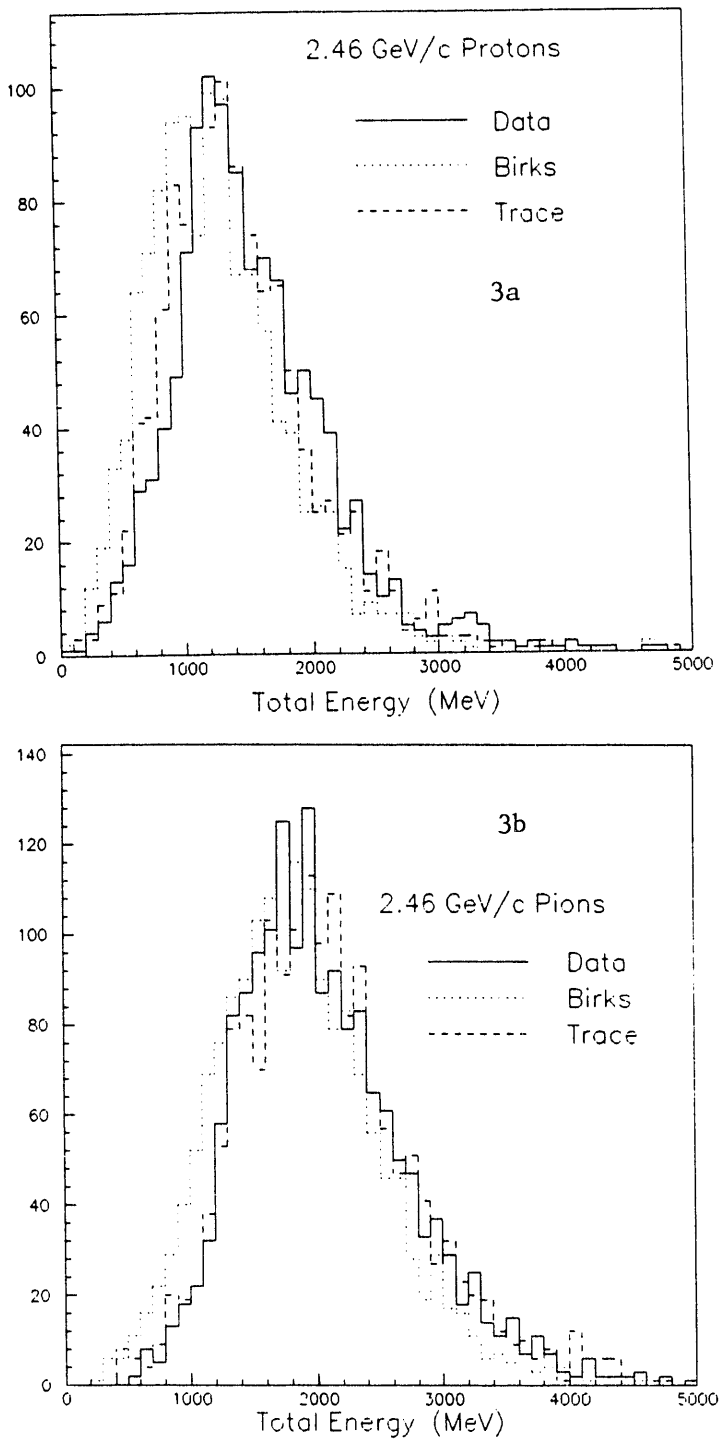

FIGURE #3: Comparison of scintillator response codes for a) protons b) pions

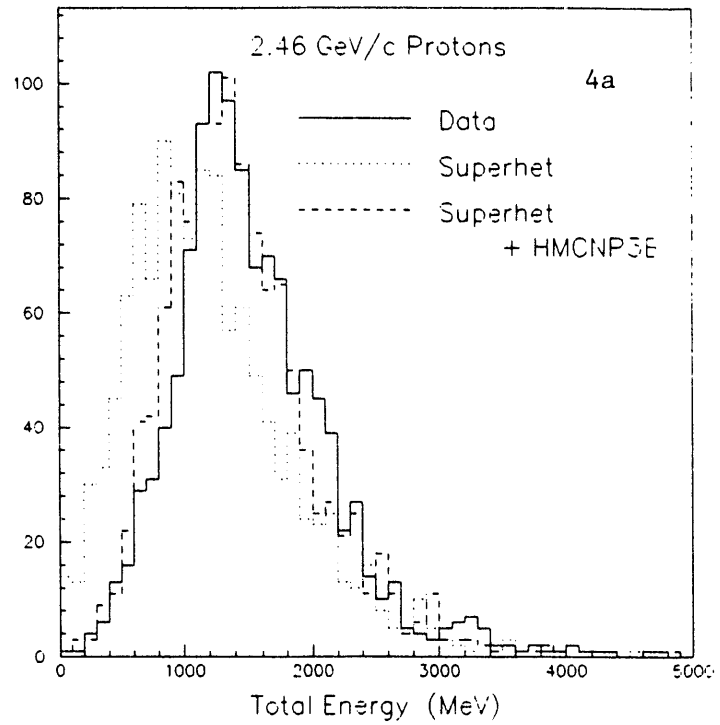

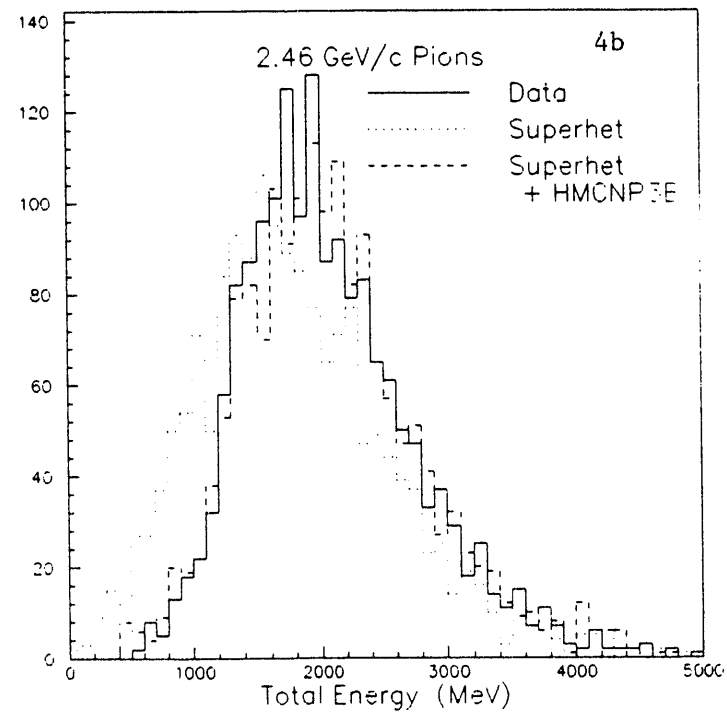

FIGURE 4: Effect of low energy neutrons

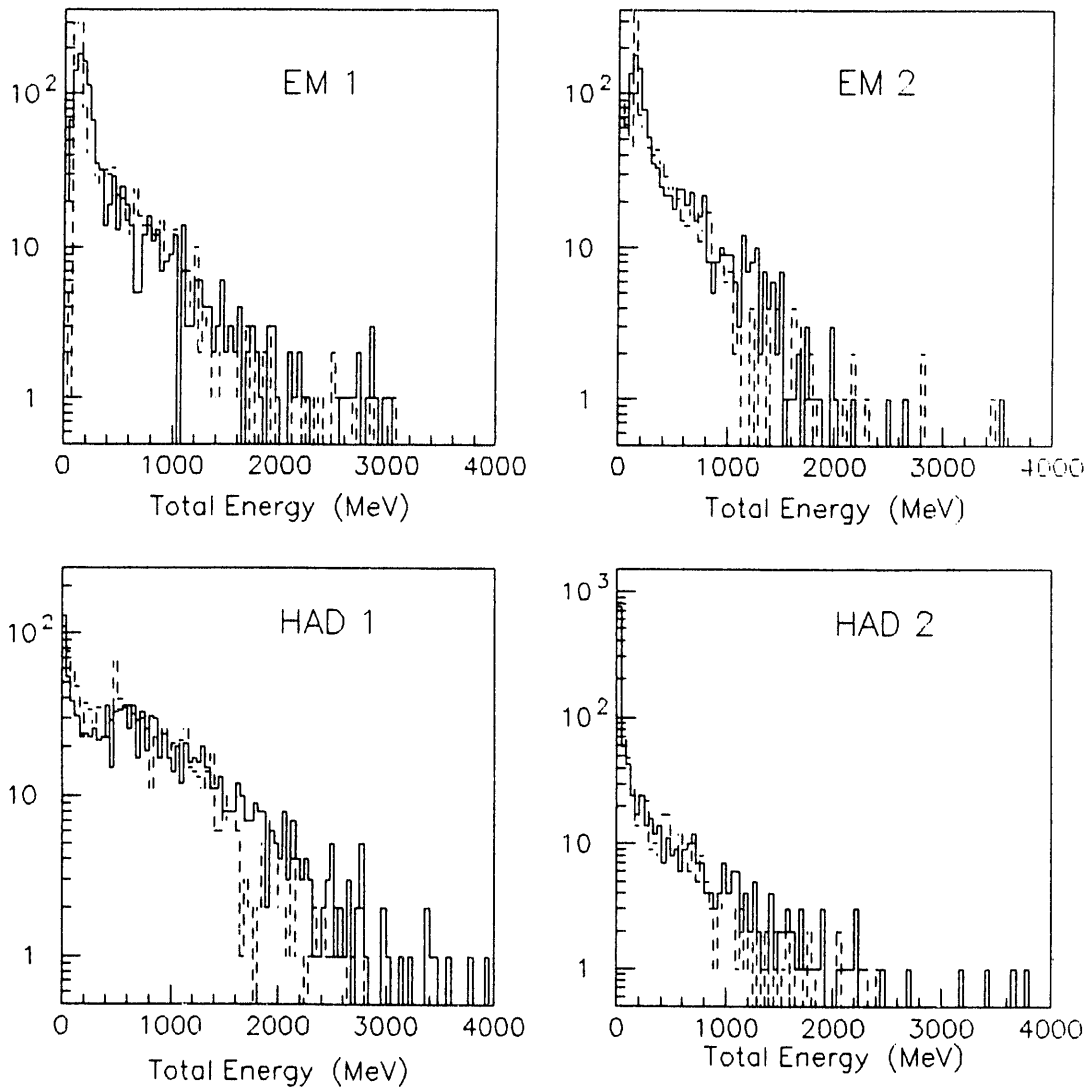

FIGURE 5: 2.46 GeV/c protons, energy deposited in various segments (data - solid) (simulation - dashed)

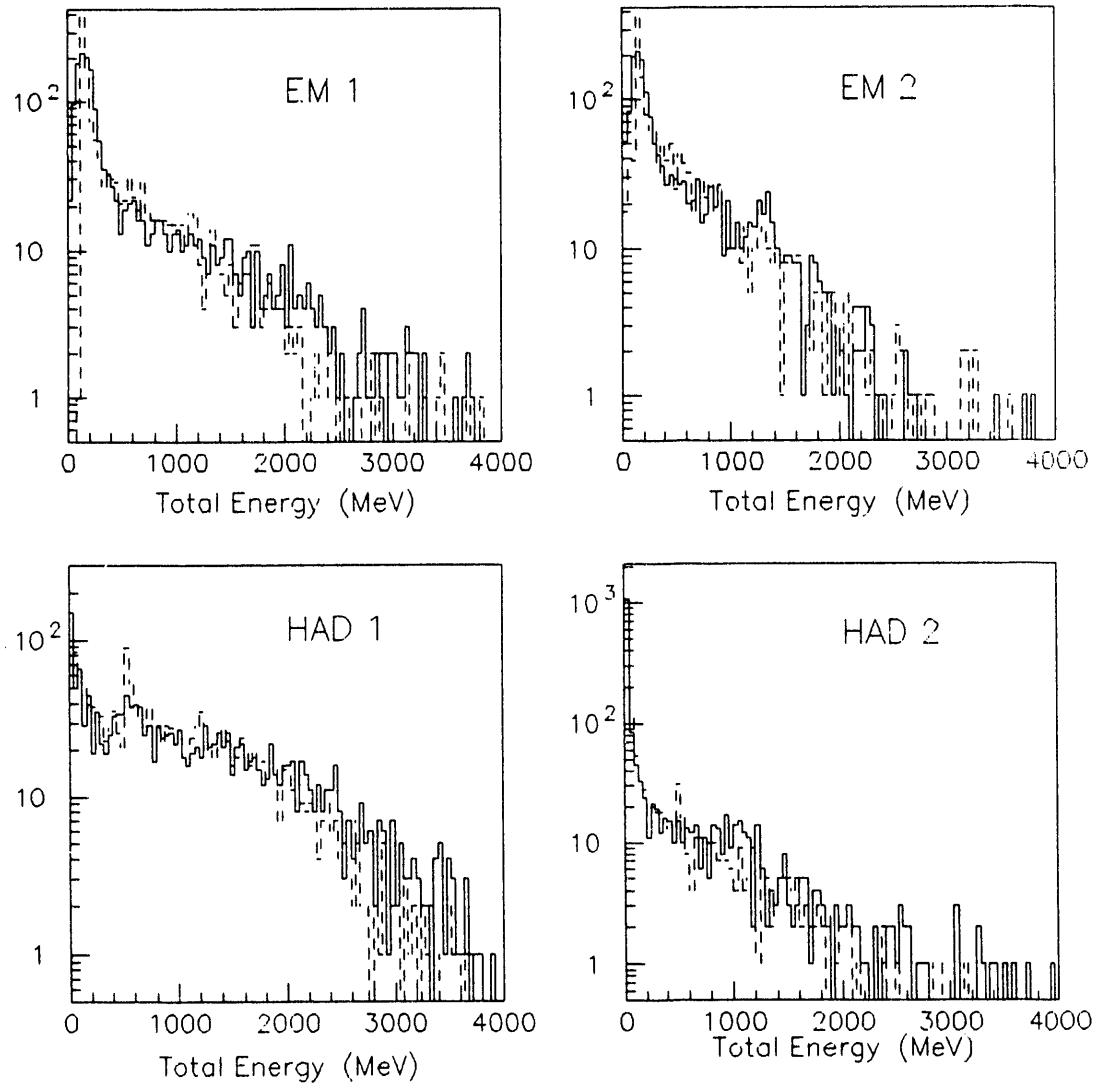

FIGURE 6: 2.46 GeV/c pions, energy deposited in various segments (data - solid) (simulation - dashed)

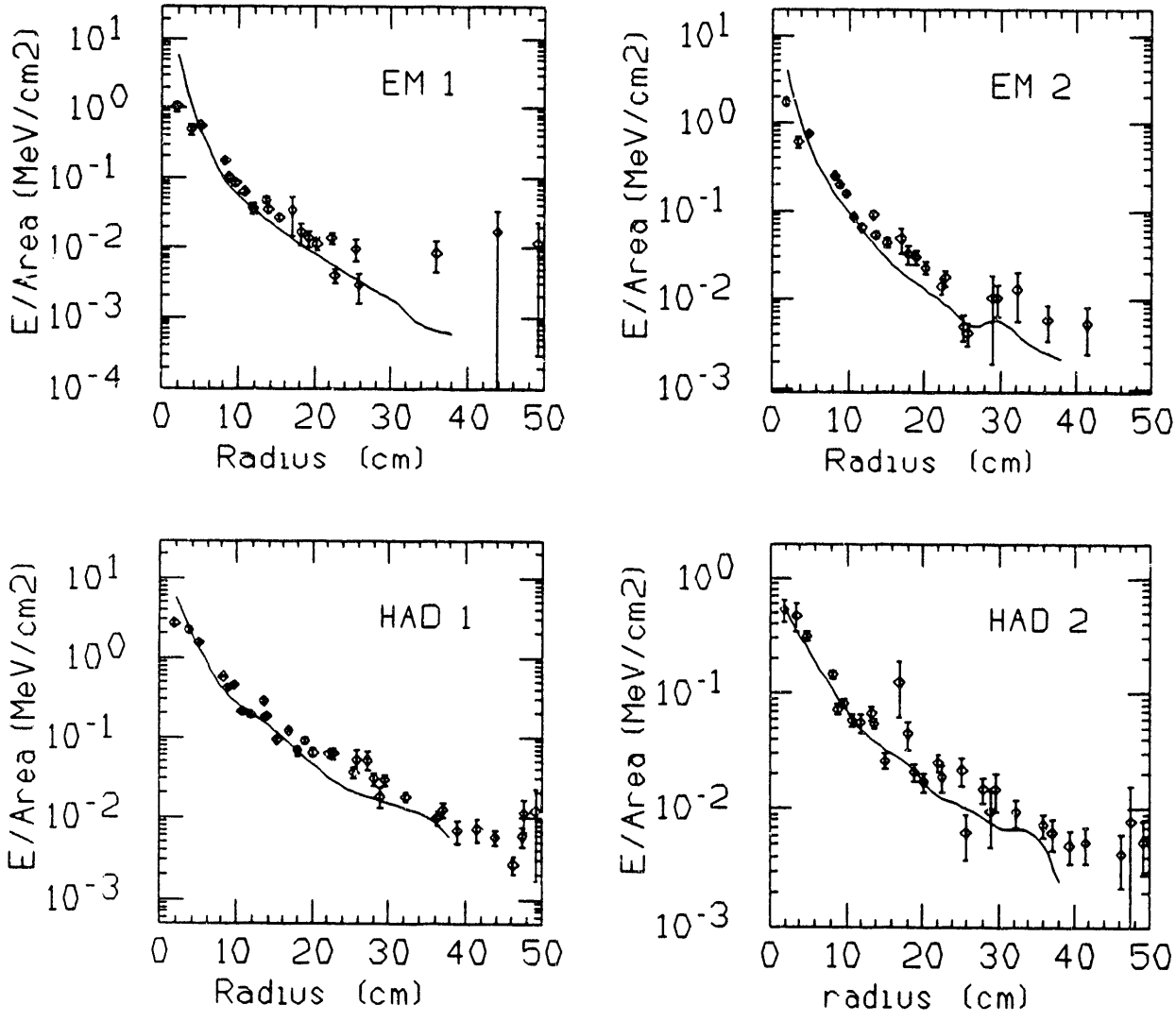

FIGURE 7: 2.46 GeV/c protons , radial energy distribution

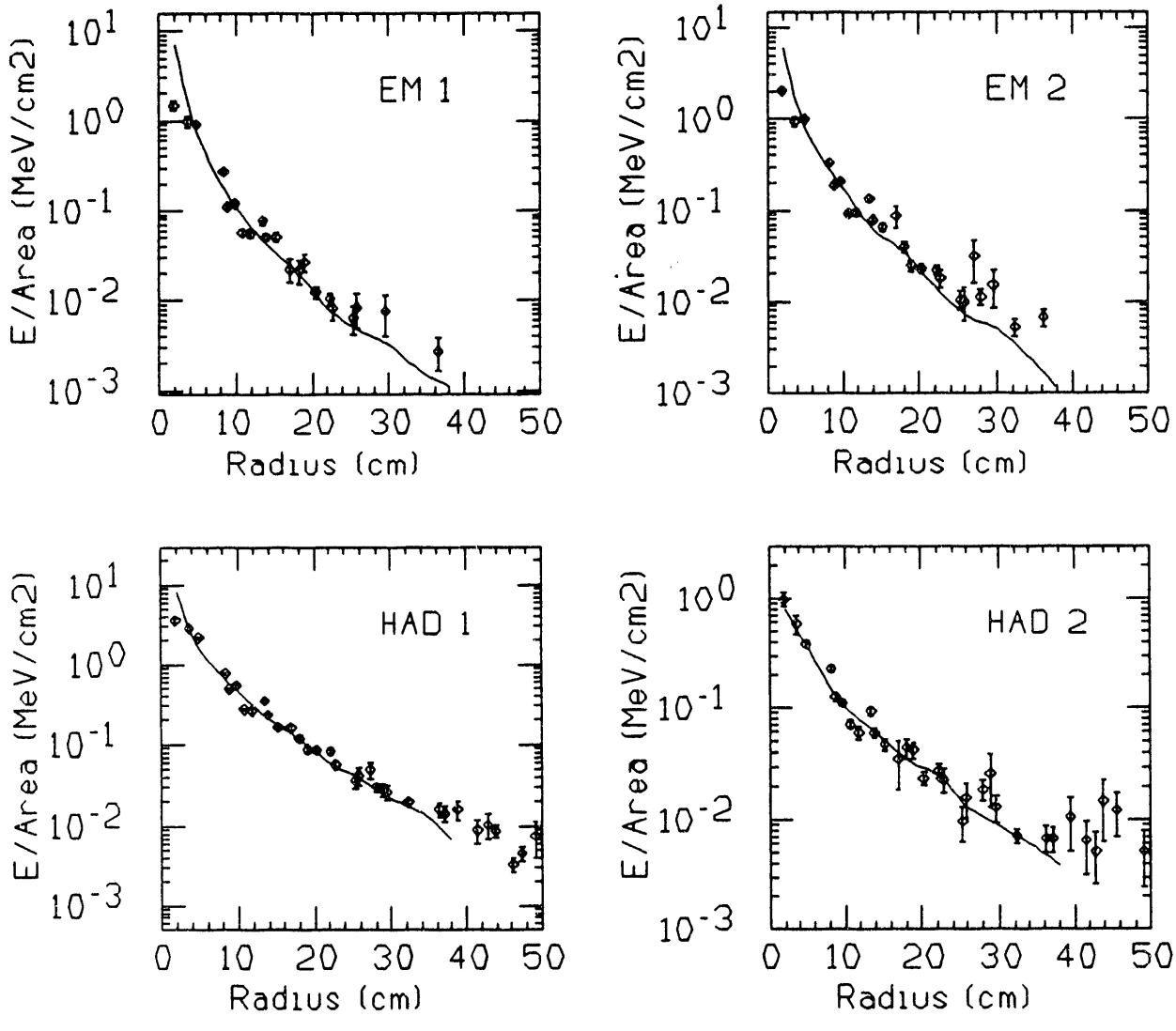

FIGURE 8: 2.46 GeV/c Pions, Radial Energy Distribution

HIGHLY SEGMENTED, HIGH RESOLUTION TIME-OF-FLIGHT SYSTEM

T.K. Nayak, S. Nagamiya, O. Vossnack, Y.D. Wu, W.A. Zajc
Columbia University, Nevis Laboratories, New York, New York 11973

Y. Miake, S. Ueno, H. Kitayama, Y. Nagasaka, K. Tomizawa, I. Arai, K. Yagi
University of Tsukuba, Institute of Physics, Tsukuba, Japan

ABSTRACT

The light attenuation and timing characteristics of time-of-flight counters constructed of 3m long scintillating fiber bundles of different shapes and sizes are presented. Fiber bundles made of 5mm diameter fibers showed good timing characteristics and less light attenuation. The results for a 1.5m long scintillator rod are also presented.

I. INTRODUCTION

A highly segmented, high resolution ($\sigma \sim 100$ ps) time-of-flight (TOF) system is being designed for hadron identification, which can handle large charge particle multiplicity ($dn_{ch}/dy \sim 1000$) events for Au+Au collisions at RHIC. Two different types of TOF counters are being considered. The first type, which is suitable for a TOF wall at a large distance ($\geq$ 3m) from the interaction region, is shown in Fig. 1(a). This is called a picket-fence design, where two phototubes are attached to both ends of a scintillator. In the second type, a phototube is mounted directly behind a block of scintillator as shown in Fig. 1(b). This is called a flashlight type design, which is more suitable for beam-beam counters to provide start time as well as interaction trigger.

Let us first consider a picket-fence design. In case of RHIC experiments, one would like to use long ($\sim$ 3m) scintillators to cover a large area, and to avoid placing phototubes in any sensitive volume or in the presence of a strong magnetic field. It is known that, one can achieve a time resolution of about 75 psec for TOF counters made of scintillating rods of dimension 1.6cm×1.6cm×80cm which are being used in the TOF wall in AGS E802-859 experiments[1] at BNL. One of the shortcomings for scintillator rods is a short attenuation length ($\approx$ 70 – 80 cm for a rod of 1.6cm×1.6cm cross section), which is mainly due to light loss in surface reflections. Thus, these rods may not be suitable for designs which require long scintillators.

Plastic scintillating fibers, on the other hand, have a longer attenuation length, because of small trapping angle for the transmitted light. In the present

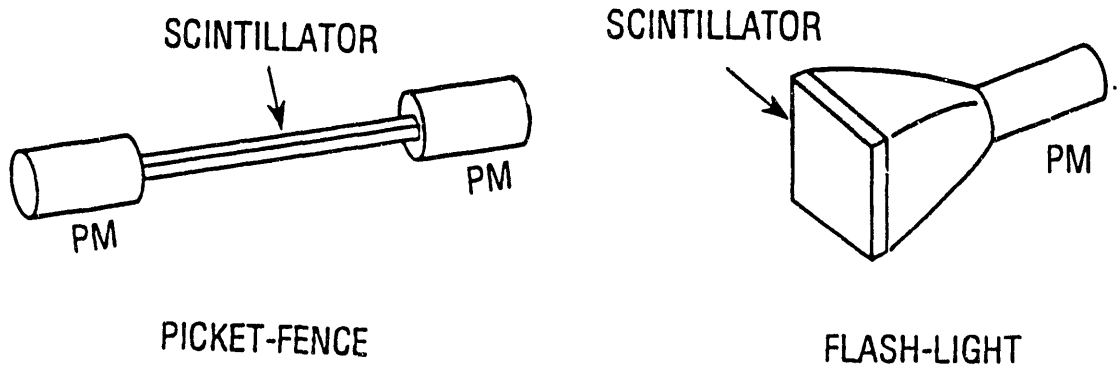

Figure 1: Two types of readout schemes for TOF counters : (a) Picket-fence type, (b) Flashlight type.

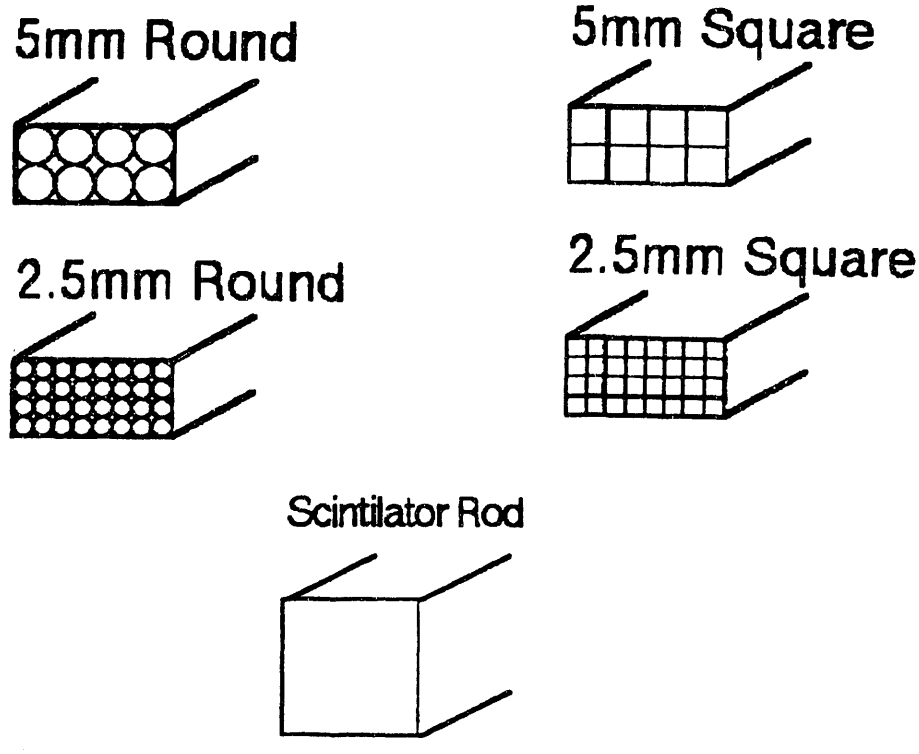

Figure 2: Four different shapes and sizes of 3m long scintillating fiber bundles, and one 1.5m long scintillator rod which are used for the test.

work, we have explored the possibility of using scintillating fiber bundles. The test results for light attenuation and timing characteristics of different types of scintillating fiber bundles are present, and they are compared to those of a scintillator rod.

Next, let us consider the case of a flash-light design. One inherent problem with conventional phototubes is that a timing shift is induced by a superposition of the Cerenkov light emitted from the window of the phototube with the scintillation light. To avoid this, a phototube with a separate photo-cathode was designed and constructed, which would suppress Cerenkov lights. A status report of the test will be presented.

Details about the test counters and experimental setup are given in section II. Specific results for TOF counters in a picket-fence design scheme will be presented in section III. The status of the Cerenkov-free phototube test will be given in section IV. Summary and plans for future will be given in section V.

II. EXPERIMENTAL SETUP

A. Counter design

We have tested four different types of TOF counters consisting of scintillating fiber bundles of dimensions 1cm×2cm×300cm in a picket-fence design. These were assembled out of round fibers of 2.5mm and 5mm diameter, and square fibers of 2.5mm and 5mm each side. This is shown in Fig. 2. Also indicated in the figure is a scintillator rod of dimension 1.5cm×1.5cm×150cm which was also tested. The scintillating fiber bundles and the scintillator rod were fabricated by Bicron, and were constructed out of BCF-99-22 and BC404 scintillating materials respectively. These two scintillating materials are practically identical and known to be the best for timing purpose.

In all cases, Hamamatsu R2083 phototubes in H2431 assembly were used for the test. The phototubes were mounted directly to both ends of a scintillator under test by using optical grease.

B. Test setup

A beam test was conducted at the KEK Proton Synchrotron using π^- beam at 2GeV/c. The goal of the test was two fold : (a) to test the performance of scintillators in a picket-fence design, and (b) to test a newly designed Cerenkov free phototube in case of a flashlight type design. A sketch of the test setup is shown in Fig. 3. Two beam defining counters and a veto counter are shown in the figure. For test (a), the time resolution was studied by measuring the time-of-flight of beam particles between the start counters and test

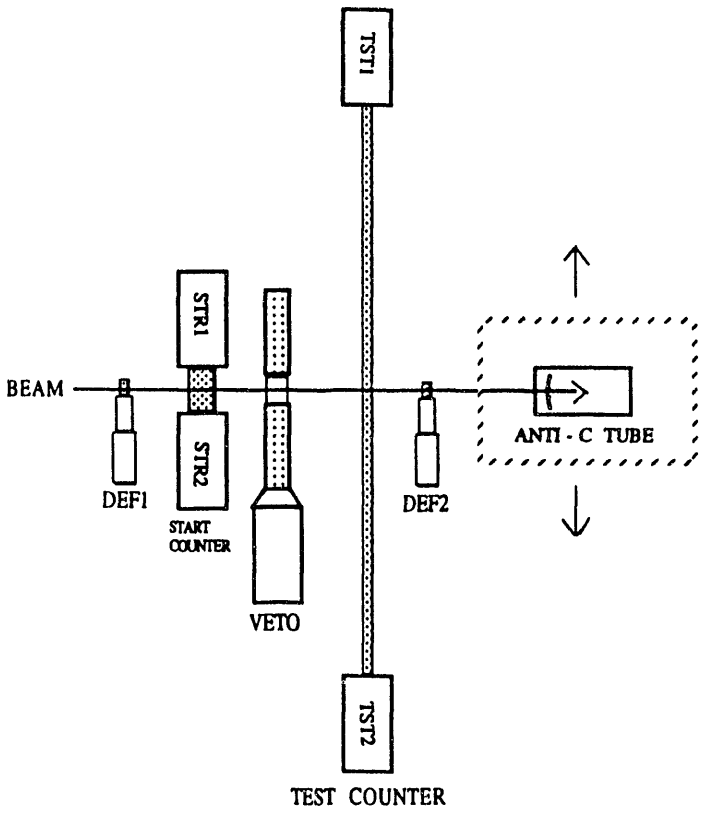

Figure 3: Schematic view of the test setup.

Table 1: Dimensions of individual counters used in the test and corresponding phototubes.

Name	Scint.(cm)	Phototube
DEF1	1 × 1 × 0.3	R647-09
DEF1	2 × 2 × 0.3	R647-09
TST1		H2431
TST2		H2431
STR1	4 × 4 × 0.5	H2431
STR2	4 × 4 × 0.5	H2431
VETO	10 × 20 × 1	H2431
ANTI-C	None	Prototype

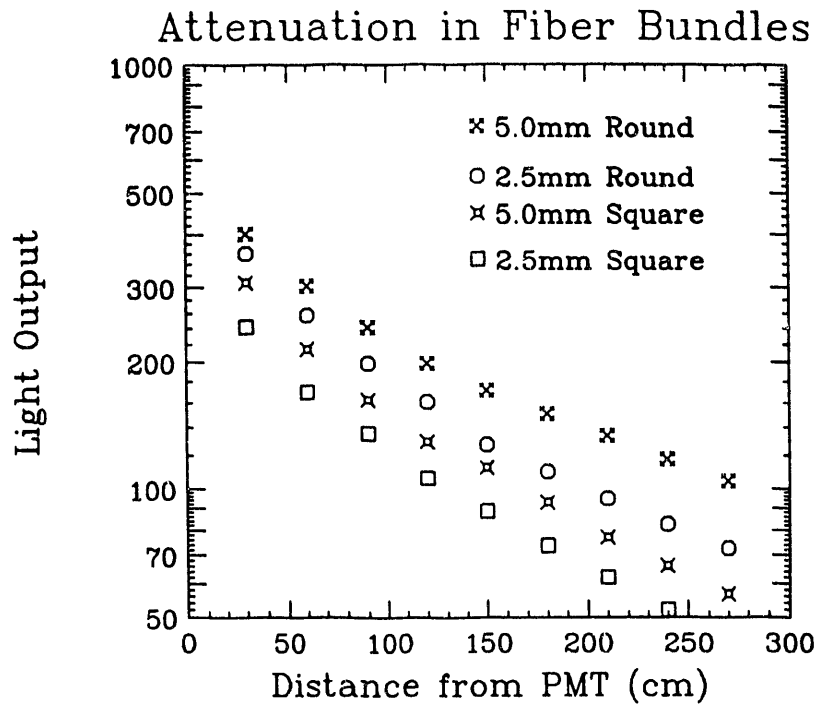

Figure 4: Light output from scintillating fiber bundles.

counters. The light attenuation and position dependence of time-of-flight was studied by shining the beam at different positions on the test counter.

For test (b), the Cerenkov-free phototube was placed directly in the beam with and without scintillators placed in front of the tube. This tube was mounted on a movable bench and could be moved with respect to the beam in order to determine if there is a timing shift when the beam enters the tube at different positions.

Table 1 summarizes the dimensions of individual counters and corresponding phototubes. All the phototubes were supplied by Hamamatsu.

III. RESULTS

A. Light yield

In Fig. 4, we show the light output as a function of the distance from the phototube for four types of scintillating fiber bundles. The curves show two components to light propagation. The attenuation lengths is about 120 cm for the first slope, and is about 200 cm for the second slope. While the origin of the two slopes is not completely understood, the attenuation length is sufficiently large for 3m long scintillators. Attenuation length is longer for bundles of round fibers as compared to square ones. Also because of this, light

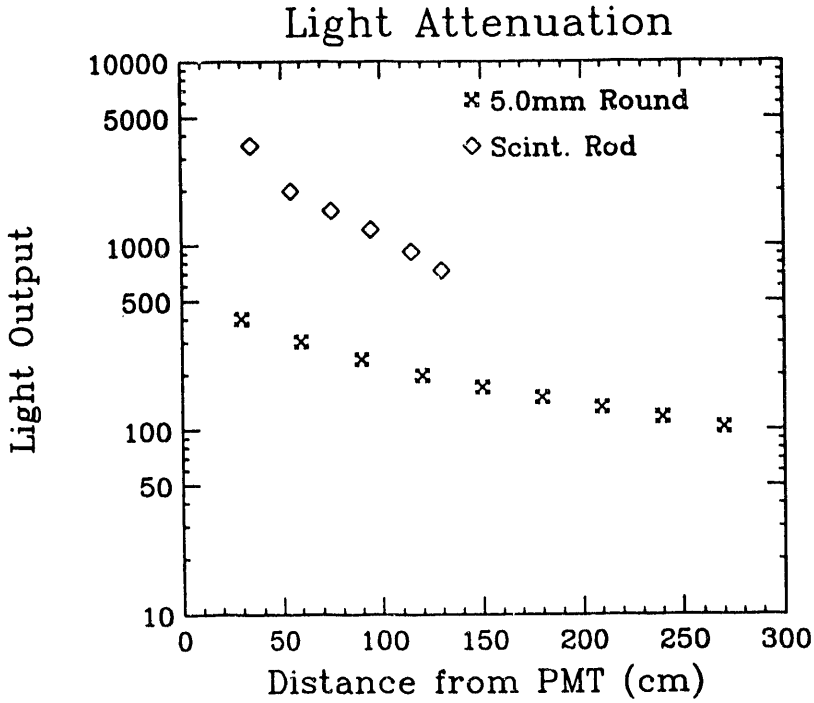

Figure 5: Light output from 5mm round scintillating fiber bundle compared to that of a scintillator rod.

outputs from round fibers are higher compared to the square ones. Larger light outputs were also observed for fiber bundles made of larger radii.

Fig. 5 shows the comparison of light output from a scintillating fiber bundle made of 5mm round fibers and a scintillator rod. The light output from the rod is larger compared to the fiber bundle, but the attenuation length is only about 80 cm.

B. Time resolution

The TOF between start counters and test counters is given by :

$$\mathrm{TOF} = \frac{t_{\mathrm{TST1}} + t_{\mathrm{TST2}}}{2} - \frac{t_{\mathrm{STR1}} + t_{\mathrm{STR2}}}{2} \qquad (1)$$

where t is the time obtained from the phototubes; TST1 and TST2 denote the tubes at both ends of the test counter, and STR1 and STR2 denote the tubes at both ends of the start counter. A scatter plot showing TOF and the integrated charge (q_{TST1}) for 5mm round fiber bundle is given in the left panel of Fig. 6, whereas the right panel shows the corresponding TOF distribution. The average value of TOF is taken to be zero.

The data for TOF is corrected for the slewing effect by replacing t with t' as :

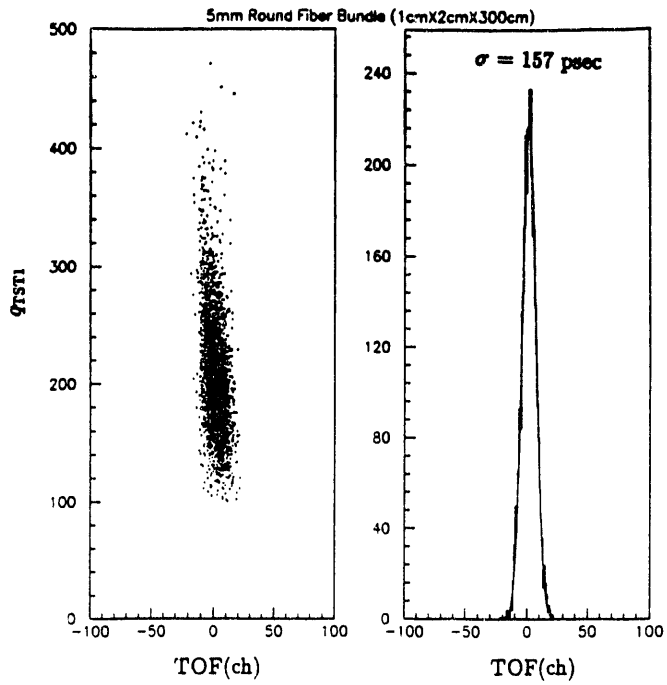

Figure 6: (a) Scatter plot of TOF and ADC values before slewing correction for 5mm round fiber bundle, (b) TOF spectrum. The solid curve is a Gaussian fit with $\sigma = 157$ psec.

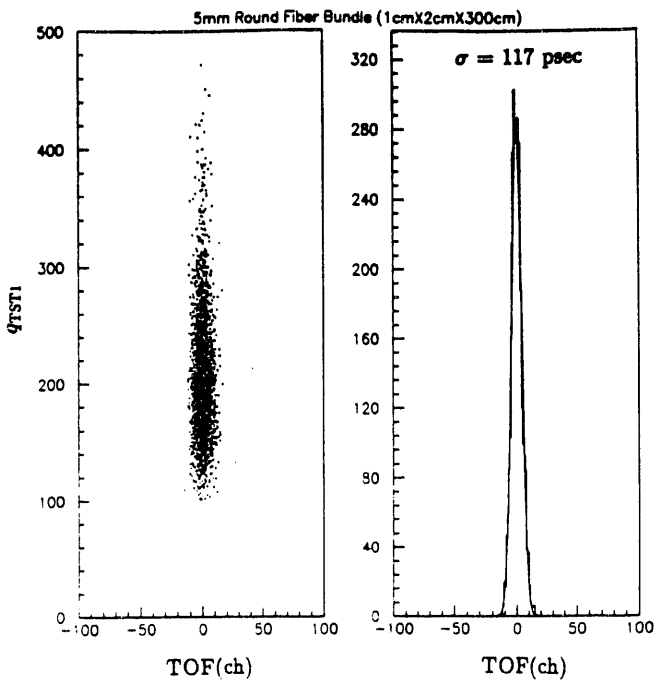

Figure 7: (a) Scatter plot of TOF and ADC values after slewing correction for 5mm round fiber bundle, (b) TOF spectrum. The solid curve is a Gaussian fit with $\sigma = 117$ psec.

Table 2: Time-of-flight resolution for different test cases.

Type	Res. w/o cor.	Res. with cor.
2.5mm Round (3m)	199 ps	133 ps
5.0mm Round (3m)	157 ps	117 ps
2.5mm Square (3m)	180 ps	127 ps
5.0mm Square (3m)	188 ps	137 ps
Scint. Rod (1.5m)	110 ps	77 ps

$t' = t + a + b/\sqrt{q}$,

where a and b are parameters for each phototube, and were determined by asymptotic method. Fig. 7 shows a scatter plot of the TOF and ADC values after slewing correction for a fiber bundle made of 5mm round fibers. The right panel in the figure gives the corresponding TOF distribution; the TOF resolution is obtained to be 117 psec.

The time resolutions obtained at the center of different scintillating fiber bundles are summarized in Table 2. In the table, the first column gives the type of the fiber. The second column gives the time resolution without the slewing correction and the third column gives the resolution after slewing correction is made. As can be seen from the table, the best TOF resolution from the fiber bundles is obtained to be 117 ps for 5mm round fibers. This could be because of large light output from 5mm round fiber bundles compared to fiber bundles made of other sizes and shapes of fibers. This can be better understood by studying time resolution from single fibers. On the other hand, TOF resolution from the 1.5m long scintillator rod is significantly better (= 77 psec).

The TOF resolutions from different scintillators were also studied as a function of hit position on the counter. This is given in Fig. 8.

IV. STATUS OF CERENKOV-FREE PHOTOTUBE TEST

A prototype of the Cerenkov-free phototube with a separate photo-cathode[2] was designed and constructed by Hamamatsu. A sketch of the tube is given in Fig. 9. In the test, the tube was placed directly in the beam with and without scintillators placed in front of the tube. From our preliminary data analysis we found some misarrangement of the phototubes during the May test runs. Therefore, more precise test runs are planned for the Fall, 1991.

V. SUMMARY AND FUTURE PLANS

We have presented results for light output and timing characteristics for four different sizes and shapes of 3m long scintillating fiber bundles. The bundles made of round fibers with larger cross section seem to have large light

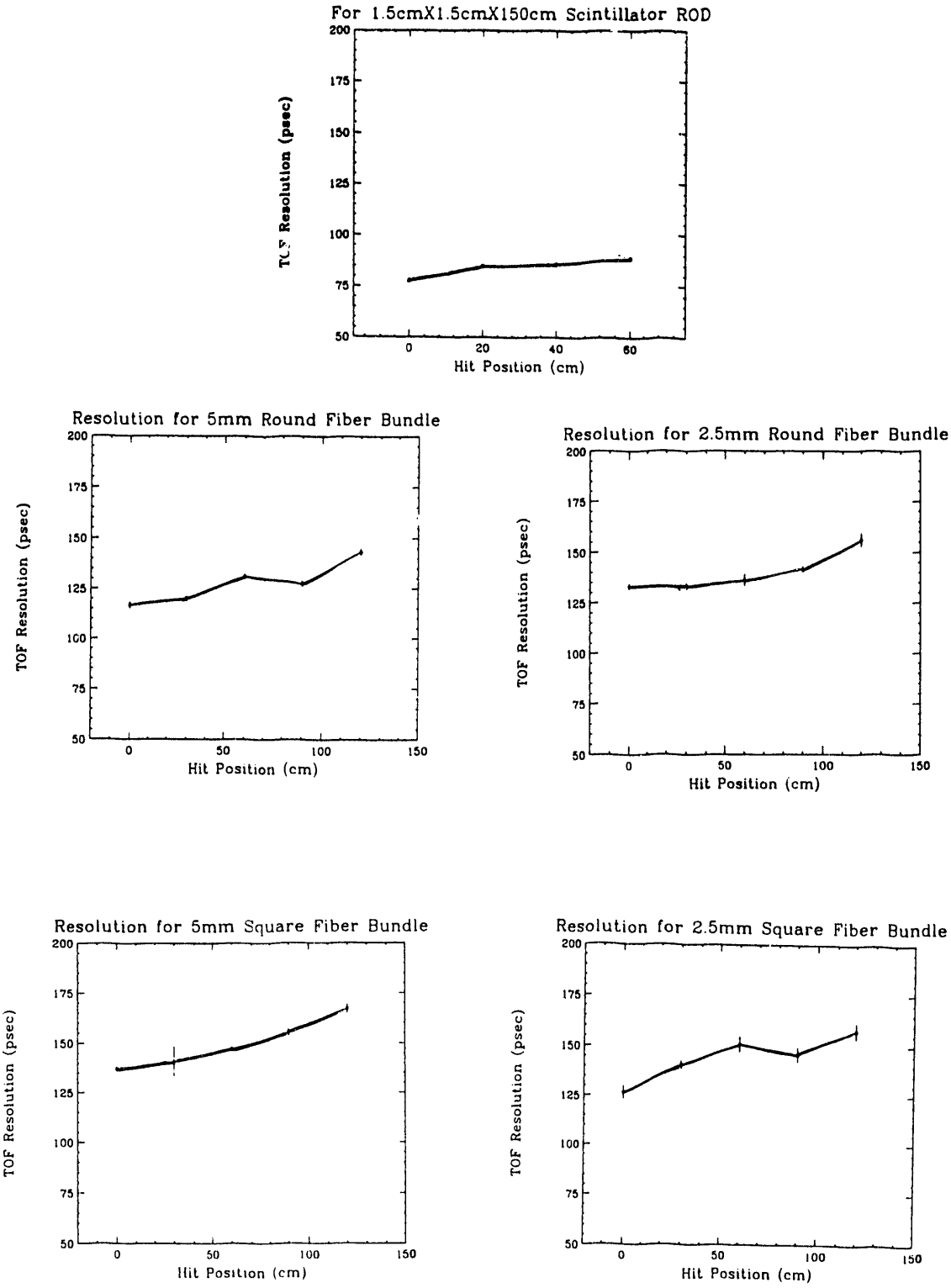

Figure 8: TOF resolutions as a function of hit position for different scintillators.

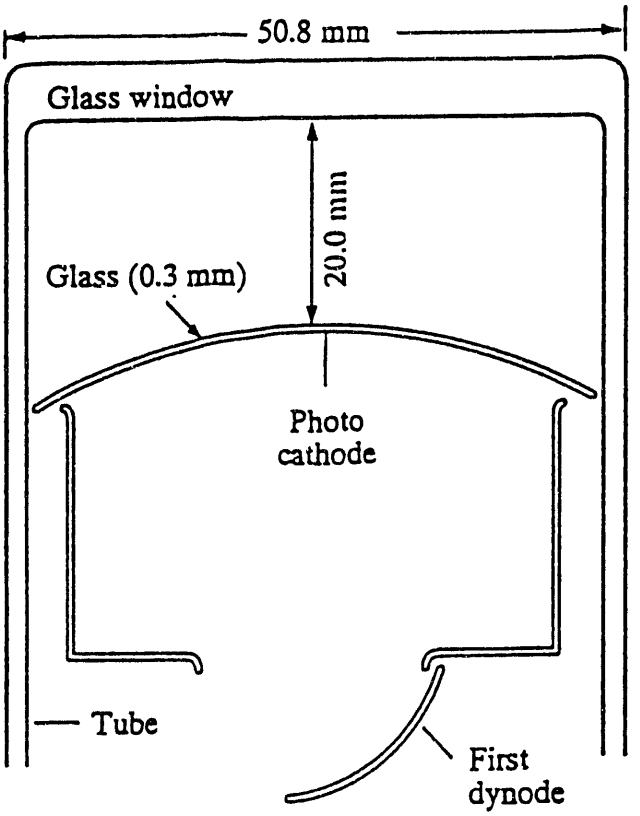

Figure 9: Sketch of the Cerenkov-free phototube

output, less light attenuation and better timing characteristics. The best time resolution (=117ps) was obtained for bundles made of 5mm round fiber bundles. A time resolution of 77 ps was obtained for a 1.5m long scintillator rod. The dependence of TOF resolution on the hit-position was studied. More careful analysis is underway to correct for the TOF value as a function of the hit-position.

Based on above results, a 3m long scintillator rod coated with low index material is prepared, and will be tested this fall. A phototube base is being designed with a discriminator and high voltage bleeder circuit mounted directly on it. This may somewhat improve the time resolution. Plans are being made to examine other types of phototubes which may improve the timing, and/or reduce the cost of the TOF counters.

REFERENCES

1. T. Abbott el al., Nucl. Instr. and Meth. A290 (1990) 41.
2. S. Nagamiya et. al., Fourth Workshop on Experiments and Detectors for a Relativistic Heavy Ion Collider, July 2-7, 1990, page 433.

RESEARCH AND DEVELOPMENT ON A SUB 100 PICO SECOND TIME-OF-FLIGHT SYSTEM BASED ON SILICON AVALANCHE DIODES

Y. Choi, A. Hirsch, A. Hauger, R. Scharenberg, M. Tincknell
Purdue University
West Lafayette, IN 47907

G. Rai
Lawrence Berkeley Laboratory
Berkeley, CA 94720

INTRODUCTION

Particle identification requires a momentum measurement and a second independent determination either energy loss (dE/dx) or time of flight (TOF). To cover a momentum range from 0.1 GeV/c to 1.5 GeV/c in the STAR detector requires both the dE/dx and TOF techniques.

This research is designed to develop the avalanche diode (AVD) detectors for TOF systems and evaluate their performance. The test of a small prototype system would be carried out at Purdue and at accelerator test beam sites. The Purdue group has developed a complete test setup for evaluating the time resolution of the AVD's which includes fast-slow electronic channels, CAMAC based electronic modules and a temperature controlled environment. The AVDs also need to be tested in a 0.5 tesla magnetic field. The Purdue group would augment this test set up to include a magnetic field.

A Schematic diagram of a typical diode is shown in Figure 1. For this diode the high field avalanche region is ~ 1μ thick and the reach-through depletion region has a ~ 120μ thickness. A minimum ionizing particle would traverse the whole detector and the FWHM pulse width would be ~ 5 n.s. We expect an internal amplification G, where 20 < G < 100, and with a signal to noise ratio S/N where 20 < S/N < 60.

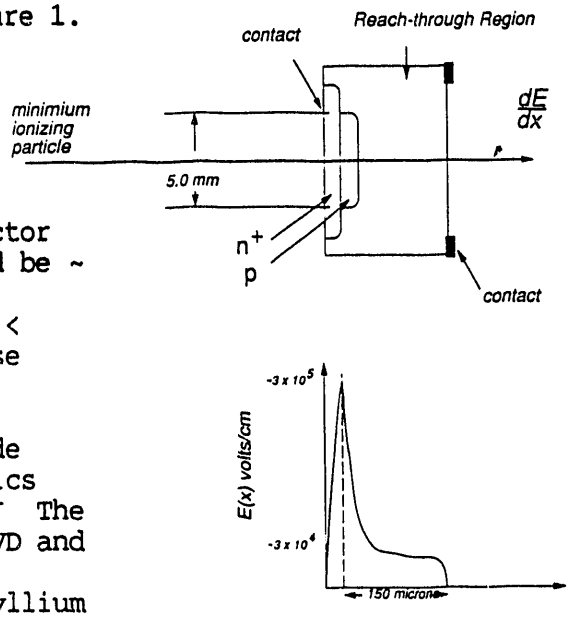

We have obtained four diode modules from the optoelectronics division of EG&G in Montreal.[1] The modules consist of a 25 mm^2 AVD and a GaAs FET preamplifier in a shielded case with a thin beryllium

window. Figure 2 shows the top and side views of the modules. The dimensions are given in inches. Table I summarizes the design considerations for these units.

Figure 2

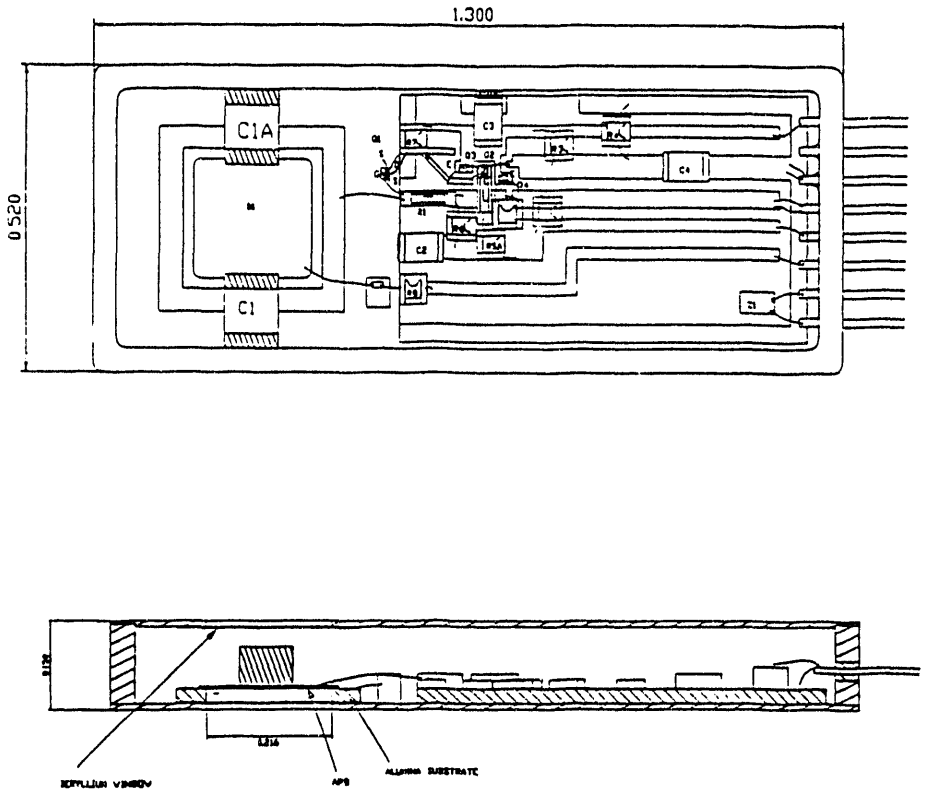

TABLE 1

Diode Description	The diode is a 5 x 5 mm silicon APD of the reach-through design. Typical diode parameters are: diode capacitance 21-25 pF; diode dark current I_{ds} = 200 nA; I_{db} = < 100 pA; $I_{total} = I_{ds} + G \cdot I_{db}$.
High Voltage	In the +300 to +500 volt range. We have moved the bypass capacitor C1 to the side, as shown in the drawing, and in fact added a second capacitor C1A, in order to minimize jitter

	resulting from signal propagation times across the diode. We coated the p^+ surface of the diode with a thin metallic layer to reduce its spreading resistance. We left part of the diode uncoated so that calibration using optical inputs is still possible.
Amplifier Gain	30
Amplifier 3 dB Bandwidth	~ 100 MHz
Maximum Noise Voltage (expected to be at about 100 MHz)	40 $nV/Hz^{1/2}$
Total Integrated Noise Voltage	~ 0.5 mV
Expected signal from a MIP at an effective gain of 40 to 50	~ 30-40 mV in a pulse with a FWHM of about 4-5 ns
Gain uniformity	Gain non-uniformity across the diode, expected to be about $\pm$ 5% typical, $\pm$ 10% maximum, at a gain of 50. Gain non-uniformity should also be suppressed somewhat by the space-charge induced gain-compression.

We are presently evaluating the performance of the diodes. Particular attention will be paid to the signal to noise behavior. The gain vs. voltage performance is similar to that reported by Petrillo et al.[2]

A schematic sketch of the test arrangement is shown in Figure 3. A beta source provides minimum ionizing particles (MIP) which traverse the diodes and stop in a scintillator. Fast-slow electronics completes the arrangement. The counter assembly can be cooled to -20°C.

Direct measurements on individual diodes with G = 40 show a triangular pulse with a full rise time of 3 ns. A pulse height of ~ 25 mv is observed for a traversing particle. The pre-amplifier noise is ~ 0.4 mv. This appears to suggest that the space charge induced gain reduction is ~ 20% as the estimate based on the small signal gain G = 40 corresponds to ~ 30 mv. Coincidence studies are in progress.

Figure 3

assembly diagram

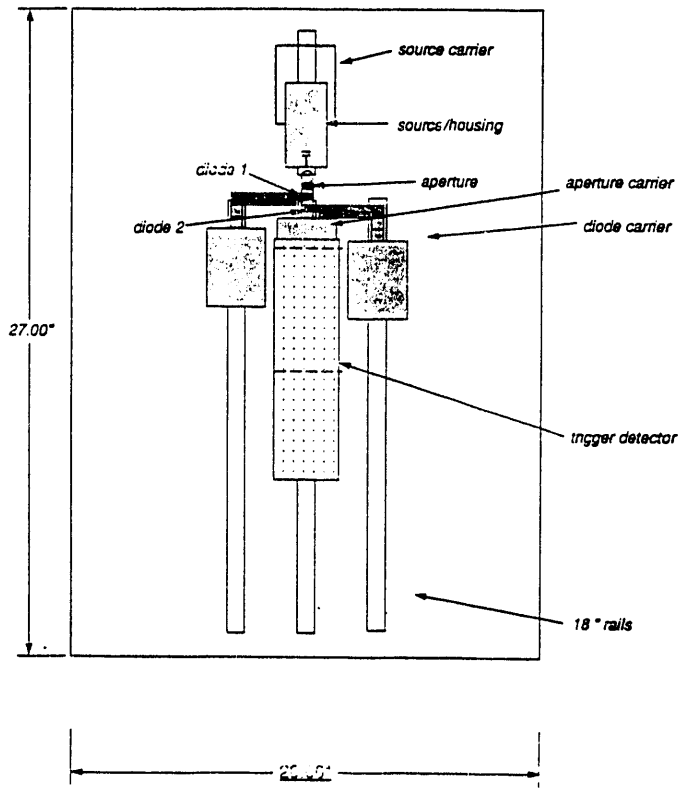

REFERENCES

1. P. R. Webb et al., Properties of Avalanche Photo Diodes, RCA Review 35, 234 (1974).

2. G. A. Petrillo et al., Scintillation Detection with Large-Area Reach through Avalanche Photodiodes, IEEE Transaction on Nuclear Science, Vol. NS-31, 417 (1984).

Behavior of TPC's in a High Particle Flux Environment*

A. Etkin, S.E. Eiseman, K.J. Foley, R.W. Hackenburg, R.S. Longacre
W. A. Love, T.W. Morris, E.D. Platner and A.C. Saulys
Brookhaven National Laboratory, Upton, New York 11973

S.J. Lindenbaum
Brookhaven National Laboratory and City College of New York

C.S. Chan, M.A. Kramer, K.H. Zhao and Y. Zhu
City College of New York, New York, New York 10031

T.J. Hallman and L. Madansky
Johns Hopkins University, Baltimore, Maryland 21218

S. Ahmad, B.E. Bonner, J.A. Buchanan, C.N. Chiou, J.M Clement
G.S. Mutchler, and J.B. Roberts
Bonner Nuclear Laboratory, Rice University, Houston, Texas 77251

Abstract

TPC's (Time Projection Chamber) used in E-810 at the AGS (Alternating Gradient Synchrotron) were exposed to fluxes equivalent to more than 10^7 minimum ionizing particles per second to find if such high fluxes cause gain changes or distortions of the electric field. Initial results of these and other tests are presented and the consequences for the RHIC (Relativistic Heavy Ion Collider) TPC-based experiments are discussed.

1 Introduction

In order to study the performance of TPC's in a high particle flux environment we have made a number of measurements utilizing the AGS experiment E-810 TPC's[1]. This experiment uses 3 TPC modules in a vertical dipole magnetic field (Fig. 1). Silicon and proton beams can be directed to a variety of nuclear targets ranging from *Si* to *Pb*. In the forward hemisphere the experiment has high acceptance and has reconstructed events with up to 130 charged particle tracks from a heavy target. Results of the initial analysis will be presented, distortions in the electric field due to positive ions, two vertex resolution and reconstruction efficiency at high track density. Application of these results to the question of luminosity limitation capability of the "STAR"[2] experiment at RHIC will be discussed.

* This research was supported by the U.S. Department of Energy under Contract Nos. DE-AC02-76CH00016, DE-AC02-83ER40107, DE-SG02-88ER40413, DE-FG05-87ER40309, and the City University of New York PSC-BHE Research Award Program.

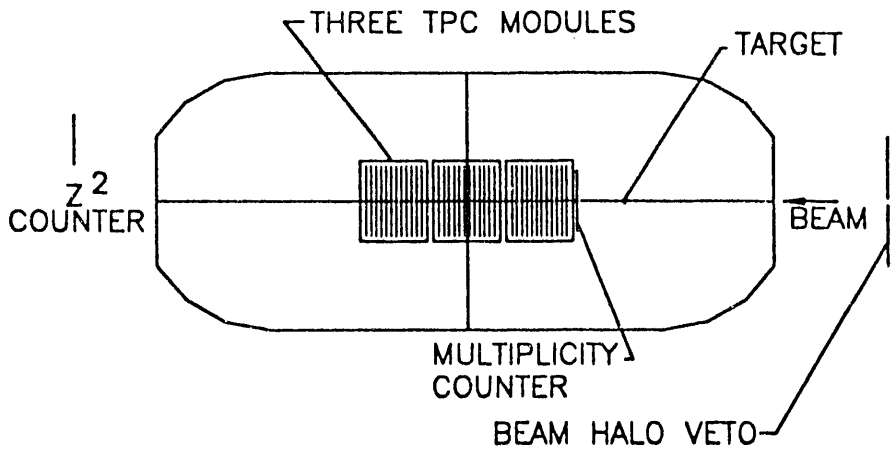

Figure 1: Plan view of E-810 apparatus.

2 Distortions Due To Ion Loading

Figure 2 shows a head on view of an E-810 TPC. The ion beam passes directly through the center of the TPC. The beam is typically 1.5 cm wide by 0.6 cm high in the center of the first TPC module. The AGS beam has a spill duration of 1 second. About 300ms after the beam starts positive ions created at the beginning of the spill reach the negative HV electrode. At this point a sheet of ions has formed from the beam to the HV electrode. This produces a distortion of the "uniform" electric field. In fact the electrons which are drifting down will see a reduction in electric field near the beam causing the drift velocity to be reduced in the vicinity of the beam. We have studied this effect by raising the *Si* beam to 67K per 1 second spill. This then produces, after $\sim$ 300ms, a positive ion loading of 10^7 ions/cm^3 along the beam path. Two distortions are produced, the first is in the drift direction Y and the second is in the horizontal direction X. In order to measure these effects the difference between the projected beam track position and the position determined in the TPC is calculated. Projected beam track positions are determined using two sets of X and Y measuring beam PWC's. A run at low rate (4K ions per spill) with a defocussed beam (10 cm wide by 12 cm high) is used to determine the relationship between row numbers, wire numbers and drift time, and the trajectory position in the TPC. The differences ΔX and ΔY (projected position - TPC position) are calculated for subsequent runs. Figure 3 shows ΔY in a high rate run at the center of the first TPC module as a function of event number during the spill with 30ms between events. As can be seen, after $\sim$ 300ms the distortion reaches a maximum and remains relatively constant until near the end of the spill when the beam intensity drops. This is consistent with the development of an ion sheet during this time that reaches equilibrium after $\sim$ 300ms.

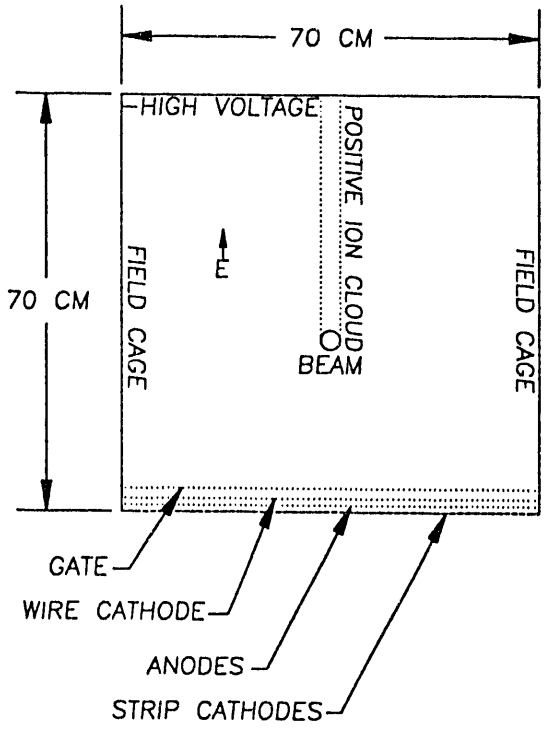

Figure 2: Section of a TPC looking along the beam showing beam spot and positive ion sheet.

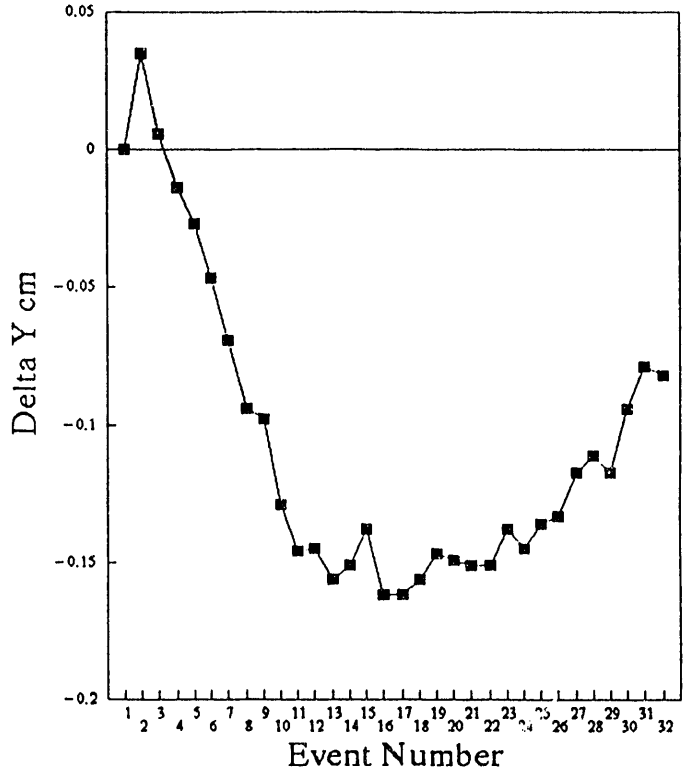

Figure 3: ΔY versus spill event number for small beam.

Each TPC has 12 rows surrounded by a field cage. In Fig. 4 we plot the distortion, ΔY, versus row number (rows 19 & 20 were not working and are not plotted) after 360ms into the spill for a small beam. We see the first and last rows (nearest to the field cage) have much less distortion then the middle . This appears to be because of the proximity of the field cage which minimizes the electric field distortions caused by the ion sheet. Figure 5 shows ΔY versus row number measured using a large beam (10 cm $\times$ 12 cm). In both cases ΔY is negative indicating a decrease in the effective drift velocity in agreement with preliminary electrostatic calculation which give a 2mm maximum shift. Figure 6 shows the ΔX measured in the middle of the first TPC module, versus X beam for the small (1.5 cm by 0.6 cm) beam. ΔX is largest near the edge of the beam and zero at the beam center as expected if the drifting electrons are attracted to the positive ion sheet.

At RHIC the Central TPC will have a minimum ionizing track rate of 2×10^6 tracks per second for $Au - Au$ collisions. At the inner radius this is spread out over an area of 3 m^2 or 70 tracks per cm^2 per second. The E-810 test had a track density of $> 10^7$ minimum ionizing tracks in a 1 cm^2 spot yet this ion loading caused a distortion in the drift direction of only 1.5 mm.

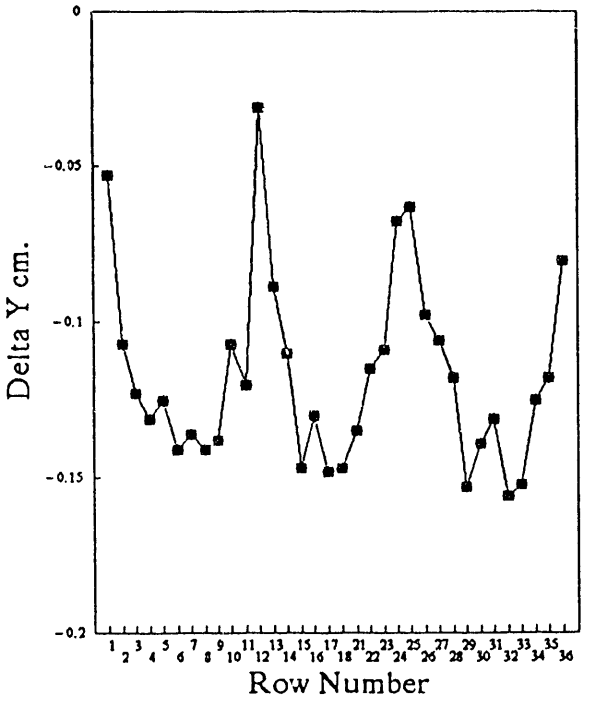

Figure 4: ΔY versus row number for small beam.

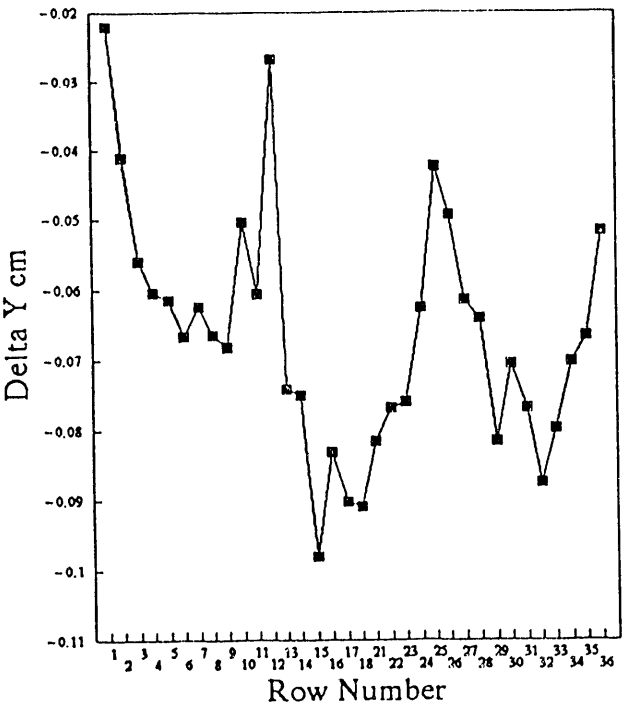

Figure 5: ΔY versus row number for big beam.

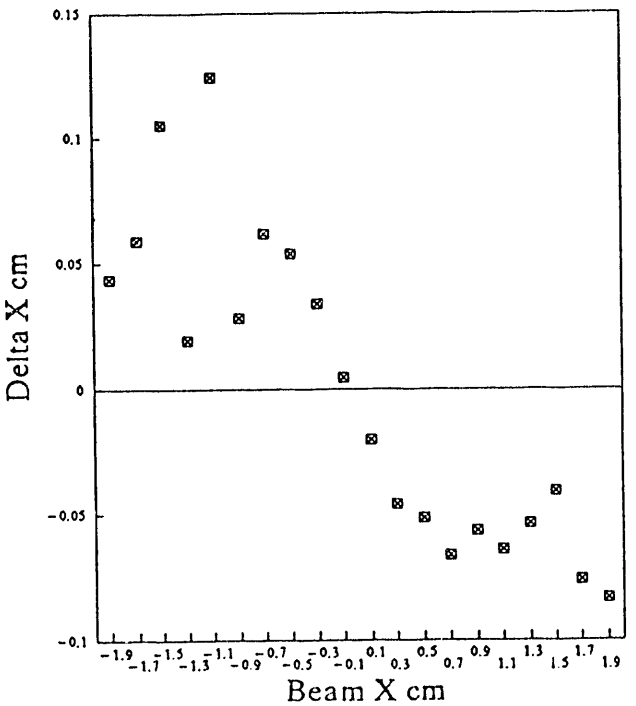

Figure 6: ΔX versus projected X for small beam.

3 Two Vertex Resolution

In experiment E-810 a typical event from $p - Pb$ has 3 charged particles. After reconstruction, an event having a vertex displacement of 5 or more mm from the incoming beam position is easily distinguished. Therefore we expect at RHIC where $Au - Au$ collisions produce several thousand charged particles, events with even smaller two vertex separations can be distinguished. This is important because the TPC live time is $50\mu s$. We expect $p - p$ collisions to occur at 10^6 per second; an average of 50 events would occur in the live time of the TPC. Only a few percent of these will produce an apparent overlap within the vertex resolving space of two events. This condition can be detected by other devices such as silicon vertex detectors and TOF counters. These occurrences can simply be rejected from the data sample. It should be noted that 50 overlapping, $p - p$ collisions produce fewer charged particles than a single $Au - Au$ collision. Even at the highest RHIC luminosity the only penalty one pays for this long live time is increased event processing time since all tracks must be reconstructed before out of time collision can be rejected. E-810 has demonstrated that the processing time is proportional to the number of tracks since a TPC directly yields 3 dimensional points along the tracks.

4 Reconstruction Efficiency At High Track Density

In experiment E-810 the track density in the front of the first TPC is shown in Fig. 7. During this run the TPC's had only 2/3 of the rows operating. Under these conditions the track reconstruction efficiency is greater than 90%. In the "STAR" TPC the maximum track density is predicted to be less than $0.1/cm^2$ and therefore the reconstruction efficiency is expected to be in the high 90's. It should be noted that in both cases the tracking is initiated at the low density (downstream end) of the TPC system but successfully proceeds into the high density region near the interaction.

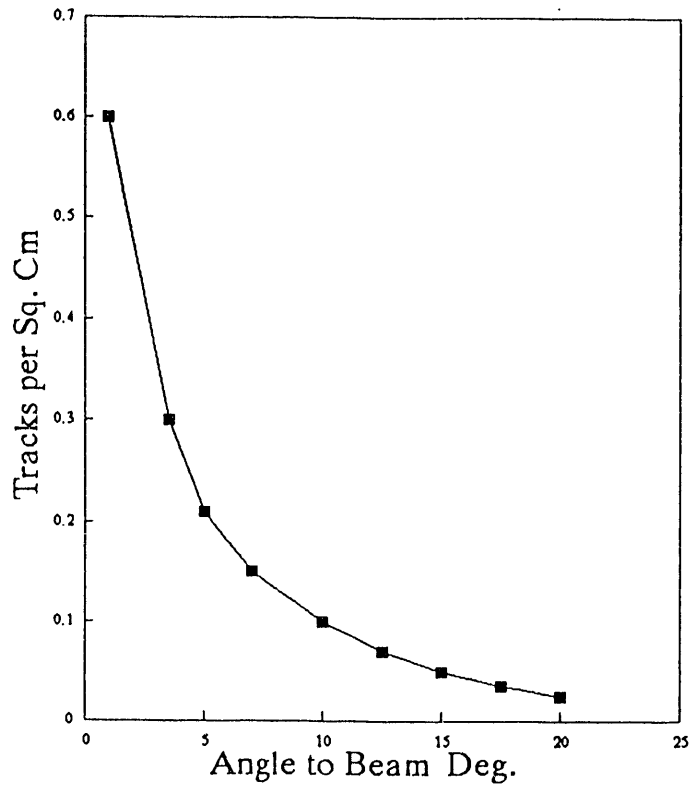

Figure 7: Track density in the first row of E-810 TPC's as a function of angle.

5 Robustness For Efficiency At High Particle Fluxes

At track densities of 10^7 minimum particles per second per cm^2 PWC's and drift chambers lose gain because each track produces an avalanche of $\approx 10^5$ per primary ionization. Thus the ion loading in the gas is 10^5 times higher than in a TPC where only tracks from events of interest are allowed to enter the avalanche space by a gating structure. In addition the gate prevents positive ions from the avalanche from entering the drift space. Therefore only the ions from the primary ionization can produce distortion in the electric field. Remarkably, this makes the TPC more robust to high event rates than either PWC's or drift chambers since they cannot be gated and there is no mechanism to trap the positive ions from the avalanche process. In the RHIC environment there can be large bursts of particles caused by distributed losses. In the TPC it will be possible in most cases to prevent the opening of the gate and therefore prevent excessive current in the TPC detector end caps.

6 TPC Development for RHIC

About half of the FY91 funding for R & D was for travel between BNL and LBL that led to the merger of LOI#3 and LOI#5. The rest was spent on a pad readout test TPC and miscellaneous electronics. Most of the productive effort was the result of simulations on high rate, high track density performance of TPC's which were confirmed by measurements with the E-810 apparatus, shown previously in Fig. 1.

Software was developed to simulate the electrostatic field. In addition electron drift in this field is simulated all the way to the charge distribution induced in the pad readout. One important result of this simulation is better that 200 μ position resolution is achieved by recording charge on the 3 pads nearest the avalanche even with a 20% noise contribution.

Progress was also made in custom electronics for TPC readout, two parallel efforts are under way. The charge amplifier-shaper and analog memory efforts at LBL are discussed in another paper. The BNL effort consists of a transresistance amplifier-shaper under development at UCSC that has a very high degree of integration and reamarkably low power. We expect to have prototypes for testing early in 1992. An analog storage with data compaction logic IC is under development at Analytek under an SBIR contract. This is complementary to the LBL analog memory effort.

A prototype radial drift TPC is being designed and will be built for testing in calendar 1992 running at the MPS. This radial TPC is proposed for external tracking at "STAR".

7 Conclusions

Measurements of distortions due to ion loading in the E-810 TPC's have been found to be small even at very high effective particle fluxes. This result supports the use of TPC's at RHIC even at the highest planned luminosity. In addition measurements of two vertex resolution and reconstruction efficiency at high track density show that a TPC is an excellent detector for RHIC.

8 References

[1] A. Etkin, *et al.* "Modular TPC's for Relativistic Heavy-Ion Experiments", *Nuclear Instruments and Methods*, Vol. A2837, No. 3, pp. 557-566, November 1989. A. Etkin, *et al.* "A TPC for Large Solid Angle Relativistic Heavy Ion Experiments", *IEEE Transactions on Nuclear Science*, Vol. 36, No. 1, Part I, pp. 58, February 1988.

[2] "STAR", Solenoidal Tracker At RHIC, approved major detector for RHIC, see LBL-31040, 1991 and LBL-29651, 1990. K. Kadija, G. Paic, D. Vranic - Rudjer Boskovic Institute; G. Danby, S. Eiseman, A. Etkin, K.J. Foley, R.W. Hackenburg, M.J. LeVine, R.S. Longacre, W. A. Love, E.D. Platner, A.C. Saulys, J.H. Van Dijk - Brookhaven National Laboratory; F.P. Brady, J.E. Draper, J.L. Romero - University of California at Davis; J.B. Carroll, V. Ghazikhanian, E. Gulmez, T.J. Hallman, G.J. Igo, S. Trentalange, C.A. Whitten, Jr. - University of California at Los Angeles; M. Kaplan, P. Karol, Z. Milosevich, E. Vardaci - Carnegie-Melon University; M.G. Cherney - Creighton University; S. Margetis, R.E. Renfordt, D. Röehrich, R. Stock, H. Ströebele, S. Wenig - University of Frankfurt; L. Madansky - The Johns Hopkins University; B.D. Anderson, D. Keane, R. Madey, J. Watson - Kent State University; F. Bieser, M.A. Bloomer, D.A. Cebra, W. Christie, E. Friedlander, D. Greiner, C. Gruhn, J.W. Harris, H. Huang, P.M. Jacobs, S.A. Kleinfelder, P.J. Lindstrom, H. Matis, C. McParland, R. Morse, C.J. Naudet, G. Odyniec, D.L. Olson, A.M. Poskanzer, G. Rai, H.-G. Ritter, I. Sakrejda, J.O. Schambach, L.S. Schroeder, P.A. Seidl, T.M. Symons, H. Wieman, W.K. Wilson - Lawrence Berkeley Laboratory; C.S. Chan, M.A. Kramer, S.J. Lindenbaum - City College of New York; A. Aprahamian, N.N. Biswas, U. Garg, V.P. Kenney, J. Piekarz - University of Notre Dame; T. Humanic University of Pittsburgh; D.D. Carmony, Y. Choi, A. Hirsch, E. Hjort, N.T. Porile, R.P. Scharenberg, B. Srivastava, M.L. Tincknell - Purdue University; D.L. Adams, S. Ahmad, B.E. Bonner, J.A. Buchanan, C.N. Chiou, J.M. Clement, M.D. Corcoran, T. Empl, H.E. Miettinen, G.S. Mutchler, J.B. Roberts, J. Skeens, I. Stancu - Rice University; A.D. Chacon, K.L. Wolf - Texas A & M University; W. Dominik, M. Gazdzicki - Warsaw University; T. Pawlak, W. Peryt, J. Pluta - Warsaw University of Technology; W.J. Braithwaite, J.G. Cramer, D. Prindle, T. Trainor, - University of Washington; A. Breskin, R. Chechik, Z. Fraenkel, I. Tserruya - Weizmann Institute of Science.

Generic R&D on Undoped Cesium Iodide and Lead Fluoride

J.A.Kierstead, P.W.Levy, S.Stoll, C.L.Woody

Physics Department
Brookhaven National Laboratory

M.Goldberg, N.Horwitz, T.Skwarnicki, Z.Sobolewski

Physics Department
Syracuse University

D.F.Anderson, E.J.Ramberg, J.Zimmerman

Fermilab

A.Ray

Oak Ridge National Laboratory

ABSTRACT

A summary is given on the recent progress on generic R&D on undoped CsI and PbF_2. Both of these materials are being investigated for use as a high resolution electromagnetic calorimeter for RHIC, as well as for other potential applications. Results are given on the development of a low gain readout system for use with undoped CsI crystals. A study has also been made of radiation damage in both undoped and thallium doped CsI. The progress on the growth of large, high quality PbF_2 crystals, which would be suitable for calorimeter applications, is discussed, and some first test beam results with a prototype PbF_2 calorimeter are given. Finally, results are presented on the improved radiation resistance of the new PbF_2 material.

INTRODUCTION

This report is a brief summary of our generic R&D work on undoped cesium iodide and lead fluoride. A more complete discussion of the current status of both of these projects can be found in reference [1]. The work on undoped CsI began several years ago as part of the detector R&D program for RHIC [2-3]. This project has successfully completed its generic phase and is now part of the detector R&D program of one of the major RHIC experiments [4-6]. Some of the results of this R&D has already been published [7] and additional progress is described in a separate report [8]. The work on lead fluoride began last year as a R&D project originally intended for RHIC [9], but was approved as more generic investigation. It is hoped that the effort on PbF_2 can be continued in order to develop this material to a point where it can be considered for practical applications as was done in the case of undoped CsI.

PROGRESS ON UNDOPED CSI

Our work on undoped CsI has focused in two main areas. One has been the development of a readout system consisting of a low gain readout device followed by a matching system of readout electronics. The other area has been the study of radiation damage in undoped CsI, and a comparison of the observed radiation effects with those measured in CsI(Tl) and other crystals. It should be noted that the study of radiation damage is *not* part of the RHIC detector R&D on undoped CsI proposed in ref.[4], although radiation hardness is certainly an important factor in detector performance. This is true even for applications such as at RHIC where radiation levels are expected to be relatively low, but where high precision and stability are required.

The development of the readout system has involved the design of a fast, low noise preamplifier with characteristics which are well matched to the fast component scintillation light of undoped CsI. The basis for this design was taken from the preamplifier used in the CLEO II detector for the readout of large CsI(Tl) crystals [10]. The design was modified to accomodate the much faster decay time ($\tau_s \sim 10$ ns and 35 ns) and reduced light output of undoped CsI. Our original design followed the CLEO II concept, with four silicon photodiodes (Hamamatsu S-3590) mounted in a common package viewing one 3.5 x 3.5 x 30 cm^3 crystal. This gives reasonably good photocathode coverage with standard 1 cm^2 diodes, and provides redundancy by having more than one readout device per crystal. The final design of the preamplifier and shaping amplifier is shown in Fig. 1. The shaping amplifier has a peaking time $\tau_p \sim 100$ ns and a total pulse width of $\tau_w \sim 500$ ns. It provides a smooth, shaped pulse which integrates the fast component signal from the CsI for approximately 3 τ_s and cancels the tail of the residual slow component to restore the baseline to zero after τ_w. The zero crossing of the bipolar pulse can also be used in conjunction with a zero crossing discriminator to provide timing information.

Nine of these readout assemblies were built at Syracuse University. They were tested using the central nine blocks of a prototype detector, described in

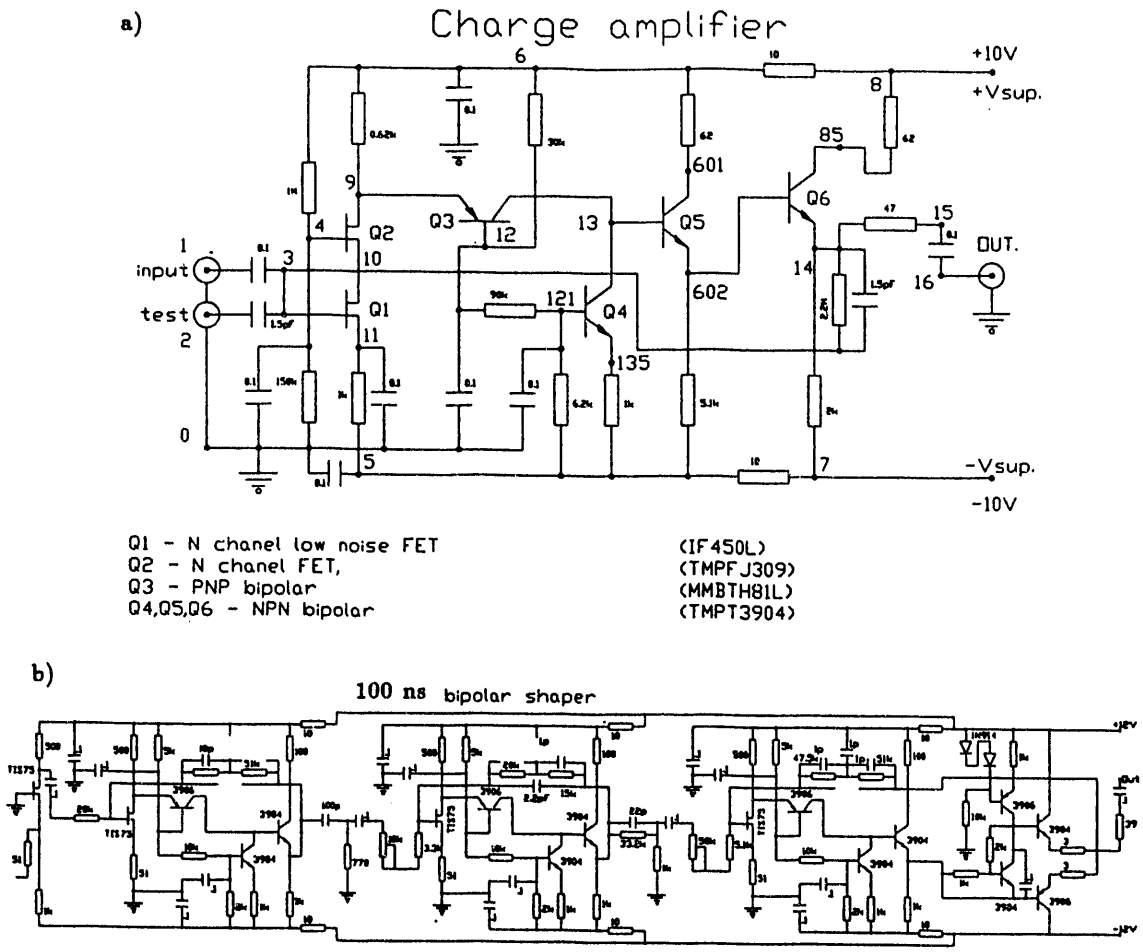

Fig.1 a) Final preamplifier design for silicon photodiode readout b) circuit diagram of the bipolar shaping amplifier

ref.[4], consisting of a 5x5 array of 3.5 x 3.5 x 30 cm^3 crystals. This array was studied in a test beam earlier this year at the AGS using beams of electrons and pions with momenta from 1-10 GeV/c. A description of additional results from this test using photomultiplier tubes to read out the crystals can be found in ref.[4]. The results with the silicon photodiode readout showed that, while the electronics performed quite well, the light output from the fast component of undoped CsI is simply not large enough to achieve a good signal to noise ratio at energies $\lesssim$ 1 GeV/c with silicon photodiodes. The electronic noise from the four diodes summed together was $\sim$ 3000 electrons rms under ideal conditions in the lab, and $\sim$ 9750 electrons rms in the test beam at the AGS. The additional noise was primarily due to electrical interference from the AGS enviroment. This could have been reduced with better shielding and grounding of the detector while in the beam, but the limited time available for the beam test did not permit an attempt to reduce the noise below this point. The signal

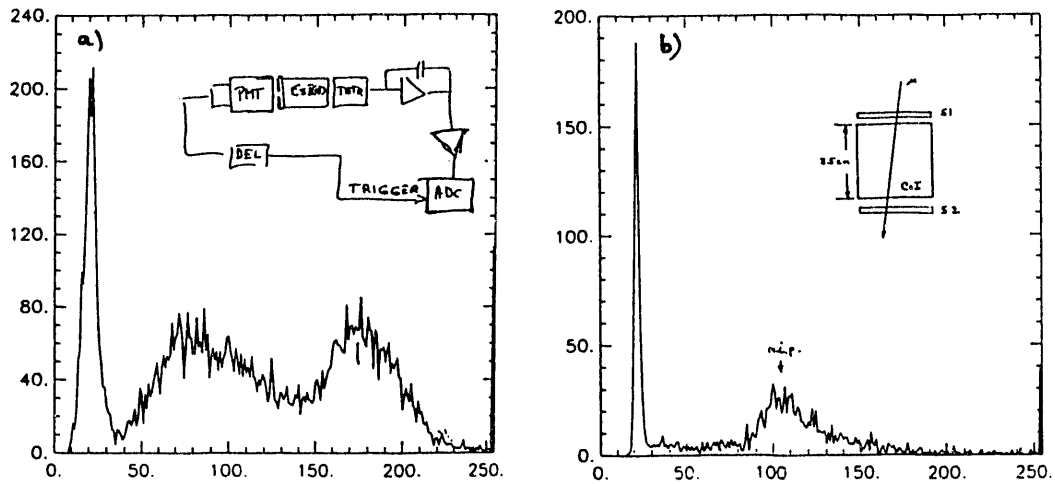

Fig.2 Pulse height spectrum for a) ^{137}Cs gamma rays (662 KeV) in a 1" dia. x 1" long CsI crystal using vacuum phototetrode readout with 2 μsec shaping time b) cosmic rays passing through the 3.5 cm path length of a 3.5 x 3.5 x 30 cm^3 sample using vacuum phototetrode readout with 100 ns shaping time.

measured for 1 GeV/c electrons was $\sim$ 100,000 electrons. While this signal to noise ratio may be adequate for measurements at higher energies, it is not satisfactory for the energy range of interest at RHIC if good energy resolution is required. We do not, however, discount the use of a silicon photodiode readout for undoped CsI for higher energy applications.

It is clear that a readout device with modest gain would greatly improve the signal to noise ratio in the lower momentum range. We have therefore begun to investigate several types of low gain vacuum readout devices for this purpose. These include vacuum phototriodes and phototetrodes which provide gains $\sim$ 10-30. In addition to the advantage of higher gain, they provide better photocathode coverage of the crystal and have lower capacitance than silicon photodiodes, which results in lower noise. These devices also operate at lower voltages, have a larger dynamic range and are more stable with respect to voltage variations than conventional photomultiplier tubes. They also work inside a magnetic field. The electronics required for this type of readout is very similar to that which was used for the silicon photodiodes, consisting of a preamplifier and shaping amplifier with very similar characteristics.

We have tested two such low gain devices, one vacuum phototriode (Hamamatsu R2148) and one phototetrode (Hamamatsu 2149). Figure 2a shows the pulse height spectrum for ^{137}Cs gamma rays in a 1" dia. x 1" long crystal otained with the phototetrode with a shaping time of 2 μsec. The peak corresponds to a signal of $\sim$ 11,550 electrons into the preamplifier for an energy of 662 keV with the tetrode operating at a gain of $\sim$ 30. Figure 2b shows a spectrum for cosmic rays passing through the 3.5 cm path length of a 3.5 x 3.5 x 30 cm^3 crystal ($\sim$ 19.6 MeV energy deposit) with a 100 ns shaping time. The peak corresponds to

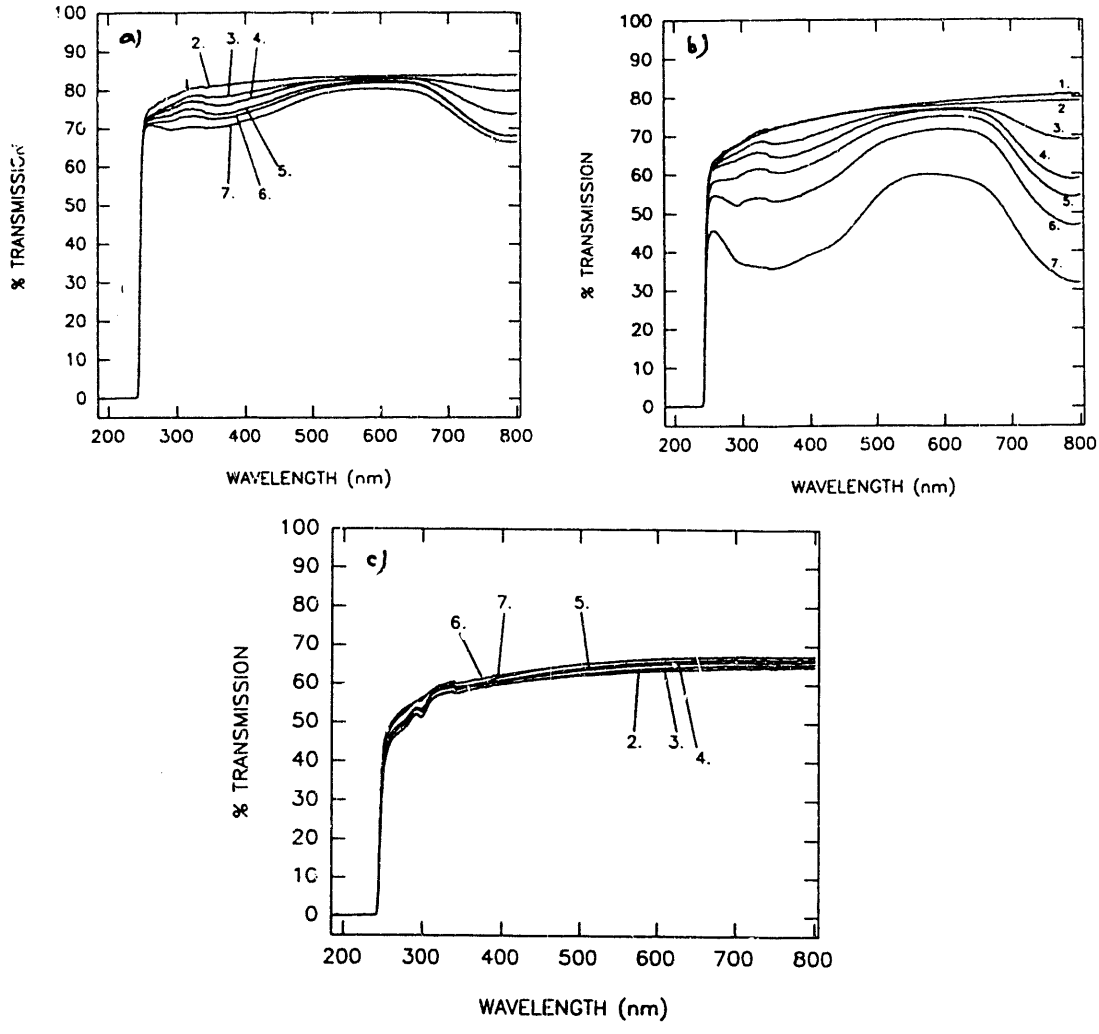

Fig.3 Transmission vs. wavelength for 1" dia. x 1" long undoped CsI samples (a) BDH, (b) Horiba and (c) Q&S for doses of:(1) unirradiated, (2) 10^3, (3) 10^4, (4) 6 x 10^4, (5) 2.6 x 10^5, (6) 9.0 x 10^5 and (7) 4.2 x 10^6 rad.

$\sim$ 4000 electrons per MeV at the input to the preamplifier with a noise of 1100 electrons rms, implying $\sigma_{noise} \sim 0.27$ MeV. These first measurements are quite encouraging and show that this type of readout can be used down to very low energies with a good signal to noise ratio.

We have used the HIRDL [11] facility at Brookhaven National Lab to simultaneously irradiate a number of 1" dia. x 1" long samples of undoped CsI and CsI(Tl) from several different suppliers [12–14] up to a dose of 4.2 x 10^6 rad. The samples were irradiated in sealed container in an atmosphere of dry nitrogen to minimize any possible surface deterioration due to moisture during irradiation. The optical transmission of all of these samples has been measured as a function of dose, as well as the light output of some of the samples. We have now also discovered a short term phosphorescense in undoped CsI. To our knowledge, this is the first time this effect has been observed in undoped CsI. We have made an

attempt to characterize this phosphorescence in terms of its emission spectrum and decay time, as described below. It does, however, also interfere with the light output measurements after irradiation due to the high level of background current produced in the photomultiplier tube.

Figure 3 shows the transmission spectra as a function of dose for three 1" dia. x 1" long samples of undoped CsI. The spectra have not been corrected for losses due to reflection and scatter off of the end surfaces of the samples. Unfortunately, some of the pre-irradiation transmission spectra were rendered unusable when the samples were inadvertently cleaned with alcohol before irradiation, causing a change in their surface condition which affected the transmission measurements. Nevertheless, it is clear that different samples show different amounts of damage. The sample from Quartz and Silice showed very little change from 10^3 rad to 4.2 x 10^6 rad (the slight variation in transmission with increasing dose is within the systematic errors due to surface conditions). The BDH sample developed some absorption in the region of 300-400 nm, along with a broad absorption band in the region of 800 nm. The Horiba crystal showed the most damage, developing more absorption in the same regions as in the BDH sample. These results are qualitatively the same as those given in ref.[7], but with some samples damaging more and some less than previously observed. This shows that the amount of damage in the material is highly sample dependent, probably caused by different levels of impurities or defects. However, the results obtained with the Q&S sample indicates that intrinsic radiation hardness of undoped CsI may be quite good.

Figure 4 shows the relative change in light output as a function of dose for the three undoped samples. We again see a strong sample to sample variation, with the Quartz and Silice sample showing a $\sim$ 35% loss of light output in the fast component, while the Horiba sample lost essentially all of it useful light output after a dose of 9 x 10^5 rad. We have seen such sample to sample variations before, as described in ref.[7]. We also note that the amount of loss in light output is greater than one would naively expect from the amount of induced absorption. This effect was also noted in [7] and has been observed in other materials [15]. We are presently in the process of simulating the light output from the crystal with a Monte Carlo program which takes into account the absorption losses, multiple surface reflections and scatter, coupling to the photomultiplier, etc., to determine how much of the observed loss in light output can be accounted for by these effects.

We have also irradiated a large 3.5 x 3.5 x 30 cm^3 sample from BDH at the HIRDL facility and measured the change in transmission and light output for various doses. The sample was was irradiated in dry nitrogen at a dose rate of 3.45 x 10^4 rad/hr with a uniformily of $\lesssim$ 10% over the 30 cm length. Figure 5 shows the transmission along the longitudinal axis for doses from 10^3 to 10^6 rad. A substantial amount of induced absorption is observed. Figure 6 shows the light output as a function of position along the sample after 10^3 and 10^4 rad. The light output was too low to measure at all positions along the crystal for higher doses. The loss in light output at lower doses appears to be rather

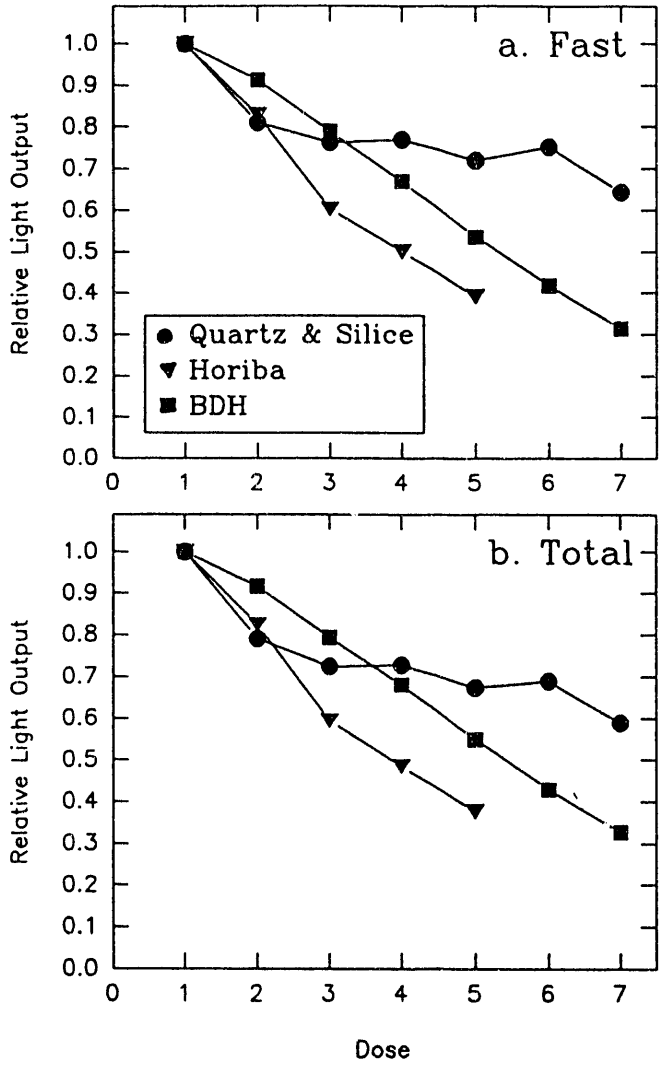

Fig.4 Relative light output as a function of dose for (a) fast and (b) slow : (1) unirradiated, (2) 10^3, (3) 10^4, (4) 6 x 10^4, (5) 2.6 x 10^5, (6) 9.0 x 10^5 and (7) 4.2 x 10^6 rad. Fast and slow are for 100 ns and 1 μsec integration times, resp.

uniform along the length. However, a measurement made eight days after the irradiation showed that the fast component light output had recovered to $\sim$ 23% of its original value near the end closest to the phototube, although, the light output was still too low to measure near the middle and far end of the crystal. This indicates that there was a position dependence to the damage at higher doses, implying that there may have been a higher concentration of impurities at one end. We intend to irradiate more large samples from BDH, as well as other suppliers, to see if this effect is observed in other material.

The phosphorescense observed in undoped CsI is similar to an effect recently seen in BaF_2 [16]. The amount of phosphorescense seems to be correlated with

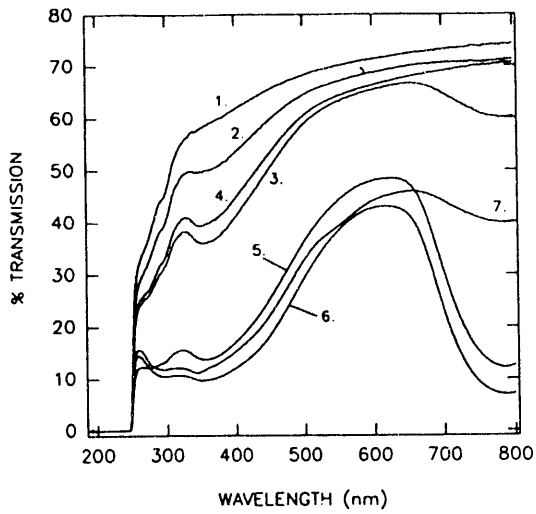

Fig.5 Transmission spectrum for a 3.5 x 3.5 x 30 cm^3 undoped CsI sample from BDH. Curves indicate (1) unirradiated, (2) 10^3 rad, (3) 10^4 rad, (4) 22 hrs. after 10^4 rad, (5) 10^5 rad, (6) 10^6 rad, (7) 24 hrs after 10^6 rad.

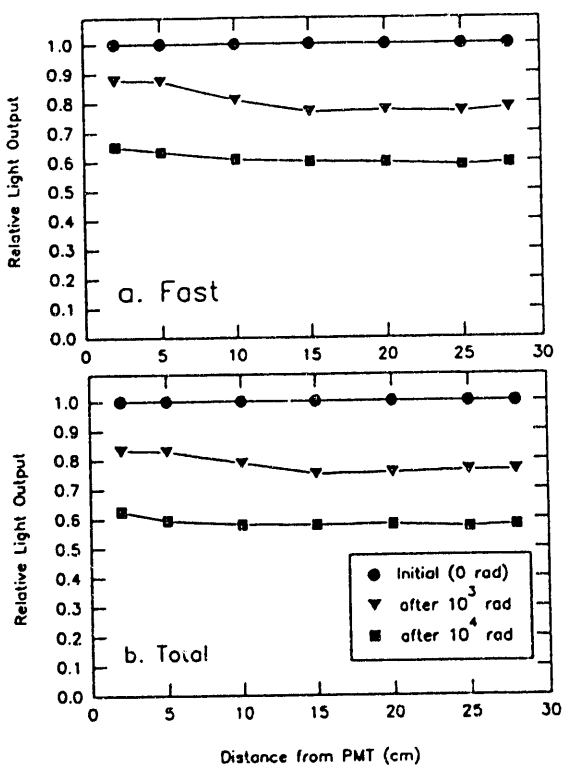

Fig.6 Light output for fast (a) and total (b) as a function of position along the length of a 3.5 x 3.5 x 30 cm^3 undoped CsI crystal from BDH after 10^3 and 10^4 rad.

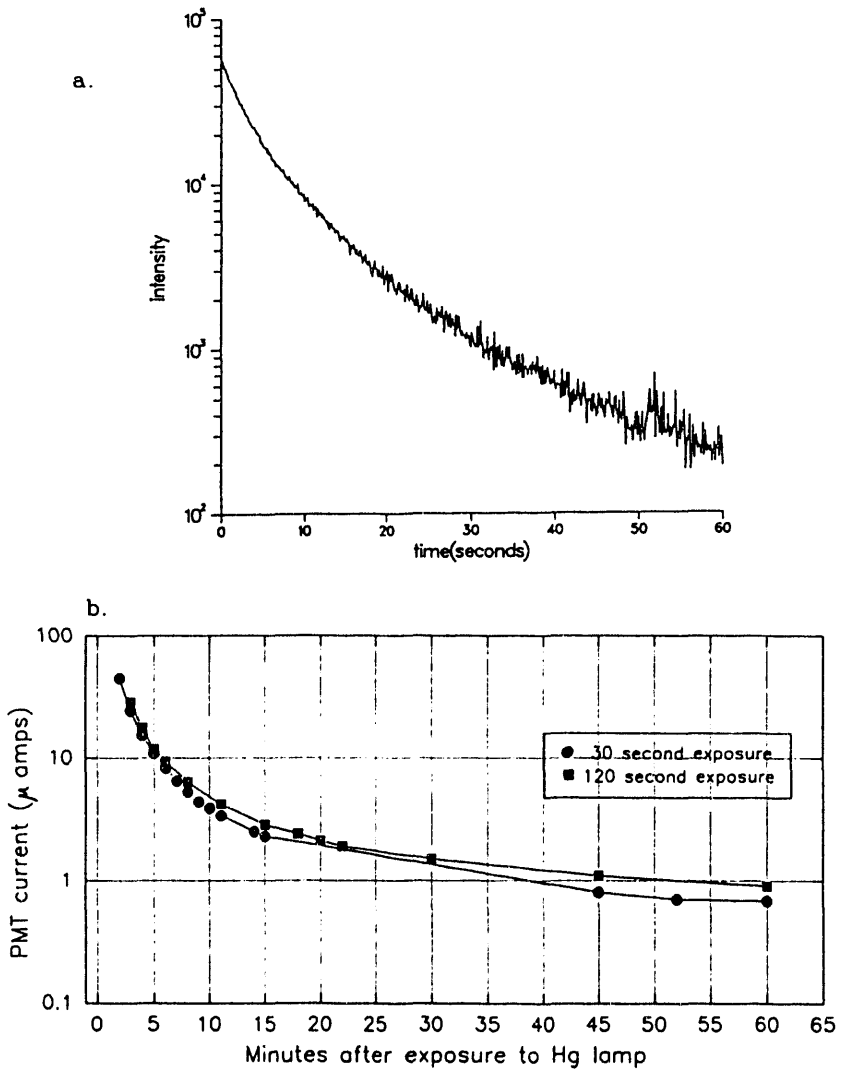

Fig.7 Phosphorescense decay time of two 1" dia. x 1" long undoped CsI samples a) after exposure to 10^5 rad of ^{60}Co radiation and b) after several short exposures to a strong mercury lamp.

the induced absorption and loss in scintillation light output due to radiation, and appears to die away with a relatively short decay time. Figure 7a shows the phosphorescense intensity as a function of time in a sample after exposure to $\sim 10^4$ rad of ^{60}Co radiation. Figure 7b shows the decay in a different sample given a short exposure to a strong mercury lamp. Both curves show a component with a rapid decay time, although the time constants appear to be somewhat different. The exposure to the mercury lamp also indicates a component with a much longer decay time. It is nevertheless interesting to note that the phosphorescense can be induced by relatively low energy UV photons, as well as higher energy gamma rays.

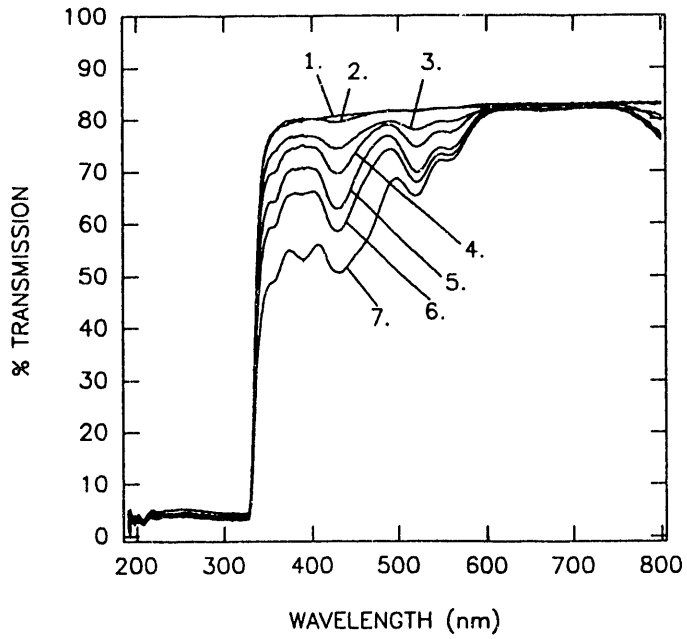

Fig.8 Transmission vs. wavelength for a CsI(Tl) sample from BDH for doses of:(1) unirradiated, (2) 10^3, (3) 10^4, (4) 6 x 10^4, (5) 2.6 x 10^5, (6) 9.0 x 10^5 and (7) 4.2 x 10^6 rad.

Figure 8 shows the transmission spectra as a function of dose for a CsI(Tl) sample from BDH. There is clearly a significant amount of absorption produced near the band edge, and an absorption band is forming in the infrared. The shift from zero transmission below the band edge is an instrumental effect due to luminescense produced in the sample by the spectrophometer beam. These results indicate that the thallium doped CsI currently available on the market is considerably more radiation hard than previously reported [17].

PROGRESS ON LEAD FLUORIDE

Lead fluoride is newly rediscovered Cherenkov material [18–19] with very high density (7.77 g/cm^3), short radiation length (9.3 mm) and small Moliere radius (2.2 cm). The Moliere radius is smaller than the densest commonly used scintillating crystal, BGO, and is effectively even smaller given that very soft particles in the periphery of a shower do not produce Cherenkov light. Due to its high density, it is a very attractive candidate for use in heavy ion reactions where particle multiplicities are very high. However, it does have other properties which make it attractive for other purposes as well. Being a Cherenkov material, it does not produce as much light as a scintillating crystal, but its light output is sufficiently high to expect an energy resolution $\sim$ 2-4%/$\sqrt{E}$. In addition, it shows good radiation hardness. Our studies of these and other properties of PbF_2 are described below.

We have recently started an R&D program to develop lead fluoride for use as a high resolution electromagnetic calorimeter. The first part of this project consisted of an R&D effort by one of the crystal manufacturers, Optovac, Inc.[20], to grow high quality, long crystals suitable for use in an electromagnetic calorimeter. At the time of our last proposal [9], Optovac had produced several PbF_2 crystals of reasonably good quality up to $\sim$ 13 cm long. Two of these crystals have been measured in test beams at Brookhaven and KEK with encouraging results [18]. Since that time, the main emphasis has been on increasing the length of the finished crystals and improving their optical transmission. This effort has been highly successful and a report on the progress made by Optovac is included in Appendix A of ref.[1]. It should also be noted, however, that at least two other companies, Solon Technologies [21] and NKK [22], are also growing PbF_2 on an R&D basis. Although the efforts by these companies have not been as successful as Optovac's, there is now considerable interest in this material throughout the crystal growing industry.

We have now obtained a total of more than 25 PbF_2 crystals with dimensions of 2.1 x 2.1 x 18.5 cm, as well as a number of other pieces 17.5 cm long. The transmission of most of these blocks is extremely good. Figure 9 shows the transmission along the long axis of one of the 17.5 cm blocks, compared with several previously measured PbF_2 samples given in ref.[9]. None of the curves shown have been corrected for the loss of $\sim$ 17% due to reflections off of the two end surfaces. There is clearly a considerable improvement in the new sample compared with the previous longer ones. The short wavelength cutoff in the new material is now well below 300 nm, comparable to the 2.4 cm "best" sample. Compared to the longer samples, the transmission at longer wavelengths has improved as well. There are still several small absorption bands in the new crystal, one at $\sim$ 450 nm and another at $\sim$ 720 nm, indicating that some residual impurities or defects still remain. Optovac is now taking steps to eliminate these impurities by refining the purification and pregrowth treatment of the raw material. By measuring the transmission of the new 18.5 cm blocks along the transverse (2.1 cm) direction for various positions along the samples, it can be seen that the transmission is better at one end than the other, which is mainly due to scatter at one end. This scatter is beleived to be caused by hydrolysis due to the absorption of OH^- ions during growth. Optovac has proposed several steps to eliminate this hydrolysis, as outlined in Appendix A of ref.[1], which should greatly reduce the scatter in the future.

We have carried out a series of beam tests using the new longer crystals to study their response to various types of particles. The first set of tests were carried out at the AGS at Brookhaven during May of this year. These tests were very limited due the short amount of beam time available, and the fact that the crystals arrived only a few days before the tests. Six crystals measuring 2.1 x 2.1 x 17.5 cm^3 were tested in the beam. Three proved to be of very good quality, and the other three turned out to be poor. Each crystal was measured using one of two 3/4" UV-glass window photomultiplier tubes (Hamamatsu R2076). The crystals were coupled to the phototubes with a UV transmitting optical

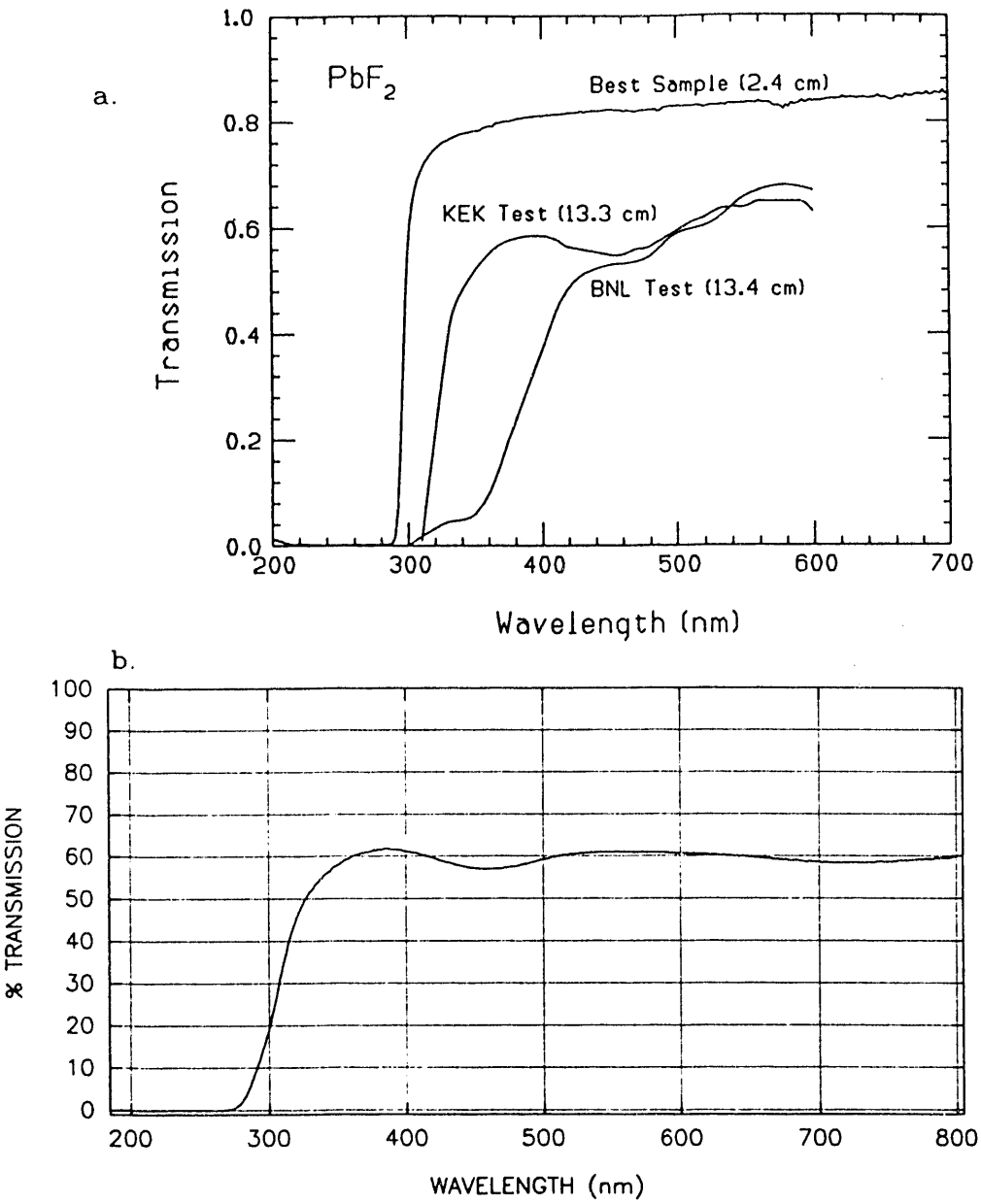

Fig.9 a) Transmission spectra of several PbF_2 crystals taken from ref.[9], and b) transmission spectrum taken along the longitudinal axis of a new 2.1 x 2.1 x 17.5 cm^3 PbF_2 crystal.

grease (Viscasil 600M). Figure 10 shows the pulse height spectrum for minimum ionizing particles (1 GeV/c pions) passing down the center of each of the three good crystals. A mimimum ionizing peak, corresponding to an energy deposit of 168 MeV, is clearly resolved in each crystal.

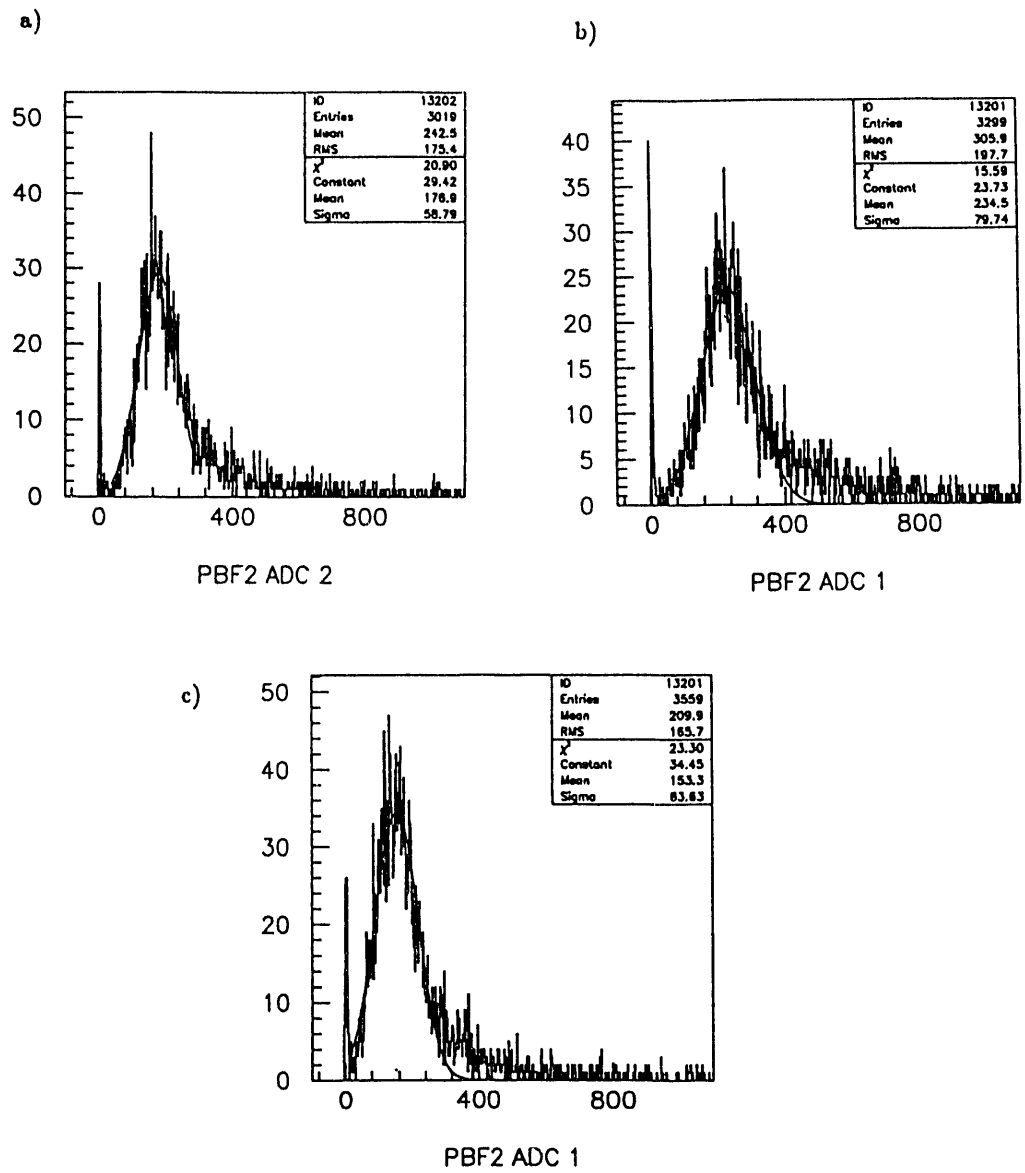

Fig.10 Minimum ionizing pulse height spectra for three 2.1 x 2.1 x 17.5 cm^3 PbF_2 crystals.

The minimum ionizing peaks were used along with an independent calibration of the charge gain of the photomultiplier tubes to determine the photoelectron yield of each crystal. The phototube calibration was done using an LED whose intensity was adjusted using neutral density filters to give $\sim$ 100 photoelectrons from the photocathode, as determined by the width of the LED pulse height distribution. The charge per photoelectron was then determined as a function of voltage for each phototube. Table I gives the measured photoelectron yields for each of the three good crystals. The yield for crystal 3 is lower due to poorer optical coupling between the crystal and phototube.

Table I

Photoelectron Yields of 2.1 x 2.1 x 17.5 cm^3 PbF_2 Crystals

Crystal	Photoelectrons per GeV (measured)	Photoelectrons per GeV (corrected)
1	585	1463
2	607	1518
3	397	993

Due to the small diameter photomultiplier used, the photocathode area coverage of the readout end of the crystal was only $\sim$ 40%. In order to compare with our previous results with other crystals, which were measured with a larger phototube with complete photocathode coverage, we have also listed in Table I the photoelectron yields corrected for this area factor. The previous values obtained were 1100 p.e./GeV for a 4.4 cm diameter by 13.4 cm long crystal, and 1300 p.e./GeV for a 4.3 cm octagonal cross section by 13.3 cm long crystal. The yields obtained with the new crystals, which are $\sim$ 30% longer than the ones previously measured, are greater by $\sim$ 15%. Also, these values were not obtained under ideal conditions due to the time constraints of the beam test, and probably do not represent the maximum yields obtainable with these crystals. For example, a recent measurement of the 4.3 cm octogonal crystal by a group at TRIUMF, where more care was give to optimize the light collection and optical coupling, increased the yield of this crystal to 1800 p.e./GeV [23]. However, even using 600 p.e./GeV, we would expect the statistical contribution to the energy resolution to be $\sim 4\%/\sqrt{E}$.

Another series of tests with the longer PbF_2 crystals is now in progress at Fermilab. A total of twenty five 2.1 x 2.1 x 18.5 cm^3 (20 X_o) crystals have been obtained and are being assembled into a 5x5 array prototype detector. The readout consists of 3/4" diameter photomultiplier tubes (Phillips XP1911), similar to the ones used at Brookhaven, but with reduced gain to better match the higher energies at Fermilab. The test utilizes the E731 spectrometer [24] to provide momentum analyzed electrons with precise direction and angle determination. Preliminary results from this test with a 3x3 array have just recently been obtained. Although the statistics in the data are quite limited, they do show that the detector is basically working well. Figure 11 shows the mean pulse height for 6 GeV/c electrons as a function of incident position across each crystal. The average values are different for each crystal because the gains of each channel were not matched because of time constraints. A much more extensive series of tests with this detector is planned for the coming months at Fermilab, as well as tests early next year at Brookhaven. It is hoped that these measurments will establish the basic properties of PbF_2 as an electromagnetic calorimeter, and serve as a starting point for its development into a full detector.

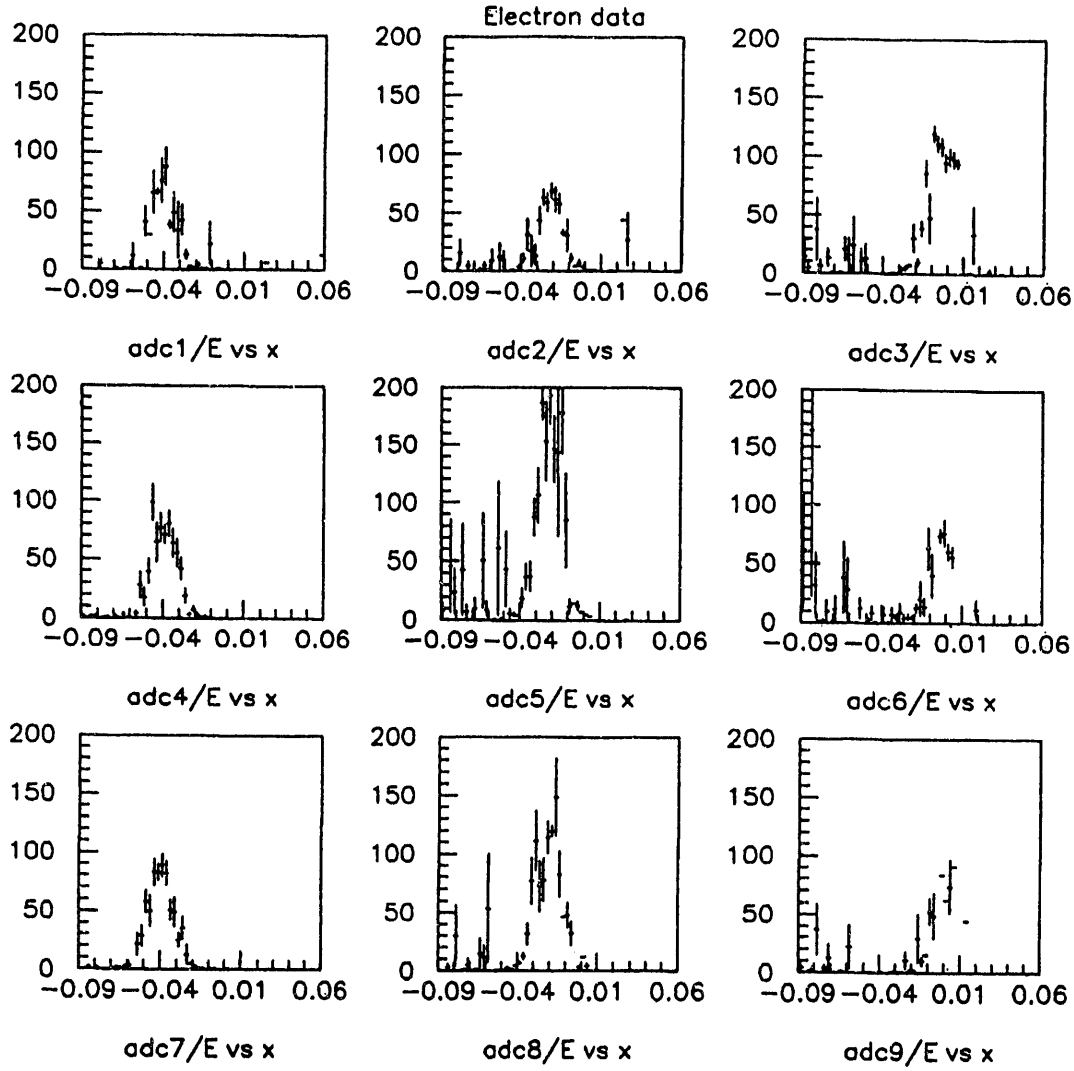

Fig.11 Average pulse height for 6 GeV/c electrons vs position across each crystal of 3x3 array of 2.1 x 2.1 x 18.5 cm^3 PbF_2 blocks.

Our previous measurements showed that PbF_2 was fairly radiation hard (about 500 times more so than lead glass), and was easily annealed with short exposure to UV light [9]. We have recently studied the radiation damage in a small 1" dia. x 1" long sample of the new material and found that the radiation hardness has been significantly improved. Figure 12a, taken from [9], shows the change in transmission of a 1 cm^3 sample after exposure to doses of several Mrad of neutron and gamma irradiation. After the maximum dose, the transmission in the short wavelength region is severely reduced. Figure 12b shows the transmission of the new sample before and after exposure to 1.4 Mrad of gamma rays. The transmission loss is considerably less even with the factor of 2.5 longer path length. It is likely that the radiation hardness of PbF_2 will increase even further as the purity and quality of the material improves with continued R&D.

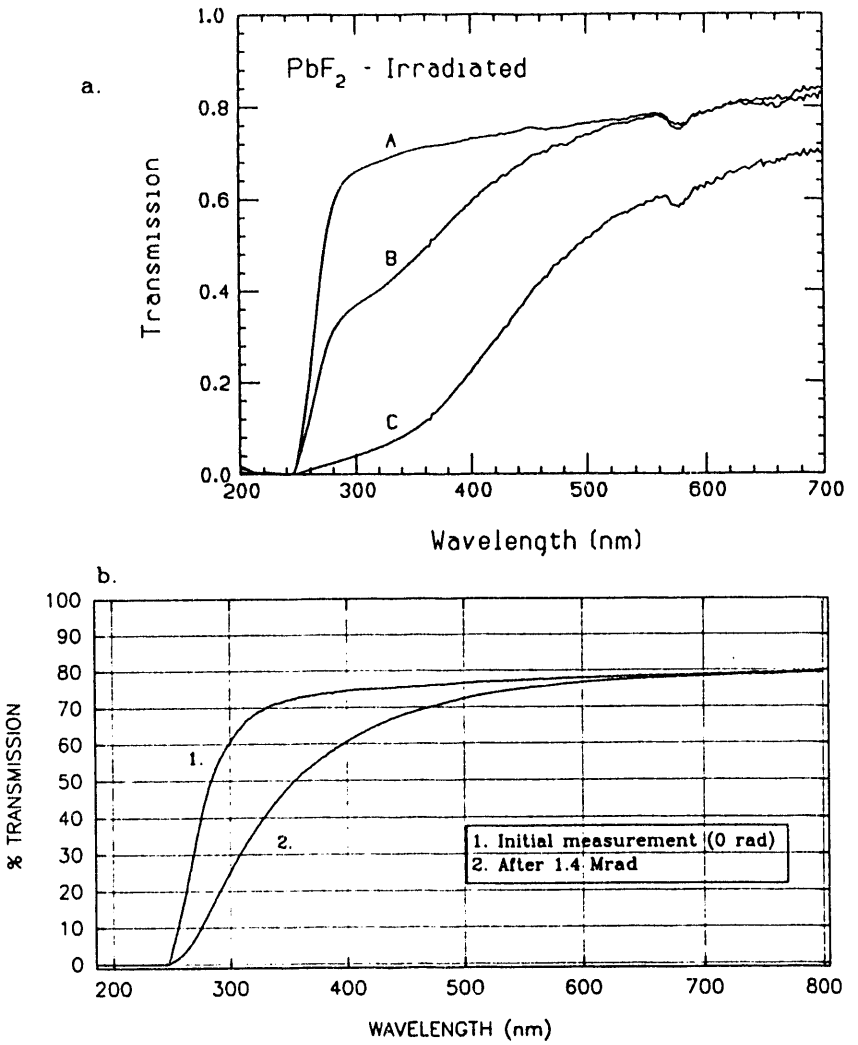

Fig.12 a) Transmission spectrum for a 1 cm^3 PbF_2 sample (A) before irradiation, (B) after 3 x 10^5 rad of neutrons and 1 x 10^5 rad of gamma rays, and (C) after 3 x 10^6 rad of neutrons and 1 x 10^6 rad of gammas (from ref.[9]). b) Transmission spectrum before and after irradiation to 1.4 Mrad of a 1" dia. x 1" long PbF_2 sample.

PROPOSED CONTINUATION OF R&D

As stated above, our generic R&D on undoped CsI is essentially complete. This effort has now become a part of a more directed project to develop a high resolution electromagnetic detector for RHIC [4]. In that sense, our generic R&D has been successful in spawning a new use for this type of detector. We do, however, plan to continue our R&D on radiation damage in undoped CsI, which is not being carried out under the other proposal. This invesitgation, although more generic in nature, has direct implications on the performance of a detector under actual running conditions, either at RHIC, or in other applications.

The R&D effort on PbF_2 has just begun under our current program. The first phase of R&D with Optovac has been completed with very encouraging results. We now wish to continue this program in order to increase the capability to produce large, high quality crystals, and study ways to reduce the cost for larger scale production. Until now, the crystals have been grown on R&D basis with an emphasis on improving the quality of individual crystals. This has been highly successful, but it is now time to develop the capability to produce the crystals in a cost effective way. This is an essential part of our continued development effort with the manufactures. In addition, we wish to explore several new possibilities which were not investigated under the first phase of our R&D. These include trying to improving the basic properties of the material, such as the radiation hardness, as well as altering its properties to improve its performance. One such possibility is to study the addition of dopants to the crystal in order to produce scintillation light. This would give a much higher light output than is presently achievable with Cherenkov light, and, if fast enough, could also be used at high counting rates. Some preliminary work has already been done in this area and there is reason to beleive that some rare earth materials may produce the desired result [25]. In addition, it is possible that some dopants may also improve the radiation hardness. Clearly, the development of a new, fast scintillator with the density of PbF_2 would be a major breakthrough in scintillator technology.

We further plan to replace some of the crystals in the present 5x5 array with better quality pieces which we anticipate being able to obtain shortly. We must also re-equip the readout with higher gain photomultipliers in order to study the lower energy response of the detector at Brookhaven. We will also add a laser calibration system to the prototype detector in order to provide intercalibration of each channel and monitor gain drifts of the phototubes. This is an *extremely* important requirement if one is to control systematic effects and minimize the constant term in the energy resolution. Finally, we wish to continue our studies of radiation damage in PbF_2, especially as the quality of the material improves, and as we begin to study material with different dopants.

REFERENCES

1. "Progress Report on Generic R&D on Undoped Cesium Iodide and Lead Fluoride", J.A.Kierstead et.al., Oct. 10, 1991.
2. "Proposal to Study Large Pure CsI Crystals as a Potential High Resolution Electromagnetic Calorimeter for RHIC", C.L.Woody et.al., BNL-Syracuse University, Sept. 1988.
3. "Proposal to Develop a High Resolution Electromagnetic Calorimeter for RHIC Using Pure Cesium Iodide Crystals", J.A.Kierstead et.al., BNL-Syracuse University, Aug. 1989 (revised March 1990).
4. "Proposal to Develop a High Resolution Electromagnetic Calorimeter for RHIC Using Undoped Cesium Iodide Crystals",

   BNL-Stony Brook-Syracuse, submitted to the RHIC Detector R&D Committee, Sept. 1991.

5. "The TALES/SPARHC Experiment at RHIC", RHIC LOI #12, July 1991.
6. "High P_t Photons, Charged Particles and Jets at RHIC", RHIC LOI #9, Sept. 1990.
7. C.L.Woody et.al., IEEE Trans. Nucl. Sci. $NS-37$, 492 (1990).
8. "Progress Report on Generic R&D on Undoped Cesium Iodide", J.A.Kierstead et.al., Dec. 1990.
9. "Propsal to Study Lead Fluoride as a Potential High Resolution Electromagnetic Calorimeter for RHIC", BNL-Oak Ridge-Fermilab, Sept. 1990.
10. C.Bebek, Nucl. Inst. Meth. A265, 258 (1988).
11. The High Intensity Radiation Development Laboratory (HIRDL) at BNL.
12. Quartz and Silice Company, a division of Saint Gobain, Nemours-Cedex, France.
13. BDH Chemical Co. Ltd., now CRYSTRAN Merck Ltd., Poole, England.
14. Horiba Crystal Products, a division of Horiba Instruments, Inc., Kyoto, Japan.
15. A.Murakami et.al., Nucl. Inst. Meth. A301, 435 (1990).
16. Report by C.Woody at the GEM Calorimetry Meeting at SSCL, GEM TN-91-00006, August 8, 1991.
17. M.Kobayashi et.al., Nucl. Inst. Meth. A524, 275 (1987).
18. D.F.Anderson et.al., Nucl. Inst. Meth. A290, 385 (1990).
19. E.B.Dally and R.Hofstadter, Rev. Sci. Inst. 39, 658 (1968); E.B.Dally and R.Hofstadter, IEEE Trans. Nucl. Sci. $NS-15$, 76 (1968).
20. Optovac, Inc., North Brookfield Mass..
21. Solon Technologies (formerly Harshaw), Solon Ohio.
22. Nihon Kessho Koogaku Co., Ltd, 810-5 Nobe-cho, Tatebayashi City, Gunma-pref., Japan.
23. Y.Kuno, TRIUMF, private communication.
24. Fermilab Experiment E731/799, CP Violation in K^o-long decays.
25. R.Sparrow, General manager of Optovac, private communication.

A TRANSITION RADIATION DETECTOR FOR RHIC FEATURING ACCURATE TRACKING AND dE/dx PARTICLE IDENTIFICATION*

E. O'Brien, D. Lissauer, S. McCorkle, V. Polychronakos, H. Takai
Brookhaven National Lab, Upton, New York, 11973

C.Y. Chi, S. Nagamiya, W. Sippach, M. Toy, D. Wang,
Y.F. Wang, C. Wiggins, W. Willis
Columbia University, New York, New York, 10027

V. Cherniatin, B. Dolgoshein
Moscow Institute of Physics and Engineering, Moscow, U.S.S.R.

M.Bennett, A.Chikanian†, S. Kumar, J.T. Mitchell, K. Pope
Yale University, New Haven, Connecticut, 06511

Abstract

We describe the results of a test run involving a Transition Radiation Detector that can both distinguish electrons from pions with momenta greater than 0.7 GeV/c and simultaneously track particles passing through the detector. The particle identification is accomplished through a combination of the detection of Transition Radiation from the electron and the differences in electron and pion energy loss (dE/dx) in the detector. The dE/dx particle separation is most efficient below 2 GeV/c while particle ID utilizing Transition Radiation is effective above 1.5 GeV/c. Combined, the electron-pion separation is better than 5×10^2. The single-wire, track-position resolution for the TRD is $\sim 230 \mu$m.

*Work supported in part by the U.S. Department of Energy
†Lebedev Institute, Moscow, U.S.S.R.

Introduction

Experiments being designed for the Relativistic Heavy Ion Collider (RHIC) at Brookhaven National Laboratory will need to distinguish electrons from pions to better than 0.1% over a momentum range of 0.1 GeV/c to 8.0 GeV/c. The particle multiplicity will be high (dN/dy$\geq$1000) but the event rate for central Au-Au collisions will be relatively modest (1-10 kHz). Transition Radiation Detectors (TRD's) are well suited for separating electrons from pions in a high multiplicity environment within a colliding beam geometry. By conducting a test run with a TRD prototype we have been able to quantify many of the RHIC TRD performance parameters.

We have designed a TRD for inclusion in a RHIC experiment that allows electron-pion separation utilizing both TR and dE/dx information, while simultaneously tracking charged particles with good position accuracy[1]. A prototype of this detector has been tested in a secondary beam of the Alternate Gradient Synchrotron at Brookhaven National Laboratory. In this test run we have determined the e/π separation of our prototype over a momentum range of 0.7 GeV/c - 4.0 GeV/c, evaluated a variety of potential radiator materials for the TRD and measured the TRD tracking resolution.

The Test Run

The TRD used in our test run was a modified version of the NA34 TRD[2]. It consisted of four wire chambers interleaved with radiator material. Each wire chamber was a xenon-filled Time-Expansion Chamber with a 1 cm drift space and a proportional region of 8 mm x 2.5 mm per anode wire (Fig. 1). A single wire chamber consisted of a 10μm aluminized mylar front entrance window that served as both a cathode to the chamber's drift section and a gas barrier, a plane of vertical cathode wires located at the beginning of the chamber's proportional region, a plane of horizontal, 25μm, Au-W anode wires spaced $\sim$2.5 mm apart and cathode strips etched into a rear aluminized mylar window. Each of the four wire chambers was separated from the next by 16.8 cm in the z-direction (beam direction). The radiator material of the TRD consisted of either 10 cm thick blocks of polyethylene foam or 120 layers of 12μm polypropylene foils spaced by 800μm. Several radiator materials were tested. The RHIC TRD and prototype differ in the

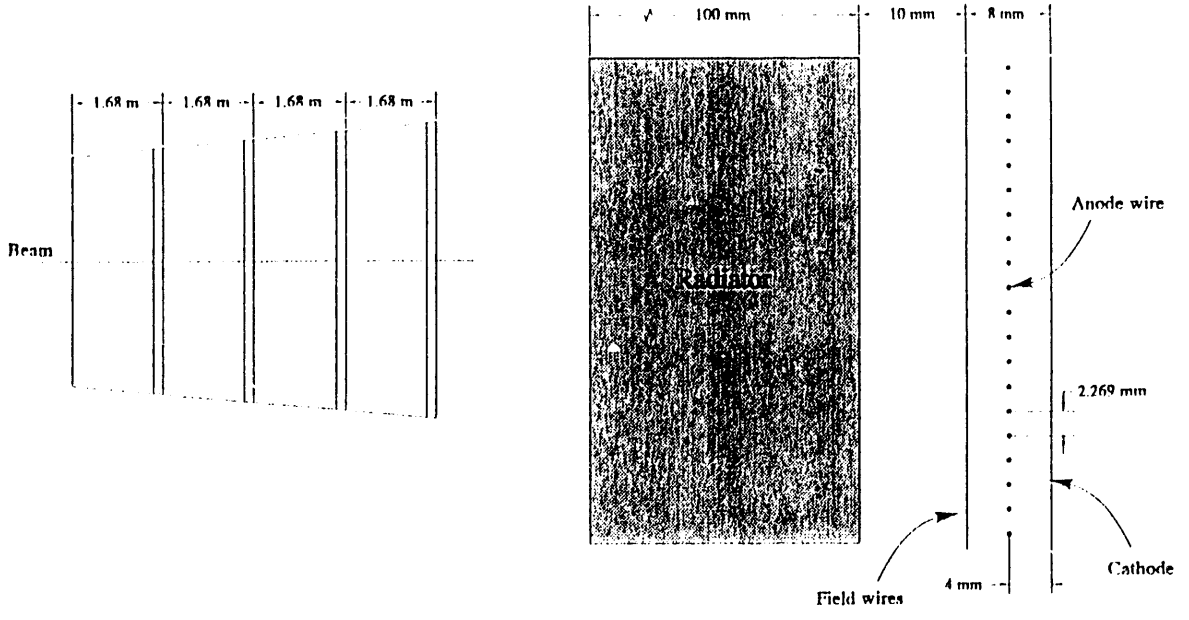

Figure 1: Schematic of Test TRD

length of the drift region, cathode orientation and number of detector planes. The prototype contains 4 planes of radiator-detector, a 1 cm drift space and cathode strips perpendicular to the anode wires, while the RHIC TRD will have 8 detector planes, a 3 cm drift space, and cathode strips oriented for stereo readout.

The electronics chain on each anode wire or cathode strip consisted of a preamplifier, a shaping amplifier and a 6-bit Flash ADC clocked at 24.5 nsec. The FADC had a memory depth of 256 bins or 6.25 μsec. The digitized FADC signal was read through a VME DR11W into a VME crate that also received CAMAC data from detector elements in the beamline (Fig. 2). The whole data aquisition system was controlled by a Macintosh running Mac-UA1 software from CERN.

The test run took place at the A2 beamline of the AGS at BNL and used a secondary beam containing e^-'s, π^-'s and K^-'s. The beamline was instrumented with two beam defining scintillators S1 and S2, a veto counter S3, two Cerenkov counters C1 and C2, and a block of Pb-glass 10 radiation lengths deep (Fig. 3). The data were taken either with a minimum bias trigger ($S1 \cdot S2$), or an electron trigger ($S1 \cdot S2 \cdot C1 \cdot C2$), where both the Cerenkov counters were set for e/π discrimination. The e/π ratio in the beam ranged

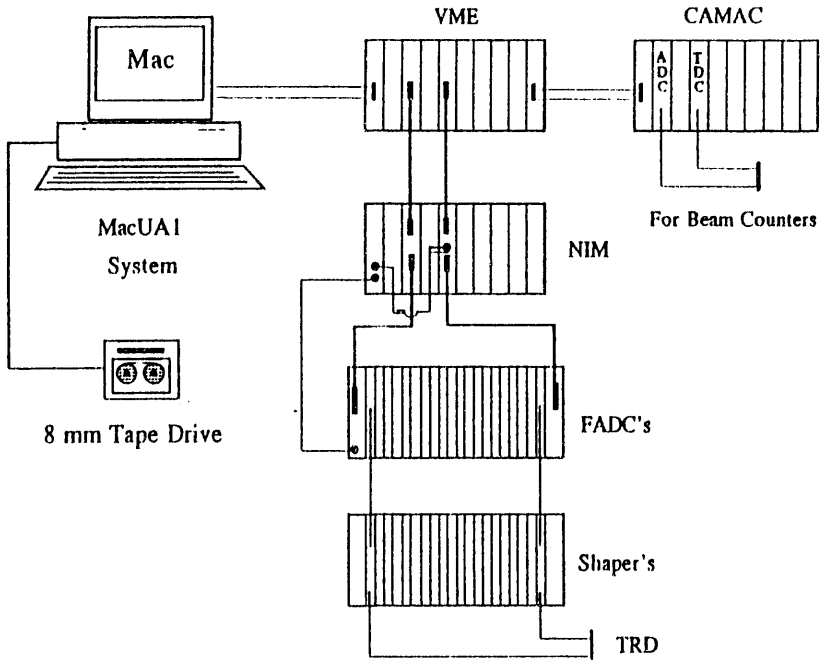

Figure 2: Test run electronics chain

from 0.5% to 20% depending on the beam momentum.

Radiator Tests

The number of transition radiation photons produced for 6 different polyethylene foam radiators, and a polypropylene foil radiator, was measured. Each radiator was 10 cm thick. Our goal was to determine the absolute transition radiation production of each radiator *and* the production of TR photons per radiation length of material. The cell sizes and densities of our test radiators are listed in the following table.

Radiator Type	Density	Cell Size or Foil Gap
Foil	0.018 gm/cm^3	800μm
Foam 1	0.024 gm/cm^3	800μm
Foam 2	0.044 gm/cm^3	1000μm
Foam 3	0.018 gm/cm^3	600μm
Foam 4	0.024 gm/cm^3	200μm
Foam 5	0.033 gm/cm^3	600 – 700μm
Foam 6	0.045 gm/cm^3	200 – 250μm

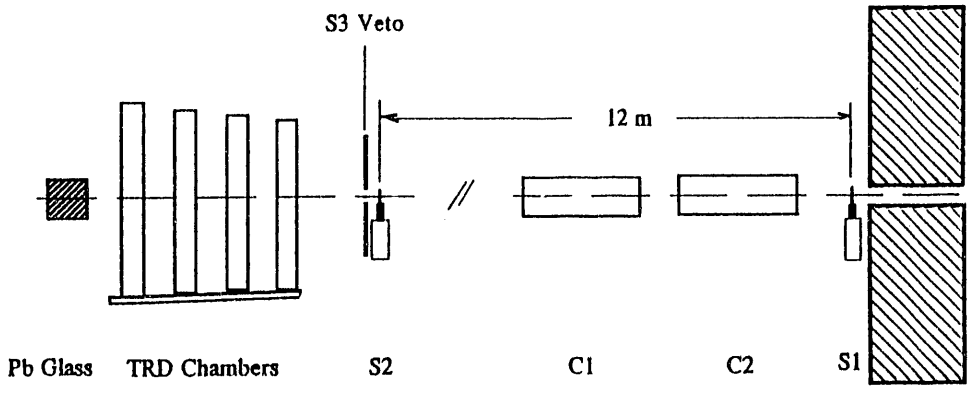

Figure 3: Overview of Test Beamline Set-up

Both electron and pion data were taken for each radiator at three or more momentum settings. The FADC data from each event was scanned for photon clusters. A photon cluster was defined as $E \geq 4.5$ keV deposited inside the xenon gas chamber in a volume 0.5 to 1.5 mm in diameter. We called this an identified TR photon. The size of the cluster seen in our detector is determined by a combination of the initial electron cluster size due to the absorption of the X-ray, the gas diffusion over the drift distance, and the rise time of our shaping amplifier. The energy scale of the clusters were set by normalizing the FADC pulse heights to an ^{55}Fe source. The relative normalization of each wire was obtained with pulser calibration runs that involved injecting a known amount of charge into the input of each preamplifier. The ^{55}Fe normalization was performed at least once every eight hour running period. The pulser calibration was found to be consistent over many days.

The mean numbers of TR photons, as defined above, were calculated for each radiator at each beam momentum and are shown in figure 4. We can normalize the mean number of TR photons produced per radiation length of the radiator material (Fig. 5) and see that on average the foil radiator produces 50% more TR photons than the foam radiators. It should be noted

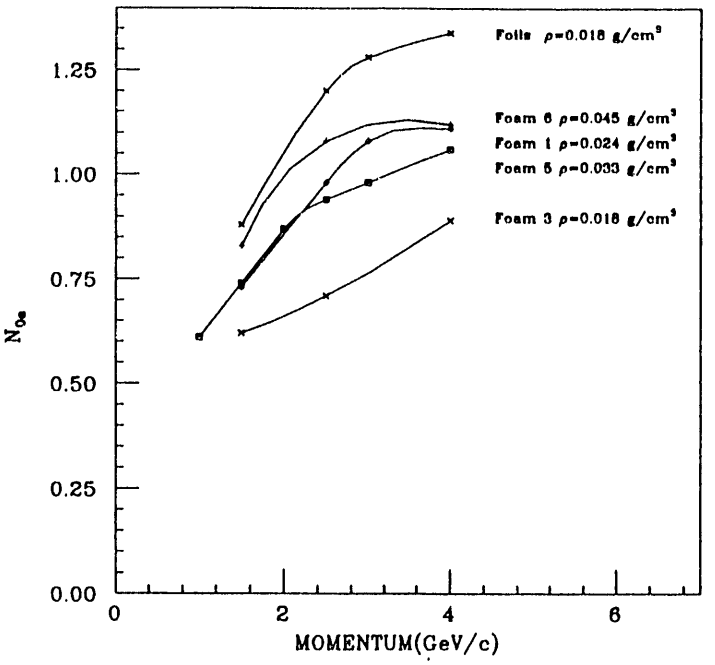

Figure 4: Number of photon clusters over threshold per 10 cm layer of radiator. The data is from electrons at different momenta.

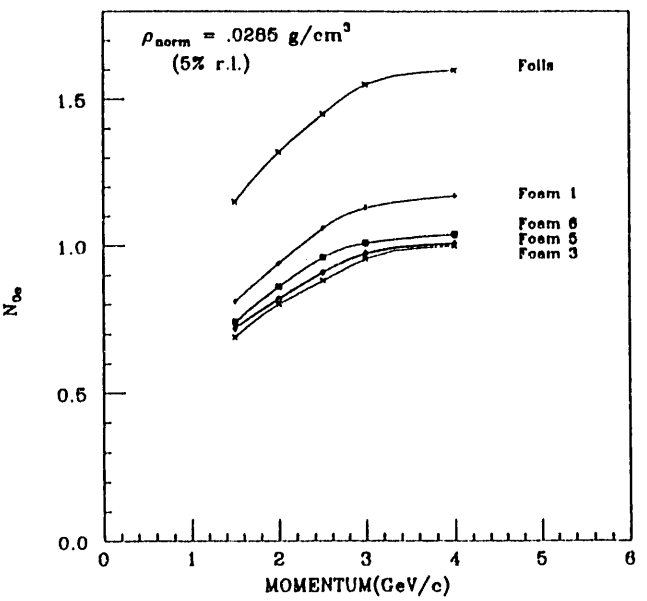

Figure 5: Number of photon clusters produced by electrons in 1 layer of radiator normalized where 8 layers of radiator= 5% radiation length.

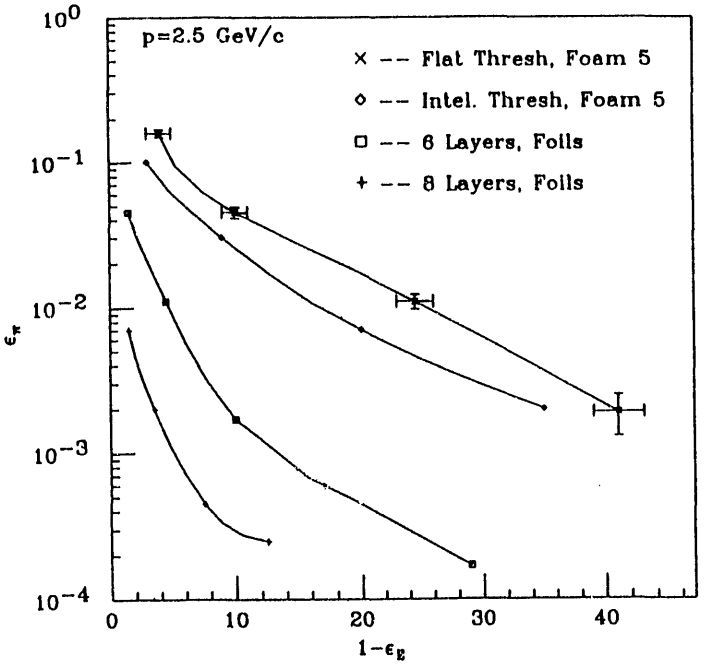

Figure 6: Pion rejection vs. electron efficiency for 2.5 GeV/c particles. Curves shown are for 8-layer foam radiators with simple threshold, 8 layer foam and intelligent threshold, 6 layer foils and 8 layer foils each with intelligent threshold

that pure pion data also show pions producing what are apparently TR photons, although at a much lower rate than electrons. Large energy clusters in pion data come from δ-rays, and it is this background that ultimately limits the ability of a TRD to separate electrons from pions.

Transition Radiation e/π Separation

Once transition radiation can be identified in our detector the e/π rejection can be determined by histogramming the TR photon cluster distributions for electrons and pions traveling through many layers of the TRD. The TRD that we have designed for RHIC experiments will include 8 layers of radiator and gas detector, so to calculate e/π separation with data from our 4 layer test detector we have paired consecutive electron or pion events. Large statistical samples of both electrons and pions were accumulated at a few momenta for one particular foam radiator. Additional data were taken with the foil radiator for normalization purposes. Large statistics are required to determine e/π separation to the 10^{-3} level and beyond.

In the analysis we accepted events that contained only single tracks,

summed charge from neighboring wires to reduce diffusion effects, and employed threshold cuts as outlined in the previous section. We also utilized a cut called the intelligent threshold, which applies a sliding ADC threshold that moves from low to high as the cluster location moves away from the radiator. The intelligent threshold is effective because δ-rays from pions are evenly distributed in the z direction (beam direction) inside the drift volume while transition radiation photons are not. Lower energy TR photons tend to be absorbed earlier in the Xe gas, that is closer to the radiator, whereas higher energy TR photons penetrate farther into the gas detector before being absorbed.

Results of the analysis of data taken at 2.5 GeV/c can be seen in figure 6. This figure shows four curves:(a) e/π rejection for 8 TRD planes using foam radiator and a simple threshold cut,(b) the same detector-radiator combination and an intelligent threshold,(c) 6 TRD planes using foil radiator and the intelligent threshold, and (d) 8 TRD foil radiator planes and the intelligent threshold. One sees that with 8 layers of foam radiator and 90% electron efficiency one retains 3×10^{-2} pions. Likewise, 90% electron efficiency and 6 or 8 planes of foil radiator retain 2×10^{-3} and 3×10^{-4} pions respectively. We conclude that the foil radiators will easily provide us with the desired e/π rejection above 2.0 GeV/c, but that the foam radiators needs further study if they are to be used in a RHIC experiment. Mechanical construction of the TRD would be considerably easier if one used foam radiators rather than foil radiators, but it is still possible to construct a large area TRD with foil radiators.

dE/dx e/π Separation

Below a momentum of 2.5 GeV/c the effectiveness of e/π separation using TR photons starts to diminish because as the electron becomes less relativistic, the probability of a TR photon being emitted by the radiator decreases. Since it is desirable to have good e/π separation below this momentum, other methods must be considered. Particle ID using dE/dx in the Time-Expansion Chamber can be used to achieve good e/π separation below 2.5 GeV/c.

In the momentum region 200 MeV/c to 3.0 GeV/c, an electron loses more energy through dE/dx than a pion due to its position on the relativistic rise

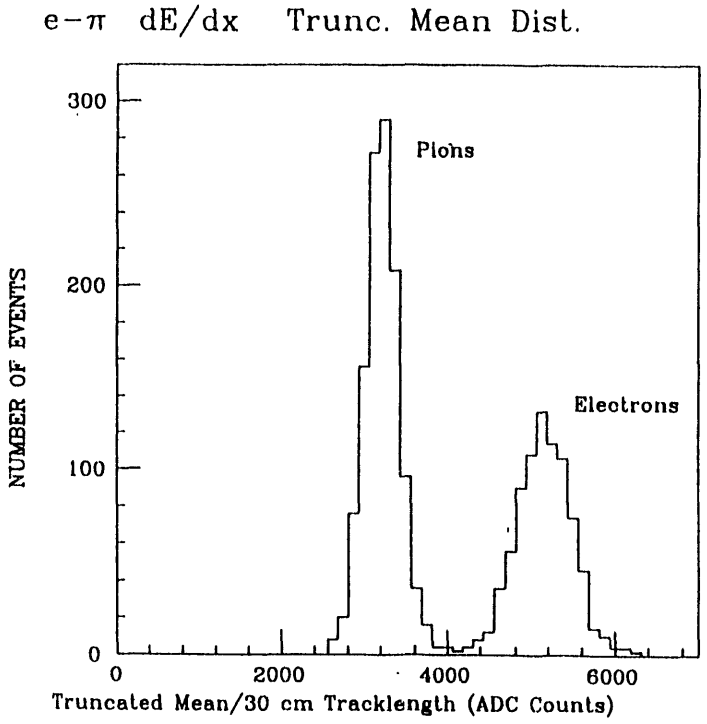

Figure 7: Electron, pion dE/dx distribution for 30 cm track length and 60% truncated mean. The data is for particles with momenta 1.0 GeV/c and 35° incident angle.

of the dE/dx curve as described by the Bethe-Bloch formula. Energy losses in xenon gas are large, so a low momentum track traveling through a sufficient path length of xenon can be identified as either an electron or a less relativistic particle by evaluating the truncated means of the dE/dx distributions. The average charged track moving through the RHIC TRD passes through 30 cm of xenon gas as it crosses the eight layers of the detector. In our analysis of the test data we have combined multiple pion or electron events to obtain the equivalent 30 cm track length in the xenon gas to evaluate the dE/dx e/π rejection. The dE/dx data have been taken at three angles $(0°, 20°, 35°)$ and with two different gas mixtures (95%Xe+5%C_4H_{10}, 50%Xe+45%He + 5%C_4H_{10}).

The drift velocity in the test TRD is ~20 mm/μsec which translates to a drift distance of 0.5 mm per 24.5 nsec FADC time bins. If one takes each FADC time bin as an independent measurement, one obtains 600 ADC data samples for each 30 cm charged track. We combined events containing either electrons or pions until we obtained data equivalent to a 30 cm track length. We created a pulse area(PA) distribution of the 600 FADC values/track, eliminated the highest 40% of the FADC values and calculated the mean PA value of the remainder. This is the standard truncated-mean technique. A

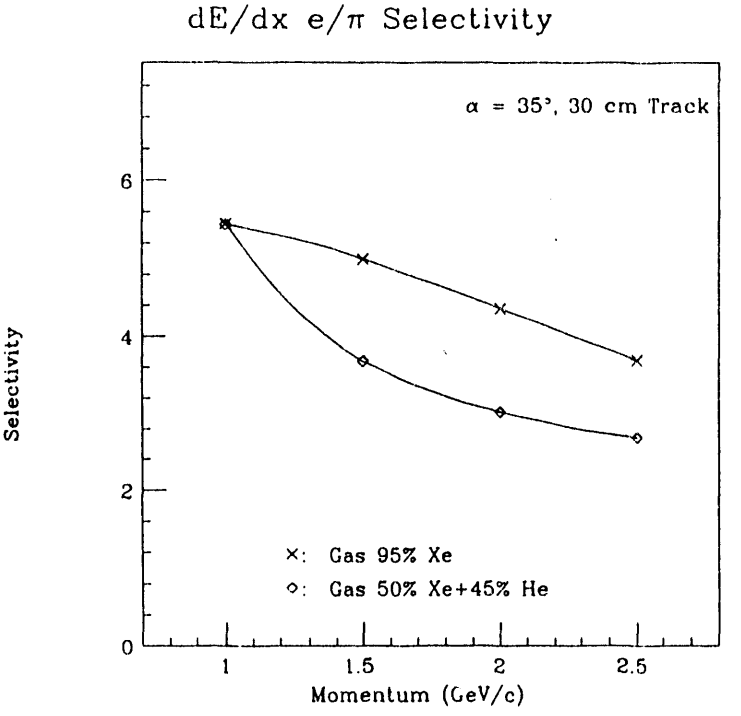

Figure 8: S-value for 2 different gas mixtures. 95% Xe + 5% C_4H_{10} and 50 % Xe + 45% He + 5% C_4H_{10}. The data is for 30 cm track length and 35° incident angle.

distribution of these mean PA values shows a large separation between the mean PA of electrons and pions (Figure 7). The electron-pion separation shown in figure 7 can be described by the selectivity value (S-value) where:

$$S = \frac{(E_e - E_\pi) - 2\sigma_e}{\sigma_\pi}$$

Figure 8 shows the S-value plotted versus momentum as obtained from our 35° dE/dx data. Our results agree with that of previous studies [3, 4]. The S-value is larger for data taken with the TRD filled with a higher percentage of xenon, which is expected since a larger percentage of xenon yields larger dE/dx losses.

The e/π separation in figure 9 shows that for 35° tracks at 1.5 GeV/c, one has 97% electron efficiency while keeping only 1.5×10^{-3} pions. The average track angle in the RHIC TRD is predicted to be 35° – 40°. The e/π separation in our data has a strong dependance on track angle. The dependance is understood to be due to space charge building up along the anode wires, which effectively reduces the chamber gas gain for the electron

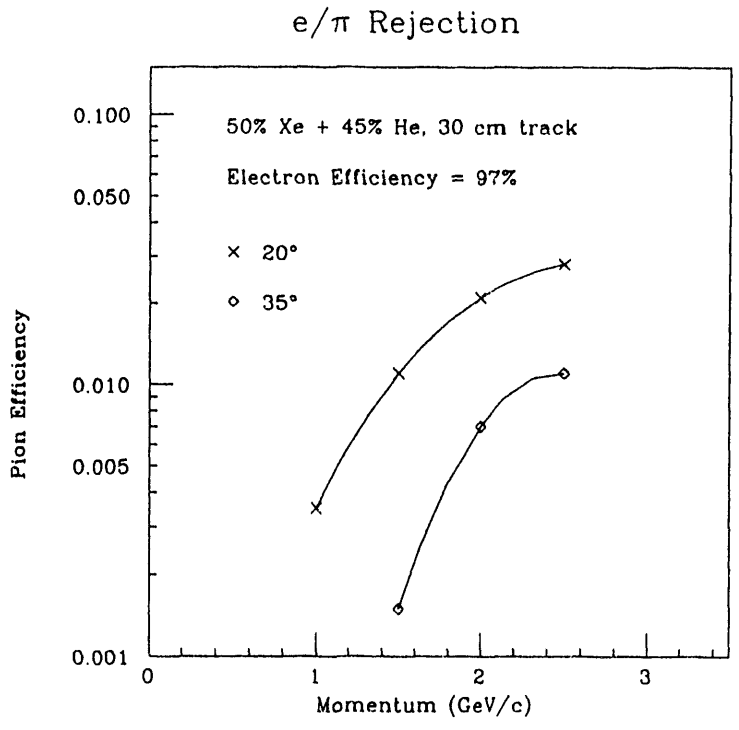

Figure 9: dE/dx e/π rejection for 97% electron efficiency and 50% Xe + 45% He + 5% C_4H_{10} gas. The track length is 30 cm and the incident angles are 20° and 35°.

clusters drifting in at times later in the avalanche process. One expects that this effect could be ameliorated with a careful optimization of the gas mixture and detector gain.

It is important to understand how the ADC resolution effects the dE/dx e/π separation so that the minimum number of ADC bits required to do the job can be determined. The resolution of our 6-bit FADC was artificially reduced in our analysis to make the data appear as if it had come from an ADC with a fewer number of bits. The result of this procedure shows that the S-value improves with ADC resolution until one reaches 4-bits, after which the S-value increases only marginally (Figure 10).

Track Reconstruction

Instrumenting the TRD with FADC electronics allows one to not only do e/π separation using dE/dx techniques but to also track all charged particles through the detector. Our RHIC experiment requires the momentum of each

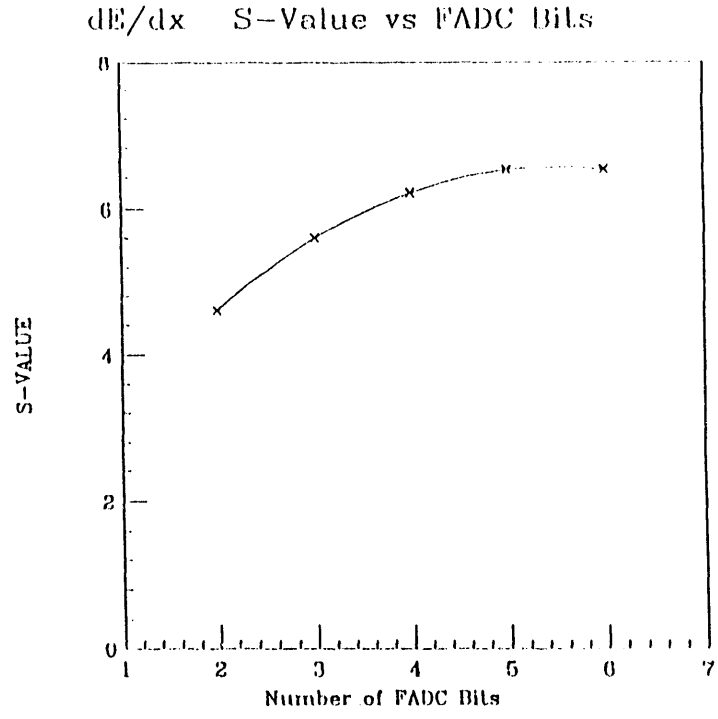

Figure 10: S-value for dE/dx e/π rejection vs. effective number of FADC bits

charged track in the detector to be reconstructed with a $\Delta p/p = 0.2\%$ at 1.0 GeV/c. GEANT calculations show that to achieve this one requires a single point resolution of $\sim 250\mu$m RMS. Reconstructing 4-plane detector tracks in our test data using a simple χ^2 algorithm yields a single point resolution of $230\mu m$ RMS for 0° tracks and $200\mu m$ RMS for 35° tracks (Fig. 11). Since the geometry and FADC clock cycle for both the prototype and our RHIC TRD are quite similar, we expect the position resolution for the test TRD to be about the same as that of the final TRD.

Summary

We have conducted a test run with a TRD that has the ability to do particle ID using both transition radiation and dE/dx measurements, while also tracking all charged particles through the detector with a single point resolution better than 250μm RMS. We have tested a variety of polyethylene foam radiators and found that, when normalized to a constant thickness in radiation lengths, they produce on average 50% less TR photons than polypropy-

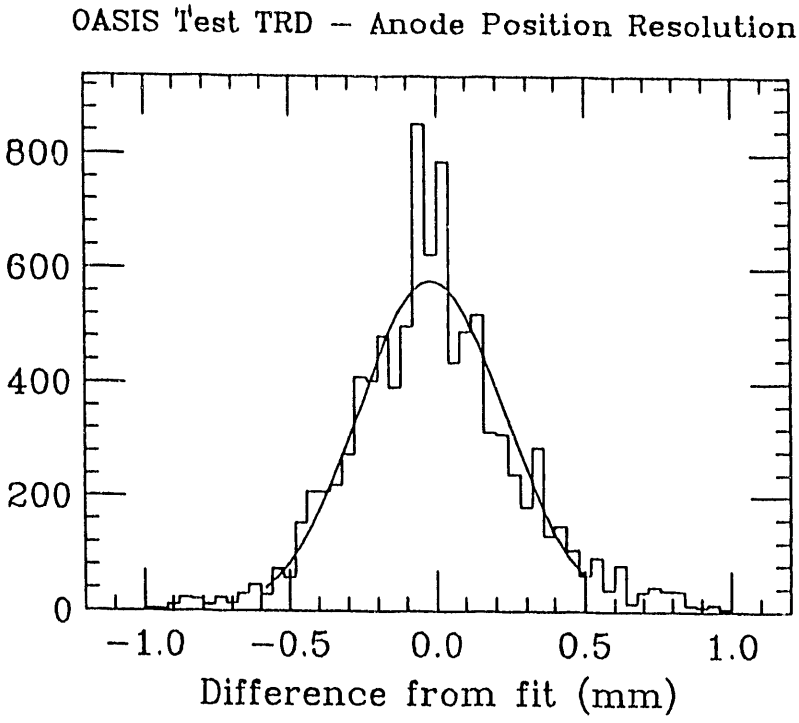

Figure 11: Single point, single plane track resolution of 230μm RMS using TRD anode wires, 0° track angle.

lene foil radiators. Results from foam radiator tests show that we can expect an e/π rejection of 3×10^{-2} for 8 planes of TRD and $p \geq 2.5 GeV/c$, while the equivalent foil radiator would yield a rejection of 3×10^{-4}. The e/π rejection using dE/dx run from 1.5×10^{-3} for 35° tracks at 1.5 GeV/c to 1×10^{-2} at 2.5 GeV/c. The dE/dx rejection is a function of both xenon content in the gas and track angle, however the dependance on track angle may be reduced with optimization of the gas mixture. The particle ID and tracking ability of the TRD we have tested is well matched to the performance requirements for detectors at RHIC.

Acknowledgments

We gratefully acknowledge the technical assistance of August Hoffmann. We would like to thank Bo Yu for his assistance with the figures and the analysis. We would also like to thank our AGS liaison engineer Dave Dayton, and the rest of the AGS staff.

References

[1] S. Nagamiya et al., RHIC OASIS experiment Letter of Intent, Brookhaven National Laboratory, unpublished.

[2] M. Clemen et al., Proc. of Symposium on Particle ID at High Luminosity Hadron Colliders, FNAL(1989),339.

[3] P. Rehak and A. Walenta,*IEEE Trans. Nucl. Sci.* NS-27, pp.54(1980).

[4] T. Ludlam et al.,*IEEE Trans. Nucl. Sci.* NS-28, pp.439(1981).

☆ U.S. GOVERNMENT PRINTING OFFICE: 1992—613-356

END

DATE FILMED

6 / 29 / 93